



HAL
open science

Behaviour of monopile under combined cyclic load

Ritesh Gupta

► **To cite this version:**

Ritesh Gupta. Behaviour of monopile under combined cyclic load. Materials Science [cond-mat.mtrl-sci]. Université Grenoble Alpes [2020-..], 2020. English. NNT : 2020GRALI019 . tel-02890439

HAL Id: tel-02890439

<https://theses.hal.science/tel-02890439>

Submitted on 6 Jul 2020

HAL is a multi-disciplinary open access archive for the deposit and dissemination of scientific research documents, whether they are published or not. The documents may come from teaching and research institutions in France or abroad, or from public or private research centers.

L'archive ouverte pluridisciplinaire **HAL**, est destinée au dépôt et à la diffusion de documents scientifiques de niveau recherche, publiés ou non, émanant des établissements d'enseignement et de recherche français ou étrangers, des laboratoires publics ou privés.

THÈSE

Pour obtenir le grade de

DOCTEUR DE L'UNIVERSITÉ GRENOBLE ALPES

Spécialité : 2MGE : Matériaux, Mécanique, Génie civil,
Electrochimie

Arrêté ministériel : 25 mai 2016

Présentée par

Ritesh GUPTA

Thèse dirigée par **Christophe DANO**, Maître de Conférences,
Université Grenoble Alpes

préparée au sein du **Laboratoire Laboratoire Sols, Solides,
Structures et Risques**
dans l'**École Doctorale I-MEP2 - Ingénierie - Matériaux,
Mécanique, Environnement, Énergétique, Procédés,
Production**

Comportement de monopieu sous chargement cyclique combinée

Behaviour of monopile under combined cyclic load

Thèse soutenue publiquement le **15 mai 2020**,
devant le jury composé de :

Monsieur CHRISTOPHE DANO

MAITRE DE CONFERENCES, UNIVERSITE GRENOBLE ALPES,
Directeur de thèse

Monsieur STEPHANE GRANGE

PROFESSEUR DES UNIVERSITES, INSA LYON, Président

Monsieur GUDMUND REIDAR EIKSUND

PROFESSEUR, NTNU A TRONDHEIM - NORVEGE, Examineur

Madame DIANA SALCIARINI

MAITRE DE CONFERENCES, UNIVERSITE DE PEROUSE - ITALIE,
Examineur

Monsieur PANAGIOTIS KOTRONIS

PROFESSEUR DES UNIVERSITES, ECOLE CENTRALE NANTES,
Rapporteur

Monsieur ALESSANDRO MANDOLINI

PROFESSEUR, UNIVERSITE DE LA CAMPANIE - ITALIE, Rapporteur



*dedicated to younger me
whose ambition became reality*

Acknowledgements

I want to express my sincere thanks to all the people who came across my PhD life with motivation, support and encouragement and made my ambition a reality. I am thankful to my parents and brothers for their blessings and continuous support on my career choice. I want to thank my sister-in-law and my niece for bringing joy and happiness into our family. I am thankful to my school teachers for paving my academic path and inculcating the interest and curiosity to explore scientific studies.

I am thankful to my thesis supervisor Christophe DANO for giving me the freedom in organizing my research work and exploring the subject. I am thankful to the jury members for reading and reviewing my thesis and providing me with encouraging and constructive remarks. I am thankful to the pôle PEM (Communauté UGA) for providing financial support for my thesis project through IRS-AGIR-PEPS program.

I am sincerely thankful to Prof. Stéphane GRANGE for my acquaintance with macro-element modelling and to Prof. Gudmund Reidar EIKSUND for sharing finite element modelling expertise and devoting valuable time in my thesis. I am thankful to Jean Benoit TONI for throughout technical support in my thesis work and being patient with me for French communication.

I am delighted to say thank you to Prof. Cino VIGGIANI for providing me with the wonderful opportunity to pursue my higher education in France. No amount of words can describe the influence you have brought in my life. I am grateful to you for having faith in me all these years. I want to thank Prof. Daniel LEVACHER and Dr Andry RAZAKAMANANTSOA, for their encouragement and support which made me come back to France for higher studies. I am wholeheartedly thankful to Prof. Rakesh Kumar DUTTA for motivating me to pursue a research career. I am earnestly thankful to Prof. Vijay Shankar DOGRA for ever-so-encouraging conversations and continuous guidance and support all these years.

I am blessed to have met so many amazing people during my time in Grenoble and I am delighted to call them my friends. A big part of my personal and professional growth belongs to the influence brought in my life by you all. I would like to mention how much you all mean to me by presenting a summary of the trip to my memory lane.

Marielle and David - the best office-mates one could ever wish for - thank you for your encouragement, love and care; Celly, thank you for accompanying me in both happy and difficult times; Yannick, thank you for inspiring with your work-ethic, Maria, thank you for all the insightful conversations, countless coffees and continuous motivation and care; Floriana, Chiara and Marta, thank you for all the food and drinks celebrations and fun conversations; Imane, thank you for both professional and personal motivation and support; Hani, thank you for all those deep philosophical discussion and mindset-development; Ivan and Aina, thank you for bringing a big positive influence in my life, motivating and mentoring me to pursue climbing and for numerous memories to cherish for life; Alex, thank you for being my climbing buddy, sharing that big laughter and random American idioms including our favourite one.

Anshul, thank you for your trust, honesty, positive influence, support and care; Nisha, Kritika, Nikita and Thoi, thank you for all our family alike cultural celebrations, food and conversations; Pushpendra, thank you for helping me in personal growth, for numerous adventures

and memorable experiences; Nisith, thank you for taking care of me like a younger brother and for all those countless table-tennis games. Finally, saving the best for the last: Parul and Ankit - my dear badkas, thank you for making the stay in Grenoble like a home away from home.

Concluding, I would like to thank the reader for going through all the acknowledgments. I sincerely hope you enjoy reading my PhD thesis.

Ritesh GUPTA

Abstract

Monopile is the most common foundation system for offshore wind turbine structures, statistically about 73%, as per Wind Europe, 2020 report. A pile can be defined as flexible or rigid depending on the embedded length to diameter ratio (L_e/D) and the relative stiffness of pile and soil. The existing codes for pile design are mainly developed for flexible piles, whereas monopile for new offshore wind turbines typically falls in the rigid category. The dominant complex cyclic wind and waves loads on offshore wind turbine structure and consequently on the monopile foundation, act in the lateral direction. The API design procedure, representing the lateral and vertical soil response through uncoupled non-linear springs, is developed for flexible piles and is recognised as conservative for rigid piles. The behaviour shall represent a coupled vertical and lateral soil-structure interaction because a rigid pile presents rotation deformation mode instead of deflection. The deformation mode further demands a different formulation mechanism, including the distributed moments along the pile shaft and shear & moment behaviours at the pile base as an essential part of the soil response investigations.

This work presents the numerical models aimed to address the limited understanding of coupling consideration of monopile installed in sand. The cone penetration tests performed in the calibration chamber, data treatment with ICP method and available Fontainebleau sand NE34 properties database in the literature provide the constituent parameters for model definition.

First, a PLAXIS 3D finite element model presents the model pile in the calibration chamber configuration with representative boundary conditions and the constitutive behaviour of the sand. The model pile geometry and load magnitudes are the outcomes of a similitude relationship with a representative prototype. A constant mass placed on the pile head represents the vertical load (the dead weight of the wind turbine structure). A simplified lateral point load represents the complex environmental loads, acting at a distance above foundation level, represents the lateral and moment load at mudline. Thus, vertical (V), lateral (H) and moment (M) collectively represent the combined load, investigated in both monotonic and cyclic loading cases. Different combined loading cases in the limits of horizontal and vertical load capacities represent the overall behaviour of the model pile. The observation of normal and shear stress changes close to the pile-soil interface at different depths quantify the pile-soil interaction. The response investigation at some strategic stress points in the FE model soil volume provides a basis for soil-stress transducers (SSTs) layout plan in the experimental soil volume. A methodology to formulate the lateral and shear stresses evolution close to the pile surface as representative of the coupled interaction is presented.

Second, a local-macro element (LME) model, an assembly of non-linear springs formulated using a Matlab toolbox ATL4S, presents the soil-pile interaction with inherent coupling considerations at different embedment depths. The PLAXIS model outcomes define the basis for a corresponding model scale LME model. The obtained results from both numerical investigations demonstrate the significance of vertical-lateral coupled interaction as a set of hypothesised equations for rigid monopile foundation. A similitude work provides a relation between a prototype scale and the lab-scale monopile model. It further aids in comparison and validation with the available experimental and numerical results in the literature.

Résumé

Le monopieu est le système de fondations le plus courant pour les structures d'éoliennes en mer, avec une occurrence d'environ 73% d'après le rapport Wind Europe de 2020. Un pieu peut être qualifié de souple ou rigide en fonction de son élancement (L_e / D) et de la rigidité relative du pieu et du sol. Les codes existants pour la conception de pieux sont principalement développés pour les pieux flexibles, alors que les monopieux pour les nouvelles éoliennes en mer entrent généralement dans la catégorie des pieux rigides. Les charges dominantes dues au vent et à la houle, de nature cyclique, sur le mât de l'éolienne et, par conséquent, sur la fondation, agissent dans la direction latérale. La réglementation API, qui représente la réponse du sol sous charges latérales et axiales au moyen de ressorts non linéaires non couplés, est développée pour les pieux flexibles et est reconnue comme étant sécuritaire pour les pieux rigides. Néanmoins, le comportement doit représenter une interaction sol / structure couplée axial-latéral puisqu'un pieu rigide présente un mode de déformation en rotation plutôt qu'une déflexion. Le mode de déformation exige en outre une formulation différente des mécanismes, incluant la distribution des moments le long du pieu ainsi que la prise en compte de la résistance au cisaillement de la base du pieu.

Ce travail présente un modèle numérique visant à prendre en compte le couplage axial / latéral pour un monopieu installé dans du sable. Les essais de pénétration au cône effectués dans la chambre de calibration traités avec la méthode ICP, et la base de données des propriétés du sable de Fontainebleau NE34 disponible dans la littérature fournissent les paramètres constitutifs pour la définition du modèle.

Tout d'abord, un modèle Eléments Finis PLAXIS 3D présente un pieu modèle dans la configuration de la chambre d'étalonnage avec des conditions aux limites représentatives et le comportement constitutif du sable. La géométrie du modèle de pieu ainsi que l'intensité des charges respectent les relations de similitudes entre modèle et prototype. Une masse constante placée en tête du pieu représente la charge verticale (la charge permanente de la structure de l'éolienne). Une charge ponctuelle latérale simplifiée représente les charges environnementales complexes, agissant à un certain excentrement par rapport au niveau de la fondation. Il en résulte une combinaison de charges verticale (V), latérale (H) et un moment (M), étudiée dans les cas de chargement monotone et cyclique. Différents cas de charge combinés dans les limites des capacités portantes horizontale et verticale représentent le comportement général du pieu modèle. Les variations de contraintes normale et de cisaillement à proximité de l'interface pieu/sol ont été étudiées, afin de caractériser cette interaction. L'étude des contraintes en plusieurs points stratégiques du modèle EF a fourni une base pour le calepinage des capteurs de pression utilisés dans la partie expérimentale. Une méthodologie permettant de formuler l'évolution des contraintes latérale et de cisaillement à proximité de la surface du pieu, en prenant en compte l'interaction couplée, est présentée.

Deuxièmement, un modèle de macro-éléments locaux (LME), un assemblage de ressorts non linéaires formulé à l'aide d'une boîte à outils Matlab ATLAS, présente l'interaction sol-pieu avec la considération du couplage inhérent à différentes profondeurs. Les résultats du modèle PLAXIS définissent la base d'un modèle LME à l'échelle du modèle correspondant. Les résultats obtenus dans les deux études numériques démontrent l'importance de l'interaction couplée vertical-latéral pour une fondation rigide de type monopieu. Un travail de similitude

concernant fournit une relation entre l'échelle du prototype et le modèle en laboratoire. Il aide en outre en comparaison et à la validation avec les résultats expérimentaux et numériques disponibles dans la littérature.

Contents

List of Figures	xv
List of Tables	xxi
1 Introduction	1
1.1 Offshore wind potential	1
1.2 Why monopiles?	3
1.3 Why combined loads?	5
1.4 Overview of the numerical modelling practices	6
1.5 Thesis outline	7
2 Literature review	9
2.1 Design of monopile foundation	9
2.1.1 Loading scenarios	10
2.1.1.1 Wind load	10
2.1.1.2 Wave load	11
2.1.1.3 1P and 3P loads	11
2.1.2 Simplification of complex loads	13
2.1.3 Design requirements	15
2.2 Pile-soil interaction	18
2.2.1 Axial pile-soil interaction	18
2.2.2 Lateral pile-soil interaction	23
2.2.3 Coupled pile-soil interaction	29
2.3 Macro-elements modelling	33
2.3.1 Global macro-element model	34
2.3.2 Local macro-element model	35
2.4 Stiffness parameters	36

2.5	Similitude	42
2.6	Conclusions	47
3	Simple local macro-element model	49
3.1	Objective	49
3.2	General description	49
3.3	Constitutive framework	50
3.4	Return mapping algorithm	52
3.5	Simple prototype scale model parameters	54
3.6	Model components	55
3.6.1	Lateral soil reaction (p-y) element	55
3.6.1.1	Reese p-y method	56
3.6.1.2	API p-y method	58
3.6.2	Drag element	59
3.6.3	Pile shaft resistance element	60
3.6.4	Pile base resistance element	61
3.7	Loading	63
3.8	Results	64
3.8.1	Flexible check	66
3.9	Conclusions	67
4	Lab scale models	69
4.1	Objective	69
4.2	General description	69
4.3	Similitude analysis	70
4.4	Model definition	72
4.5	Model analysis	76
4.5.1	Dummy beam approach	79
4.5.2	Structural volume approach	80
4.5.3	Lateral stress evolution hypothesis	82
4.5.4	Distributed moments hypothesis	85
4.6	From PLAXIS to LME model definition	87
4.7	Model components	88
4.7.1	Lateral soil-reaction element	89

4.7.2	Pile shaft resistance element	94
4.7.3	Distributed moment element	99
4.7.4	Pile base resistance element	103
4.7.5	Base shear element	106
4.7.6	Base moment element	107
4.7.7	Drag element	108
4.8	Results	109
4.8.1	Monotonic	109
4.8.2	Cyclic	109
4.8.3	Multi-directional loading	115
4.8.4	Modelling of the pile installation	117
4.9	Conclusions	119
5	Validation	121
5.1	Objectives	121
5.2	General description	121
5.3	Validation 1: LeBlanc [2010] lab-scale model	121
5.3.1	Similitude relations	122
5.3.2	LME model parameters calibration	123
5.3.3	Results	124
5.4	Validation 2: Prototype scale LME model with $Le/D = 3$	126
5.4.1	Similitude relations	128
5.4.2	Results	129
5.5	Validation 3: New prototype model with Le/D 4.5 and 6	131
5.5.1	Similitude relations	131
5.5.2	Results	131
5.6	Cyclic response for a large number of load cycles	135
5.7	Local element level similitude validation	137
5.8	Global stiffness check	138
5.9	How to use LME model for field-scale structures?	139
5.10	Conclusions	141
6	Conclusions and perspectives	143
	Bibliography	145

List of Figures

1.1	The wind energy trend production in Europe over the last decade, from WindEurope [100]	2
1.2	Overview of the existing offshore wind farms in Europe, from WindEurope [100]	2
1.3	Different types of offshore foundations, illustration by Josh Bauer, NREL, from Delony [33]	3
1.4	Share of monopile for substructure foundations, from WindEurope [100]	4
1.5	Components of OWT supported on monopile, from Arany et al. [10]	4
1.6	Pile-soil interaction modelling practices, from Abadie [2]	6
2.1	Flow chart of the iterative monopile design procedure, from Arshad and O’Kelly [11]	10
2.2	Demonstration of the typical loading in offshore wind turbines, from Nikitas et al. [73]	11
2.3	Simplified waveform of wind and wave loading representing the applied bending moment profile at mudline, from Cui and Bhattacharya [31]	12
2.4	Demonstration of the typical frequency band of wind and wave loads and the frequency band of 1P and 3P loads, from Kallehave et al. [55]	12
2.5	Utilization of complex load form as point loads, from Nikitas et al. [73]	13
2.6	The lab scale model setup reported by Leblanc et al. [60]	14
2.7	Simplified non-uniform lateral loading application using the ζ_b and ζ_c parameters, from Leblanc et al. [60]	15
2.8	Stiffness ratio vs aspect ratio, from Abadie et al. [3]	16
2.9	Rigid pile deformation about a pivot point (left) and flexible pile deflection (right) demonstration, from Sørensen et al. [96]	16
2.10	A demonstrations of the failure limit states for the monopile foundation design, from Arany et al. [10]	17
2.11	The conceptual demonstration of pile-soil interaction for an axially loaded pile (left) and its representation as per the T-Z and Q-Z methods (right), from Randolph and Wroth [84]	18

2.12	T-Z method definition, as per API [6] standard	19
2.13	Q-Z method definition, redrawn from the recommendation by API [6] standards .	20
2.14	The conceptual demonstration of p-y method for the lateral pile-soil interaction definition, modified from Arshad and O’Kelly [11]	23
2.15	Standard analytical model representing beam on non-linear Winkler foundation, from Kerner et al. [56]	24
2.16	The lateral soil reaction evolution with lateral displacement, modified from Reese et al. [85] reported theory	25
2.17	The depth factor coefficients A and B, reported by Reese et al. [85]	26
2.18	Distribution of lateral soil pressure at ultimate state by (a) Broms [20]; (b) Petrasovits and Award [80]; and (c) Prasad and Chari [82], from Lee et al. [61] . . .	27
2.19	Two types of soil-pile interaction on a monopile supported wind turbine, from Nikitas et al. [74]	29
2.20	Representation of the combined pile loading input and subsequent deformations, from Achmus and Thieken [5]	30
2.21	A typical interaction diagram obtained under the application of the combined vertical and lateral loading, from Achmus and Thieken [5]	31
2.22	The finite model for monopile foundation proposed in the framework of PISA project, (a) assumed soil reaction acting on the monopile and (b) 1D model, from Byrne et al. [25]	32
2.23	The comparative pile head displacement response from PISA models and standard API/DNV estimations for piles in sand, from Byrne et al. [24]	32
2.24	Demonstrative layout of the contribution from each reaction component of 1D PISA model pile, from Byrne et al. [24]	33
2.25	The 3D failure envelope of pile-soil interaction obtained under V-H-M loading application	33
2.26	The macro-element modelling concept demonstration, modified from Grange et al. [42]	34
2.27	Demonstration of all the stiffness parameters representing the pile-soil interaction, from Arshad and O’Kelly [12]	36
2.28	Transition from field scale pile-soil system to the global stiffness parameters representing the behaviour of monopile, from Bhattacharya et al. [19]	37
2.29	Stiffness parameters empirical estimation for rigid (a) and flexible (b) pile behavior, as reported by Bhattacharya et al. [19]	38
2.30	The moment rotation plot representing the concept of the long term cyclic response for model monopile, (a) cyclic loading, (b) static loading, from Leblanc et al. [60]	40

2.31	Demonstration of the pile head rotation accumulation for a long term cyclic loading, from Abadie et al. [1]	41
2.32	Demonstration of the backbone curve for the monotonic and cyclic loading correlation, modified from Abadie et al. [3]	41
2.33	Demonstration of the degrading soil secant stiffness under cyclic loading, from Arshad and O’Kelly [11]	42
2.34	Prototype to lab scaled model, from Kerner et al. [56]	44
3.1	Demonstration of the constitutive framework of the isotropic hardening plasticity, from Simo and Hughes [95]	50
3.2	Expanding yield surface in the isotropic hardening mechanism, from Simo and Hughes [95]	51
3.3	Demonstration of the return mapping algorithm, from Simo and Hughes [95]	53
3.4	Simple prototype local macro-element model assembly with a typical element composition presented in the a dotted box. The grey box (redrawn from Taciroglu et al. [98]) represents the local macro element at different depths	55
3.5	Visual representation of the drag element concept, soil response during loading (left) and unloading (right) scenarios, modified from Abadie et al. [3]	59
3.6	The lateral soil reaction (p-y) element evolution as per the definition from Reese et al. [85] and API [6] methods	60
3.7	Final deflection profile of model pile after the ULS design loading	64
3.8	Pile head displacement evolution for monotonic (ULS) and cyclic (SLS) loading cases	65
3.9	Comparative evolution of the lateral soil reaction at depths 1.5, 3.5 and 5.5m depths	65
3.10	Deflection profile for equivalently reduced diameter pile representing flexible pile behavior	66
4.1	General layout of the calibration chamber setup in 3SR laboratory, from Celeste [26]	73
4.2	PLAXIS 3D model of monopile in calibration chamber	73
4.3	Contour plots of PLAXIS 3D model phases of calibration chamber setup	76
4.4	Stress points layout	77
4.5	Lateral total stress variation at different stress points	78
4.6	Contour plot of shear stress in model soil under combined loading	78
4.7	Shear stress variation at different stress points	79
4.8	Bending moment and lateral soil resistance profiles from dummy beam approach	80
4.9	Shear force and lateral soil resistance profile pile 3D volume elements	81

4.10	The stress points along the pile surface (with 20mm offset) at different depths along pile embedment	82
4.11	Lateral soil resistance evolution around the pile under action of combined loading, modified from Arshad and O’Kelly [11]	83
4.12	Evolution of the lateral soil reaction with lateral displacement at different depths	84
4.13	Contour plot for the lateral displacement of the model soil under combined loading	85
4.14	Demonstration of the change in vertical shear stresses in the pile segment under combined loading resulting in the distributed moments	86
4.15	Evolution of the vertical shear stress as distributed moment in pile segment under combined loading	87
4.16	Normalised pile head displacement contours evaluated from the 10 combined loading cases on a circular failure surface	89
4.17	Soil reaction profile dummy beam and structural volume approach for the combined loading cases on the failure surface	90
4.18	The lab scale local macro-element model assembly with new definition of axial and lateral pile-soil interaction elements, distributed moment-rotation elements, pile base shear and moment elements	91
4.19	FEM analysis and mathematical formulations of the soil reaction evolution at 250 and 650 mm depths for all combined loading cases	92
4.20	The empirical formulation of ultimate soil reaction and lateral displacement for the definition of the lateral soil reaction element	93
4.21	Plot for vertical shear force and vertical displacement relation for the determination of standard element parameters	95
4.22	The empirical formulation of elastic and ultimate vertical displacement for the definition of the pile shaft resistance element	96
4.23	FEM analysis and mathematical formulations of the vertical shear force evolution at 250, 450 and 650 mm depths for all combined loading cases	97
4.24	The empirical formulation of plastic stiffness for the definition of the pile shaft resistance element	98
4.25	FEM analysis and mathematical formulations of the distributed moments evolution at 250, 450 and 650 mm depths for all combined loading cases	100
4.26	The empirical formulation of ultimate pile segment rotation for the definition of the distributed moment-rotation element	101
4.27	The empirical formulation of plastic rotational stiffness for the definition of the distributed moment-rotation element	102
4.28	FEM analysis and mathematical formulation for the pile base resistance evolution for pure axial loading case	104

4.29	Empirical formulation of the changing pile base resistance obtained from the LME model analysis	105
4.30	Normalised pile head displacement contours evaluated from the 10 combined loading cases on a circular failure surface	110
4.31	Demonstration of the consideration of a load combination within the failure circular load surface for input parameter determination for the element definition	111
4.32	Model triaxial test outcomes for Hardening soil model with different small strain stiffness parameters	111
4.33	Comparative PLAXIS and LME Pile head displacement plot for OW cyclic loading application	112
4.34	FEM analysis and mathematical formulations comparison of lateral soil reaction evolution at all local depth levels for 5 cycles of OW loading	113
4.35	FEM analysis and mathematical formulations comparison of distributed moment evolution at some local depth levels for 5 cycles of OW loading	114
4.36	Demonstration of the backbone curve feature from the LME model simulations under OW cyclic loading inputs with different amplitudes	114
4.37	Demonstration of each element contribution for the rigid pile behavior case 4 pile head displacements	115
4.38	Stress path evolution under the application of OW cyclic loading	115
4.39	Response analysis of the stress points under multi-directional loading application	116
4.40	Representation of the pile installation effect in jacked pile case	117
4.41	Comparison between PLAXIS and ICP method outcomes for pile installation	118
5.1	The pile head moment-rotation evolution plots	123
5.2	The contour plot for the normalised pile head displacement for LME model of LeBlanc lab scale model equivalent	125
5.3	Pile head lateral displacement evolution for 5 cycles of one-way cyclic loading	125
5.4	The demonstration of the backbone curve feature for different cyclic loading cases simulated using LME model	126
5.5	The local level element evolution for LeBlanc lab scale LME equivalent model	127
5.6	The comparative plot for soil reaction evolution	129
5.7	Contour plot for combined pile head total displacement with $L_e/D = 3$	129
5.8	The pile head moment rotation plots	130
5.9	Demonstration for the element contribution for new prototype scale model definition with coupled interaction	130
5.10	The contour plots for the different combined load cases present on the failure surface for two different prototype scale pile geometries	132

5.11 Plot for pile head displacement under one-way combined loading ($H = 13.5$ MN and $V = 27$ MN) for L_e/D 4.5 and 6 pile geometry	133
5.12 Coupled interaction effect demonstration with increasing pile aspect ratio	133
5.13 Element level evolution demonstrating the lateral soil reaction element response above and below the pile rotation point and three pile-soil interaction zones for the distributed moment element	134
5.14 The evolution of the normalised pile head rotation with increasing number of lateral load cycles applied at the model pile head	135
5.15 The evolution of the normalised pile head displacement with normalised lateral load applied at the model pile head	136
5.16 Flowchart of the guidelines for LME model calibration and utilisation	140

List of Tables

2.1	Defining parameters of T-Z curve as per API [6] standard	19
2.2	Defining parameters of Q-Z curve as per API [6] standard	20
2.3	Non-dimensional groups presenting scaling laws, reported by Kerner et al. [56]	43
2.4	Non-dimensional groups presenting scaling laws, reported by Bhattacharya et al. [17]	45
2.5	Non-dimensional groups presenting scaling laws, reported by Leblanc et al. [60]	45
2.6	Non-dimensional groups presenting scaling laws, reported by Byrne et al. [25]	46
2.7	Non-dimensional groups presenting scaling laws, reported by Burd et al. [22]	46
2.8	Non-dimensional groups presenting scaling laws, reported by Klinkvort and Hededal [57]	46
3.1	Pile and soil parameters defining simple prototype macro-element model	54
4.1	Prototype and model geometrical features and soil properties	71
4.2	Load magnitudes and deformation modulus for prototype and model pile cases	71
4.3	Similitude parameters for load and geometry	72
4.4	3D FE model parameters for pile, soil and calibration chamber representative confinements	74
4.5	Normalised load magnitudes collectively composing the circular failure loading surface	88
5.1	Pile and soil parameters for the LME model definition with Leblanc et al. [60] lab scale model features	122
5.2	Similitude relations for load and displacements between PLAXIS model and LeBlanc lab scale model	122
5.3	LME model parameters estimated for equivalent LeBlanc lab scale model	124
5.4	LME model parameters estimated for new prototype model with $L_e/D = 3$	128
5.5	Similitude relations for load and displacements between PLAXIS model and new prototype model with $L_e/D = 3$	128

5.6	LME model parameters estimated for new prototype model with $L_e/D = 4.5$ and 6	131
5.7	Similitude relations for load and displacements between PLAXIS model and new prototype model with $L_e/D = 4.5$ and 6	132
5.8	Similitude parameters estimation for the local level element behaviour definition	137
5.9	Global stiffness response check for all LME model cases simulations	138

Chapter 1

Introduction

The thesis project is inspired by the exploration of the offshore wind energy envisioned as a prominent source of renewable energy for sustainable development and the mitigation towards limiting the global climate change.

The present thesis work aims to understand the soil-structure interaction behaviour of pile foundations in offshore wind turbine applications. In this chapter, a brief introduction to the thesis project is presented. The motivation behind the PhD thesis project is reflected through the description of the project title. The background of offshore wind potential, wind turbines supported on monopile foundation, combined loading input, pile-soil interaction and different modelling methodologies are presented briefly. The goal of the project is to understand rigid pile-soil interaction mechanisms under combined horizontal (H), vertical (V) and moment (M) cyclic loading conditions through numerical studies.

1.1 Offshore wind potential

Wind energy generation through wind turbines has proven to be of great value for large scale future investments in the energy industries worldwide. A constant search for enormous wind potential has pushed the industry from onshore towards offshore solutions with superior and more stable wind conditions. A recent report by WindEurope [100] presents the growing wind energy production trend over the last decade in Europe, as shown in Figure 1.1.

A significant share of the total energy production comes from the onshore wind farms. Even though the percentage of the offshore wind farms is comparatively low, it is gaining more attention year after year. Figure 1.2 presents an overview of the existing offshore wind farms in North Europe majorly in the UK, Denmark and Germany.

The offshore wind power is rapidly growing as an ideal renewable energy source in the context of the present global climate situation. The French Grenelle laws have aimed towards the installation of wind farms on the north-west coasts by 2020 with a generation capacity of 6 GW, as reported by [56]. As the industry blooms, the technologies are progressing for more efficient design practices and construction cost reduction to reduce the cost of produced energy further. To this date, Hornsea One wind farm is becoming the world's largest offshore wind farm, located 120 km off England's Yorkshire coast. It comprises of 174 wind turbines each of

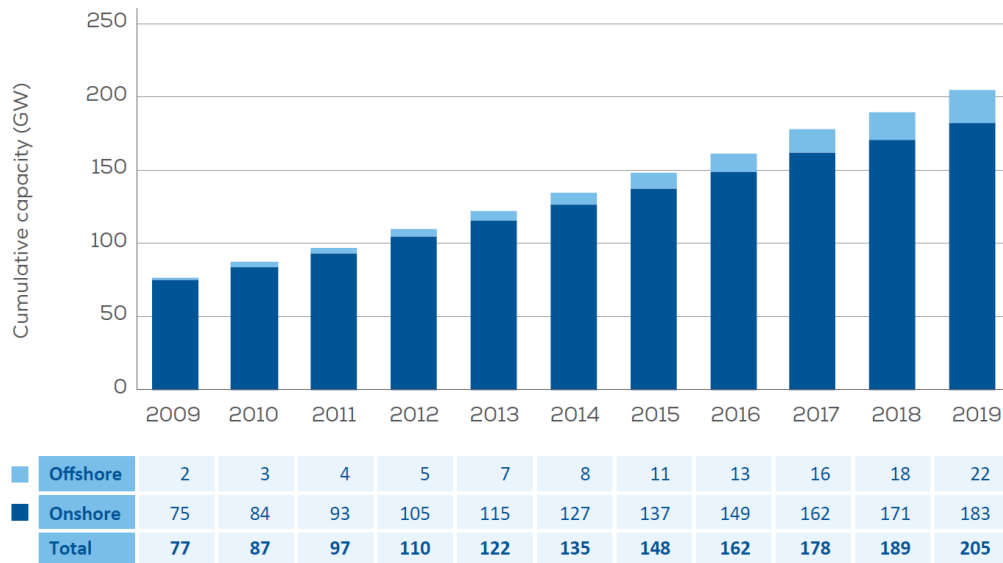


Figure 1.1: The wind energy trend production in Europe over the last decade, from WindEurope [100]

7 MW capacity with towers that are each nearly 100 meters tall. Upon completion in 2020, it will produce enough energy to supply 1 million UK homes with clean electricity.

The size of the wind turbine structure is ever increasing with an aimed capacity of the wind turbine beyond 10 MW. The subsequent effect of the increasing size is translated proportionally to the support structures. There are several foundation designs used in practice to support these structures. Aiming for more effective wind conditions corresponds to seeking for more remote offshore sites and consequently higher sea depths. Installing the wind turbines at such depths involves high stakes and high expenses, both from the financial and the engineering point of view. Nonetheless, several different foundation structures for various sea depths and soil conditions have been proposed for the offshore wind turbines.

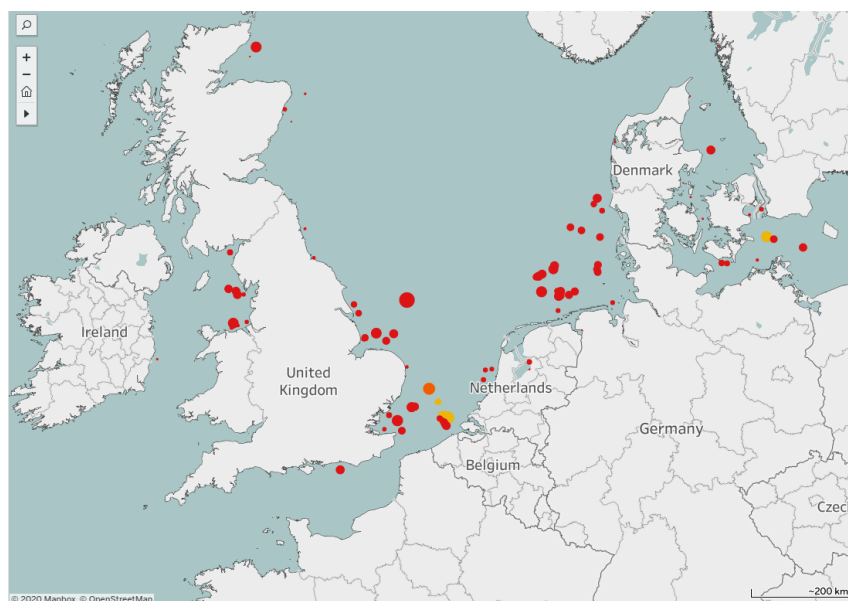


Figure 1.2: Overview of the existing offshore wind farms in Europe, from WindEurope [100]

Bhattacharya and Adhikari [16] have reported the viability of the offshore wind farms as a solution to the modern days' energy problems. The significant distance (more than 10 km) away from the landmass eliminates the noise, vibration and size effects on the locality. The foundation cost alone covers a significant portion of the allocated budget for the offshore wind farm construction. Hence, a detailed understanding of the foundation structure is necessary for cost-effective, optimised and durable design practices.

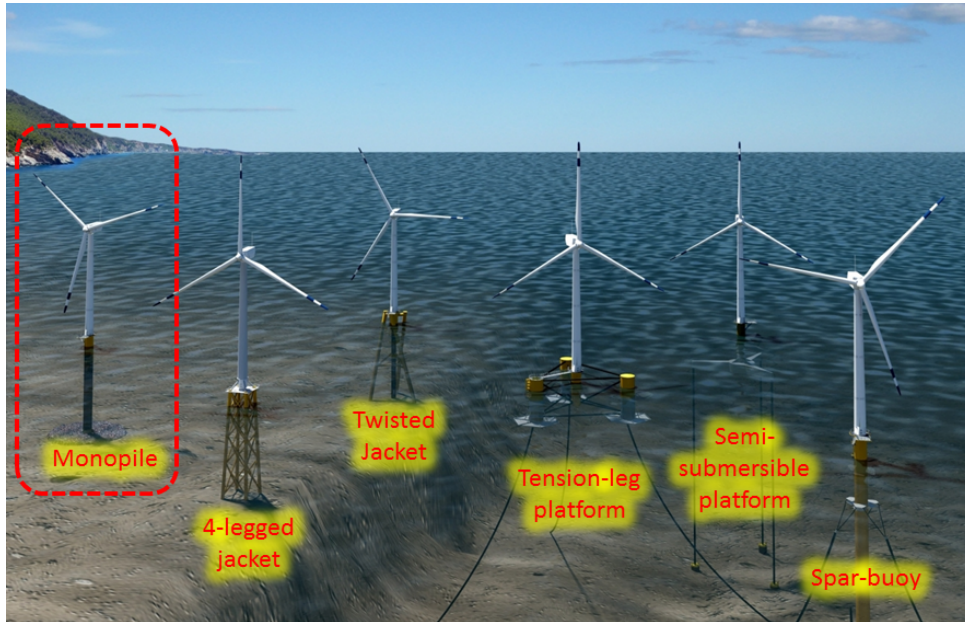


Figure 1.3: Different types of offshore foundations, illustration by Josh Bauer, NREL, from Delony [33]

Figure 1.3 presents different support structures under consideration, namely monopile, jacket and twisted jacket structures for shallow water levels (around 30 m water depth). Some other foundation designs such as twisted jacket, semi-submersible and tension-leg platforms, and spar buoy for deeper water levels (more than 60 m) are also getting considered by the industries. A monopile is a steel tube bored or driven into the seabed and attached to the tower via a transition piece. Jacket foundations comprise either three or four small diameter poles, connected with a truss structure, attached to seabed driven small piles. In the present research work, the study on only the monopile type of foundation structure is carried out. A brief description of this motivation is presented hereafter.

1.2 Why monopiles?

Monopile is the most popular foundation choice in terms of ease of installation, economy, and logistics in most parts of the world. As reported by Negro et al. [72], the trending research is focused on the typical hollow, steel cylinder with large diameter monopiles used as foundation and sub-structure for offshore wind turbines. This type is the most common in offshore wind turbine structures, having been used as the foundation of 4258 wind turbines, which represents about 73% of the OWT installations, as per the report of WindEurope [100] (see Figure 1.4).

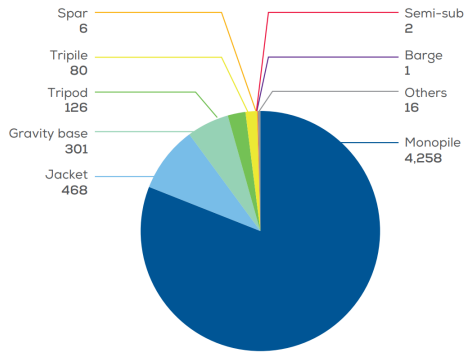


Figure 1.4: Share of monopile for sub-structure foundations, from WindEurope [100]

The monopile concept is the dominated foundation design, jackets and gravity base foundation structures are second and third on this list, as reported by the National Renewable Energy Laboratory (NREL) of US Department of Energy [33]. Statistically, monopile cover 75 per cent, jackets cover 10 per cent, and gravity base includes 8 per cent of the market share, as per NREL report. A gravity-based foundation, as its name represents, is a concrete foundation buried in the seabed and is applicable for shallow (up to 10m) water depth.

The monopiles have emerged as a highly valuable tool for offshore wind turbine installation issues. Many researchers for about the last two decades are

working on the development of offshore foundation systems with a high emphasis on linking the existing knowledge of deep foundation systems to the new aspects applicable for offshore foundation systems. Figure 1.5 presents typical components of the offshore wind turbine supported on the monopile foundation. Three key elements are pile, tower and transition piece connecting the other two.

The required monopile length and diameter are primarily dependent on the OWT's power generation capacity, which is an indirect measure of the applied loading. In general, the factors affecting the cyclic response include the monopile diameter and embedment length, soil properties, soil-pile relative stiffness, loading characteristics, and pile installation method. The length (L_e), diameter (D) are indeed not independently controlled for monopile foundations. Instead, there exists a link between two called L_e/D ratio or aspect ratio. This parameter is the first and foremost parameter to address and justify a monopile foundation. Arany et al. [10] stated that this ratio determines whether the pile will be flexible or rigid. Moreover, Negro et al. [72] and Nikitas et al. [74] presented clear statistics for a preliminary estimate of main dimensions for monopile foundation design.

To this date, there are several offshore wind farms supported on monopile foundations. Oh et al. [76] presents a technical report of the offshore wind farms constructed in monopile foundation in Europe with each tower power generation capacity ranging from 2 to 6 MW where the majority of wind farms are with around 3.5 MW capacity. A piece of brief information on some of the existing wind farms is presented hereafter.

One of the biggest offshore wind farms with 80 Vestas 2 MW wind turbines is Horns Rev near Esbjerg, Denmark, where all turbines are founded on monopiles and were fully operational

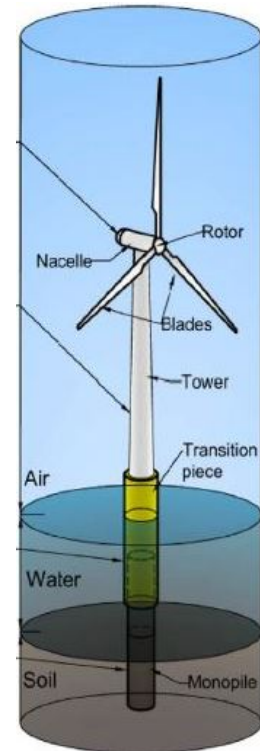


Figure 1.5: Components of OWT supported on monopile, from Arany et al. [10]

on 11 March 2002. This 20 km^2 wind farm has a production capacity of 160 MW, serving approximately 150,000 Danish households annually.

Moreover, NREL reported that the jacket structure could be an ideal candidate for the deeper water levels. The jacket structures are founded on piles mainly under the vertical load application. However, the improvement and further development in the monopile design practices have extended their applicability beyond the shallow water depth ranges. The continuous research work is highly likely to push these limits even farther than the original expectations. One of the most in-depth applications of monopile foundations is at Veja Mate — a 402 MW project in the German North Sea using 6 MW Siemens wind turbines in 40-meter depths, fully commissioned in May 2017.

1.3 Why combined loads?

The monopile foundation experiences a vertical load (V) as the dead weight of the wind turbine superstructure. The lateral loading (H) is experienced by the tower structure as a combination of wind and wave loads with an eccentricity, allowing the additional moment load (M) application on pile head at mudline level. Thus, a monopile is subjected to a combined V-H-M loading input. In standard design practices, the axial and lateral pile-soil interactions due to vertical and lateral loading respectively are considered uncoupled, because these design guidelines are based on the flexible pile design.

The combined load input results into the axial and lateral pile-soil interaction. In usual practice, standard API design procedure comprising nonlinear p-y interaction methodology is used to investigate the lateral loading behaviour of a monopile foundation. This approach is recognised as a highly conservative [14]. Instead, the soil-structure interaction for rigid monopile foundation is preferably coupled vertically and laterally. Also, the base of the pile contributes towards the lateral loading response in the rigid pile-soil interaction, as reported by [25]. Therefore, a combined loading study presents a research strategy to describe the coupled pile-soil interaction for a rigid monopile foundation.

Achmus and Thieken [5] reported from 3D numerical simulations that the application of a combined lateral and axial compression loads increase the pile stiffness and capacity, where the rigid piles present particularly strong interaction effects. The tension combined loading shows the opposite effect. Therefore, the coupled pile-soil interaction can offer either favourable or unfavourable consequences; hence, its investigation is necessary. The DNV recommendations DNV [36] for offshore wind turbine structures also include the update F.2.4.1 stating the standard lateral soil reaction and displacement curves are not applicable for monopiles with a large diameter. The pile base resistance, shear stresses along the pile shaft, and moment-rotation relationships contribute significantly to the overall rigid pile behaviour [25], making the coupled response investigation more extensive.

Some researchers have studied the foundation behaviour for combined vertical (V), horizontal (H) and moment (M) loading conditions for shallow foundations [30], [23], [47] and deep foundations [63]. In this work, the available literature on the combined loading behaviour is used as a benchmark to study the same for rigid monopile foundation and to introduce ‘coupling’ under combined load application.

1.4 Overview of the numerical modelling practices

In geotechnical engineering practice, the understating and representation of the pile-soil interaction is crucial work. Over many past years, three modelling approaches have been widely used in this regard. Figure 1.6 presents the demonstration of the different modelling practices namely (1) 3D finite element, (2) Winker's beam based and (3) global stiffness model, to carry out the pile-soil interaction studies. The three design approaches are described briefly hereafter.

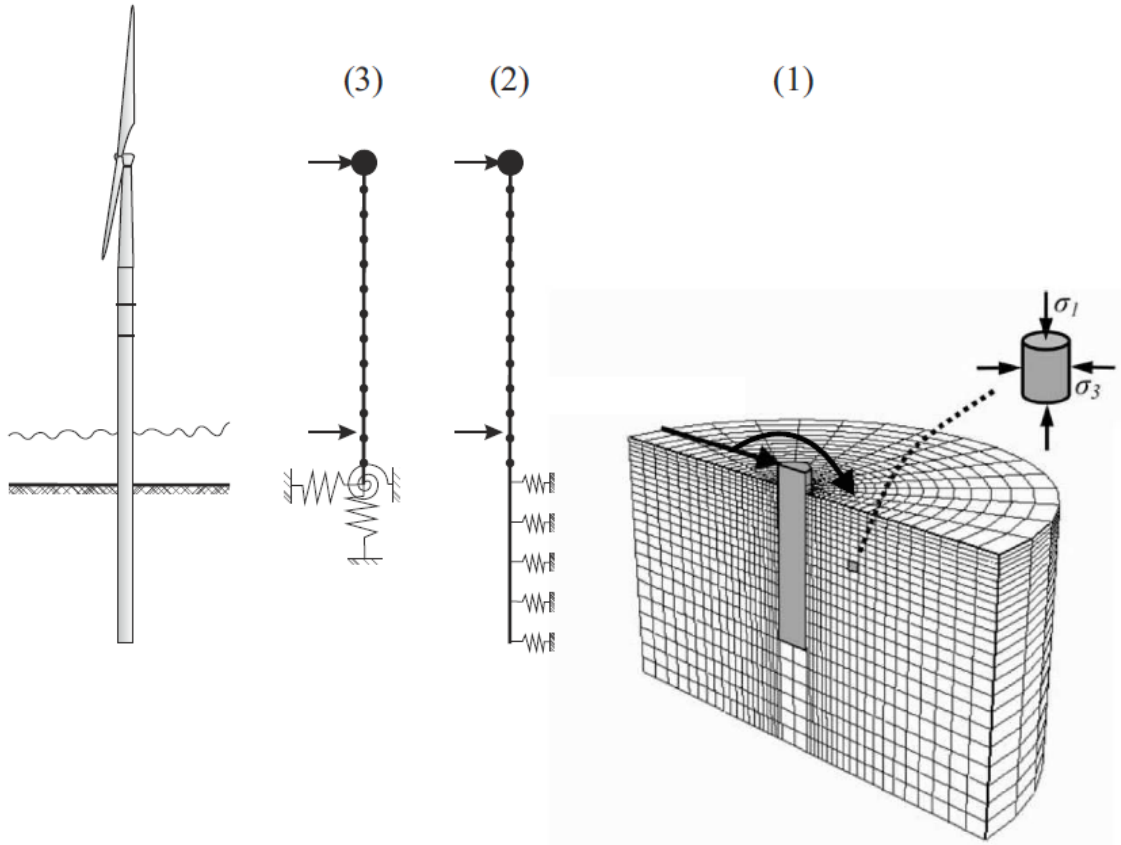


Figure 1.6: Pile-soil interaction modelling practices, from Abadie [2]

1. Complete 3D Finite Element (FE) analysis allows the entire soil continuum to be modelled and can predict the detailed and realistic response of the foundation. It requires an appropriate constitutive model and input soil parameters representative of the equivalent field characteristics. It is the most accurate numerical modelling method and probably the most suitable for modelling complex soil stratigraphies and foundation geometries. However, rigorous cyclic loading modelling using 3D FE analysis is not possible due to the absence of a robust constitutive soil model. The SANISAND model ([32]) is one of the recently introduced soil model having stress-ratio controlled and critical state compatible sand plasticity model features. The model definition ensures realistic simulation of the sand behaviour under undrained cyclic loading. Liu et al. [64] have used this model to study the cyclic ratcheting behaviour of sands. Besides, the use of 3D FEM models for cyclic loading study brings add-ons difficulties regarding the computation time as a cycle by cycle method would probably become prohibitive for use in long-term cyclic loading analysis. Hence some more simple methods are also used to optimise the time, and the degree of the information explored.

2. The Winkler-type approach is a 1-D model where the pile acts as a beam, and the soil-pile interaction response is represented by a series of independent springs down the pile embedment length (L_e). Soil layers can be considered, but the model cannot capture the interaction between the strata. It is computationally fast and is, therefore, a satisfactory compromise between accuracy and time. In current practice, the design of offshore piles to resist lateral loading is addressed using the nonlinear Winkler modelling approach. The design method does not provide a means of calculating the accumulated pile deflection (rotation) that occurs during cyclic loading. Changes in the surrounding soil stiffness as a result of long-term cyclic loading, which typically densifies (but in some circumstances may loosen) are also poorly accounted for in current design methodologies based on Winkler modelling approaches ([2]). Recent experimental and numerical studies have reported the over-conservative nature of these bespoke methods while estimating the foundation capacity. Some estimates have suggested that new design methods can potentially improve the design guidelines with approximately 30% reduction in steel requirement and subsequently significant cost reduction.

3. Finally, the most straightforward technique consists of a surface spring model where the entire behaviour of the foundation is reduced to representative springs at the soil surface, also called a global macro-element model. This type of model is very simplistic and is consequently can be considered the least accurate. It is also challenging to calibrate when considering layered soil profiles. However, it is computationally fast and efficient in modelling the foundation within structural analysis packages. Many researchers over past years have extensively studied the macro-element concept (e.g. [41], [86], [63], [78]). The present thesis work has a key focus in the understanding and the development of a local macro-element model to represent rigid pile-soil interaction under combined loading. Therefore, more details on macro-element modelling are presented in the following chapters.

1.5 Thesis outline

The present work comprises of six chapters briefly outlined hereafter.

Chapter 1 (*Introduction*) presents the different components of the thesis project title. A brief description of the offshore wind turbine support structures is presented, focusing on the monopile foundation type. A general trend of the pile-soil interaction under lateral load and by extension, the combined load application is presented. Lastly, the current design and analysis practices describing the monopile behaviour under combined cyclic loading is presented.

Chapter 2 (*Literature review*) presents a synthesis of the soil-pile interaction study carried out by many researchers over the past many years. The design requirements for the offshore wind turbine foundation with a simplification of the complex environmental loads is presented. The different failure mechanisms of the rigid and flexible foundations highlight the challenges in the current practices. The basis of axial, lateral and aspired coupled pile-soil interaction methods is presented. The concept of macro-element for pile-soil interaction modelling is presented with a general description of its components and relevance with the present thesis project. A synthesis of the stiffness parameter representative of the key characteristic of the macro-element and pile-soil interaction is presented. Lastly, the correlation between prototype and model scales examined by previous researchers based on the similitude study of pile-soil interaction are

summarised.

Chapter 3 (*Simple local macro-element model*) presents the development of a simple local macro-element model of rigid monopile foundation where the axial and lateral interaction elements are developed following the well-established pile-soil interaction mechanisms. The constitutive law and numerical solution algorithm used in the definition of the local macro-element model are presented. The obtained results are validated against the analytical methods to check the quality of the local macro-element model.

Chapter 4 (*Lab scale models*) presents two lab-scale numerical models of lab-scale monopile foundation assuming placed in the calibration chamber setup. A similitude work between simple prototype scale model and lab-scale model defines the model geometry and loading parameters. A methodology to extract and process the soil-stress data for the definition of the pile-soil interaction is presented. The 3D FE model analysis is further carried out to define a coupled pile-soil interaction hypothesis as empirical mathematical formulations. A new local macro-element model definition with coupled interaction feature is developed as an outcome of the mathematical formulations.

Chapter 5 (*Validation*) presents the validation of the lab-scale local macro-element model against a previously reported lab-scale model of monopile under lateral load application. The validation is further extended to the field-scale models by reuse of the similitude relations correlating the model outcomes with the prototype scale. The necessity of the coupled interaction study is highlighted through the comparison of different model outcomes. Lastly, the general guidelines to use the local macro-element model are presented.

Chapter 6 (*Conclusions and perspectives*) presents the key findings of the thesis and proposals for future research work.

Chapter 2

Literature review

The present chapter highlights the literature review focusing on pile-soil interaction behaviour for offshore wind turbine foundation applications. A brief description of the loading conditions in the offshore wind turbine environment is presented, along with the simplified load representation for model studies and the essential design requirements concerning pile-soil interaction. The previous research work on the concept of macro-element modelling and its components is presented. Lastly, the concept of similitude study is presented, defining a correlation between the prototype and lab-scale investigations.

2.1 Design of monopile foundation

The design of a monopile foundation for offshore wind turbine (OWT) applications comprises many components. Arany et al. [10] reported the steps towards a monopile foundation design with an emphasis on the geotechnical design. In the practical aspect, some key factors to be considered for the foundation design are the complexity of the loading conditions and the geotechnical profile. The allocated budget for a project strongly influences the exploration of these two components.

Arshad and O’Kelly [11] reported an iterative procedure for the design of the OWT supported on a monopile foundation. The procedure is illustrated in Figure 2.1. The input data required for the design process comprises of environmental load, turbine capacity, geometry and soil profile data. The iterations amongst trial pile geometry, extreme load cases, pile embedment length and pile strength estimations define the design process. Here, the pile geometry and embedment length are the two key parameters of interest for geotechnical investigation concerning the monopile interaction with the surrounding soil. The environmental database is used to determine the required work-platform and hub elevations for the OWT. The initial trial dimensions and geometry for the monopile foundation are also selected based on the environmental data. A monopile design process also involves the determination of the natural frequency of the whole system and its relation with the input load components. The predictions of the anticipated rotation, deflection, and settlement responses produced by the applied loads and moments are determined from the environmental and wind turbine data. The fatigue and buckling checks are performed at a more advanced stage of the design process, usually using computer software packages.

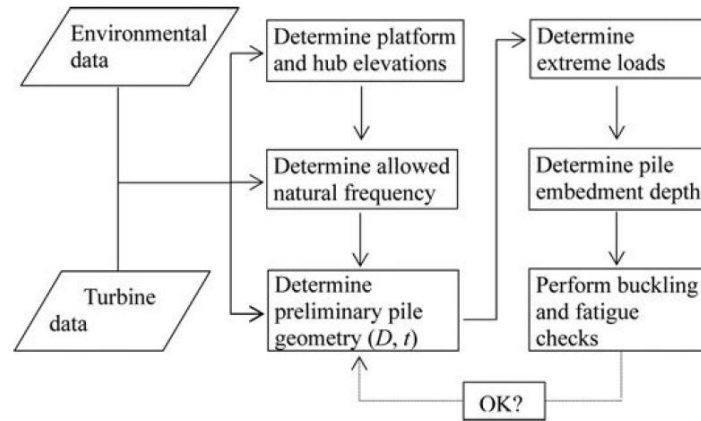


Figure 2.1: Flow chart of the iterative monopile design procedure, from Arshad and O’Kelly [11]

Overall, for OWT monopile foundations, the pile must mobilize sufficient soil resistance over its embedded length for applied load transfer from pile to the soil, with adequate safety factors to prevent the excessive deflection/rotation of the pile and consequently the OWT tower structure. The geotechnical conceptual understanding of the monopile supported OWT mainly comprises of the input environmental loads and the mechanism of the pile interaction with the surrounding soils. A brief description of these components is presented hereafter.

2.1.1 Loading scenarios

One of the key challenge and significant step in offshore foundation design is to explore the actual loading scenarios on an offshore wind turbine. A typical wind turbine is exposed to lateral wind and wave loadings in general. Arany et al. [10], Bhattacharya et al. [19] presented detailed information about loading in offshore foundations and also highlighted the constraints in the representation of the corresponding lab experimental work. There are four types of loads, namely wind, wave, 1P and 3P, which act on a typical offshore wind turbine structure and subsequently transferred to the foundation. Here, 1P and 3P loads are representative of the interaction of wind with the turbine’s rotor and wings, respectively. Figure 2.2 below demonstrates a typical waveform of all these load types.

The loads acting on the wind turbine rotor and substructure comprise of static load due to the self-weight of the components and the cyclic/dynamic loads arising from the wind, wave, 1P and 3P loads. A brief description of the load types is presented as follows.

2.1.1.1 Wind load

Wind loading in an offshore wind turbine is a very complex waveform with high variation in amplitude, speed and direction. Wind loads on offshore structures are seldom greater than the hydrodynamic loads. They often play a relatively minor role, compared with the hydrodynamic loads for load input in the foundation. However, wind loading has a longer lever arm when considering moments generated about the structure’s foundation. Byrne and Houlsby [23] reported that in a typical North Sea environment, the rotor thrust reaction due to the wind loads contributes about 25% of the total horizontal load but generates 75% of the total overturning

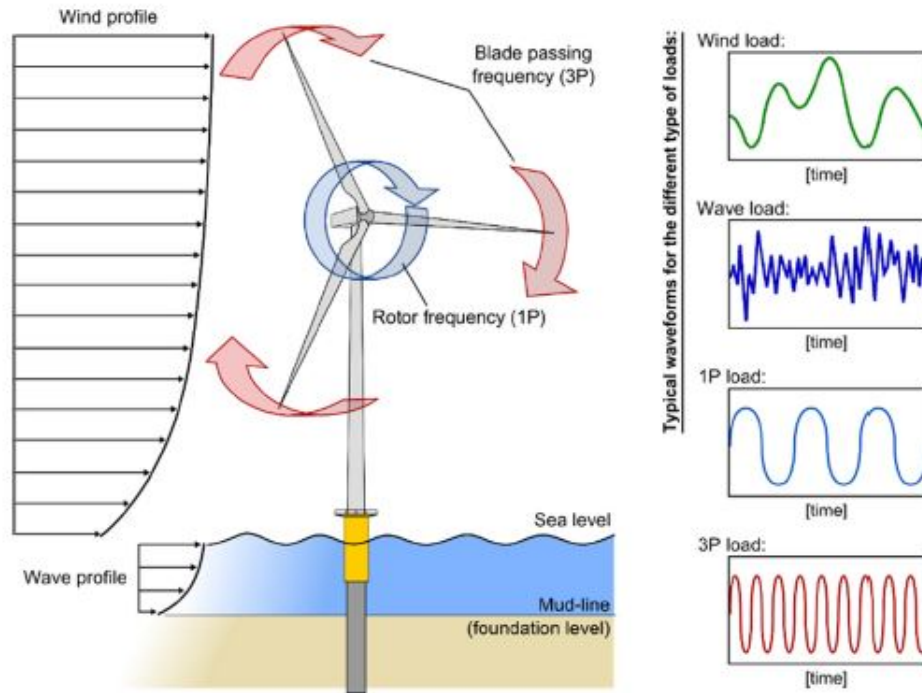


Figure 2.2: Demonstration of the typical loading in offshore wind turbines, from Nikitas et al. [73]

moments. The rotating blades apply a cyclic/dynamic lateral load at the hub level (top of the tower) and are a function of the wind turbulence. A wind speed of 25 m/sec is considered very high for a wind turbine, and usually, it is shut down for operation at this speed.

2.1.1.2 Wave load

Likewise, wind loading, the wave loading has also a very complex waveform having frequency typically about ten times to that of typical wind loading [31]. Most importantly, wave loading is highly dependent on the water depth. Normally, monopiles are preferred up to 30m of water depth. Arshad and O'Kelly [11] reported that a correct evaluation of the total hydrodynamic load must consider the combined current flow and wave-particle velocities. The frequency of the wave loads is typically in the range of 0.1-0.12Hz [56]. In order to utilize the wind and wave load scenarios in laboratory experiments, many researchers [10], [19], [31] recommend a cyclic waveform as presented in Figure 2.3. Also, as per Arany et al. [10], Wave load depends on the monopile diameters, and therefore, the wave load estimate is possible after the availability of the initial pile geometry parameters. The cyclic behaviour of a monopile foundation is mainly due to the combination of these two loading.

2.1.1.3 1P and 3P loads

The rotor mass and aerodynamic imbalances generate vibration at the hub level and apply lateral load. This load possesses a frequency equal to the rotational frequency of the rotor. It is referred to as 1P loading in the literature [10]. The industrial wind turbines machines are mostly

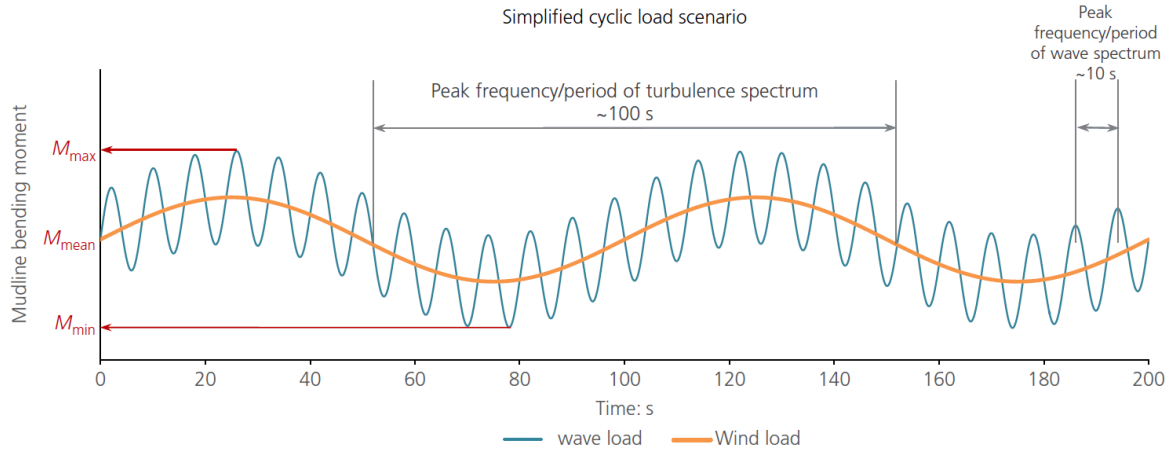


Figure 2.3: Simplified waveform of wind and wave loading representing the applied bending moment profile at mudline, from Cui and Bhattacharya [31]

variable speed machines, and thus 1P is a frequency band associated with the lowest and the highest revolutions per minute (rpm). The 3P load is an extension to the 1P load conceptualised from the passing of turbine blades in front of the tower structure. The frequency of this load is three times for a typical three-blade wind turbine and could be 2P if wind turbine possesses two blades. The frequency of these loads plays a vital role in the design of the wind turbine structure. The frequency magnitude decides the design the natural frequency of the system.

1P and 3P load forms may not be prominent concerning magnitude compared to wind and wave loads [8], but they play a critical role in the control of the dynamic response of wind turbine-foundation system. Figure 2.4 presents the power spectral density (PSD) map of the wind and wave load forms along with the frequency band of 1P and 3P loads.

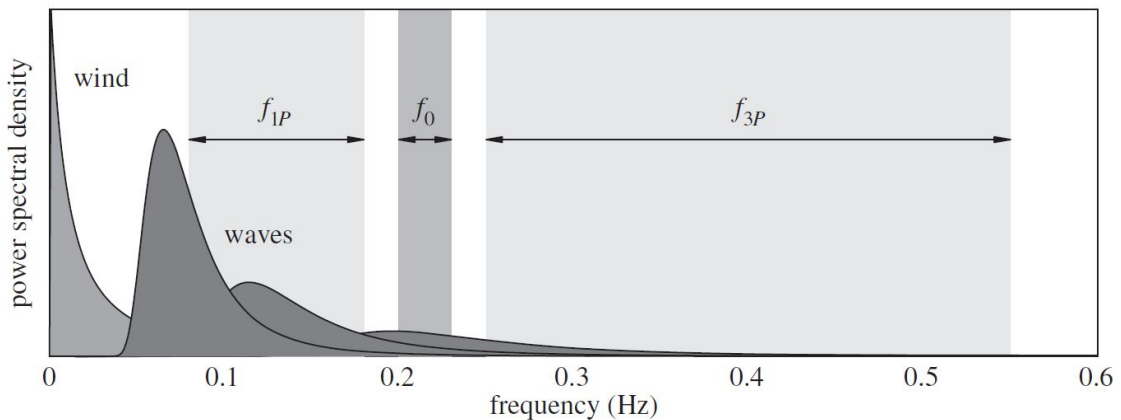


Figure 2.4: Demonstration of the typical frequency band of wind and wave loads and the frequency band of 1P and 3P loads, from Kallehave et al. [55]

The primary driving motive for the design procedure is to avoid the occurrence of resonance in the dynamic behaviour of the structural system under in-service loading [10]. The designed frequency of the overall system must be kept away from the frequency content of applied loads, to avoid the resonance of the system. Specifically, the natural frequency of the wind turbine should be at least $\pm 10\%$ away from the 1P and 2P/3P frequencies. With these

considerations, there are three possible slots where the natural frequency of the system may necessarily lie. They correspond to three different design approaches namely: soft–soft (natural frequency $<1P$), soft–stiff (natural frequency between $1P$ and $2P$ or $3P$) and stiff–stiff (natural frequency $>2P$ or $3P$). The most common design use is in ‘soft–stiff’ range, which implies that the natural frequency lies between $1P$ and $3P$ [31].

Bhattacharya and Adhikari [16] reported that designing foundations for OWTs is critical due to the dynamic characteristics of the tower–foundation system. It results in the natural frequencies of these structures very close to the forcing frequencies. A designer apart from predicting the global natural frequency of the structure must also ensure that the overall natural frequency due to soil–structure–interaction does not shift towards the forcing frequencies.

2.1.2 Simplification of complex loads

The work reported by Arany et al. [10] extensively elaborates the waveforms and the worst loading scenarios. These waveforms are very complex and hence a simplified, but representative load magnitudes, amplitude and frequency of wind and wave loadings are used for lab experiments. The database available for existing wind turbines provides a way to downscale the representative inputs for lab experimentation. Arany et al. [8] reported a simplified way of converting the wind and wave spectrum into mudline bending moment spectra. For practical design purposes, the complex loads could be idealised in fore–aft and side–to–side vibrations of offshore wind turbines. Depending on the study of interest, the complex loads on an OWT can be simplified as presented in Figure 2.5 for cyclic or dynamic load applications, reported by Nikitas et al. [73].

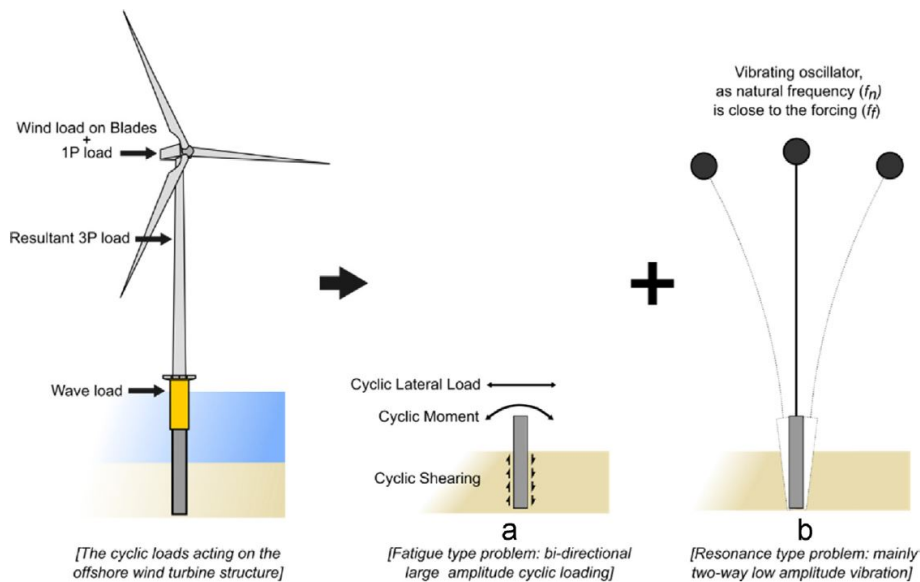


Figure 2.5: Utilization of complex load form as point loads, from Nikitas et al. [73]

A non-operational OWT experiences equal aerodynamic damping in the fore–aft as in the side–to–side directions. Notably, for water depths less than 30 m, wind loading is the dominant load, while for medium to deep water, the wave loading is expected to have equal or higher magnitude than wind load. The yaw mechanism of the wind turbine structure changes the turbine orientation aligning it in along–wind direction. This continuously changing characteris-

tic indirectly infer that the monopile foundation experiences cyclic loads in all the directions. Thereby, the multi-directional soil-structure interaction study is vital. Also, due to the probable misalignment in wind and wave loads, the input load form could be bi-axial [74].

The research work on monopile foundations is important concerning both cyclic and dynamic loading conditions. However, for the definition of the soil-pile interaction in the geotechnical perspective, the cyclic loading study is prominent over the dynamic loading. It is because the hysteric damping with the number of load cycles is essential for pile-soil interaction mechanism definition. For the frequency range below 1 Hz, the wave radiation damping, viscous damping and pore fluid-induced damping are negligible. At low frequencies, the relative velocity of the substructure is low, and therefore, viscous damping being proportional to the square of velocity is consequently low. Thus, the inertia effects are negligible, and subsequently, the investigation of the dynamic pile-soil interaction is irrelevant.

Another simplified approach has been presented in work by Leblanc et al. [60] through performing a long term lateral cyclic loading study on a lab-scale pile-soil system. A motor rotating at 0.106Hz frequency along with a system of cables connecting the model pile head to the loading setup is utilised. Figure 2.6 presents the lab-scale model layout. Authors presented a method to breakdown the complex loading scenarios in simple waveforms so that they can be experimentally applied as presented in Figure 2.7.

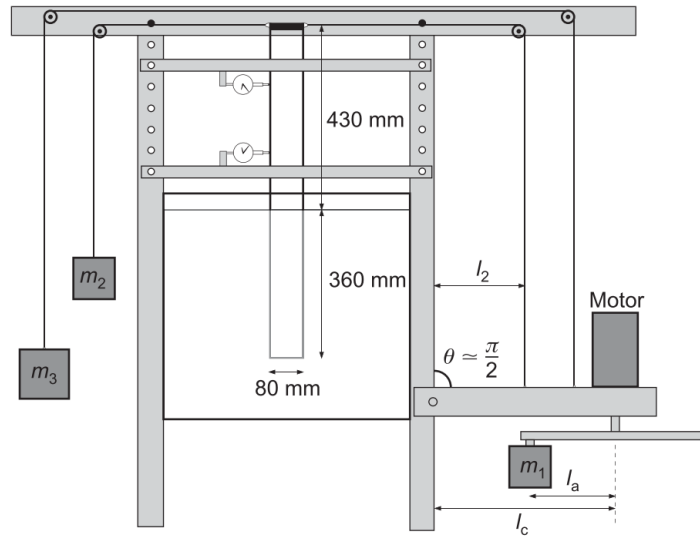


Figure 2.6: The lab scale model setup reported by Leblanc et al. [60]

The cyclic load profile is assumed as a constant amplitude sinusoidal waveform. A complex cyclic loading scenario is decomposed into a sequence of sinusoidal cyclic load input by using an extended rain-flow counting method [60]. The authors utilised two cyclic waveform parameters, ζ_b and ζ_c to define a one-way, two-way or in between the two cyclic load profile. The parameter ζ_b defines the amplitude of the cyclic load normalised with the ultimate moment capacity (M_R). It possesses value between 0 and 1. The parameter ζ_c characterises the load profile with a value -1 for two-way, 0 for one way and 1 for a monotonic load. The cyclic loading

parameters are presented in Equation 2.1.

$$\begin{aligned}\zeta_b &= \frac{M_{max}}{M_R} \\ \zeta_c &= \frac{M_{min}}{M_{max}}\end{aligned}\quad (2.1)$$

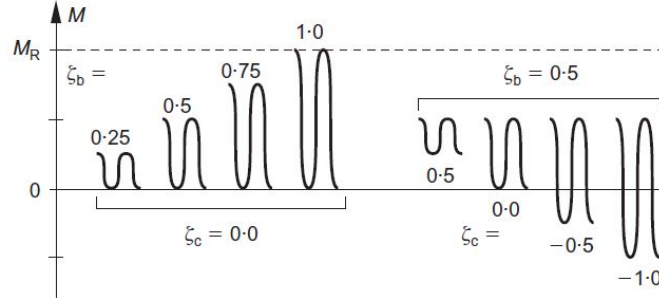


Figure 2.7: Simplified non-uniform lateral loading application using the ζ_b and ζ_c parameters, from Leblanc et al. [60]

Notably, some recent physical model studies suggest that non-symmetric two-way loading is more damaging to the lateral stability of the monopile [11], [103]. The prominence of one-way loading over two-ways is due to the sizeable aerodynamic damping. Overall, in terms of the lab-scale experimental or numerical studies, a cyclic loading scenario with one-way loading type is more prominent and representative of the offshore wind turbine loading environment. After establishing the understanding of the practical loading scenario, the investigation proceeds towards the design requirements for the pile-soil interaction features.

2.1.3 Design requirements

The pile behaviour is defined as rigid or flexible depending on the stiffness ratio measurements as presented by Abadie et al. [3] in a rearranged form of what has been initially proposed by Poulos and Hull [81], defined in Equation 2.2. The authors give the characterization of pile dimensions and stiffness ratio to decide whether pile-soil interaction follows stiff or flexible criteria (see Figure 2.8).

$$K_R = \frac{E_p I_p}{E_{SL} L^4} \begin{cases} > 0.208 \text{ for rigid pile} \\ < 0.0025 \text{ for slender pile} \end{cases} \quad (2.2)$$

where,

E_p = Young's modulus of pile material;

I_p = Pile cross-section second moment of area;

E_{SL} = Soil deformation modulus measured for small strain range;

L = Pile embedment length;

Figure 2.9 demonstrates the response of the rigid and flexible foundations to the lateral load applications. The rigid pile ideally rotates about a pivot point whereas the flexible pile

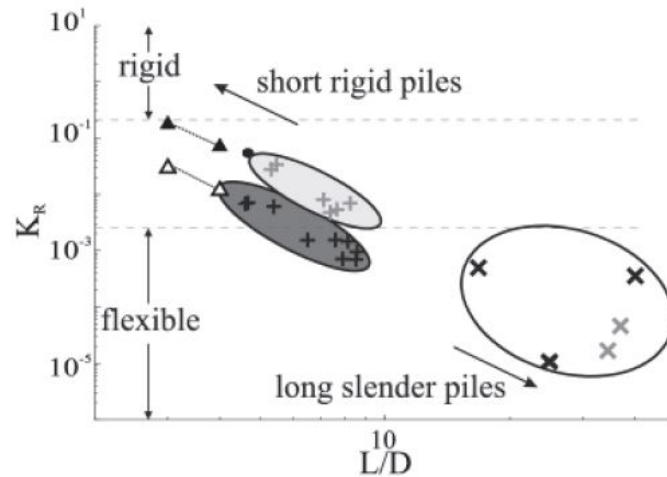


Figure 2.8: Stiffness ratio vs aspect ratio, from Abadie et al. [3]

deflects where the embedment length below a critical length displaces negligibly. It provides a clear insight into why it is necessary to understand the rigid pile-soil interaction in a different way than using well-established methods in the framework of a flexible pile foundation. More details on the methods to represent the pile-soil interaction are presented in the next section.

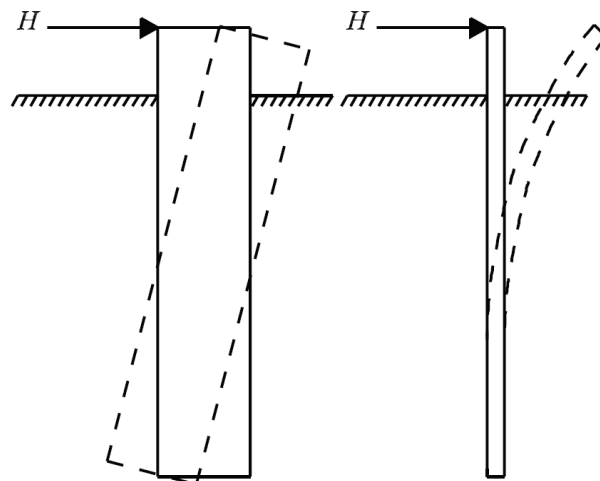


Figure 2.9: Rigid pile deformation about a pivot point (left) and flexible pile deflection (right) demonstration, from Sørensen et al. [96]

The ultimate limit state (ULS) and serviceability limit state (SLS) modes of failure are the first and foremost priority of any design consideration. For a monopile supported foundation, ULS failure (which can also be described as collapse) can be of two types: (a) where the soil fails; (b) where the pile fails by forming a plastic hinge. On the other hand, in SLS failure, the displacement and rotation deformation will exceed the allowable limits. The practical demonstration of the ULS and SLS loading scenarios is presented in Figure 2.10.

Typical estimates suggest that offshore wind turbine foundations are subjected to 10–100 million load cycles of varying amplitudes over their lifetime (25 to 30 years) [74]. Therefore, in addition to the ULS and SLS loading conditions, the long term performance of the OWT structure and the supporting foundation is also necessary to investigate. In structural

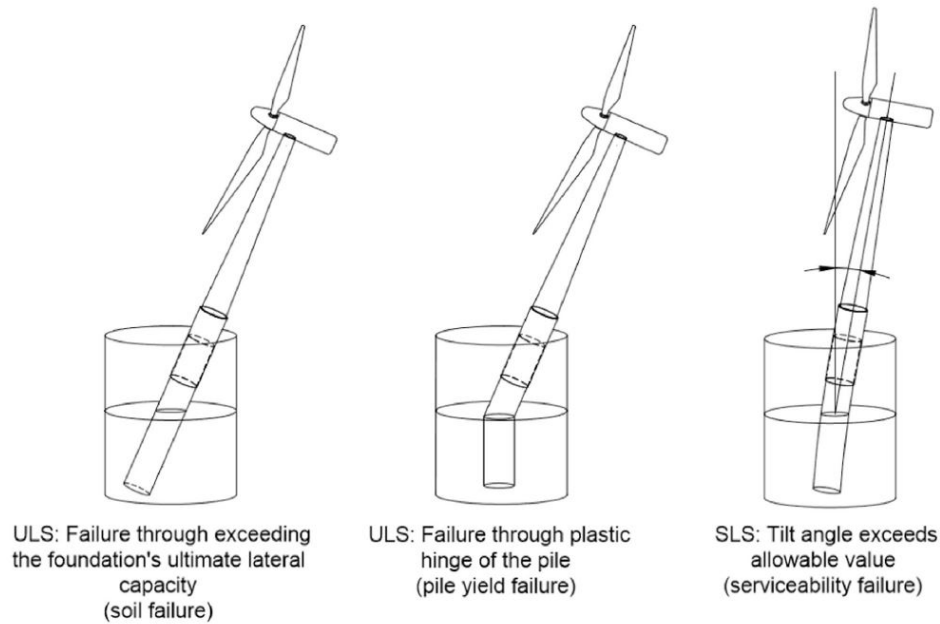


Figure 2.10: A demonstrations of the failure limit states for the monopile foundation design, from Arany et al. [10]

design perspective, the long term performance is governed by the fatigue limit state (FLS), which accounts for a phenomenon called ratcheting [15], a key feature of monopile-soil long term interaction.

Besides, the design of a monopile foundation shall deal with the challenges and the limitations in the current practices briefly presented here. The monopiles have been used predominantly to support OWT structures up to the depth of 30 m. The future design practices are intended to push to greater water depths of more than 40 m; the monopile is termed as ‘XL’ monopile. Bhattacharya [14] highlighted the key challenges concerning foundation design for current and aspired wind farm projects ambitions. The long term performance with foundation and tower tilt within the safety limits guidelines are not readily available in the codes. As a general rule, under field loading, rotation of the monopile of up to 0.5 degrees from its vertical alignment is considered as limiting values for the proper operation of the wind turbine [36] [60].

Moreover, monopiles are designed to possess the characteristic of a rigid pile. The excessive tilt will lead to the rigid body movement of the foundation, and subsequently, the surrounding soil will fail, technically termed as ‘wedge-type failure’ [15]. The rectification of a tilting foundation is costly work if necessary.

The pile installation costs are likely very high compared to the installation vessels available. Hence, there is a need to upgrade the vessel designs too. The pile drilling and driving repetition might be required for soft soil profiles, adding extra cost to the foundation design and construction schedule. Authors have also pointed out that driving reduces fatigue life.

Conclusively, the monopile foundation design process is extensive and incorporates collective knowledge from several engineering fields. In geotechnical research perspective, the critical feature of interest in the design process is the interaction between the pile structure with the surrounding soil. Bhattacharya and Adhikari [16] have reported that the monopile

foundation design is aimed to keep the pile material stresses and strains within its elastic limit. Thereby the overall performance of an OWT supported on monopile relies primarily on pile-soil interaction.

2.2 Pile-soil interaction

The research on the pile-soil interaction under axial or lateral loading application is not a recent topic of interest. The studies have been presented by many researchers, in which the works reported by Broms [20] and Reese et al. [85] have been prominent. The findings from these research works lead to the development of the standard guidelines such as API [6] and DNV [35] which are extensively used to the date for pile-soil interaction behaviour studies. Bhattacharya [14] reported that the pile-soil interaction mechanisms for the OWT application should be explored to establish redundant design guidelines to avoid a single point of failure, such as a plastic hinge. A brief description of the pile-soil interaction methods in the context of the present research work is presented hereafter.

2.2.1 Axial pile-soil interaction

A typical viewpoint in the pile foundation design comprises of the relationship between applied load and the consequent resistances at the base and around the pile shaft. For the axial pile-soil interaction representation, a typical concept called transfer-curve or T-Z method is widely used. It was first proposed by Coyle and Reese [29], aiming to calculate the vertical displacement of a pile subjected to axial stress. The method is based on the definition of curves connecting the shear stress on the lateral surface of the pile, the vertical displacement of the pile section, and this at different depths. Figure 2.11 below presents a general context of T-Z method with consideration to the axially loaded pile and mobilised shaft and base resistances. Notably, the pile base resistance is represented by similar guidelines and named as Q-Z method.

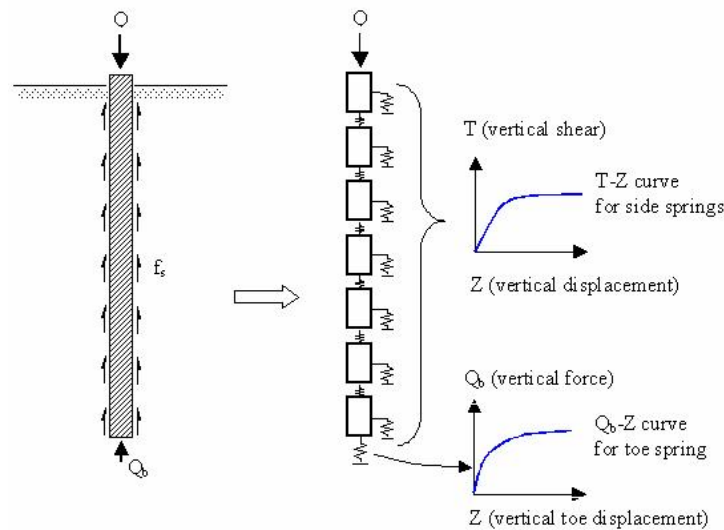


Figure 2.11: The conceptual demonstration of pile-soil interaction for an axially loaded pile (left) and its representation as per the T-Z and Q-Z methods (right), from Randolph and Wroth [84]

The construction of these curves is based on data collected during in-situ instrumented pile loading tests or laboratory tests on model piles, or from in-situ tests. API [6] standard recommends the following procedure for the use of the transfer curves method. This method consists in dividing the pile into several sections considered as compressible columns and modelling the ground by a set of nonlinear springs which support the pile halfway up each section. The spring elements are considered independent of each other. A typical response of t-z curve as per API [6] standards has been presented in Figure 2.12.

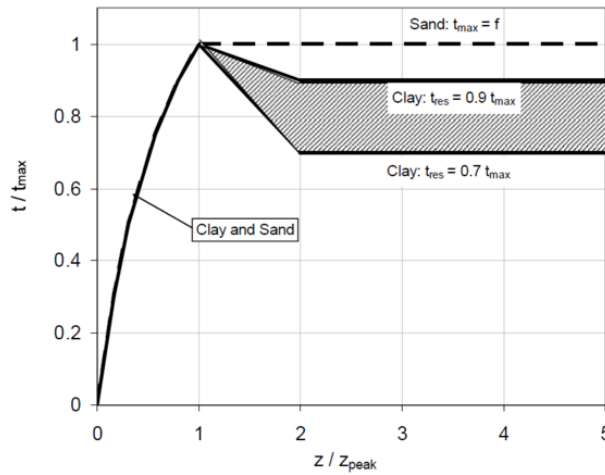


Figure 2.12: T-Z method definition, as per API [6] standard

Here the curve is a normalized representation of following parameters:

t_{max} = maximum unit friction resistance calculated in the studied element;

t = mobilized frictional resistance per unit element length;

z = axial displacement;

z_{peak} = maximum axial displacement

The definitions of the $t - z$ curves are given in the Table 2.1 below:

Table 2.1: Defining parameters of T-Z curve as per API [6] standard

z/z_{peak}	t/t_{max}
0.16	0.30
0.31	0.50
0.57	0.75
0.80	0.90
1.00	1.00
2.00	1.00
infinite	1.00

The standard recommends a value $z_{peak} = 0.01D$, where D is the pile diameter. This value is a bit uncertain and can range from $0.0025D$ to $0.02D$.

Similarly, the Q-Z method is formulated in API [6] standards, representing the evolution of pile base capacity (see Figure 2.13).

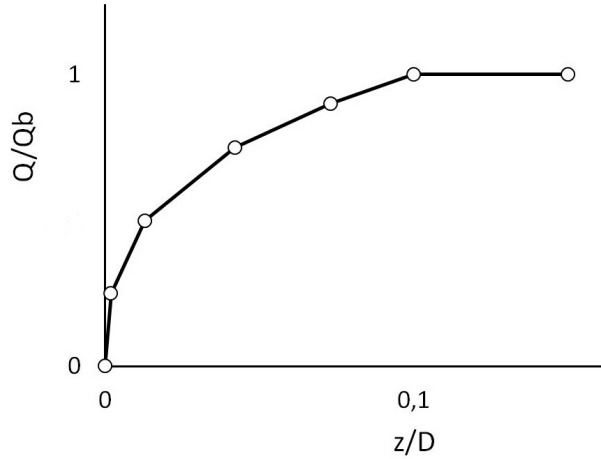


Figure 2.13: Q-Z method definition, redrawn from the recommendation by API [6] standards

Here the curve is a normalized representation of following parameters:

Q = mobilized point resistance;

Q_b = point resistance;

The definitions of the $q - z$ curves are given in the Table 2.2 below:

Table 2.2: Defining parameters of Q-Z curve as per API [6] standard

Z/D	Q/Q_b
0.002	0.25
0.013	0.50
0.042	0.75
0.073	0.90
0.100	1.00
infinite	1.00

Conclusively, the required parameters to define the axial pile-soil interaction are unit shaft segment capacity (t_{max}) and base capacity (Q_b) only, assuming the axial displacement evolution as per API [6] standard recommendations. Now, there are two different possibilities to extract these input parameters considering a bored or a driven pile case.

The input parameters for a bored pile case can be estimated from the analytical solution of the foundation capacity formulations, briefly presented as follows.

The total pile capacity (Q_p) is the sum of the shaft (Q_s) and base (Q_b) resistances. Meyerhof and Ghosh [67] presents the formulation of this sum (see Equation 2.3) for a pile in dry soil under compression.

$$\begin{aligned}
 Q_p &= Q_s + Q_b \\
 Q_p &= K_o \times \tan(\delta') \times \pi D \frac{1}{2} \gamma' L_e^2 + N_q \times \gamma' \times L_e \times \frac{\pi}{4} D^2
 \end{aligned} \tag{2.3}$$

Here, γ' is the unit weight of the soil, N_q is the bearing capacity parameter, δ' is the

interface friction angle, K_o is the earth pressure coefficient at rest and D , L_e are the diameter and embedment length of the pile respectively.

The estimation of base capacity (Q_b) is direct from Equation 2.3, whereas the shaft segment capacity (t_{max}) can be determined as distribution of total shaft capacity (Q_s) in the range of the pile segment depth. It can be done by simple mathematical correlation, presented in Equation 2.4 for a segment defined by the upper (z_a) and lower (z_b) depth levels along pile embedment.

$$t_{max} = K_o \times \tan(\delta') \times \pi D \frac{1}{2} \gamma' (z_b^2 - z_a^2) \quad (2.4)$$

On the other hand, the estimation of the input parameters is not direct for a driven pile, mainly because of the change in the initial state of stress in the soil as a consequence of pile driving. The Imperial College Pile method, known as ICP method, reported by Jardine et al. [51] presents an empirical formulation for the evaluation of the short-term static axial capacity (also as a sum of shaft and base resistances) of a single displacement pile in silica sands. The method description is briefly presented hereafter.

The ICP method is intended to predict the capacities that may be mobilized in slow maintained load tests, conducted around ten days after driving, on previously not failed piles. Authors have pointed out that the pile capacity varies with the age and mode of testing (bored or driven). Therefore it is necessary to comprehend the domain of the applicability of the ICP method. Also, the calculation procedure is intended to be compatible with the modern pile design practice, which includes pause periods that allow creep straining to stabilize between loading increments.

The input ingredient for the ICP method application is the tip resistance (q_c) profile obtained from the cone penetration test (CPT). For a circular pile of diameter (D_p), the base capacity (Q_b) is estimated using ICP method, as presented in Equation 2.5, using CPT tip resistance and relative diameters of design pile (D_p) and CPT pile (D_{CPT}).

$$Q_b = q_b \times \pi \frac{D_p^2}{4} \quad (2.5)$$

here,

$$q_b = q_c [1 - 0.5 \log(\frac{D_p}{D_{CPT}})]$$

Notably, Equation 2.5 is directly applicable to a closed-ended pile case. For an open-ended pile, the formulation modifies slightly considering the effect of soil plugging. Further, the pile shaft resistance (Q_s) is determined from the integration of the local shear stresses along the embedded shaft length (see Equation 2.6).

$$Q_s = \pi D_p \int \tau_f dz \quad (2.6)$$

The ICP experiments showed that at failure, the local shear stresses acting on the pile

shaft, τ_f , follow the simple Coulomb failure criterion, presented in Equation 2.7.

$$\begin{aligned}\tau_f &= \sigma'_{rf} \tan \delta_{cv} \\ \sigma'_{rf} &= \sigma'_{rc} + \Delta\sigma'_{rd}\end{aligned}\quad (2.7)$$

The local effective stress at failure (σ'_{rf}) is defined as the sum of local radial effective stress (σ'_{rc}), representative of an equalized value acting a few days after installation, and dilatant increase in the local radial effective stress during pile loading ($\Delta\sigma'_{rd}$). The equalised value is representative of the stress state when pore pressure and radial stresses are relatively stable. Also, the local shear stress is estimated considering the constant volume friction angle (δ_{cv}) as representative of the interface friction angle at failure. ICP method presents an empirical formulation to estimate both parameters, presented in Equations 2.8 and 2.9.

$$\sigma'_{rc} = 0.029q_c \left(\frac{\sigma'_v}{p_a} \right)^{0.13} \left(\frac{h}{R} \right)^{-0.38} \quad (2.8)$$

$$\begin{aligned}\Delta\sigma'_{rd} &= 2G \frac{\Delta r}{R}, \\ \text{where } G &= q_c [0.0203 + 0.00125\eta - 1.21 \times 10^{-5}\eta^2]^{-1} \\ \text{with } \eta &= \frac{q_c}{(\sigma'_v p_a)^{0.5}}\end{aligned}\quad (2.9)$$

Here,

h = Relative distance of a particular depth level with reference to the pile tip,

G = Small strain shear modulus,

Δr = Pile-soil interface dilation estimated from the pile roughness (R_{cla}) estimated 0.028mm for smooth steel pile. ($\Delta r = 2 \times R_{cla}$)

R = Pile radius,

q_c = CPT tip resistance at the $z = L_e$,

p_a = Atmospheric pressure,

σ'_v = Vertical effective stress of soil in free-field

The CPT profiles specific to a particular site are essential for the application of the ICP approach. ICP method recommends that total shaft capacity must be calculated by summing short sections to cope with soil layering and variation of crucial parameters. Even if the soil is nearly uniform, at least 15 subdivisions are recommended with smaller increments are recommended near the pile tip.

The local value of σ'_{rc} varies strongly with sand relative density, as reflected by local CPT tip resistance q_c . They are also sensitive to the relative pile depth h/R . The effective radial stress developed at any depth decline sharply as the pile tip is driven on past that depth level and ' h ' increases. This feature is a cause of well-known tendency in uniform sands for the average shear stress at the failure to reach a quasi-constant limit once a "critical depth" of around 10D has been exceeded.

Besides, similar to the ICP method, there are few other empirical formulations reported over past years for the axial pile capacity determination based on CPT test results. Gavin et al. [39] reported a review of all the relevant methods in the context of the offshore wind turbine foundation design. Nevertheless, the ICP method based formulations are used in the present thesis work.

2.2.2 Lateral pile-soil interaction

The advent of pile foundations for structures exposed to the lateral environmental loading such as offshore oil and gas structures and offshore wind turbines have initiated the requirement of studying the lateral pile-soil interaction. A well-renowned technique called p-y method has been extensively used over decades for the lateral soil-pile interaction studies. The basic concept is to establish a non-linear relationship between lateral soil reaction (p) and lateral pile deflection (y) locally at different depths along pile embedment upon the application of lateral loading at the pile head. The p-y based method is most prominent because the designs based on this theory have failed to the least on several decades [60].

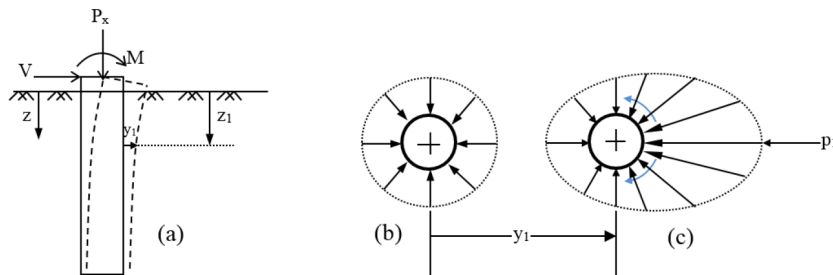


Figure 2.14: The conceptual demonstration of p-y method for the lateral pile-soil interaction definition, modified from Arshad and O’Kelly [11]

Figure 2.14 presents a demonstration for a cylindrical pile under lateral loading. When the pile deflects a distance of y_1 at a depth of z_1 , the distribution of stresses, which was constant all around the pile for unloaded pile (see Figure 2.14b), looks similar to Figure 2.14c with a resisting force per unit length of p_1 . The stresses increase in the front (lead) side of the pile and decrease on the back (rear) side of the pile, containing both normal and shearing components as the displaced soil tries to move around the pile. Hence, the evolution of the lateral displacement and subsequent lateral soil reaction defines the phenomenon of the lateral pile-soil interaction.

For p-y method analysis, the main parameter to determine from the soil is a reaction modulus. It is defined as the ratio of the soil reaction and the horizontal pile deflection at a point along pile embedment. Many studies in previous years have provided the range of magnitudes for the soil reaction modulus determination, e.g. Broms [20], Reese et al. [85] and API [6].

The practical implementation of the p-y methods is done through the use of ‘Beam on Non-linear Winkler Foundation’ (BNWF) models, as demonstrated in Figure 2.15. The beams at different depths are independent of each other. The BNWF models have been initially deployed for shallow foundation settlement analysis. Notably, the use of Winkler type foundation has a limitation that there is no unique distribution that preserves the global foundation stiffness for all degrees of freedom. Nevertheless, they have been and are very popular amongst structural

engineer for pile design, as they provide essential information concerning the distribution of shear forces and bending moments along the pile axis through Euler–Bernoulli beam theory. The usage of this theory also inspired the lab-scale model development with usage of a pair of strain gauges (in Half-Wheatstone bridge configuration) to record the profile of bending moment with depth and subsequently deduce the p-y curve. One such lab-scale model study is reported by Klinkvort and Hededal [57] for pile driven in the sand and tested in centrifuge setup.

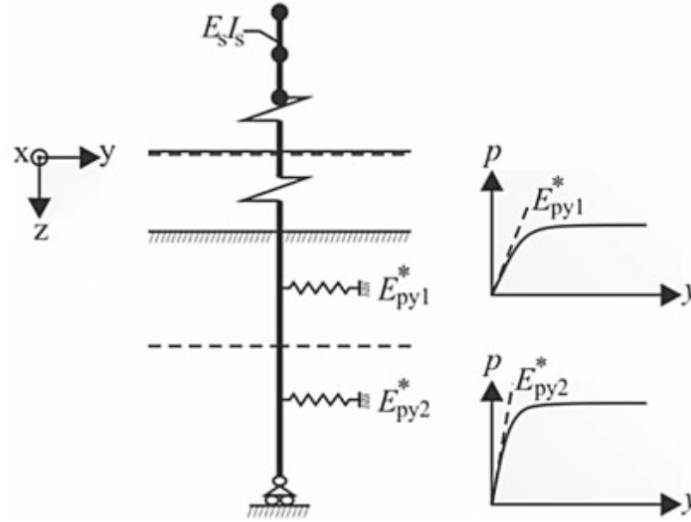


Figure 2.15: Standard analytical model representing beam on non-linear Winkler foundation, from Kerner et al. [56]

The input parameters for p-y method definition are initial stiffness (E_{py}), ultimate lateral soil reaction (p_u) and deflection (y_u). The initial stiffness of each beam is given by the slope of the tangent to the $p - y$ curve passing through the origin as expressed by Equation 2.10 :

$$E_{py} = \left(\frac{dp}{dy} \right)_{y=0} = kz \quad (2.10)$$

The stiffness E_{py} depends on the initial modulus of subgrade reaction k (in Pa/m) and the considered depth z . k is a function of friction angle ϕ and the relative density of the sand I_D . From experimental evidence, the stiffness magnitude is considered by an increasing trend with depth. Many studies have reported the p-y method development based on experimental studies on long and small diameter piles. For piles in sand, the tests were performed by Cox et al. [28] on a long flexible pile of 0.61 m diameter and 21 m length. The p-y methodology was described by Reese et al. [85] and adopted in design practices to address the ultimate capacity of long flexible piles (e.g. API [6]). A few details of these research works and additions over the years are briefly presented here.

Reese et al. [85] p-y method: The development of the p-y curve for sand is presented in Figure 2.16. Initial stiffness ($k_{py}z$) is determined by soil modulus (k_{py}) which is a function of the soil relative density.

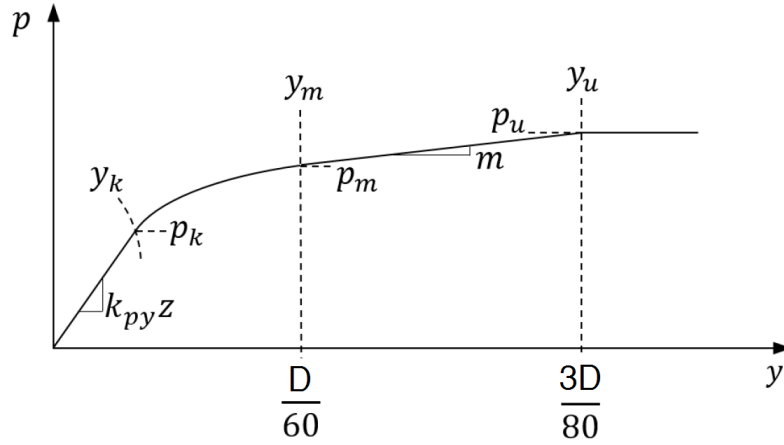


Figure 2.16: The lateral soil reaction evolution with lateral displacement, modified from Reese et al. [85] reported theory

The initial straight line portion lasts until (p_k, y_k) coordinates and the response between this point till (p_m, y_m) is a parabola defined as follows.

$$p = p_m \left(\frac{y}{y_m} \right)^{\frac{1}{n}} \quad (2.11)$$

where

$$n = \frac{p_m}{m y_m}, \quad m = \frac{p_u - p_m}{y_u - y_m} \quad (2.12)$$

Afterwards, till p_u, y_u (representing ultimate limit) a linear evolution is defined. The y_m and y_u lateral displacements are defined as a function of pile diameter as $D/60$ and $3D/80$ [85]. The estimation of the static soil reaction (p_s) is made by using the expressions presented in Equation 2.13 and 2.14.

$$p_s = \gamma z \left[\frac{K_0 z \tan \phi \sin \beta}{\tan(\beta - \phi) \cos \alpha} + \frac{\tan \beta}{\tan(\beta - \phi)} (b + z \tan \phi \sin \beta) + K_0 z \tan \beta (\tan \phi \sin \beta - \tan \alpha) - K_a b \right] \quad (2.13)$$

$$p_s = K_a b \gamma z (\tan^8 \beta - 1) + K_0 b \gamma z \tan \phi \tan^4 \beta \quad (2.14)$$

Here,

$$\alpha = \frac{\phi}{2}, \beta = 45 + \frac{\phi}{2}, K_0 = 0.4, K_a = \tan^2 \left(45 - \frac{\phi}{2} \right) \quad (2.15)$$

The maximum (p_m) and ultimate (p_u) soil reaction magnitudes are calculated using the smaller of the values given by p_s , multiplied by coefficients A and B estimated from Figure 2.17, called depth factors.

$$p_u = \bar{A}_s p_s, \quad p_m = B_s p_s \quad (2.16)$$

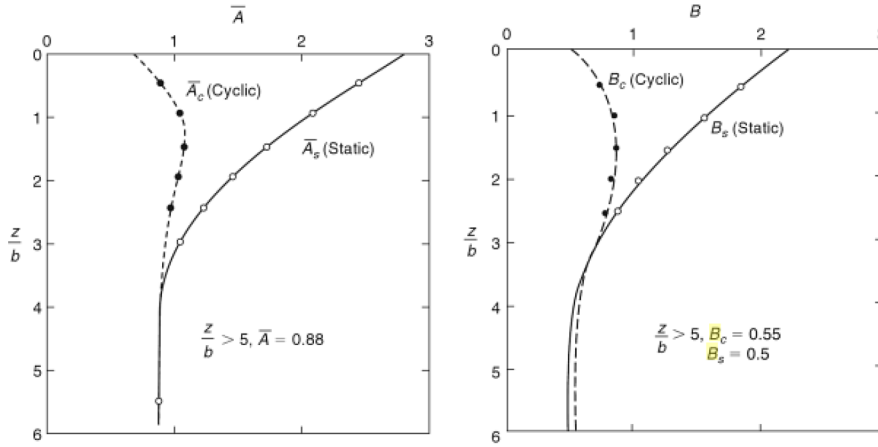


Figure 2.17: The depth factor coefficients A and B, reported by Reese et al. [85]

API [6] standards p-y method: The API standards present a tangent hyperbolic evolution of lateral soil reaction (p) with lateral displacement (y) presented in Equation 2.17.

$$p = A \times p_u \tanh\left(\frac{k \times z}{A \times p_u} y\right) \quad (2.17)$$

here, A is a factor to account for static or cyclic loading. $A = 0.9$ for cyclic loading is recommended as per API [6] guidelines, while for static load $A = 3 - 0.8 \frac{z}{D} \geq 0.9$ is defined for depth 'z'. The parameter 'k' is representative of the rate of increase with depth of initial modulus of sub-grade reaction; a parameter dependent on the internal friction angle of the soil. p_u is the ultimate lateral resistance at depth 'z', evaluated as minimum of p_{us} and p_{ud} estimations (shallow and deep depths) presented in Equation 2.18.

$$\begin{aligned} p_{us} &= (C_1 z + C_2 D) \gamma' z \\ p_{ud} &= C_3 D \gamma' z \end{aligned} \quad (2.18)$$

Where C_1, C_2 and C_3 are coefficients determined as a function of the internal friction angle of soil.

Further improvements in the API method were suggested by Kallehave et al. [54] taking into account the diameter of the structure and thus resulting in an increases the initial stiffness E_{py} as per Equation 2.19.

$$E_{py} = k \cdot z_{ref} \left(\frac{z}{z_{ref}}\right)^b \left(\frac{D}{D_{ref}}\right)^c \quad (2.19)$$

with:

k Initial modulus of subgrade reaction (Pa/m);

$z_{ref} = 2.5$ m, reference depth;

$D_{ref} = 0.61$ m, reference diameter;

$b, c = 0.6$ and 0.5 respectively are dimensionless parameters governing the course of the initial stiffness with the depth.

Moreover, some studies have reported the methods in the determination of ultimate lateral soil reaction (p_u) for short rigid piles by use of earth pressure theories and CPT test based formulations. A brief description of such developments is presented hereafter.

Broms [20] method for rigid piles assumes a pile rotates according to the pile base and p_u is fully mobilized along the entire pile embedded depth, as illustrated in Figure 2.18. p_u in Broms's method is presented in Equation 2.20. Due to three dimensional characteristics of the lateral soil resistance, p_u is much greater than the passive earth pressure [37]. It indirectly justifies the factor '3' present in Equation 2.20.

$$p_u = 3 \times K_p \times \sigma'_v \quad (2.20)$$

where

K_p =Rankine's passive lateral stress ratio= $\tan^2(45 + \phi'/2)$;

ϕ' =internal friction angle of soil; and

σ'_v =vertical effective stress.

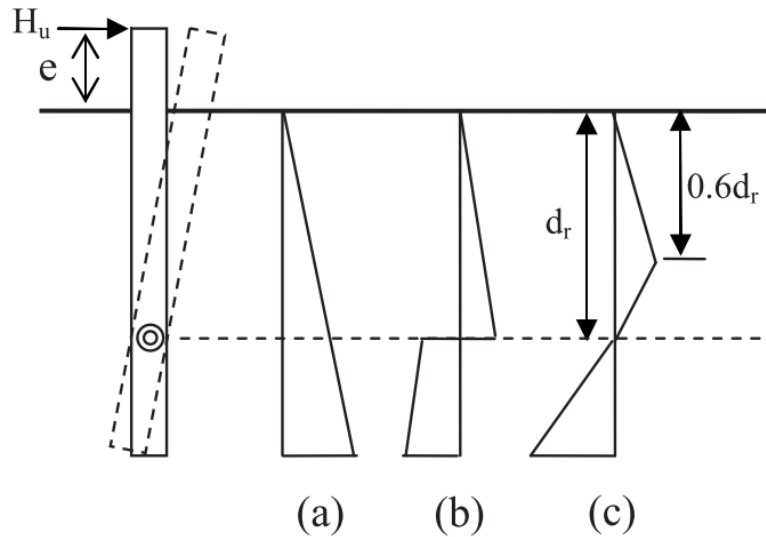


Figure 2.18: Distribution of lateral soil pressure at ultimate state by (a) Broms [20]; (b) Petrasovits and Award [80]; and (c) Prasad and Chari [82], from Lee et al. [61]

Figures 2.18 (b and c) show the methods by Petrasovits and Award [80] and Prasad and Chari [82] respectively. These methods consider a point of the pile rotation, below which stress reversal occurs. In Prasad and Chari's method, the depth to the pile rotation point (i.e., d_r in Figure 2.18c) is given as a function of pile embedded length (L) and load eccentricity (e). In Petrasovits and Award's method it is obtained from trial-and-error iteration until the equilibrium condition of the resultant forces is satisfied. Equations 2.21 and 2.22 of p_u for Petrasovits and Award's and Prasad and Chari's methods are given, respectively, as follows:

$$p_u = (3.7 \times K_p - K_a) \times \sigma'_v \quad (2.21)$$

$$p_u = 10^{(1.3 \tan \phi' + 0.3)} \times \sigma'_v \quad (2.22)$$

where K_a = Rankine's active lateral stress ratio = $\tan^2(45 - \phi'/2)$

Notably, in Prasad and Chari's method, the p_u estimated at $0.6d_r$ is multiplied by a factor 1.7 to determine p_u at the pile base.

Further work on the estimation of p_u was presented by Lee et al. [61] using the CPT test-based analysis. The CPT test is widely used in foundation design mainly for axially loaded piles due to the similar loading processes of the cone and pile. For laterally loaded piles, less attention was given to the direct application of CPT results because the lateral load capacity of piles is associated with lateral displacements of surrounding soils. Hence, the correlation between the lateral response and CPT tip resistance is not directly observable. Authors proposed a hypothesis to use CPT tip resistance q_c to formulate p_u based on the fact that both q_c and p_u are dependent on the similar state soil variables of the effective horizontal stress and relative density. Notably, authors used the mechanisms of cavity expansion theory [87] to estimate p_u from CPT tip resistance profile. According to the cavity expansion theory, key soil variables that control values of q_c are the relative density D_R and horizontal effective stress σ'_h . The lateral pile loading capacity is affected by the σ'_h , which in-turns affects the p_u , thereby establishing a correlation between q_c and p_u .

Lee et al. [61] also stated that the effective horizontal stress is also an important parameter to consider in the estimation of p_u . For normally consolidated soils having K_o in 0.4-0.5 range there is no significant effect but for higher values, a 'lateral stress correction factor' β_L has been suggested in the estimated p_u . Equation 2.23 presents the factor, where ϕ' is the internal friction angle of the soil.

$$\beta_L = \left(\frac{K_o}{1 - \sin \phi'} \right)^{0.6} \quad (2.23)$$

The relationship between q_c and p_u is be obtained, as presented in Equation 2.24. Here σ'_m refers to the mean effective stress, p_{atm} is the atmospheric pressure and a^* , b^* , c^* and d^* are called correlation parameters evaluated for different methods [20], [80] and [82] presented before.

$$p_u = a^* \frac{q_c^{b^*}}{\sigma_m^{c^*}} p_{atm}^{d^*} \quad (2.24)$$

Notably, the CPT test performance to obtain q_c profile is also dependent on the domain of soil profile. In general, values of q_c measured from calibration chamber CPT test is smaller than those estimated from comparable field conditions due to the effect of chamber size [90]. Salgado et al. [88] reported a study to incorporate the chamber size effect from the input information of relative density, stress state, and chamber-to-cone diameter ratio. The quantification of this size effect allows correlating lab-based CPT q_c profile to the equivalent of the free-field.

Further, Arshad and O'Kelly [11] have reported that the analysis or design of large diameter (rigid) monopile foundations for current and proposed OWT structures is well outside the scope of present design methods. The DNV recommendations DNV [36] for offshore wind

turbine structures also include the update F.2.4.1 stating the standard lateral soil reaction and displacement curves are not applicable for monopiles with a large diameter. Also, according to Lombardi et al. [65], the widely used [6] standards developed primarily for the offshore oil/gas industry are based on flexible pile mechanism with pile embedment length to diameter ratio (also called aspect ratio) of order 30-50, whereas the OWT monopile foundation is in the target range 4-8. Hence, there is an apparent necessity to understand the mechanism of the pile-soil interaction for a large diameter rigid pile, termed as coupled pile-soil interaction from here onward.

2.2.3 Coupled pile-soil interaction

The p-y method and t-z method based lateral and axial pile-soil interactions are well established and useful for a flexible pile mechanism. For a slender (flexible) piles, the upper part ($z < 8 D$) takes most of the lateral load while the lower part ($z > 15 D$) takes most of the axial loads. It is, therefore, reasonable to assume uncoupled lateral and axial pile-soil interaction response for flexible piles. Hence, the application of the uncoupled Winkler's beam model application provides the requisite outputs. For rigid piles, the axial and lateral soil response is likely at the same pile depth, because of the shorter aspect ratio and large diameter of the monopile; hence the coupled interaction is expected. The French SOLCYP+ project [83], a joint industry project for piles under axial and lateral cyclic loads, also emphasises the coupling considerations. Besides, an OWT structure is subjected to a combined V-H-M loading condition, subsequently initiating the axial and lateral pile-soil interactions simultaneously, thus demanding the coupled interaction study. Some previous studies on combined loading are summarised to collect all the relevant information to understand, define and develop the coupled pile-soil interaction mechanism for rigid piles for the present thesis work.

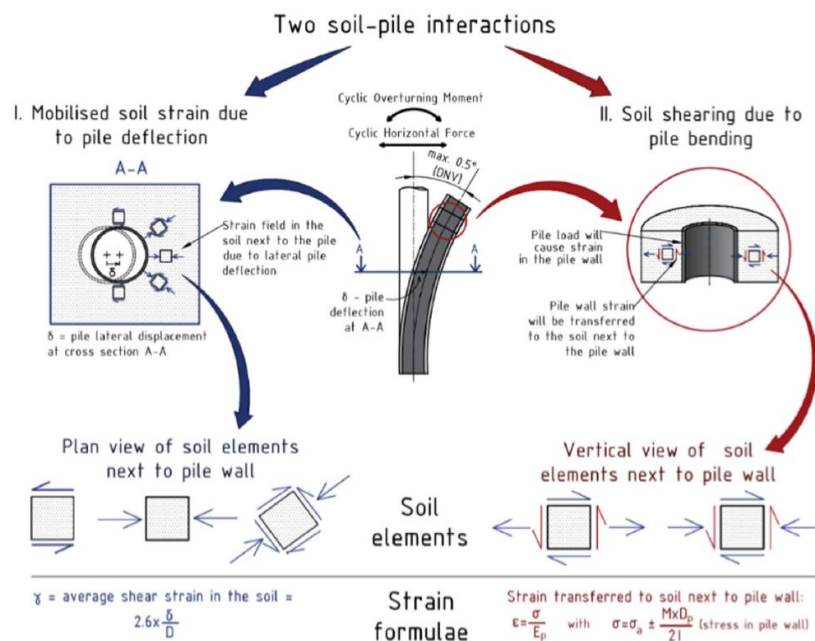


Figure 2.19: Two types of soil-pile interaction on a monopile supported wind turbine, from Nikitas et al. [74]

Nikitas et al. [74] reported a study on the 3D deformation mechanism of monopile-soil interaction under the application of cyclic lateral and moment loading applications, as presented in Figure 2.19. It represents two different pile-soil interactions, (I) due to mobilised soil strain as a result of the pile deflection and (II) soil shearing due to pile bending. The complexity of the 3D deformation mechanism results in the requirement of a robust modelling method and necessarily high computational data for analysis. As a simplified approach, some studies have reported the pile-soil interaction assuming 1D-deformations.

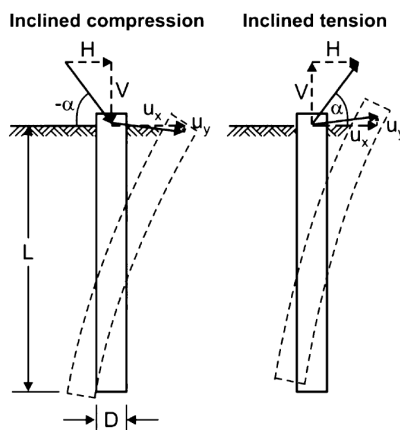


Figure 2.20: Representation of the combined pile loading input and subsequent deformations, from Achmus and Thieken [5]

Achmus and Thieken [5] presented a normalised vertical and lateral loading interaction diagram defining the combined load effect for compressing and tension loading cases where the angle of inclination (α) is varied to define different combined loading cases. This is demonstrated in the Figure 2.20. Authors examined the pile geometry with aspect ratio in a range of both rigid and flexible pile behaviour. The size and shape mesh formed as a result of plotting lateral and vertical displacement isolines are examined to address the combined loading interaction effect—one such interaction diagram reported by the authors, as presented in Figure 2.21. Authors reported that the axial and lateral coupled interaction presents comparatively strong effects for rigid piles then for a flexible pile.

Further, the PISA - Pile Soil Analysis project [25] presented a 1D finite model of model monopile with interaction components additional to typically used lateral soil reaction-displacement (p - y), demonstrated in Figure 2.22. In the project framework, the pile-soil interaction is featured as a combination of distributed load, distributed moments along the pile shaft along with shear and moment resistance components at the pile base. The assembly of the interaction components is presented in Figure 2.22.

PISA is a £3.5 million joint industry project, established in 2013 by DONG Energy and ten other partner companies and run through the Carbon Trust's Offshore Wind Accelerator program. The project aims to develop new design methods for soil structure interaction tailored for offshore wind turbine monopiles [25]. The project extensively comprises of the field scale monopile experimentation. Subsequently, a 3D FE analysis and 1D parametric study are presented to define the pile-soil interaction mechanism for a large diameter monopile foundation.

Field testing on two different sites with clay and sand profiles, representative of the

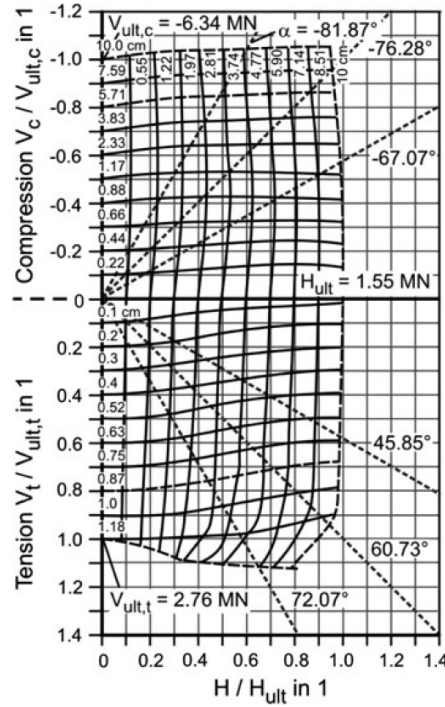


Figure 2.21: A typical interaction diagram obtained under the application of the combined vertical and lateral loading, from Achmus and Thieken [5]

North Sea soil profile, provided data for the development of the 1D design model. A site in Cowden UK representative of the clay conditions and a site in Dunkirk France for sand conditions. Most importantly, the research work findings have been made open access for the public via eight publications in *Géotechnique* journal. Ørsted demonstrated the application of the new design methods in their Hornsea wind farm project.

Byrne et al. [24] presented a comparison of the 1D numerical model, the parent 3D model and the API/DNV guidelines based responses at the pile head for both short and long pile installed in sand. Figure 2.23 presents the comparative outcomes for the evolution of the lateral displacement at the pile head with the applied lateral load. A significant deviation from the standard API/DNV based methods for short piles is reported, which highlights the importance of a coupled interaction. The long pile presented a similar response for all the said approaches inferring the accuracy of p-y based methods for flexible pile analysis.

Authors also highlighted the significance of additional interaction components for the representation of the pile-soil interaction for a rigid pile. Figure 2.24 presents one such plot for the short pile case examined with the proposed 1D model. It is clearly observed that the pile-soil interaction representative for a rigid pile through p-y curves (equivalent to distributed lateral load) only is highly conservative. The successive addition of the reaction components provides more relevant information about rigid pile-soil interaction.

As a step further to V-H [5] or H-M [25] combined loading study, Li et al. [63] presented a combined V-H-M loading application numerical study for pile foundations with diameter 0.72m and length 13m. As a result of a series of numerical loading tests on the FE model of the pile-soil system, authors proposed a 3D failure surface representing the combined V-H-M loading

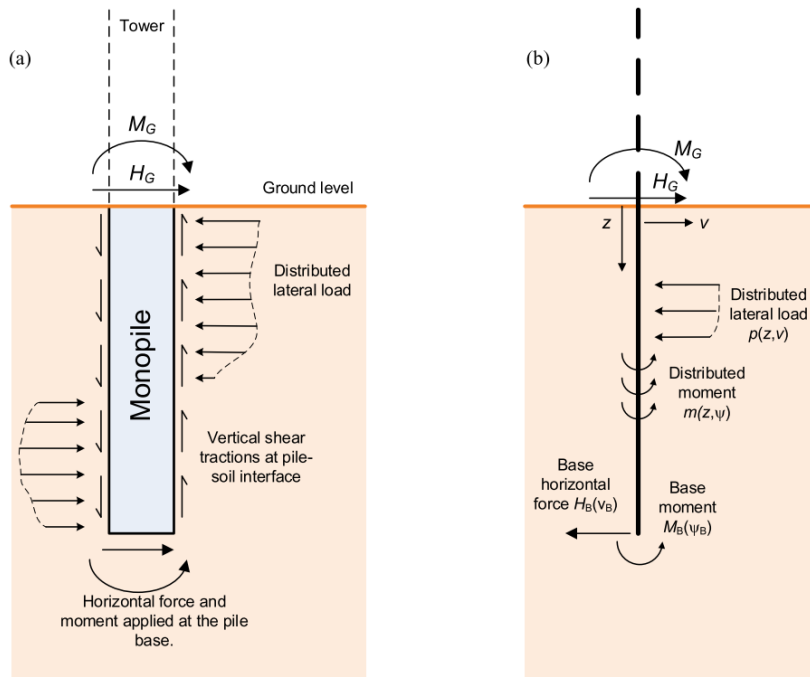


Figure 2.22: The finite model for monopile foundation proposed in the framework of PISA project, (a) assumed soil reaction acting on the monopile and (b) 1D model, from Byrne et al. [25]

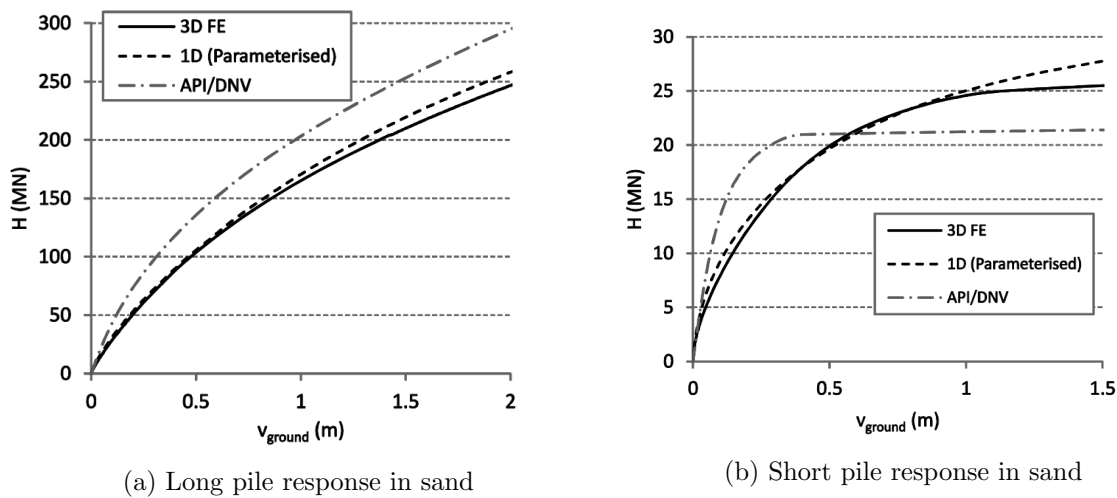


Figure 2.23: The comparative pile head displacement response from PISA models and standard API/DNV estimations for piles in sand, from Byrne et al. [24]

interaction as the overall behaviour at the pile head. Authors performed a series of numerical tests using radial displacement method and swipe tests to define the 3D failure surface. As a simplified geometrical shape, the authors concluded the ellipsoid shape (See Figure 2.25a) of the 3D failure envelop of pile-soil interaction under combined loading application. Byrne and Houlsby [23] reported similar yield surface for the shallow foundations, as presented in Figure 2.25b.

Conclusively, the pile-soil interaction study for a large diameter monopile foundation

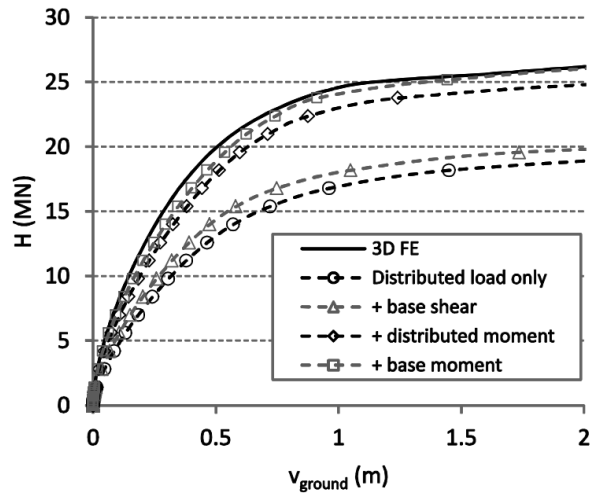
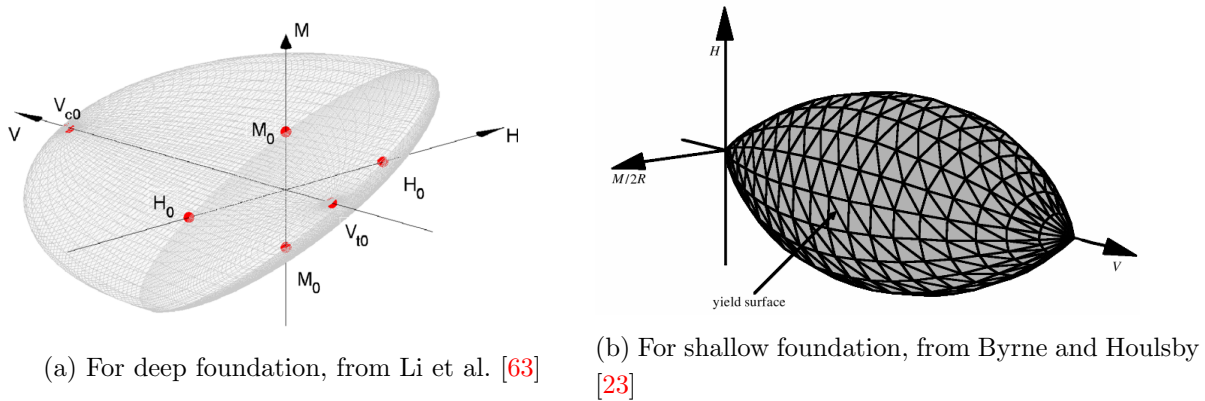


Figure 2.24: Demonstrative layout of the contribution from each reaction component of 1D PISA model pile, from Byrne et al. [24]



(a) For deep foundation, from Li et al. [63]

(b) For shallow foundation, from Byrne and Houlsby [23]

Figure 2.25: The 3D failure envelope of pile-soil interaction obtained under V-H-M loading application

necessarily presents a need to explore the mechanism beyond the traditional p-y and t-z methods. The combined loading application representation via a 3D failure load surface, investigation of coupled pile-soil interaction through additional reaction components and using the interaction diagrams information are key insights taken from the literature to proceed with the present thesis work.

2.3 Macro-elements modelling

Macro-element modelling has gained significant importance for pile-soil interaction representation, over conventional finite element modelling in recent times, due to its computational ease and readily available information for numerical parametric studies and engineering concept design. Nova and Montrasio [75] first introduced the term macro-element.

The particularity of the macro-element is that the foundation behaviour is entirely described by a system of generalized variables (forces and displacements) defined at the foundation

centre. This feature allows for elementary and straightforward analysis of pile-soil interaction problems. Figure 2.26 demonstrates the macro-element concept as a single point behaviour relating forces to displacement employing the stiffness parameters. The only relation between the applied loads and subsequent displacements through stiffness matrix presents the complete definition of the macro-element concept. The size and form of the stiffness matrix, load and displacement vectors depends on the degree of freedoms (DOFs) under investigations and vary from one to six DOFs investigations. Most importantly, the coupled pile-soil interaction definition is highly feasible in the macro-element concept mathematically, by the exploration of the non-diagonal elements of the stiffness matrix.

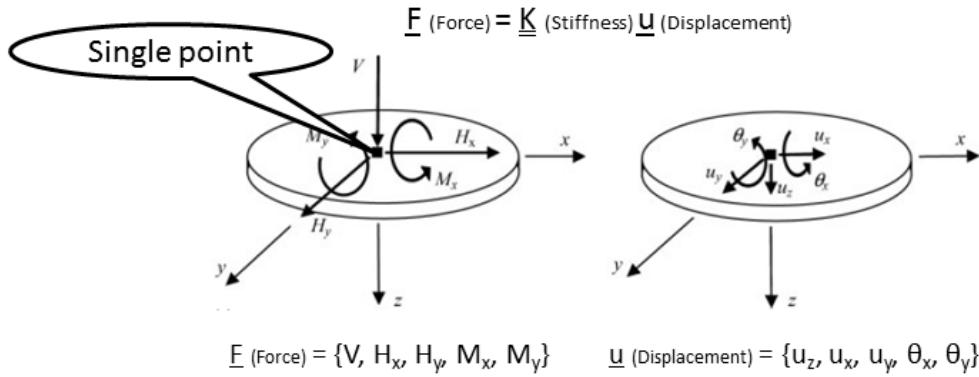


Figure 2.26: The macro-element modelling concept demonstration, modified from Grange et al. [42]

Based on the pile-soil interaction study either at the pile head only or at different depths along pile embedment, two different macro-element terminologies are used in the present work, namely global and local macro-element respectively. A brief synthesis of previous studies on the macro-element concept is presented hereafter.

2.3.1 Global macro-element model

The macro-element approach has been widely studied for the shallow foundation models e.g. [30], [41], [86]. The similar global macro-element model has been extended for the deep foundations by some researchers, e.g. Li et al. [63], Page et al. [78]. Due to the development in both experimental techniques and computing facilities, the development of single point behaviour has gained more and more significance. Many researchers over the last decades have studied a global constitutive equation capable of reproducing the observed non-linear, irreversible, hysteric behaviour of the soil-pile system under cyclic/dynamic loading conditions.

The constitutive equation of the macro-element model is often formulated in rate-form, to capture the non-linear, irreversible and history-dependent character of soil behaviour [63]. There are basically two-types of macro-element models widely used in literature with the difference lying in the framework used to construct the constitutive equations, namely Plasticity theory-based macro-elements and Hypo-plasticity theory-based macro-elements.

In the first group of models, the basic principles of isotropic or anisotropic hardening plasticity are used to define the elastic behaviour, yield criteria, the flow rule and the hardening

law of the macro-element. Byrne and Houlsby [23] reported the description of the different components of the elastoplastic constitutive law summarised here. The yield surface defines the allowable load combinations; the strain-hardening law represents the expansion/contraction or translation as isotropic or kinematic hardening, respectively. A combination of both can also be formulated in the elastoplastic framework. Further, the flow rule defines the plastic displacement at yield with two possible frames, namely associated or non-associated flow rule. The associated flow rule assumes the direction of the plastic displacement to be normal to the expanding/contracting or translating yield surface; the non-associate flow rule formulation is otherwise. Lastly, the behaviour within the yield surface is formulated as an elastic response.

The second group of models are an inelastic, rate-type macro-element model based on the principles of the theory of hypo-plasticity. One such model has been first developed by Salciarini and Tamagnini [86]. A hypo-plastic model presents the incrementally non-linear character of the constitutive equations. It reflects the key difference between hypo-plastic and other elastoplastic models. It also precludes the existence of an elastic domain in the generalized loading space. The model incorporates a vector-like internal variable (the internal displacement) which accounts for the effects of recent deformation history. This feature allows reproducing satisfactorily most of the relevant experimentally observed response of the foundation-soil system under rather complex loading paths, including load reversals. Notably, the hypoplastic model shares some common features with elastoplastic macro-element.

Moreover, the REDWIN project [78] proposed an alternative approach for the Monopile design as a global macro-element model placed at mudline, combining both pile and soil responses. The proposed macro-element is based on the theoretical formulation of multi-surface-plasticity deploying the concepts of both isotropic and kinematic hardening for both monotonic loading and general cyclic loading, thereby describing both foundation stiffness and damping characteristics.

2.3.2 Local macro-element model

The local macro-element (LME) model is a term derived from the concept of macro-element modelling to represent the local behaviour of the foundation-soil interaction. The LME concept can be visualised as equivalent to the ‘Beam on Non-linear Winkler Foundation’ (BNWF) models. Nevertheless, BNWF models have the main drawback concerning the impossibility of modelling correctly the experimentally observed coupling between axial and lateral pile-soil interaction response. It is because of the independent nature of beams at different depths. Overall, the BNWF approach can be placed somewhat in between the continuum-based finite element (FE) modelling and global macro-element modelling.

In the present thesis work, a study is presented to utilise the global macro-element modelling knowledge and BNWF approach, to develop a local macro-element model which captures the coupled pile-soil interaction while resembling the BNWF model appearance. There are two important motivational reasons to proceed with the local macro-element modelling idea. (1) The failure mechanism of a pile foundation is rather complex to be generalised into a single constitutive framework as a global macro-element model. The pile head response characteristics are intriguing; however, the different modes of interaction along the pile embedment and base are oversimplified with the global macro-element. A local macro-element approach may bridge

this gap and hence is worthy of exploring. (2) There has already been a study on a local macro-element framework, presented by Taciroglu et al. [98] for deep flexible foundations on clay. The conceptual idea to develop a local macro-element model for rigid pile foundations is inspired by this work.

Although the macro-element approach seems a somewhat simplified version of sophisticated FE modelling, previous researcher studies [19], [41], [53], [63], [78], [86] have shown that the qualitative comparison of spring and FE approaches provide the agreeable result of significant interest. Hence, further developments in the definition of spring models for local as well as global macro-element sees a right path to follow to gain computational advantage and produce readily available and reliable results.

2.4 Stiffness parameters

The macro-element modelling essentially revolves around the stiffness parameter, which continues to evolve as per the parent constitutive law to capture the non-linear characteristics of the pile-soil interaction. Also, Leblanc et al. [60] stated that for offshore wind turbine foundation applications, the primary design drivers for the monopile and tower are deformation and stiffness and not the ultimate capacity. Hence, it is vital to understand the stiffness feature of monopile-soil interaction.

The basis of macro-element modelling is the stiffness parameters relating the load to the deformations. The selection of correct stiffness characteristics is intrinsic to the strain level in the soil. Arshad and O’Kelly [12] presented a detailed description of the stiffness parameters (see Figure 2.27).

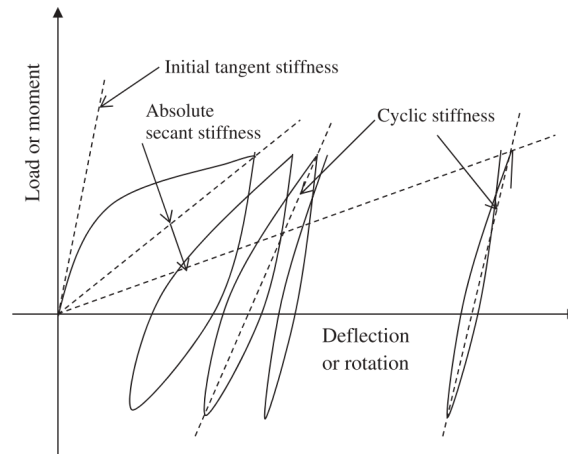


Figure 2.27: Demonstration of all the stiffness parameters representing the pile-soil interaction, from Arshad and O’Kelly [12]

The shear modulus characterises the initial tangent stiffness, also called the elastic stiffness at small strain levels (G_o). The secant stiffness is representative of a higher strain level and is defined as the slope from the origin. The absolute secant stiffness parameter specifies the stiffness degradation due to cyclic loading feature of the pile-soil interaction. Further, the cyclic stiffness defines the loading-unloading characteristics of the interaction.

The elastic stiffness is a crucial ingredient in the macro-element model concept definition. For offshore wind turbine applications, Bhattacharya et al. [19] proposed a three elastic springs model to represent the monopile foundation response to the lateral and moment loading as coupled global pile-soil interaction. Figure 2.28 presents the transition from the field offshore wind turbine supported on monopile to the global three springs model equivalent for elastic stiffness estimation.

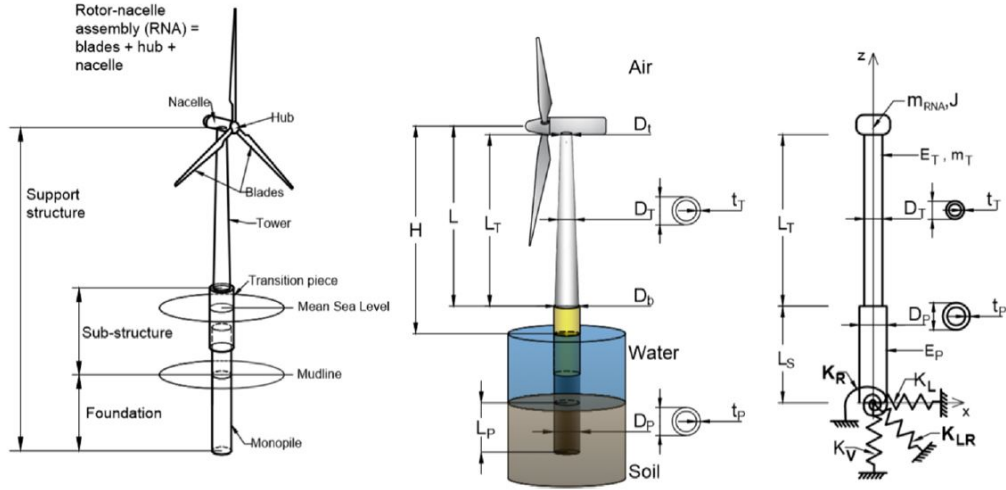


Figure 2.28: Transition from field scale pile-soil system to the global stiffness parameters representing the behaviour of monopile, from Bhattacharya et al. [19]

Bhattacharya [15] presented a method to estimate the global stiffness parameters, namely K_L , K_R and K_{LR} from FE analysis. The method is briefly described here.

Equation 2.25 presents global behaviour as a relation between the applied load and resulting displacement and rotations by the stiffness parameters.

$$\begin{bmatrix} H \\ M \end{bmatrix} = \begin{bmatrix} K_L & K_{LR} \\ K_{LR} & K_R \end{bmatrix} \begin{bmatrix} y \\ \theta \end{bmatrix} \quad (2.25)$$

Equation 2.25 is rewritten in terms of the flexibility matrix relating the displacement and rotation to the applied load levels. This is presented in Equation 2.26.

$$\begin{bmatrix} y \\ \theta \end{bmatrix} = \begin{bmatrix} I_L & I_{LR} \\ I_{LR} & I_R \end{bmatrix} \begin{bmatrix} H \\ M \end{bmatrix} \quad (2.26)$$

The method involves two steps. First, the pile is laterally loaded (H) at mudline level, and head displacement (y_1) and rotation (θ_1) are estimated in the initial elastic response zone. Second, the pile is loaded with moment load only, and similar head displacement (y_2) and rotation (θ_2) are recorded. Equations 2.27 and 2.28 presents the first and second step respectively.

$$\begin{bmatrix} y_1 \\ \theta_1 \end{bmatrix} = \begin{bmatrix} I_L & I_{LR} \\ I_{LR} & I_R \end{bmatrix} \begin{bmatrix} H \\ 0 \end{bmatrix} \quad (2.27)$$

$$\begin{bmatrix} y_2 \\ \theta_2 \end{bmatrix} = \begin{bmatrix} I_L & I_{LR} \\ I_{LR} & I_R \end{bmatrix} \begin{bmatrix} 0 \\ M \end{bmatrix} \quad (2.28)$$

By a simple mathematical analysis, the resulting solution for global stiffness parameters is presented in Equation 2.29.

$$K = \begin{bmatrix} K_L & K_{LR} \\ K_{LR} & K_R \end{bmatrix} = I^{-1} = \begin{bmatrix} y_1/H & y_2/M \\ \theta_1/H & \theta_2/M \end{bmatrix}^{-1} \quad (2.29)$$

This model can be economical in the conceptual design phase of the monopile foundation project. Shadlou and Bhattacharya [92] provided equations for three stiffness springs for both rigid and flexible foundations as presented in Figure 2.29 below for rigid and flexible foundations.

Ground profile	K_L	K_{LR}	K_R
homogeneous	$3.2 \left(\frac{L}{D_p}\right)^{0.62} f_{(vs)} E_{SO} D_p$	$-1.8 \left(\frac{L}{D_p}\right)^{1.56} f_{(vs)} E_{SO} D_p^2$	$1.65 \left(\frac{L}{D_p}\right)^{2.5} f_{(vs)} E_{SO} D_p^3$
parabolic	$2.65 \left(\frac{L}{D_p}\right)^{1.07} f_{(vs)} E_{SO} D_p$	$-1.8 \left(\frac{L}{D_p}\right)^2 f_{(vs)} E_{SO} D_p^2$	$1.63 \left(\frac{L}{D_p}\right)^3 f_{(vs)} E_{SO} D_p^3$
linear	$2.35 \left(\frac{L}{D_p}\right)^{1.53} f_{(vs)} E_{SO} D_p$	$-1.8 \left(\frac{L}{D_p}\right)^{2.5} f_{(vs)} E_{SO} D_p^2$	$1.58 \left(\frac{L}{D_p}\right)^{3.45} f_{(vs)} E_{SO} D_p^3$

(a)

Ground profile	K_L	K_{LR}	K_R
homogeneous	$1.45 \left(\frac{E_p}{E_{SO}}\right)^{0.186} f_{(vs)} E_{SO} D_p$	$-0.3 \left(\frac{E_p}{E_{SO}}\right)^{0.5} f_{(vs)} E_{SO} D_p^2$	$0.19 \left(\frac{E_p}{E_{SO}}\right)^{0.73} f_{(vs)} E_{SO} D_p^3$
parabolic	$1.015 \left(\frac{E_p}{E_{SO}}\right)^{0.27} f_{(vs)} E_{SO} D_p$	$-0.29 \left(\frac{E_p}{E_{SO}}\right)^{0.52} f_{(vs)} E_{SO} D_p^2$	$0.18 \left(\frac{E_p}{E_{SO}}\right)^{0.76} f_{(vs)} E_{SO} D_p^3$
linear	$0.79 \left(\frac{E_p}{E_{SO}}\right)^{0.34} f_{(vs)} E_{SO} D_p$	$-0.27 \left(\frac{E_p}{E_{SO}}\right)^{0.567} f_{(vs)} E_{SO} D_p^2$	$0.17 \left(\frac{E_p}{E_{SO}}\right)^{0.78} f_{(vs)} E_{SO} D_p^3$

(b)

Figure 2.29: Stiffness parameters empirical estimation for rigid (a) and flexible (b) pile behavior, as reported by Bhattacharya et al. [19]

here,

$$f_{(vs)} = 1 + 0.6|v_s - 0.25|;$$

v_s = Poisson's ratio;

D_p = pile diameter;

L = pile length;

E_p = equivalent modulus of pile; and

E_{SO} = Young's modulus of the ground at one diameter below the ground;

In addition, Bhattacharya and Adhikari [16] reported a method to estimate the stiffness parameters K_L and K_R in laboratory experimentation. Notably, all three foundation stiffness parameters are not independent. However, some parameters relevant to pile (D_p , t_p and L_p) and soil stiffness (k_h or n_h and G^*) are independent.

Arany et al. [9] reported the significance of the global stiffness parameters for the long term soil-pile interaction characteristics. The authors reported a closed-form solution for the estimation of the natural frequency (f_1) of the wind turbine system (tower + foundation + interaction), presented in Equation 2.30.

$$f_1 = C_L C_R f_{FB} \quad (2.30)$$

Here, f_{FB} is called the fixed base natural frequency which can be determined from the cantilever beam natural frequency estimation formula, defined in Equation 2.31. The parameter k represents the equivalent beam stiffness, estimated from the tower bending stiffness and m is the equivalent mass of the tower and rotor nacelle assembly.

$$f_{FB} = \frac{1}{2\pi} \sqrt{\frac{k}{m}} \quad (2.31)$$

The natural frequency of the turbine structure and foundation system is collectively presented by defining two interaction coefficients (C_L and C_R) incorporating the global stiffness parameters (see Equation 2.32). The foundation flexibility coefficient of $F_{FF} = C_R C_L$ determination for cohesionless soils requires two independent parameters. For slender piles, the density of soil ρ_s and the bending stiffness of the monopile $E_P I_P$; and for rigid piles they are the soil density ρ_s and the pile embedded length L_P .

$$\begin{aligned} C_R(\eta_L, \eta_R, \eta_{LR}) &= 1 - \frac{1}{1 + a \left(\eta_R - \frac{\eta_{LR}^2}{\eta_L} \right)} \\ C_L(\eta_L, \eta_R, \eta_{LR}) &= 1 - \frac{1}{1 + b \left(\eta_L - \frac{\eta_{LR}^2}{\eta_R} \right)} \end{aligned} \quad (2.32)$$

Here, η_L , η_R and η_{LR} are defined as per Equation 2.33 as a function of global stiffness and pile geometrical features namely equivalent bending stiffness ($E I_\eta$) of the tapered tower and tower's length (L_T). The coefficient 'a' and 'b' are empirical constants.

$$\eta_L = \frac{K_L L_T^3}{E I_\eta}, \quad \eta_{LR} = \frac{K_{LR} L_T^2}{E I_\eta}, \quad \eta_R = \frac{K_R L_T}{E I_\eta} \quad (2.33)$$

Previous researchers have reported that most of the contribution to the frequency change results from the rotational foundation flexibility coefficient C_R , which is around (4–15%). The lateral foundation stiffness coefficient C_L provides a limited influence (<1%) of all analyzed turbines. The coefficient, C_R , highly dependent on the rotational stiffness presents an almost constant value for higher rotational stiffness. It enables the designer to choose the rotational stiffness residing on the constant value range such that the uncertainty in the foundation stiffness estimation does not alter the natural frequency considerably. It further ensures the foundation's ability to meet the Fatigue Limit State (FLS) and Serviceability Limit State (SLS) criteria.

The elastic stiffness estimation for a local macro-element based model is equivalent to the initial stiffness of the local pile-soil interaction elements such as the ones presented in the section 2.2.2.

In addition to the elastic stiffness, the other stiffness parameters as presented in Figure 2.27 are also significant towards the macro-element model definition. In particular, the stiffness parameters displaying the cyclic behaviour parameters have been substantially studied and emphasised in previous studies (e.g. [4], [11], [60]) for the definition of pile-soil interaction concerning OWT structures subjected to a large number of lateral load cycles in its lifetime.

Leblanc et al. [60] studied the long term performance through lab-scale experimentation with a large number of cyclic loading application. Figure 2.1.2 demonstrates the conceptual framework used by the authors for the cyclic stiffness parameters determination from applied moment load and pile head rotation relationship.

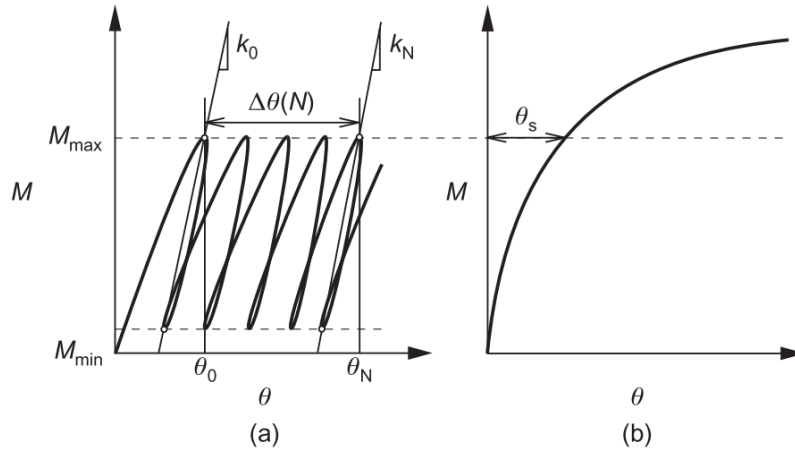


Figure 2.30: The moment rotation plot representing the concept of the long term cyclic response for model monopile, (a) cyclic loading, (b) static loading, from Leblanc et al. [60]

Here, θ_s defines the static failure limit and is determined from a monotonic load test until the prescribed pile-failure rotation of 4 degrees. The cyclic stiffness at first (k_0) and Nth load cycle (k_N) is presumed to follow a logarithmic increase as a function of the number of load cycles (N). The pile rotation change with load cycles ($\Delta\theta$) and is mathematically presented as per Equation 2.34, where T_b and T_c are two dimensional functions depending on load characteristics (see Equation 2.1) and relative density (R_d).

$$\frac{\Delta\theta(N)}{\theta_s} = T_b(\zeta_b, R_d) \times T_c(\zeta_c) \times N^{0.31} \quad (2.34)$$

Abadie et al. [4] presented an analytical solution to represent and calibrate the long term cyclic loading behaviour of the Hyperplastic Accelerated Ratcheting Model (HARM) [48]. The solution implements the kinematic hardening and ratcheting features to predict the accumulated rotation after Nth load cycle directly. It allows for a very fast FLS estimation for monopile design after thousands of numbers of load cycles, instead of conducting the equivalent lab studies for the said number of load cycles. Figure 2.31 presents a demonstration of the accumulated rotation over 100,000 load cycles (grey), experimentally studied by Abadie et al. [1] and superimposed by the HARM analytical solution (blue/black).

The authors also reported the correlation between monotonic and cyclic moment rotation plot. The moment rotation evolution under cyclic loading follows the monotonic evolution

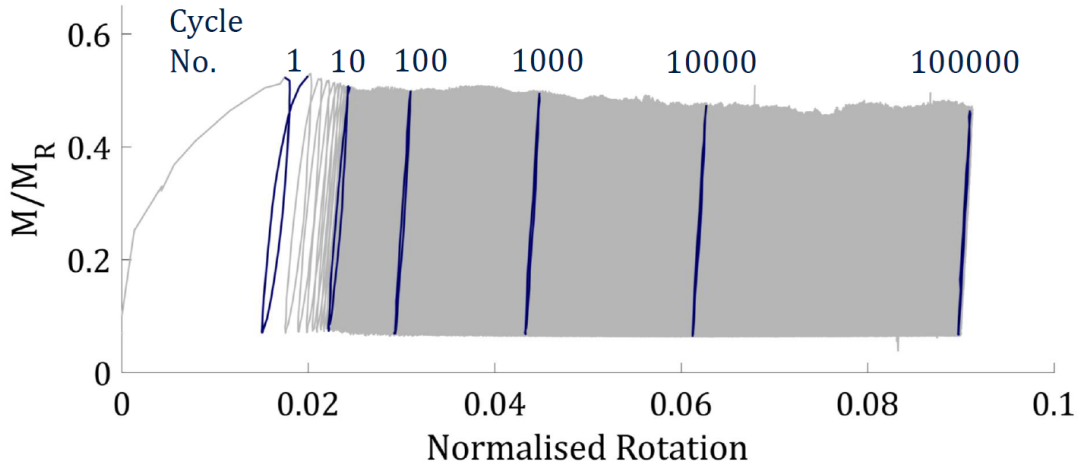


Figure 2.31: Demonstration of the pile head rotation accumulation for a long term cyclic loading, from Abadie et al. [1]

as a backbone envelope. Many researchers [3], [7], [14], [45] have reported the backbone (also known as initial loading curve) feature; an outcome of the Masing rules [66] application. This feature is demonstrated in Figure 2.32, where a monotonic response plot (dashed) is superimposed over a multi-amplitude cyclic loading test (grey) with three different amplitudes. The observation allows having an estimate of the cyclic loading magnitudes in practical design conditions. It also confirms the significance of the backbone curve by the presentation of a multi-amplitude cyclic load (representative of complex environmental loading conditions) does not surpass the backbone curve.

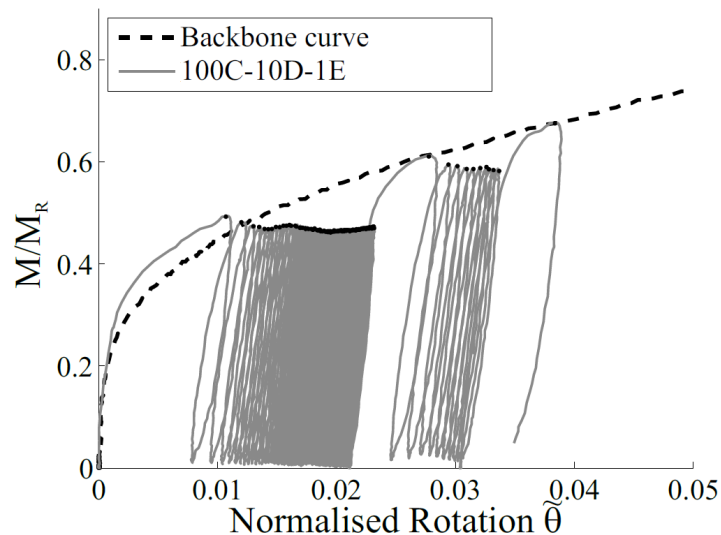


Figure 2.32: Demonstration of the backbone curve for the monotonic and cyclic loading correlation, modified from Abadie et al. [3]

Arshad and O'Kelly [11] reported a hypothesis to estimate the degrading absolute secant stiffness for a cyclic loading scenario as the equivalence with the inverse ratio of stiffness at Nth cycle to 1st cycle and the ratio of accumulated plastic strain between these two cycles. Figure 2.33 presents the representation of the stiffness parameters in deviatoric stresses and axial strain plane. Equation 2.35 presents the mathematical formulation for the correlation between

axial strain and the absolute secant stiffness.

$$\frac{\epsilon_{p(N=1)}}{\epsilon_{p(N=N)}} = \frac{E_{s(N=N)}}{E_{s(N=1)}} \quad (2.35)$$

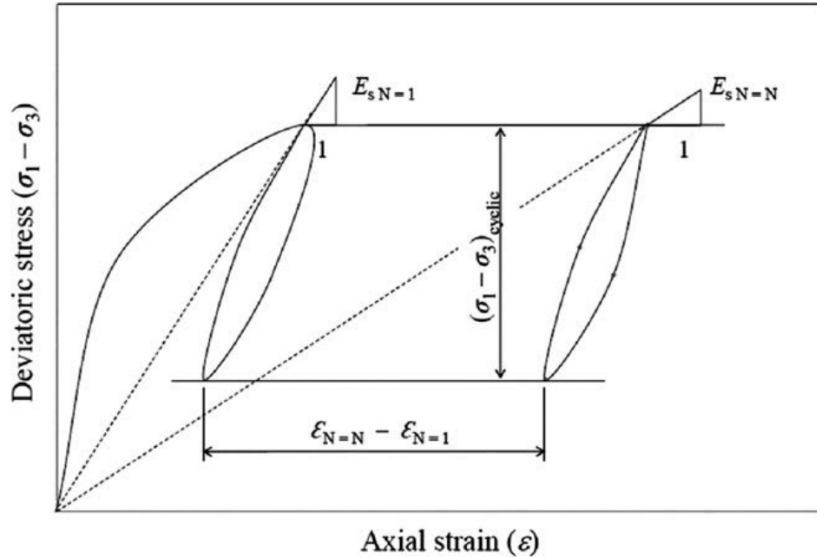


Figure 2.33: Demonstration of the degrading soil secant stiffness under cyclic loading, from Arshad and O’Kelly [11]

2.5 Similitude

The similitude conditions are intended to fulfil the objective of correlating the field-scale prototypes to the lab-scale models. A model is the representation of a physical system that may be used to predict the behaviour of the system ‘in some desired respect’. Langhaar [59] stated that the critical point in similitude studies is ‘to have identical self-weight stresses in both model and prototype’. A prototype and model are said to be in similitude if a point to point correspondence exists between the model and prototype. A similitude analysis is broadly a two-step process presented hereafter.

The first step is to choose a scaling factor of the prototype for the development of a lab-scale model incorporating the setup size, loading and geometrical limits in the laboratory. The second step is to establish and verify the equality of the non-dimensional groups (NDGs) for model and prototype and make necessary modifications. Notably, Scaling laws between models and prototypes may be obtained using either dimensional analysis or evaluating differential equations. Dimensional analysis is preferred to differential equations because it does not presuppose the relationship between the various variables involved [27]. Langhaar [59] defined dimensional analysis as ‘a method by which we deduce information about a phenomenon from the single premise that the phenomena can be described by a dimensionally correct equation among certain variables’.

The NDGs are necessary to interpret the model test results and scale up the results for actual scale prototypes. Most of the physical process can be expressed in terms of non-

dimensional groups, and the fundamental aspects of physics need to be preserved in the design of model tests. As the number of variables affecting the problem increases, it becomes progressively more challenging to determine the function which relates the various variables involved. Buckingham π -theorem is used to overcome this difficulty by grouping dependent and independent variables into a smaller number of non-dimensional products, as reported in Iskander [49]. These non-dimensional products are referred to as π -terms. Scaling laws which satisfy similitude are derived by equating all the dimensionless π -terms in both the prototype and the model as shown in Equation 2.36.

$$(\pi_i)_{model} = (\pi_i)_{prototype} \quad (2.36)$$

Ideally, if the π -terms are equal between model and prototype, then all the similarities are believed to be preserved. A complete similitude analysis shall capture both environmental load-tower structure interaction and pile-soil interaction features. Kerner et al. [56] have reported use of Reynolds, Mach, Froude and Weber numbers for the definition of fluid flow representative of the environmental load-tower structure interaction. However, in the context of the aim of the present thesis project, the similitude relationships related to the monopile-soil interactions only are presented. Many researchers have presented the similitude NDG's for pile-soil interaction study. A brief synthesis is presented as follows.

The non-dimensional groups presented by Kerner et al. [56] concerning the pile-soil interaction are listed in Table 2.3 below.

Table 2.3: Non-dimensional groups presenting scaling laws, reported by Kerner et al. [56]

	Physical mechanism	Non-dimensional groups
Soil	Stress/strain	$\frac{F_g}{GD_p^2}$
	Grain size	$\frac{D_p}{D_{sand}} \geq 30$
Soil-pile interaction	Static	$\frac{GL^4}{E_p I_p}$
	Load eccentricity	$\frac{y}{D_p}$
Monopile	Stress/strain	$\frac{F_g}{E_p D_p^2}$
	Poisson's ratio	ν_p

where,

- D_p = Monopile's diameter;
- F_g = Global point load on the wind turbine;
- y = Lever arm's of the point load, moment on foundation being $M = F_g y$;
- E_p = Monopile's Young modulus;
- ν_p = Monopile's Poisson ratio;
- G = Soil's shear modulus.

Besides, from the studies by Kerner et al. [56], it is observed that for a lab-scaled model test, the aspect ratio of the pile may not necessarily be preserved. Authors presented scaling laws to define a lab-scale model from a prototype pile (see Figure 2.34) with a diameter equal to 6m and embedment length equal to 36 m. The resulting lab-scale model pile was 16mm and length 36 cm. The length of the pile is descaled by a linear factor, whereas the diameter of the pile does not follow the same scaling procedure. Authors have analysed the pile-soil interaction with lateral load application; thereby making pile diameter a dependent parameter in the definition of the scaling laws. It is an important outcome, however, also contradicts with the description of the scaling law presented by Leblanc et al. [60], where the aspect ratio is preserved for 1g lab-scale tests. Notably, Kerner et al. [56] have utilised water-filled membrane to represent effective vertical stress in the soil volume for experimentation.

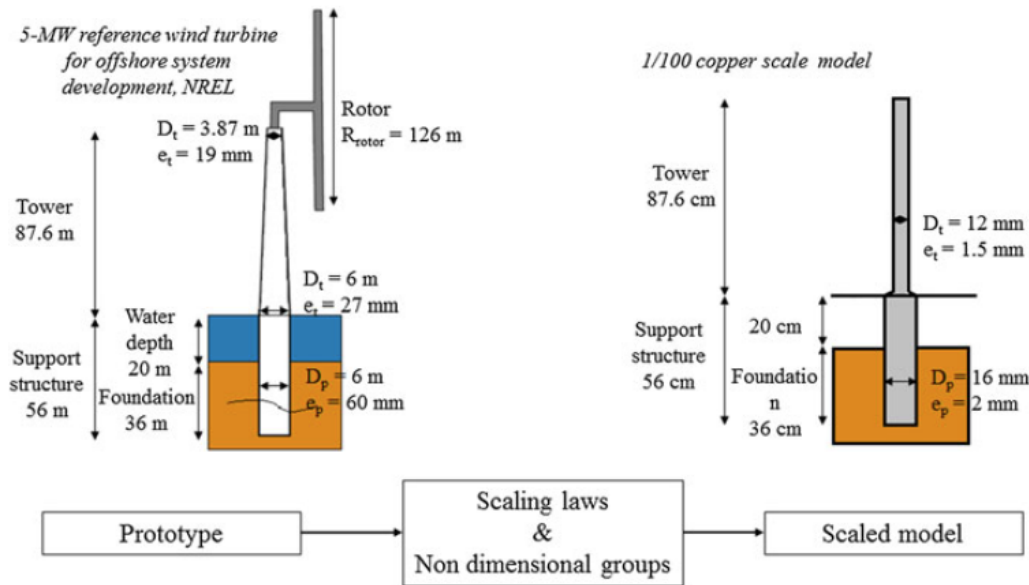


Figure 2.34: Prototype to lab scaled model, from Kerner et al. [56]

Also, it is essential to evaluate the impact of the grain size ratio between the model and the prototype. According to Sedran et al. [91], it is possible to use the same sand for the prototype and the model if the ratio between the pile diameter and the grain size is: $D_p/D_{sand} \geq 30$. Besides, Kerner et al. [56] reported the material density is also a parameter to consider for scaling laws in addition to the length parameters. A dense and flexible metal shall be used to design the scaled model. Nikitas et al. [74] have reported that the correctness of the scaling laws is subjected to the usage of the same prototype scale structure surrounding soil type for model

tests. For practical design, The monopile possess a constant diameter while the thickness of the wall might vary along the pile length. For the pile-soil global interaction estimation through the stiffness parameters, Arany et al. [9] have suggested choosing the model pile thickness equivalent to the thickness close to the mudline level. It is because these upper layers are considered the most important from the point to view to the head deflection, rotation and wedge type-failure characteristics.

Besides, Bhattacharya et al. [17] reported the scaling laws considering the relation between two types of pile-soil interaction (see Figure 2.19. Table 2.4 presents the NDGs reported for 1g lab-scale experiments; in the context of OWT applications. Authors stated that the soil-structure interaction will differ at different depths and can be described by CSR (Cyclic Stress Ratio), which is essentially the ratio of shear stress to the vertical stress. Authors reported the similitude relationship for CSR is proportional to the average shear strain in the soil around the pile.

Table 2.4: Non-dimensional groups presenting scaling laws, reported by Bhattacharya et al. [17]

Non-dimensional group	Physical meaning
P/GD^2	Strain field in the soil and cyclic stress ratio ensuring similar degradation of soil stiffness
$k_h/f_f D$	Rate of loading. Modeling consolidation/dissipation of pore water pressure
$f : f_{sys}$	Relative spacing of the forcing frequencies and the natural frequencies, i.e. system dynamics
Py/ED^2t	Strain Bending strain in the pile. Non-linearity in the pile material
$Py/\sigma_y D^2t$	Stress level in the pile. Fatigue limit state

Notably, the non-dimensional group representing the strain level in the soil is given by (P/GD^2) , which indicates that strain level in the soil adjacent to the pile decreases with the square of the diameter. These results, therefore, justify the use of large-diameter monopiles as foundations for modern offshore wind turbines [17].

Some researchers have also presented the similitude relations between input loading parameters and pile and soil properties. One such work is carried by Leblanc et al. [60] and reported the non-dimensional parameters for $V - H - M$ loading for 1g model test for driven pile, presented in 2.5.

Table 2.5: Non-dimensional groups presenting scaling laws, reported by Leblanc et al. [60]

Loading type	Non-dimensional group
Moment loading	$\tilde{M} = \frac{M}{L^3 D \gamma'}$
Vertical force	$\tilde{V} = \frac{V}{L^2 D \gamma'}$
Horizontal force	$\tilde{H} = \frac{H}{L^2 D \gamma'}$

Byrne et al. [25] reported the similitude parameters in the framework of the PISA project. The NDGs for the model pile driven in the sand are presented in Table 2.6.

Table 2.6: Non-dimensional groups presenting scaling laws, reported by Byrne et al. [25]

Normalised variable	Non-dimensional group
Horizontal load	$\tilde{H} = \frac{H}{\sigma'_v D^3}$
Lateral deflection	$\tilde{u}_x = \frac{u_x G_o}{\sigma'_v D}$
Rotation	$\tilde{\theta} = \frac{\theta G_o}{\sigma'_v}$
Soil stiffness	$\tilde{G}_s = \frac{G_o}{\sqrt{p_a \sigma'_v}}$

Burd et al. [22] reported the NDGs for the representation of the local level pile-soil interaction in the framework of PISA 1D numerical model for sand, presented in Table 2.7

Table 2.7: Non-dimensional groups presenting scaling laws, reported by Burd et al. [22]

Normalised variable	Non-dimensional group
Distributed lateral load	$\tilde{p} = \frac{p}{\sigma'_v D}$
Lateral displacement	$\tilde{u}_x = \frac{u_x G_o}{\sigma'_v D}$
Distributed moment	$\tilde{m} = \frac{m}{pD}$
Pile rotation	$\tilde{\theta} = \frac{\theta G}{\sigma'_v}$
Base shear load	$\tilde{H}_B = \frac{H_B}{\sigma'_v D^2}$
Base moment	$\tilde{M}_B = \frac{M_B}{\sigma'_v D^3}$

Klinkvort and Hededal [57] reported similitude relations both for the lateral input loading and the local soil reaction at depth, using the passive earth pressure coefficient, presented in Table 2.8. Authors reported the NDGs for centrifuge experimental study of the driven pile in sand.

Table 2.8: Non-dimensional groups presenting scaling laws, reported by Klinkvort and Hededal [57]

Normalised variable	Non-dimensional group
Horizontal load	$\tilde{H} = \frac{H}{K_p \gamma' D^3}$
Local pile-soil reaction	$\tilde{p} = \frac{p}{K_p \sigma'_v D}$

The notations used for additional parameters presented in Tables 2.4, 2.5, 2.6, 2.7 and 2.8 are listed below.

- D = Pile diameter,
 L = Pile embedment length,
 γ' = Unit weight of soil,
 G_o = Small strain shear modulus of soil,
 σ'_v = Vertical effective stress,
 p_a = Atmospheric pressure,
 K_p = Passive earth pressure coefficient.

Model experiments have proven to be useful in studying a wide range of geotechnical problems. The primary difficulty in experimental modelling of soil-structure interaction problems, such as pile driving, is the dependency of the soil strength on the stress level. This difficulty can be overcome using a geotechnical centrifuge, a hydraulic gradient, or using a pressure (calibration) chamber. Overall, the similitude study synthesised before for geotechnical problems aims to correlate, field-scale prototype to a lab-scale model prepared in 1-g or calibration chamber or centrifuge configurations.

For centrifuge modelling, a set of these non-dimensional π -terms are available in the literature [38], [57]. However, for the pressure chamber test, in-situ stresses are scaled in a pressure chamber by application of boundary stresses that simulate the effective stresses at the depth being modelled. For example, a layer of sand 30 m below the surface with anisotropic stress conditions ($K_o = 0.5$), may be represented by applying vertical and horizontal boundary stresses of 240 kPa and 120 kPa, respectively. Moreover, both centrifuge and calibration chamber setups do not correlate the pore water pressures in the similitude formulations [56]. Therefore, most of the lab experiments are conducted on dry soil, even though the field-equivalent sea-bed soil is submerged in the water for OWT applications. Klinkvort and Hededal [57] reported that the lab test on dry or saturated sand result in similar response provided that the rate of deformation is low so as not to develop any excess pore water pressure under saturated conditions.

In the present studies, the model pile analysis is made assuming a calibration chamber configuration. The small scale lab tests are most likely to face a key issue called ‘scale effect’ mainly coming from the size of the experimental setup (*e.g.* D_{sample} to D_{50} sand particle ratio). Silva Illanes [94] has reported that the use of lateral membranes in the calibration chamber setup provides a way to deal with this issue. Three circumferential radial membranes installed at the inner chamber walls were used to apply a more active boundary condition and reduce the possible scale effects. Overall, the presented similitude NDGs serves as a basis to design the lab-scale model for the present project work.

2.6 Conclusions

The background of the offshore wind turbine structure and monopile foundation is presented. The environmental loads and OWT structure components interaction loads collectively introduce the cyclic or dynamic load on the supporting foundation. The subsequent interaction between the pile and the surrounding soil is of vital interest in geotechnical investigations. Notably,

a study of either cyclic or dynamic load consideration is possible for the OWT structures and foundation depending on the research objective. In the present work, the cyclic loading condition is investigated to understand the axial and lateral pile-soil interaction without considering the inertia effect of the components of the OWT structure. An extensive background study on the pile-soil interaction provides the necessary information to proceed with the thesis objectives.

The basis of macro-element modelling for pile-soil interaction behaviour is presented. The relevant information on stiffness parameters and model types serves as a basis to proceed with the aspired local macro-element model development and analysis. A similitude framework is presented to address the pile-soil interaction features in the model and prototype scale systems. Importantly, the primary inadequacy of the calibration chamber for lab-scale models investigations are presented. Its inability to model the gradual increase in soil stresses with depth limits the modelling capabilities to model one layer at a time. Therefore, the background information on the pile-soil interaction similitude relationships shall provide aid to correlate the calibration chamber lab-scale model segment outcomes to the field scale pile.

Chapter 3

Simple local macro-element model

3.1 Objective

This chapter presents a conceptual study on the pile-soil interaction of a rigid pile installed in sand, assuming offshore wind turbine application. A 1D local macro-element model is defined to characterise the pile-soil interaction. The aim is to understand the model structure and element assembly definition in the conceptual framework of typically used pile-soil interaction methods. The work domain starting from the numerical solution algorithm definition to the model assembly analysis with combined loading application is presented.

3.2 General description

Macro-element modelling has gained significant importance over conventional finite element modelling in recent times, due to its computational ease and readily available information for numerical parametric studies and engineering concept design. This chapter presents a ‘local’ macro-element for rigid monopile in the sand. It is inspired by the macro-element developed for deep foundations by Taciroglu et al. [98]. The local macro-element (LME) model is an assembly of nonlinear elastoplastic components equivalent to Winkler’s spring model; representing pile-soil interaction through p-y, T-Z and Q-Z methods (see section 2.2). Simplified cyclic loading scenarios approximately representing the wind and wave loading have been utilised in the computation with consideration to standard ultimate and serviceability load limits criteria. The LME model response is evaluated at the pile head from global pile-soil system response and at different depths for constitutive element response. The model response results are further utilised to report significant differences between the previously studied ‘flexible pile’ and the present ‘rigid pile’ behaviours in the sand under combined loading.

Macro-element approach has been widely accepted for the soil-foundation-structure-interaction problems modelling for structures with isolated shallow foundations and deep pile foundations. The local behaviour of the soil and foundation system at different depths is described at a single point, presenting a relationship between forces and displacements through stiffness.

In the present work, a plasticity theory based macro-element is defined. The element

definition comprises of elastic behaviour, the flow rule and the isotropic hardening law. The constitutive framework of the macro-element model is presented hereafter.

3.3 Constitutive framework

The element definition of the local macro-element model follows one-dimensional, rate-independent isotropic hardening plasticity behaviour law, reported by Simo and Hughes [95], as presented in Figure 3.1. The constitutive framework is briefly presented hereafter.

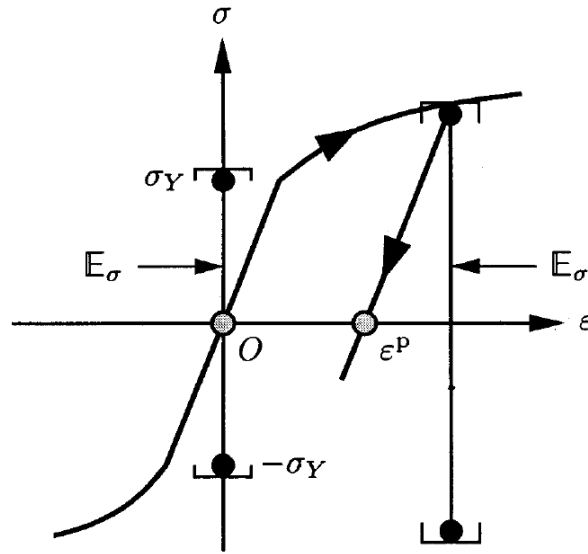


Figure 3.1: Demonstration of the constitutive framework of the isotropic hardening plasticity, from Simo and Hughes [95]

The total strain (ϵ) splits into two parts, elastic (ϵ^e) and plastic strain (ϵ^p). The elastic stress strain-relationship is postulated as follows.

$$\sigma = E(\epsilon - \epsilon^p) \quad (3.1)$$

Here, E is defined as the elastic modulus.

The hardening is assumed isotropic in a sense that at any stage of loading, the centre of expanding yield envelop (\mathbb{E}_σ) remains at the origin. Here, \mathbb{E}_σ is also called a closed convex set. It leads to a yield criterion of the form presented in the Equation 3.2 below.

$$f(\sigma, \alpha) = |\sigma| - [\sigma_Y + K\alpha] \leq 0, \quad \alpha \geq 0 \quad (3.2)$$

Here, $\sigma_Y > 0$ represents yield stress and $K \geq 0$ is defined as the plastic modulus. The variable α is a non-negative function of the amount of the plastic flow and is called an internal hardening variable. Notably, $K < 0$ represents the strain-softening response. The closed convex

set (\mathbb{E}_σ) is mathematically defined as follows.

$$\mathbb{E}_\sigma = \{(\sigma, \alpha) \in \mathbb{R} \times \mathbb{R}_+ | f(\sigma, \alpha) \leq 0\} \quad (3.3)$$

The intersection of \mathbb{E}_σ with lines $\alpha = \text{constant}$ defines the elastic range in the stress space. This is demonstrated in Figure 3.2.

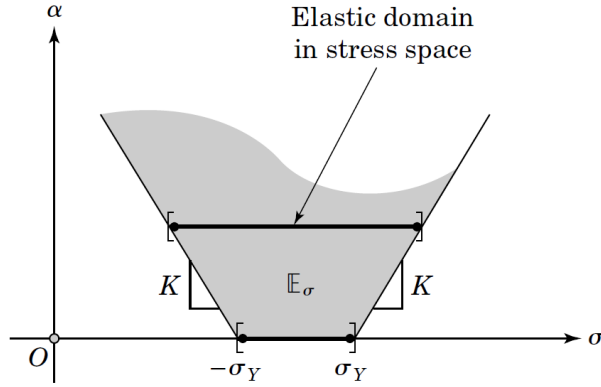


Figure 3.2: Expanding yield surface in the isotropic hardening mechanism, from Simo and Hughes [95]

The flow rule is assumed associative such that the hardening follows the direction of the plastic flow. This assumption results in the evolution of α as presented in the Equation 3.4.

$$\dot{\alpha} = |\dot{\epsilon}^p| \quad (3.4)$$

The rate of the plastic flow $\dot{\epsilon}^p$ is defined as per Equation 3.5 . Here, $\gamma \geq 0$ represents the rate at which plastic flow takes place.

$$\dot{\epsilon}^p = \gamma \text{sign}(\sigma) \quad (3.5)$$

The plastic flow presents an irreversible nature, which is captured utilising Kuhn-Tucker loading/unloading complementary conditions, defined in the Equation 3.6.

$$\gamma \geq 0, \quad f(\sigma, \alpha) \leq 0, \quad \gamma f(\sigma, \alpha) = 0 \quad (3.6)$$

Here, $\gamma \geq 0$ is determined by the consistency condition presented below.

$$\gamma \dot{f}(\sigma, \alpha) = 0 \quad (3.7)$$

The consistency condition enables to explicitly solve for the plastic flow rate (γ) and

relate stress rates to strain rates as follows.

$$\begin{aligned} \dot{f} &= \frac{\partial f}{\partial \sigma} \dot{\sigma} + \frac{\partial f}{\partial \alpha} \dot{\alpha} \\ &= \text{sign}(\sigma) E (\dot{\epsilon} - \dot{\epsilon}^p) - K \dot{\alpha} \\ &= \text{sign}(\sigma) E \dot{\epsilon} - \gamma [E + K] \leq 0 \end{aligned} \quad (3.8)$$

The complementary and consistency conditions imply that the γ can be non-zero only if,

$$f = \dot{f} = 0 \implies \gamma = \frac{\text{sign}(\sigma) E \dot{\epsilon}}{E + K} \quad (3.9)$$

This further implies

$$\dot{\sigma} = \begin{cases} E \dot{\epsilon}, & \text{if } \gamma = 0, \\ \frac{EK}{E+K} \dot{\epsilon}, & \text{if } \gamma > 0 \end{cases} \quad (3.10)$$

Here, $EK/(E+K)$ is called elastoplastic tangent modulus. The element definition with the presented constitutive framework is implemented for both linear and nonlinear hardening responses following a return mapping algorithm, shown in the next section.

3.4 Return mapping algorithm

The numerical solution of the constitutive behaviour is presented by the use of a return mapping algorithm [95], briefly presented hereafter.

Consider a one-dimensional behaviour law (σ, ϵ) and a load function f characterised by a single hardening variable (α) . The return mapping process is demonstrated in Figure 3.3. It is assumed that the state (σ_n, ϵ_n) , called the plastic deformation state, and the value of the hardening variable (α_n) at step 'n' is known. With this assumption, it is proposed to find an auxiliary state parameterised by 'trial' and is defined by considering an elastic step:

$$\sigma_{n+1}^{trial} = E \times (\epsilon_{n+1} - \epsilon_n^{pl}) \quad (3.11)$$

$$f_{n+1}^{trial} = f(\sigma_{n+1}^{trial}, \alpha_n) \quad (3.12)$$

Two cases arise:

If $f_{n+1}^{trial} \leq 0$ then the regime is elastic and $\epsilon_{n+1}^{pl} = \epsilon_n^{pl}$, $\alpha_{n+1} = \alpha_n$ and $\sigma_{n+1} = \sigma_{n+1}^{trial}$

If $f_{n+1}^{trial} > 0$ then the regime is plastic and we have to solve the equation $f(\sigma_{n+1}, \alpha_{n+1}) = 0$

To simplify the solving of the equation $f(\sigma_{n+1}, \alpha_{n+1}) = 0$ in the plastic regime, associated flow rule is assumed by considering $\dot{\alpha}_n = |\dot{\epsilon}_n^{pl}|$.

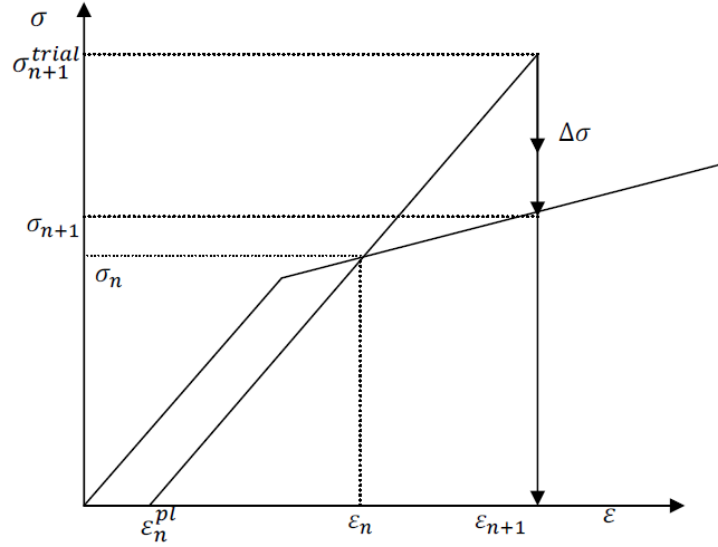


Figure 3.3: Demonstration of the return mapping algorithm, from Simo and Hughes [95]

The reaction σ_{n+1} can be written by considering the plastic multiplier $\Delta\lambda$ and an explicit integration schema in the form:

$$\sigma_{n+1} = \sigma_{n+1}^{trial} - E \times (\epsilon_{n+1}^{pl} - \epsilon_n^{pl}) = \sigma_{n+1}^{trial} - E\Delta\lambda \frac{\partial f}{\partial \sigma}(\sigma_n, \alpha_n) \quad (3.13)$$

The hardening variable α_{n+1} is written as:

$$\alpha_{n+1} = \alpha_n + \Delta\lambda \left| \frac{\partial f}{\partial \alpha}(\sigma_n, \alpha_n) \right| \quad (3.14)$$

The problem is therefore to solve an equation of a single variable $f(\Delta\lambda) = 0$. The load function is usually nonlinear and solving the equation requires the Newton-Raphson iteration method.

It is shown that at each iteration 'k' the plastic multiplier is:

$$\delta(\Delta\lambda)^k = \frac{f(\sigma_n^k, \alpha_n^k)}{E \times \left(\frac{\partial f}{\partial \sigma}(\sigma_n^k, \alpha_n^k) \right)^2 + \frac{\partial f}{\partial \alpha}(\sigma_n^k, \alpha_n^k) \times \left| \frac{\partial f}{\partial \sigma}(\sigma_n^k, \alpha_n^k) \right|} \quad (3.15)$$

So the reaction, the variable of hardening and the plastic displacement at the iteration $k + 1$ is written as:

$$\begin{aligned} \sigma_n^{k+1} &= \sigma_n^k - \delta(\Delta\lambda)^k \times E \times \frac{\partial f}{\partial \sigma}(\sigma_n^k, \alpha_n^k) \\ \alpha_n^{k+1} &= \alpha_n^k + \delta(\Delta\lambda)^k \left| \frac{\partial f}{\partial \alpha}(\sigma_n^k, \alpha_n^k) \right| \\ (\epsilon_n^{pl})^{k+1} &= (\epsilon_n^{pl})^k + \delta(\Delta\lambda)^k \times \frac{\partial f}{\partial \sigma}(\sigma_n^k, \alpha_n^k) \end{aligned} \quad (3.16)$$

If the function $f(\Delta\lambda)$ is linear, the Newton-Raphson method requires a single iteration

and we can write directly:

$$\Delta\lambda = \frac{f(\sigma_n, \alpha_n)}{E \times \left(\frac{\partial f}{\partial \sigma}(\sigma_n, \alpha_n) \right)^2 + \frac{\partial f}{\partial \alpha}(\sigma_n, \alpha_n) \times \left| \frac{\partial f}{\partial \sigma}(\sigma_n, \alpha_n) \right|} \quad (3.17)$$

Thus, the reaction, the hardening variable and the plastic displacement at step $n + 1$ write:

$$\begin{aligned} \sigma_{n+1} &= \sigma_n - \Delta\lambda \times E \times \frac{\partial f}{\partial \sigma}(\sigma_n, \alpha_n) \\ \alpha_{n+1} &= \alpha_n + \Delta\lambda \left| \frac{\partial f}{\partial \sigma}(\sigma_n, \alpha_n) \right| \\ \epsilon_{n+1}^{pl} &= \epsilon_n^{pl} + \Delta\lambda \times \frac{\partial f}{\partial \sigma}(\sigma_n, \alpha_n) \end{aligned} \quad (3.18)$$

3.5 Simple prototype scale model parameters

A local macro element in which sub-elements are used for modelling a particular process of the interaction at a particular depth along pile is presented. Its formulation for rigid monopiles in the sand is inspired by the work carried out by Taciroglu et al. [98] for flexible bored piles in clay. The parameters for soil and pile are presented in Table 3.1. Poulos and Hull [81] provided a criterion based on the stiffness ratio of pile and soil to categorise the pile behaviour as ‘rigid (>0.208)’ or ‘flexible (<0.0025)’ (see section 2.1.3 for details). Based on this, the model pile is rigid. The wall thickness is as per the recommendation for minimum thickness by API standards ($t = 6.35 + D/100$ (mm)). The resulting length to diameter ratio is ‘3’ which is typical of short rigid monopile foundation for offshore wind turbine applications. A dense Fontainebleau sand NE34 soil is assumed for the model soil definition, with parameters extracted from previously reported studies. The deformation soil modulus ($E_{soil} = 40$ MPa) is estimated as per the results reported by Mosquera et al. [69] for dense Fontainebleau Sand NE34. The maximum and minimum soil unit weight are taken as reported by Tsuha et al. [99].

Table 3.1: Pile and soil parameters defining simple prototype macro-element model

Steel pile parameters	Value	Fontainebleau Sand NE34 parameters	Value
Outer diameter, D_o (m)	4.00	Minimum unit weight, γ'_{min} (kN/m^3)	13.68
Wall thickness, t (m)	0.0464	Maximum unit weight, γ'_{max} (kN/m^3)	17.22
Embedment length, L_e (m)	12.00	Relative density, I_D (%)	84
L_e/D	3	Unit weight, γ' (kN/m^3)	16.53
Young’s modulus, E_{pile} (GPa)	210	Deformation modulus of sand, E_{soil} (MPa)	40
Stiffness ratio, K_R	0.2844	Internal friction angle, ϕ' (degree)	37
		Interface friction angle, δ' (degree)	33.3

3.6 Model components

The local macro-element represents the soil-pile interaction at a particular depth along pile embedment. It is composed of three components, namely p-y, T-Z and interface drag elements. Besides, an element, namely Q-Z, is included representing the behaviour at the base of the pile. Figure 3.4 presents the simple local macro-element model assembly where local macro-elements are present at each 1m depth between 0.5 to 11.5m depths. A macro-element construction is typically comprised of an elastic stiffness (k) and a failure state presented by element capacity (f_p). The evolution from elastic to the failure state is governed by a linear or nonlinear isotropic hardening law. The constitutive framework of each element is presented as follow.

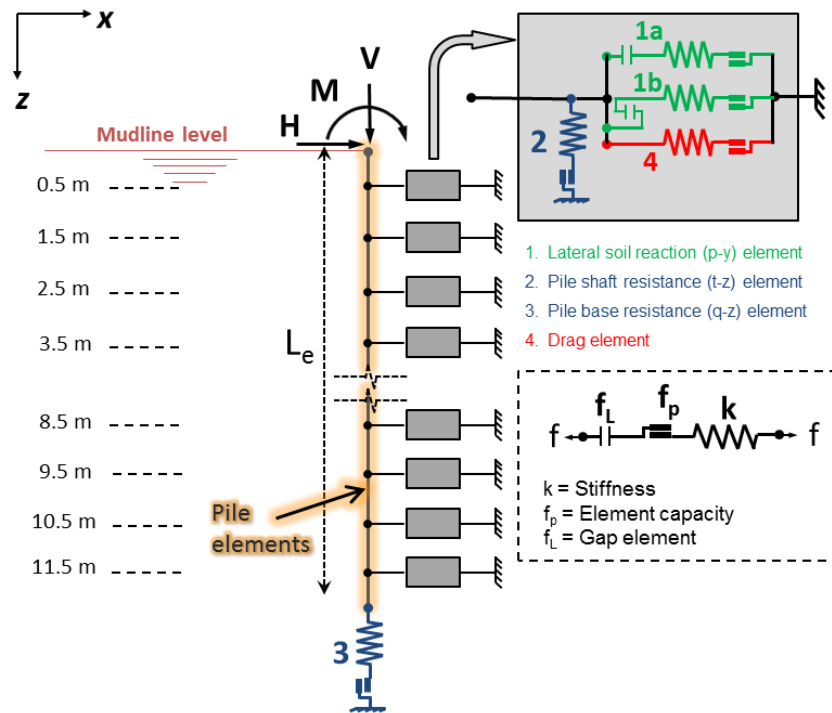


Figure 3.4: Simple prototype local macro-element model assembly with a typical element composition presented in the a dotted box. The grey box (redrawn from Taciroglu et al. [98]) represents the local macro element at different depths

3.6.1 Lateral soil reaction (p-y) element

The first component of the simple local macro-element is the relation between lateral soil reaction (p) and lateral displacement (y). The behaviour is presented as a nonlinear relationship using the profoundly known p-y method. For the present element definition, the p-y evolution presented by Reese et al. [85] and API [6] are used. These methods are developed for the flexible pile foundation analysis under lateral loading. However, in this simple local macro-element model definition, same p-y element definition for rigid pile behaviour study is presented, for conceptual understanding and constituent parameters exploration. The evolution mechanisms of both methods and the definition of the elastoplastic macro-element using return mapping algorithm is presented as follows.

3.6.1.1 Reese p-y method

The definition of Reese et al. [85] p-y method is presented in the previous chapter (see section 2.2.2). The dependency on pile diameter is a key feature of Reese et al. [85] formulation which suits in the present large diameter monopile model description. The initial stiffness is dependent on the soil reaction modulus (k_{py}), estimated to be 34.75 MN/m^3 for dense sand, as per Reese et al. [85] recommendations.

The nonlinear p-y curve element for macro-element has been defined using return mapping algorithm where the behaviour of the p-y curve is taken as elastic till the yield point p_k and plastic with hardening beyond till the point p_u beyond which the response is perfectly plastic. The macro-element definition for the lateral soil-reaction element is presented as follows. The load function is defined as per Equation 3.19.

$$f_{py} = f(p, \alpha) = -\text{sign}(p_L) \times p - (p_k + f(\alpha)) = 0 \quad (3.19)$$

Here p_k is the yield limit for the elastic soil reaction. p_L represents a gap element which is defined to address the soil reaction evolution in the direction of pile movement and no evolution on the opposite side [98]. The gap element is assigned a minimal magnitude (1 N/m), resulting in a negligible effect in the element performance. The lateral load response for a rigid pile is a rotation about a pivot point. Therefore, the lateral soil reaction evolution for depths above and below the point of pile rotation shall be identifiable. For this purpose, two sets of p-y elements called lead face and rear face elements (see element 1a and 1b respectively in Figure 3.4) are defined in association with the gap element. Further, the elastic stiffness $K_e = k \times z$, presented in Equation 3.20 enables the definition of the leading and rear face elements using the gap element.

$$\begin{aligned} \lim_{p \rightarrow \infty} \frac{K_e}{1 + 2^{p/p_L}} &= K_e \\ \lim_{p \rightarrow \infty} \frac{K_e}{1 + 2^{p/p_L}} &= 0 \end{aligned} \quad (3.20)$$

The gap element magnitude $p_L = -1 \text{ N/m}$ is used to define the lead face element and $+1 \text{ N/m}$ for rear face element. The function $f(\alpha)$ in Equation 3.19 represents hardening during plastic displacement. Here, the p-y response is formulated as parabolic beginning from the zero displacements till y_m displacement. Thus, the elastic soil reaction limit (p_k, y_k) is, therefore, not defined explicitly. The hardening is defined in Equation 3.21.

$$f(\alpha^*) = (p_e + f(\alpha)) = p_m \left(\frac{y}{y_m} \right)^{\frac{1}{n}} \quad (3.21)$$

The return mapping algorithm for the p-y element is presented as follows. The soil reaction at n^{th} step for k^{th} iteration is p_n^k . Concerning the procedure mentioned in the return mapping algorithm, the plastic multiplier ($\Delta\lambda$) is evaluated.

$$\delta(\Delta\lambda)^k = \frac{f(p_n^k, \alpha_n^{*k})}{K_e \times \left(\frac{\partial f}{\partial p}(p_n^k, \alpha_n^{*k}) \right)^2 - \frac{\partial f}{\partial \alpha^*}(p_n^k, \alpha_n^{*k}) \times \left| \frac{\partial f}{\partial p}(p_n^k, \alpha_n^{*k}) \right|} \quad (3.22)$$

$$f(p_n^k, \alpha_n^{*k}) = -\text{sign}(p_L) \times p_n^k - \alpha_n^{*k} \quad (3.23)$$

$$\frac{\partial f}{\partial p}(p_n^k, \alpha_n^{*k}) = -\text{sign}(p_L) \quad (3.24)$$

$$\frac{\partial f}{\partial \alpha^*}(p_n^k, \alpha_n^{*k}) = \frac{C}{n} \left((y_p)_n^k + \frac{p_n^k}{K_e} \right)^{\frac{1-n}{n}} \quad (3.25)$$

$$\begin{aligned} p_n^{k+1} &= p_n^k - \delta(\Delta\lambda)^k \times K_e \times \frac{\partial f}{\partial p}(p_n^k, \alpha_n^{*k}) \\ \alpha_n^{*k+1} &= \alpha_n^{*k} + \delta(\Delta\lambda)^k \left| \frac{\partial f}{\partial p}(p_n^k, \alpha_n^{*k}) \right| \\ (y_p)_n^{k+1} &= (y_p)_n^k + \delta(\Delta\lambda)^k \times \frac{\partial f}{\partial p}(p_n^k, \alpha_n^{*k}) \end{aligned} \quad (3.26)$$

Beyond y_m till y_u , the p-y evolution shall follow a linear hardening. It is formulated for the return mapping as follows.

$$f_{py} = f(p, \alpha) = -\text{sign}(p_L) \times p - (p_m + f(\alpha)) = 0 \quad (3.27)$$

The hardening function is defined in Equation 3.28.

$$f(\alpha) = m(y - y_m) \quad (3.28)$$

The return mapping algorithm for the Reese p-y element is presented as follows. The soil reaction at n^{th} step is written as p_n . Concerning the procedure mentioned in the return mapping algorithm, the plastic multiplier ($\Delta\lambda$) is evaluated. The linear hardening infers that one iteration is sufficient at each step.

$$\Delta\lambda = \frac{f(p_n, \alpha_n)}{K_e \times \left(\frac{\partial f}{\partial p}(p_n, \alpha_n) \right)^2 + \frac{\partial f}{\partial \alpha}(p_n, \alpha_n) \times \left| \frac{\partial f}{\partial p}(p_n, \alpha_n) \right|} \quad (3.29)$$

$$f(p_n, \alpha_n) = -\text{sign}(p_L) \times p_n - (p_m + f(\alpha_n)) \quad (3.30)$$

$$\frac{\partial f}{\partial p}(p_n, \alpha_n) = -\text{sign}(p_L) \quad (3.31)$$

$$\frac{\partial f}{\partial \alpha}(p_n, \alpha_n) = m \quad (3.32)$$

$$\begin{aligned} p_{n+1} &= p_n - \delta(\Delta\lambda) \times K_e \times \frac{\partial f}{\partial p}(p_n, \alpha_n) \\ \alpha_{n+1} &= \alpha_n + \delta(\Delta\lambda) \left| \frac{\partial f}{\partial p}(p_n, \alpha_n) \right| \\ (y^p)_{n+1} &= (y^p)_n + \delta(\Delta\lambda) \times \frac{\partial f}{\partial p}(p_n, \alpha_n) \end{aligned} \quad (3.33)$$

3.6.1.2 API p-y method

The definition of API p-y method is presented in the previous chapter (see section 2.2.2). For the present model soil parameters 'k = 31.2 MN/m³' is estimated as per API [6] guidelines. The lateral soil reaction (p-y) element is defined to follow a nonlinear elastoplastic evolution with hyperbolic hardening. The macro-element definition for the lateral soil-reaction element is presented as follows. The load function is defined as per Equation 3.34.

$$f_{py} = f(p, \alpha) = -\text{sign}(p_L) \times p - (p_e + f(\alpha)) = 0 \quad (3.34)$$

Here p_e is the yield limit for the elastic soil reaction. p_L presents the gap element with a similar definition and purpose as presented for the Reese p-y element in the previous section. The elastic stiffness (K_e) is also defined similarly. The function $f(\alpha)$ in Equation 3.34 represents hardening during plastic displacement. The p-y response is formulated as hyperbolic beginning from the zero displacements. Thus, the elastic soil reaction limit is, therefore, not defined explicitly. The hardening is defined in Equation 3.35.

$$f(\alpha^*) = (p_e + f(\alpha)) = A \times p_u \tanh\left(\frac{K_e}{A \times p_u} y\right) \quad (3.35)$$

The return mapping algorithm for the API p-y element is presented as follows. The soil reaction at n^{th} step for k^{th} iteration is p_n^k . Concerning the procedure mentioned in the return mapping algorithm, the plastic multiplier ($\Delta\lambda$) is evaluated.

$$\delta(\Delta\lambda)^k = \frac{f(p_n^k, \alpha_n^{*k})}{K_e \times \left(\frac{\partial f}{\partial p}(p_n^k, \alpha_n^{*k})\right)^2 - \frac{\partial f}{\partial \alpha^*}(p_n^k, \alpha_n^{*k}) \times \left|\frac{\partial f}{\partial p}(p_n^k, \alpha_n^{*k})\right|} \quad (3.36)$$

$$f(p_n^k, \alpha_n^{*k}) = -\text{sign}(p_L) \times p_n^k - \alpha_n^{*k} \quad (3.37)$$

$$\frac{\partial f}{\partial p}(p_n^k, \alpha_n^{*k}) = -\text{sign}(p_L) \quad (3.38)$$

$$\frac{\partial f}{\partial \alpha^*}(p_n^k, \alpha_n^{*k}) = K_e \left[1 - \tanh\left(\frac{K_e \times \left((y_p)_n^k + \frac{p_n^k}{K_e}\right)}{A \times p_u}\right)^2 \right] \quad (3.39)$$

$$\begin{aligned} p_n^{k+1} &= p_n^k - \delta(\Delta\lambda)^k \times K_e \times \frac{\partial f}{\partial p}(p_n^k, \alpha_n^{*k}) \\ \alpha_n^{*k+1} &= \alpha_n^{*k} + \delta(\Delta\lambda)^k \left| \frac{\partial f}{\partial p}(p_n^k, \alpha_n^{*k}) \right| \\ (y_p)_n^{k+1} &= (y_p)_n^k + \delta(\Delta\lambda)^k \times \frac{\partial f}{\partial p}(p_n^k, \alpha_n^{*k}) \end{aligned} \quad (3.40)$$

Both Reese and API soil reaction element formulations are utilised for the LME model assembly definition. The API [6] based design approach is typical for the lateral pile-soil interaction study and Reese et al. [85] based approach allows the element formulation as a function

of the pile diameter. This feature enables to use the existing definition reported for small diameter pile to a large diameter pile case. Notably, the simple LME model is presented for the conceptual understanding only. The use of the API based p-y method and its comparison with the Reese p-y method for a large diameter pile, provides a qualitative comparison between two approaches, presented in the next section.

3.6.2 Drag element

The drag element defines an element complementary to the lateral soil reaction. It is defined to account for the side friction as a separate element specifically in cyclic loading conditions. Figure 3.5 presents a visual display of drag resistance concept. The drag element is a simple elastic-perfect plastic element. The formulation of the drag element is based on the hypothesis that, in the unloading load scenario, the soil reaction element will cease the contact with the soil; however, the side frictional interaction will persist. The drag element, therefore, characterise the unloading response.

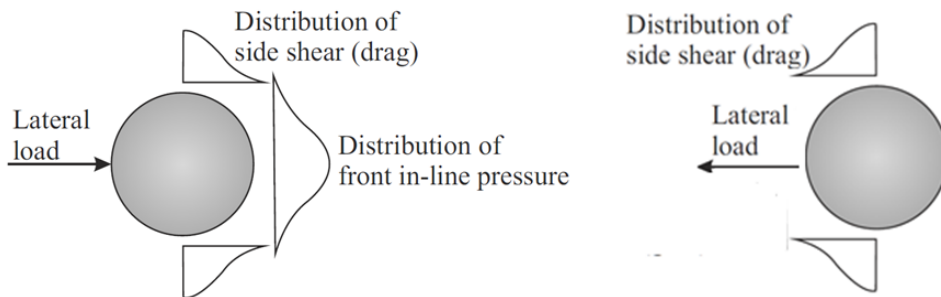


Figure 3.5: Visual representation of the drag element concept, soil response during loading (left) and unloading (right) scenarios, modified from Abadie et al. [3]

For modelling pile-soil interface friction, a similar drag element as assumed by Taciroglu et al. [98] is implemented. It comprises of a parameter, ' p_d ' called ultimate drag resistance and the elastic stiffness of the element ' K_d^e ' which represents the frictional stiffness determining shear displacements between the pile surface and surrounding soil under the action of lateral loading. For simplicity, the stiffness ' K_d^e ' is taken equal to that of a p-y element whereas the ultimate drag resistance is taken 20% of that of ultimate p-y capacity at each depth following the guidelines by Taciroglu et al. [98]. For local macro-element assembly, a linear elastic, perfect plastic drag element formulation is presented hereafter.

$$f_d = |p_d| - p_d^{ult} = 0 \quad (3.41)$$

$$\Delta\lambda = \frac{f_d}{K_d^e} \quad (3.42)$$

$$\begin{aligned} (p_d)_{n+1} &= (p_d)_n - \Delta\lambda \times K_d^e \times \text{sign}(p_d) \\ (y_d^p)_{n+1} &= (y_d^p)_n + \Delta\lambda \times \text{sign}(p_d) \end{aligned} \quad (3.43)$$

Therefore, the overall lateral soil reaction macro-element at each depth is a combination of 80% contribution from API or Reese p-y element and 20% from the drag element. The ratio is similar to the reported results by Taciroglu et al. [98]. The p-y element mentioned hereafter is considered including drag element contribution. The comparative single element evolution at 1.5m depth for both p-y elements is demonstrated in Figure 3.6. Notably, the initial subgrade reaction parameter is taken same (31.2 MN/m^3) for both Reese and API p-y curves development because the above-presented magnitudes are empirically formulated. Hence, a conservative magnitude is considered for element definition.

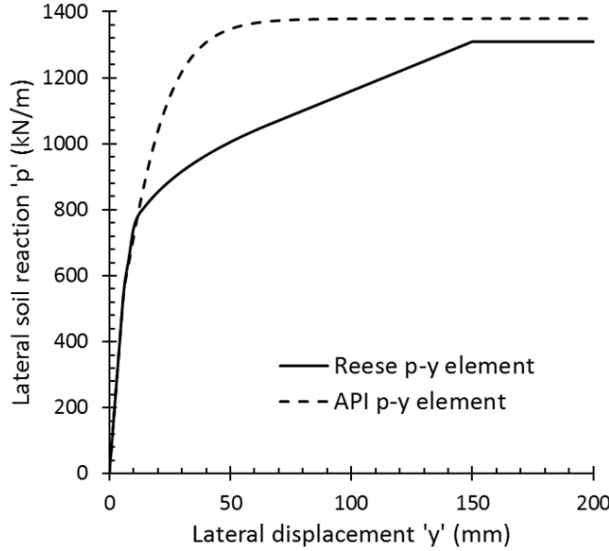


Figure 3.6: The lateral soil reaction (p-y) element evolution as per the definition from Reese et al. [85] and API [6] methods

The ultimate lateral soil resistance is slightly higher for the API p-y method. The Reese p-y curve roughly presents two different stiffness evolutions till ultimate capacity whereas, API p-y curve presents a single stiffness evolution.

3.6.3 Pile shaft resistance element

The pile shaft resistance element is formulated in the context of the T-Z element, presented in the section 2.2.1. For the simplified local macro-element model, the maximum shaft segment capacity is evaluated as follows.

$$t_z^{max} = K_o \times \tan(\delta') \times \pi D_p \frac{1}{2} \gamma' (z_b^2 - z_a^2) \quad (3.44)$$

Here, z_a and z_b are the depths 0.5 m above and below the present depth 'z'. Equation 3.44 is a representative of bored pile case. A similar definition for the pile segment capacity for a driven pile case shall be represented by using the ICP method on the CPT test outcomes. However, a bored pile case is assumed for the simple LME model definition.

The macro-element definition for the pile shaft resistance element is presented as fol-

loads. The load function is defined as per Equation 3.45.

$$f_{Q_s u_z} = f(Q_s, \alpha) = Q_s - (Q_s^e + f(\alpha)) = 0 \quad (3.45)$$

Here Q_s^e is the yield limit for the elastic vertical shear resistance. The elastic stiffness is defined as the slope of the first segment of the T-Z curve formulated as per API [6] definition (see Figure 2.12). The function $f(\alpha)$ in Equation 3.45 represents hardening during plastic displacement. The hardening function is defined in Equation 3.46.

$$f(\alpha) = K_{u_z}^p (u_z - u_z^e) \quad (3.46)$$

The return mapping algorithm for the pile shaft resistance element is presented as follows. The soil reaction at n^{th} step is written as $(Q_s)_n$. Regarding the procedure mentioned in the return mapping algorithm, the plastic multiplier ($\Delta\lambda$) is evaluated. Likewise, the drag element, the pile shaft resistance element follows the linear hardening; thereby, one iteration is sufficient at each step. The same procedure is defined for all segments of the T-Z element.

$$\Delta\lambda = \frac{f((Q_s)_n, \alpha_n)}{K_{u_z}^e \times \left(\frac{\partial f}{\partial Q_s}((Q_s)_n, \alpha_n) \right)^2 + \frac{\partial f}{\partial \alpha}((Q_s)_n, \alpha_n) \times \left| \frac{\partial f}{\partial Q_s}((Q_s)_n, \alpha_n) \right|} \quad (3.47)$$

$$f((Q_s)_n, \alpha_n) = -\text{sign}(Q_L) \times (Q_s)_n - (Q_s^e + f(\alpha_n)) \quad (3.48)$$

$$\frac{\partial f}{\partial Q_s}((Q_s)_n, \alpha_n) = -\text{sign}(Q_L) \quad (3.49)$$

$$\frac{\partial f}{\partial \alpha}((Q_s)_n, \alpha_n) = K_{u_z}^p \quad (3.50)$$

$$\begin{aligned} (Q_s)_{n+1} &= (Q_s)_n - \delta(\Delta\lambda) \times K_{u_z}^e \times \frac{\partial f}{\partial Q_s}((Q_s)_n, \alpha_n) \\ \alpha_{n+1} &= \alpha_n + \delta(\Delta\lambda) \left| \frac{\partial f}{\partial Q_s}((Q_s)_n, \alpha_n) \right| \\ (u_z^p)_{n+1} &= (u_z^p)_n + \delta(\Delta\lambda) \times \frac{\partial f}{\partial Q_s}((Q_s)_n, \alpha_n) \end{aligned} \quad (3.51)$$

3.6.4 Pile base resistance element

The pile base resistance element is formulated in the context of the Q-Z element, presented in the section 2.2.1. The ultimate resistance in the Q-Z curve is assumed to take into account of the plugging characteristics. Large diameter open-ended steel pile is assumed to be in fully plugged conditions [13]. However, in the present work, an incremental filling ratio (IFR) of 78% is assumed for conservative response estimate and to accommodate the uncertainty in the

magnitude of the bearing capacity parameter (N_q) while estimating the pile tip capacity using the following formulation.

$$Q_p = N_q \times \gamma' \times L_e \times \frac{\pi}{4} D_{eq}^2 \quad (3.52)$$

Here, N_q is the bearing capacity parameter estimated to be 43.3 as per Meyerhof, 1962 for an angle of internal friction equal to 37° . D_{eq} is the equivalent pile diameter considering plugging defined as per the following equation as per Paik and Salgado [79].

$$D_{eq} = D_o - (D_o - \sqrt{D_o^2 - D_i^2}) \times \text{IFR} \quad (3.53)$$

The macro-element definition for the pile shaft resistance element is presented as follows. The load function is defined as per Equation 3.54.

$$f_{Q_b u_z} = f(Q_b, \alpha) = Q_b - (Q_s^e + f(\alpha)) = 0 \quad (3.54)$$

Here Q_s^e is the yield limit for the elastic vertical shear resistance. The elastic stiffness is defined as the slope of the first segment of the T-Z curve. The function $f(\alpha)$ in Equation 3.54 represents hardening during plastic displacement. The hardening function is defined in Equation 3.55.

$$f(\alpha) = K_{u_z}^p (u_z - u_z^e) \quad (3.55)$$

The return mapping algorithm for the pile base resistance element is presented as follows. The soil reaction at n^{th} step is written as $(Q_b)_n$. Concerning the procedure mentioned in the return mapping algorithm, the plastic multiplier ($\Delta\lambda$) is evaluated. Likewise, drag and shaft resistance elements, the base resistance element follows the linear hardening; thereby, one iteration is sufficient at each step. The same procedure is defined for all segments of the Q-Z element.

$$\Delta\lambda = \frac{f((Q_b)_n, \alpha_n)}{K_{u_z}^e \times \left(\frac{\partial f}{\partial Q_b}((Q_b)_n, \alpha_n) \right)^2 + \frac{\partial f}{\partial \alpha}((Q_b)_n, \alpha_n) \times \left| \frac{\partial f}{\partial Q_b}((Q_b)_n, \alpha_n) \right|} \quad (3.56)$$

$$f((Q_b)_n, \alpha_n) = -\text{sign}(Q_L) \times (Q_b)_n - (Q_s^e + f(\alpha_n)) \quad (3.57)$$

$$\frac{\partial f}{\partial Q_b}((Q_b)_n, \alpha_n) = -\text{sign}(Q_L) \quad (3.58)$$

$$\frac{\partial f}{\partial \alpha}((Q_b)_n, \alpha_n) = K_{u_z}^p \quad (3.59)$$

$$\begin{aligned}
(Q_b)_{n+1} &= (Q_b)_n - \delta(\Delta\lambda) \times K_{u_z}^e \times \frac{\partial f}{\partial Q_b}((Q_b)_n, \alpha_n) \\
\alpha_{n+1} &= \alpha_n + \delta(\Delta\lambda) \left| \frac{\partial f}{\partial Q_b}((Q_b)_n, \alpha_n) \right| \\
(u_z^p)_{n+1} &= (u_z^p)_n + \delta(\Delta\lambda) \times \frac{\partial f}{\partial Q_b}((Q_b)_n, \alpha_n)
\end{aligned} \tag{3.60}$$

The components of the macro-element model are integrated using the presented return mapping algorithm in ATLAS, a Matlab toolbox for nonlinear soil-pile-structure interaction analysis, developed by Grange [40].

3.7 Loading

The model pile and LME assembly are studied under monotonic and cyclic loading conditions. The loading magnitudes are taken as that of a 2 MW wind turbine structure reported by Leblanc et al. [60]. The monotonic design loading defines the ultimate limit state (ULS) criteria. The vertical load ‘V’ (dead weight of the structure) of 5 MN is taken in the present work. The lateral loading ‘H’ has a complex nature, as described in section 2.1.1, and as an approximation, it is assumed to act as a point load at a height above the mudline level. Yang et al. [101] presented a finite element study with 6D lateral load eccentricity. Following the same recommendations, The lateral load eccentricity ‘e’ taken equal to 6.25D for model analysis in accordance with the constraints in the lab calibration chamber setup. The average value $H_{avg} = 3.4$ MN is considered for monotonic loading representing ULS/1.35 as per Leblanc et al. [60]. The lateral point load applied with eccentricity inputs a bending moment ($M = H \times e$) at the mudline level.

The authors estimate the design loads with respect to the ULS criteria defined in terms of the static moment capacity (M_R) of the laboratory pile. It indirectly infers that a constant lateral load eccentricity (e) is sufficient for all the model definitions. Bhattacharya and Adhikari [16] have reported that the monopile foundation design is aimed to keep the pile material stresses and strains within its elastic limit, so the plastic hinge or bucking of the pile foundation are never expected. Thus, in the OWT foundation design with a lateral (H) and moment (M) load input, the subsequent pile-soil interaction mechanism investigation is of the sole interest.

Subsequently, in the present work, all the model cases presented hereafter consider a constant eccentricity to quantify the additional moment load at mudline due to the lateral load application. The lateral load magnitude is varied so as to reach the requisite moment load level. A simplified sinusoidal loading profile is considered for the cyclic loading case. In the present work, the pile-soil interaction is examined in the cyclic loading scenarios only. Therefore, the frequency of the cyclic loading does not influence the model outcomes, as the inertia effects are not involved in the model element definition. Subsequently, for simplicity, a unique frequency of 0.1Hz from power spectral density diagram corresponding to typical wave loading frequency is considered concerning the work presented by Nikitas et al. [73].

The cyclic loading response defines the serviceability limit state (SLS) criteria. The lateral loading magnitude is usually lower while defining the SLS criteria. Leblanc et al. [60] recommends 100 cycles of pile loading to meet SLS conditions. This is because the pile-soil

interaction in the cyclic load case results into ratcheting [15] phenomenon, which is defined as the irreversible strain accumulation in stress-controlled load cycles (see section 2.4 for more details). Ratcheting occurs due to the degradation in the stiffness of the interaction elements. However, stiffness degradation is not considered for the simple LME model definition. Therefore, the cyclic loading response after two cycles of loading has been assumed as representative of the SLS loading scenario.

3.8 Results

The model is tested for monotonic and one way loading scenarios discussed as follows. Figure 3.7 presents the final deflection profile for loading under combined action of V-H-M components in ULS loading ($V = 5$ MN, $H = 3.4$ MN, $M = 3.4 \times 25$ MNm) condition.

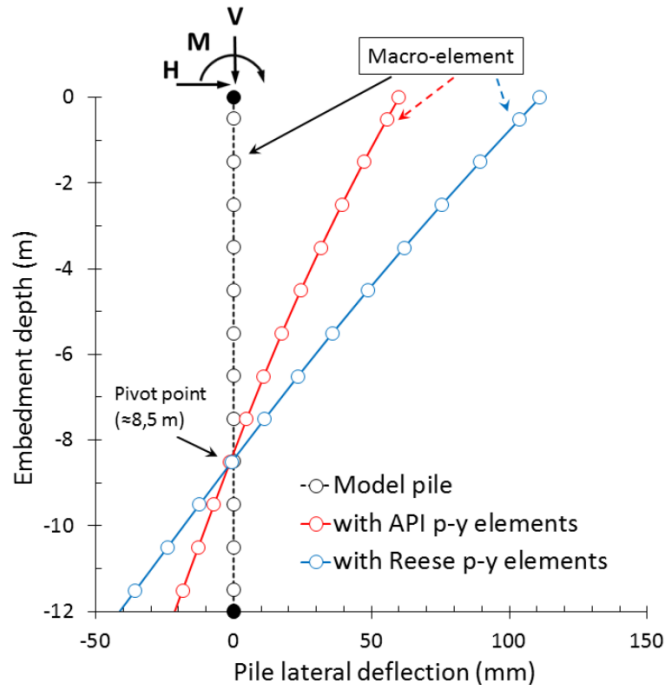


Figure 3.7: Final deflection profile of model pile after the ULS design loading

The pile rotation for monotonic ULS loading is calculated as 0.4 and 0.75 degrees with API and Reese p-y element definition, respectively. The work reported by Cui and Bhattacharya [31] and Puech and Garnier [83] states that one-way cyclic loading is practical for an offshore wind turbine foundation applications. The wind force in the fore-aft direction is resisted by the turbine blades, which is subsequently transferred to the foundation. However, on the opposite face, the wind is free to pass without posing any resistance. Therefore, the prominence of one-way loading over two-ways is due to the sizeable aerodynamic damping. Moreover, some previous studies [103], [11] have reported non-symmetric two-way loading as a representative of the severe loading case scenario. However, in the presented results, the model response is presented for one-way loading condition only.

$$\frac{1}{2}\gamma'd_r^2DK_p = \gamma'L_eDK_p(L_e - d_r) - \frac{1}{2}\gamma'(L_e - d_r)^2DK_p \quad (3.61)$$

The quality of model test results is also verified through the test of horizontal equilibrium. The distribution of lateral earth pressure is assumed linear as per the definition given by Petrasovits and Award [80] (see Figure 2.18b). The analytical equilibrium (see Equation 3.61) gives 8.48 m below mudline as a point of rotation (d_r , also called pivot point) for ULS loading conditions. The model result presents the point of rotation at 8.50 m as can be seen in Figure 3.7. This close agreement supports the quality of the presented macro-element model.

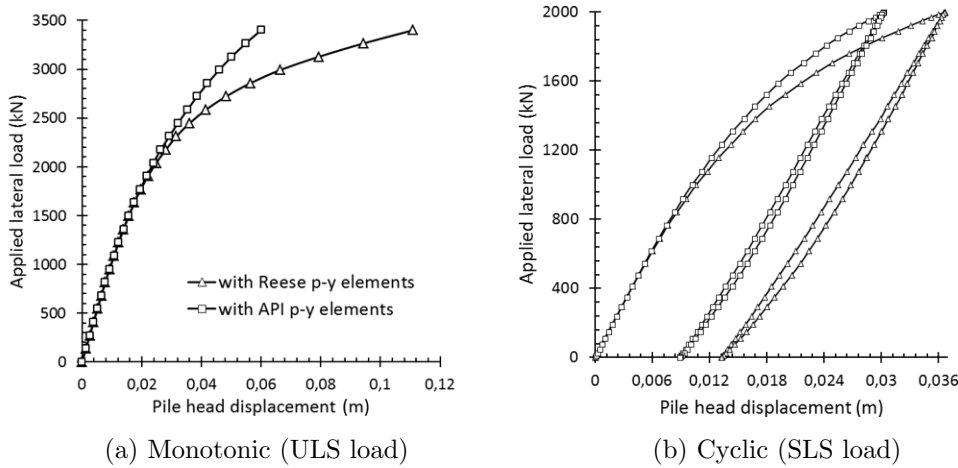


Figure 3.8: Pile head displacement evolution for monotonic (ULS) and cyclic (SLS) loading cases

Figure 3.8 presents the pile head displacement evolution for monotonic (ULS) and cyclic (SLS) loading conditions. The difference in the element behaviour affects the overall pile response. The pile head displacement is higher, with Reese lateral soil reaction elements in comparison to the API method. The initial stiffness for both types of elements is the same. Thus, the pile head displacement at the beginning of the applied load follows the same path. The elastic element stiffness characterises unloading behaviour. Hence, the pile head displacement for the cyclic loading case presents similar slopes for both API and Reese methods.

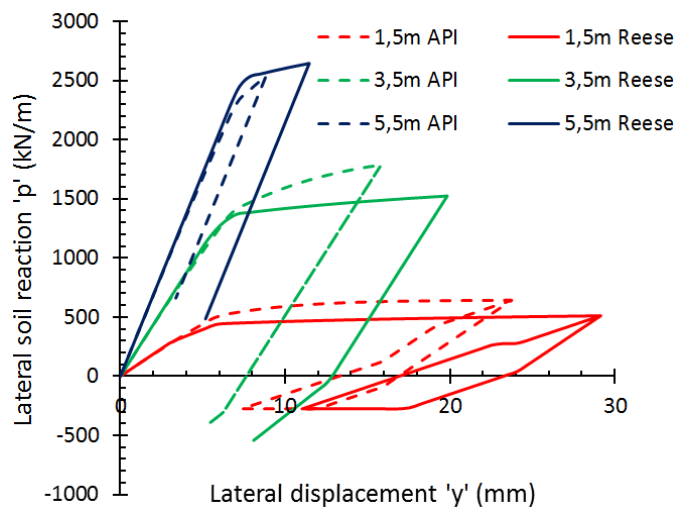


Figure 3.9: Comparative evolution of the lateral soil reaction at depths 1.5, 3.5 and 5.5m depths

Figure 3.9 presents the local level element evolution under cyclic loading condition at some selected depths only for better readability. The lateral displacement reduces with depth

until the point of rotation. The p-y curves from API and Reese methods present the same qualitative evolution. The area of the unloading/reloading loop decreases with increasing depth inferring the drag element reaches the plastic state in the shallow depths and resides within the elastic limit for the deeper depths. The hysteresis characteristics of cyclic response can be seen clearly. The model does not account for stiffness degradation in a subsequent number of cycles, and therefore, the position of a particular unloading/reloading loop does not change under the action of constant amplitude cyclic loading.

3.8.1 Flexible check

In order to reflect the quality of the present macro-element model, a comparison of the rigid model pile is made with that of the corresponding flexible model pile. For this, the diameter of the original model pile is reduced to 0.9m (outer) with 0.02m thickness. All other geometrical and soil parameters were kept unchanged. Figure 3.10 below presents the final deflection profile of the flexible model pile at the end of the monotonic loading of 1/10 reduced horizontal and vertical loading of what were considered for ULS condition previously. The moment load is reduced too based on the load eccentricity ($e = 6.25D$) formulation.

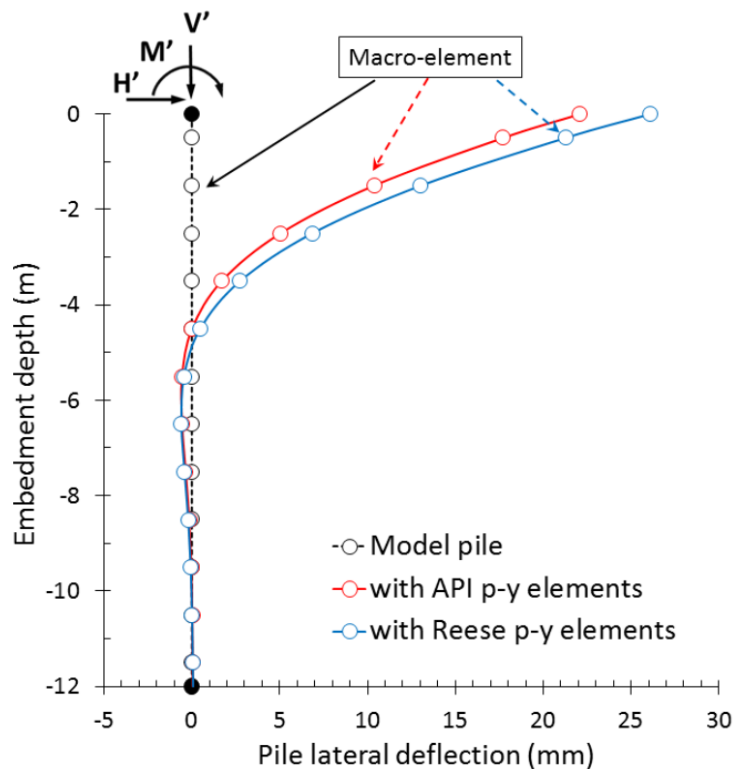


Figure 3.10: Deflection profile for equivalently reduced diameter pile representing flexible pile behavior

Figure 3.10 presents the deflection profile under monotonic loading conditions. The observed deflection profile represents a typical response of a flexible pile foundation. Thereby, the rigid vs flexible comparison ensures the quality of the presented model for monotonic loading and by extension for cyclic loading conditions. The empirical critical length (L_c definition as per the formulation presented in Poulos and Hull [81] for uniform soils, estimates the $L_c = 9.6$

m for the present model pile of diameter 0.9 with same soil properties presented in Table 3.1. The critical length is defined as the pile length beyond which the further increase in length does not alter the pile head response. From the LME flexibility check, the significant deflection ceases at around 4.5 m of embedment depth. In contrast, the model pile is observed to cease the lateral deflection completely beyond 9.0 m depth (see Figure 3.10). The close agreement between empirical and the LME model L_c estimations support the accuracy of the simple LME model.

3.9 Conclusions

The simple local macro-element model is uncoupled as the axial response is independent to the lateral response and vice-versa. The local macro-element model is presented with simplified geometry and typically used soil-structure interaction methods. The LME model incorporated the traditional nonlinear elastoplastic elements equivalent to Winkler's spring model for lateral loading response investigation in combination with the transfer-curve for axial loading. The quality of the macro-element model is well presented by the linear deflection profile of the model pile justifying the assumed rigid pile response. Moreover, the point of rotation is governed by the equilibrium of the overall system. A comparison with theoretical developments provides another positive assessment for the quality of the presented local macro-element model. A comparison with the corresponding flexible pile having reduced diameter and higher L/D ratio also present the qualitative features of the presented macro-element model. Notably, with the simple LME model, the removal of vertical load application while keeping the lateral load, does not influence the magnitude of the lateral deflection. This signifies that simple LME presents the axial and lateral interaction responses independently. Subsequently, the simple LME model presents a basis for the definition of the comprehensive lab-scale model with an emphasis on coupled interaction representation, presented in the next chapter.

Chapter 4

Lab scale models

4.1 Objective

This chapter presents the lab scale models of the pile-soil system aimed to address the coupled lateral and axial soil-structure interaction under combined loading application. The prototype model presented in the previous chapter is scaled down to the lab-scale model using similitude analysis. The lab-scale model assuming a calibration chamber configuration is numerically investigated as a 3D finite element (FE) model for coupled interaction. A hypothesis with the guidelines for the equivalent experimental campaign planning, data extraction and analysis is presented. A mathematical formulation is deduced from the 3D FE model results to quantify coupled interaction. These results are further extended to define a nonlinear elastoplastic mathematical model, called a lab-scale local macro element model, with an inherently defined coupled lateral and axial pile-soil interaction at different depths along pile embedment.

4.2 General description

The finite element (FE) modelling allows for accurate modelling of boundary conditions in the calibration chamber, pile-soil interaction and the constitutive behaviour of the sand. The numerical analysis provides the soil response to axial, rotational and lateral pile loading. An FE analysis is carried out as a supplement to a planned experimental campaign of a lab-scale pile loading test in a calibration chamber. The 3D FE analysis provides support for the prediction of the loading and geometrical parameters as well as selecting the best positions for soil-stress transducers in the soil mass for the experimental campaign.

The numerical modelling is carried out assuming three different vertical overburden pressures (50, 75 and 100 kPa) cases, studying the coupled lateral and vertical soil interaction with possible stress level dependency. The corresponding lateral stresses were chosen to get $K_0 = 0.5$, as the initial state of stress, replicating the boundary condition ‘BC 1’ [52] in the calibration chamber (CC), where constant pressures are applied both at vertical and horizontal boundaries. A mass is placed at the model pile head to represent the vertical load (V) of the wind turbine superstructure. A horizontal point load applies a lateral loading (H) in the model pile at a distance above the mudline (chamber top). This eccentricity introduces a moment load

(M) on the pile head at the mudline level. Hence, the behaviour of a relatively rigid monopile foundation model in V-H-M combined loading condition is presented.

4.3 Similitude analysis

A similitude analysis provides a basis for the evaluation of the model geometry and load parameters such that the model behaviour can be related to the corresponding prototype respecting the desired aspect of system behaviour. The simple local macro-element model of a full scale embedded monopile represents ‘prototype’. The 3D FE model pile represents the ‘model’ for similitude analysis. The non-dimensional group (NDG) framework as per Buckingham π -theorem [21] is used to establish the similitude relations between prototype and model pile cases.

Many researchers have established such a framework for monopile lab-scale experiments. Extending the available results, the similitude relations reported by Leblanc et al. [60] (see Equation 4.1) and Klinkvort and Hededal [57] (see Equation 4.2) are used in a modified^a form, taking into account the characteristics of the calibration chamber. The similitude relations presented in Equation 4.1 provides the non-dimensional parameters for load magnitudes (H , V , M), normalized for full pile embedment length (L_e), whereas, Equation 4.2 provides similar parameters for the lateral load magnitude (H) and soil-resistance (p), normalized at a particular depth (z) along pile embedment length taking into account the coefficient of passive earth pressure (K_p) and the diameter of the embedded pile.

$$\tilde{H} = \frac{H}{L_e D \sigma'_{v,L_e}}, \quad \tilde{V} = \frac{V}{L_e D \sigma'_{v,L_e}}, \quad \tilde{M} = \frac{M}{L_e^2 D \sigma'_{v,L_e}} \quad (4.1)$$

$$\tilde{H}^* = \frac{H}{K_p \sigma'_{v,z} D^2}, \quad \tilde{p} = \frac{p_z}{K_p \sigma'_{v,z} D} \quad (4.2)$$

The outcomes from Equation 4.1 provide the input loading parameters for the model pile, whereas Equation 4.2 is used for a qualitative comparison between model outcomes and the prototype at a particular depth. The geometrical dimensions of the pile and Fontainebleau NE34 sand properties are presented in Tab. 4.1 for both prototype and model. The loading magnitudes applicable for the ultimate limit state (ULS) in the prototype pile are used in this study, presented in Table 4.2. The non-dimensional groups (NDG) for the prototype pile are evaluated (see Table 4.3) using the geometrical and loading data. Subsequently, the model pile parameters are chosen to achieve the same values for the NDG (from Leblanc et al. [60]) as the prototype pile. The model case is simulated under the estimated load levels, and the NDGs reported by Klinkvort and Hededal [57] are estimated at the representative depth. Tables 4.1 and 4.2 present the resulting parameters for the model pile and corresponding non-dimensional groups are presented in Table 4.3.

Notably, the soil parameters for the model pile presented in Table 4.1 are an outcome of the calibration chamber filling process with air pluviation process, resulting in the different soil

^aThe σ'_v in Eqns.4.1 and 4.2 are equal to $(q + \gamma' L_e)$ (at the pile tip) and $(q + \gamma' z)$ (at a depth ‘z’) respectively, including the the contribution to the vertical stress from the applied vertical membrane stress in the calibration chamber.

Table 4.1: Prototype and model geometrical features and soil properties

Parameter	Prototype	Models
Outer diameter of pile, D_o (m)	4.00	0.08
Embedment length of pile, L_e (m)	12.00	0.80
Representative depth, z^b (m)	3.00	0.25
Lateral load eccentricity, e (m)	25.00	0.50
Unit weight of the soil, γ (kN/m^3)	16.53	15.83
Relative density, I_D (%)	84	66
Angle of internal friction, ϕ' (degree)	37	33
Coefficient of the passive earth pressure, K_p	4.02	3.39

properties for prototype and model piles. The three cases are simulated with loading magnitudes equivalent to the prototype pile as an outcome of the similitude work. By extension, the three cases are correlated amongst themselves.

Table 4.2: Load magnitudes and deformation modulus for prototype and model pile cases

Parameter	Prototype	Model cases		
Vertical surcharge pressure, q (kPa)	0	100	75	50
Lateral load, H (kN)	3400	2.55	2.00	1.43
Vertical load, V(kN)	5000	3.80	2.95	2.10
Moment load, M (kNm)	85000	1.275	1.000	0.715
Lateral soil reaction at z, p_z (kN/m)	2368.55	13.79	10.92	7.84
Young's modulus of pile, E_{pile} (GPa)	210	115	115	115
Deformation modulus of soil, E_{soil} (MPa)	40.0	13.6	12.0	10.2
Shear modulus of soil, G_{soil} (MPa)	8.18	5.23	4.63	3.94

The accuracy of the established similitude relations and evaluated model parameters are checked for the expected stress levels in the soil (σ_{soil}) and pile volumes (σ_{pile}) and their interface ($\sigma_{pile-soil}$). The NDG proposed by Kerner et al. [56] stated in Equation 4.3 are evaluated for both prototype and model piles and presented in Table 4.3.

$$\tilde{\sigma}_{soil} = \frac{H}{G_{soil}D^2}, \quad \tilde{\sigma}_{soil-pile} = \frac{e}{D}, \quad \tilde{\sigma}_{pile} = \frac{H}{E_{pile}D^2} \quad (4.3)$$

The soil stress $\tilde{\sigma}_{soil}$ magnitude is in good agreement for the three model cases and are more than twice of that for the prototype soil stress. It can be attributed to the uncertainty in the prediction of a unique deformation modulus value for the prototype soil along pile embedment. Also, the outcomes for $\tilde{\sigma}_{pile}$ are in decreasing trend for the three model cases because the denominator of the mathematical expression is constant for all three cases. Also, the $\tilde{\sigma}_{pile}$

^bThe depth 'z' for prototype pile (3.00m) is an outcome of the correlation of prototype and model NDGs, \tilde{H} and \tilde{p} (as per Equation 4.2) from model pile outputs at 0.25m depth, named as the 'representative depth'.

for the prototype is 2-3 times less from the model because of the different elastic modulus of prototype and model piles. In particular, the strains in the model pile are one order of magnitude less than the prototype. In practice, monopiles are rigid and are designed to remain elastic in design life [16]. Therefore this low strain in the model piles would not affect the test results in the present work.

Table 4.3: Similitude parameters for load and geometry

NDG	Prototype	Model cases		
Modified after Leblanc et al. [60]				
\tilde{H}	0.357	0.354	0.356	0.357
\tilde{V}	0.525	0.527	0.526	0.524
\tilde{M}	2.232	2.210	2.228	2.229
Modified after Klinkvort and Hededal [57]				
\tilde{H}^*	1.065	1.130	1.167	1.221
\tilde{p}	2.968	0.489	0.510	0.535
As per Kerner et al. [56]				
$\tilde{\sigma}_{soil}$	0.014	0.076	0.068	0.057
$\tilde{\sigma}_{soil-pile}$	6.250	6.250	6.250	6.250
$\tilde{\sigma}_{pile} (\times 10^6)$	1.012	3.463	2.716	1.942

Lastly, it is essential to note that \tilde{p} in Table 4.3 is an outcome from the finite element analysis of soil-resistance (p) under combined loading application on the three model cases whose loading magnitudes (see Table 4.2) are a consequence of non-dimensional group framework. An agreement between all three model cases for the NDG ' \tilde{p} ' presents the accuracy of the similitude analysis.

4.4 Model definition

The finite element model implemented in PLAXIS 3D is a replication of the experimental setup of the lab-scale model pile in a calibration chamber. Figure 4.1 presents the general layout of the calibration chamber in the 3SR laboratory. The calibration chamber is cylindrical with a 1.2m diameter and 1.5m height. Three lateral water-filled membranes in the cylinder periphery, each 0.5m in height, and one membrane in the chamber top surface apply the initial state of stress in the chamber filled with soil. A circular opening of 0.2m diameter is present in the top cap for pile installation and testing.

Figure 4.2 presents the mesh of the model pile-soil system. It comprises the embedded model pile in the Fontainebleau NE34 sand volume inside the chamber. A linear elastic material with a unit weight of water, high volume stiffness and low shear stiffness surrounding the soil volume replicates the lateral membrane water pressure of the calibration chamber. The top plate (with properties of PVC material) covers the top surface of the soil volume. A surface load over the top plate replicates the vertical overburden stress (q) application through the top membrane in the calibration chamber.

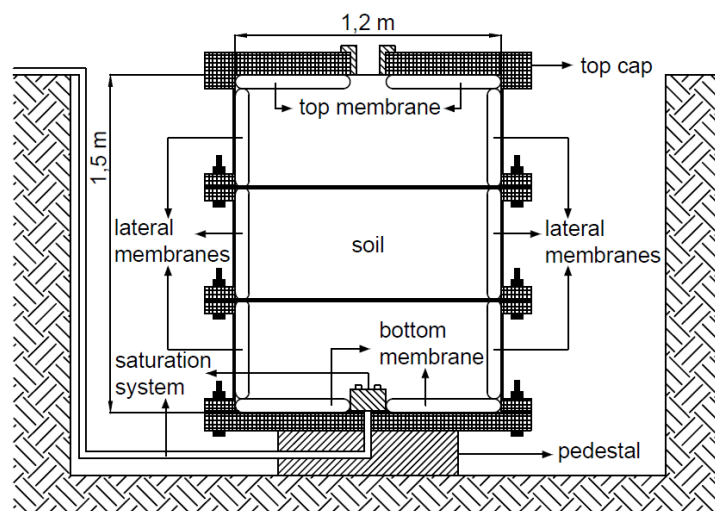


Figure 4.1: General layout of the calibration chamber setup in 3SR laboratory, from Celeste [26]

The stiffness ratio ($K_R = 0.041$), calculated as per the Poulos and Hull [81] formulations, categorises the pile-soil interaction as semi-rigid ($K_R > 0.208$, < 0.0025 for rigid and flexible interaction respectively). Moreover, the combination of this stiffness ratio and aspect ratio (L_e/D) falls in the category of some existing UK wind farms in sandy soils, reported in Abadie et al. [3]. Thus, the extrapolation of the model results to the field scale database is practical for the qualitative comparison.

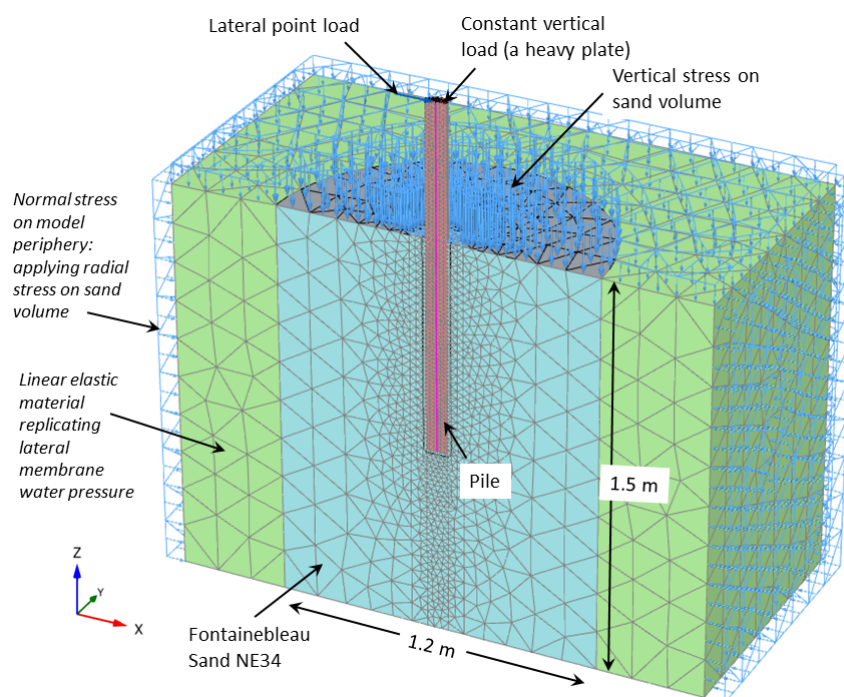


Figure 4.2: PLAXIS 3D model of monopile in calibration chamber

The half geometry modelling along the plane of symmetry (see Figure 4.2) provides the computational advantage of simulation time optimisation. A heavy plate placed on the top surface of the model pile represents the vertical load application. A point load oriented in a direction along the plane of model symmetry applies lateral loading at the pile top, additionally

introducing a moment load in the mudline level (chamber top).

Table 4.4: 3D FE model parameters for pile, soil and calibration chamber representative confinements

Sand: Hardening soil material	Value
Tangent oedometric stiffness, E_{oed}^{ref} (MPa)	18
Secant stiffness in drained triaxial test, E_{50}^{ref} (MPa)	18
Unloading/reloading stiffness, E_{ur}^{ref} (MPa)	45
Reference pressure for stiffness, p_{ref} (kPa)	100
Power for stress-level dependency of stiffness, m	0.5
Interface strength reduction factor, R	0.9
Pile: Linear elastic material	Value
Young's modulus, E_{pile} (GPa)	210
Unit weight of steel, γ_{pile} (kN/m ³)	78.5
Poisson's ratio, ν_{pile}	0.3
Lateral confinement: Linear elastic material	Value
Stiffness modulus, E_{LC} (kPa)	100
Unit weight, γ_{LC} (kN/m ³)	10
Poisson's ratio, ν_{LC}	0.495

PLAXIS 3D program models the volume elements through 10-node tetrahedral elements. The pile is modelled using volume elements with linear elastic constitutive law (see Table 4.4). Bhattacharya and Adhikari [16] have reported that the monopiles are designed to reside within the elastic range for the entire design life. The pile stiffness (EI) remains in the elastic range until yielding occurs, usually at a fairly high moment value. Many previous studies (e.g. [25], [55], [53]) have used a linear elastic material law to model the monopile foundation.

The pile and the soil just below the pile tip are fine-meshed, producing around 15 volume elements around the model pile. Furthermore, the soil volume near the model pile is medium size meshed, and the remaining soil volume is coarse meshed. The pile-soil interface along the shaft and the tip include interface elements with an interface strength reduction factor of 0.9 to take into account a reduction in soil strength arising from installation as it will disturb the soil volume. The interface friction angle (δ') is therefore evaluated from the internal friction angle (ϕ') as per Equation 4.4 [93]. The interface element follows Mohr-Coulomb's behaviour characterised by the internal frictional angle (ϕ').

$$\tan \delta' = R \tan \phi' \quad (4.4)$$

The hardening soil model [89] is used to model sand behaviour with stiffness parameters reported by Sheil and McCabe [93] for Fontainebleau sand (see Table 4.4). The following two reasons explain the choice of the hardening soil model. Firstly, the model has stress-dependent stiffness and hence is suitable for the three cases (100, 75 and 50 kPa). Secondly, the model is a strain hardening elastoplastic model along with a nonlinear elastic region, making a realistic prediction of soil behaviour. Moreover, the $E_{50}^{ref} = 18\text{MPa}$ results in secant modulus, $E_{sec} =$

13.59 MPa for 100 kPa surcharge case. The E_{sec} is estimated using the stiffness modulus relation reported by Schanz et al. [89] for Hardening soil model (see Equation 4.5).

$$E_{sec} = E_{50} = E_{50}^{ref} \left(\frac{\sigma_3}{p_{atm}} \right)^m \quad (4.5)$$

The estimated E_{sec} is in the range of 5-20 MPa reported for dense sand by Heib et al. [43], thus supporting the model parameters selection. Also, the hardening soil model definition presented by Schanz et al. [89] has been validated by pressuremeter tests in calibration chamber, thus additionally supporting the model selection.

An equivalent solid circular section (instead of a tube) represents the pile for modelling simplicity, respecting the equivalent flexural rigidity (E^*I^*) and weight of the model pile. The equivalent Young's modulus formulation for the model pile is presented in Equation 4.6. The equivalent unit weight of the model pile, γ_{pile}^* , gives the same pile weight as a tubular steel pile following the same formulation presented in equation 4.6.

$$E^* = E \left\{ 1 - \left(\frac{D_o - 2t}{D_o} \right)^4 \right\} \quad (4.6)$$

The model cases are simulated in phases replicating the steps to be followed in the planned experiments in the calibration chamber. Note that the compressive stresses follow 'negative' and tensile stresses follow 'positive' sign convention. The initial phase represents the chamber filled with sand at the end of air-pluviation. The peripheral and top membranes are then pressurised to apply the confining stress representing the initial state of stress. Figures 4.3a and 4.3b present the lateral and vertical stress profiles respectively after the confinements application, for the 100 kPa vertical surcharge case.

The PVC plate and membrane do not cover the central region in the top surface (see Figure 4.1) in the actual calibration chamber setup. Therefore, the applied vertical stress in the soil through the top membrane does not evenly distribute in this region. Further, the presence of this opening continues to influence the vertical stress distribution until a certain depth in the soil beyond which the applied vertical stresses are less disturbed in the soil volume. The vertical stress contour plot (Figure 4.3b) points out the influence of this opening where a relatively minimal vertical stress in the central top region of the model soil (≈ 5 kPa) in comparison to the applied 100 kPa vertical stress is visible.

The second phase (not shown in Figure 4.3) represents the pile installation in the soil volume only by replacing the material of the volume elements from sand to pile at the pile position. This way, the physical phenomenon of a bored pile is represented. The next phase applies the vertical load at the pile head followed by the lateral load (as point load) with an eccentricity producing moment, in the last phase. Figures 4.3c and 4.3d display the vertical and lateral stress contour plots in the soil volume only for vertical and lateral loading phases, respectively.

Notably, the lateral load is applied in the model pile at an eccentricity ($e = 0.5$ m) from the top sand surface, respecting the actual experimental setup limits available in the calibration chamber. The particular eccentricity ($e = 6.25D$) is chosen based on the 3D FE study reported by Yang et al. [101] with $6D$ lateral load eccentricity. Moreover, Klinkvort and Hededal [57]

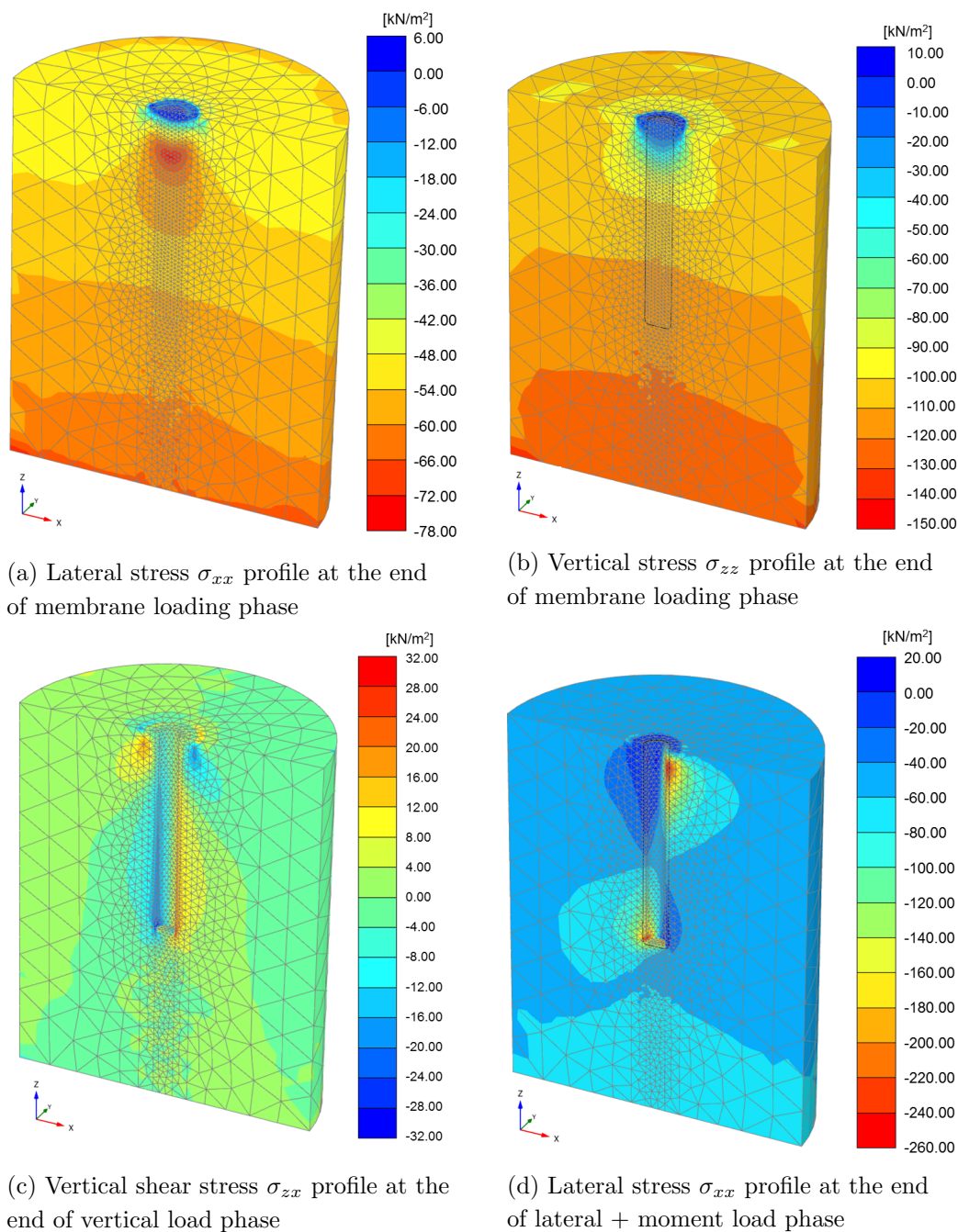


Figure 4.3: Contour plots of PLAXIS 3D model phases of calibration chamber setup

reported that the different load eccentricities only provides a moderate influence on the overall failure mechanism. Hence, a fixed load eccentricity of 0.5m is therefore selected. The calibration chamber also restricts the eccentricity in the selected range. Thus, the 3D FM model analysis is performed, keeping in mind the equivalence with the lab experimentation.

4.5 Model analysis

A vertical dead load of 3.80 kN followed by a lateral point load of 2.55 kN on the pile top (at a height 0.5m above mudline level) represent a combined V-H-M static loading at mudline level.

Figure 4.3d presents the contour plot of lateral stress in the soil volume (for the 100 kPa vertical surcharge case) under combined monotonic loading. The soil stress contour plot infers that the depth where the lateral stress is equal on both (front and rear) sides of the pile is the position of the zero resulting soil reaction in the x-direction. This depth seems to be present close to the middle of the embedded pile length.

Further, the model output analysis is carried out along a radial line at a particular depth to understand the stress evolution at some specific locations called ‘stress points’. The idea behind exploring the outcomes from these stress points is to mimic a similar response from the soil-stress transducers placed in the corresponding locations in the planned experimental campaign.

It is possible to extract all stress components from the stress point in the model. However, the soil stress transducer in actual lab experiments is only capable of measuring stress in one direction only corresponding to its orientation in the soil volume. The analysis of stress points in the model soil volume aids in the decision making for optimised soil-stress-transducers layout and orientation in the calibration chamber.

Three stress points are analysed for stress evolution located at a depth of 0.25m and placed radially outwards at distance 1R, 3R, and 5R from pile axis where ‘R’ is the radius of the model pile. These three stress points are named SP1, SP2 and SP3, respectively (see Figure 4.4). The choice of this particular depth is arguable, and some other depth along the embedded model pile might be a better representative of the model pile. Nevertheless, the 0.25 m depth is below the zone significantly influenced by the free surface close to the pile. It is also above the pile rotation point where the change in lateral soil is expected to be small. This depth is therefore selected to study the changes in lateral soil stresses due to combined pile loading.

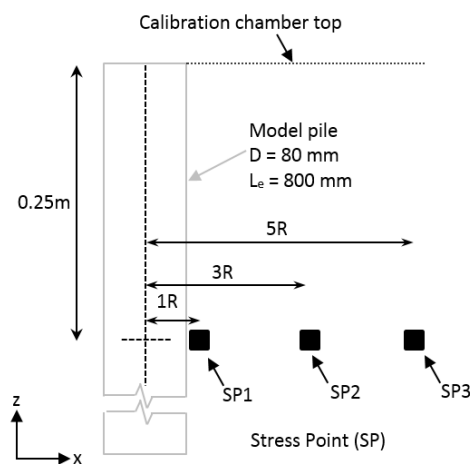


Figure 4.4: Stress points layout

The rigid pile rotation point is expected somewhere around $2/3$ rd of the embedment length (L_e) from the mudline level, assuming an ultimate lateral soil reaction proportional to the outcome from lateral earth pressure equilibrium theory. Therefore, the expected rotation point in the present study is at around 0.53 m from mudline. It supports the choice of a 0.25 m depth as approximately half-way from surface (mudline) and point of zero soil reaction.

Figure 4.5 presents the lateral stress evolution with the lateral displacement of the

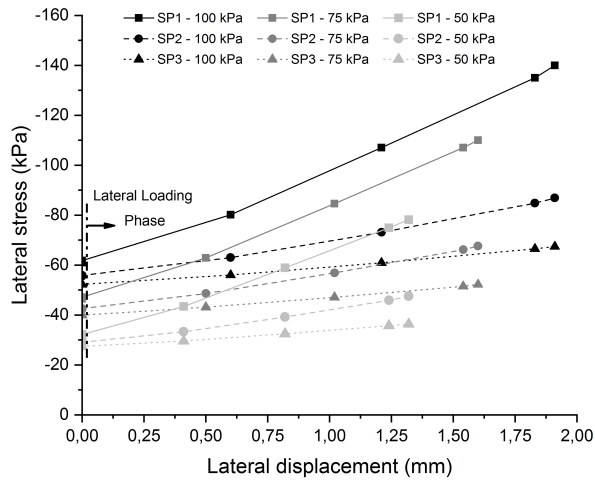


Figure 4.5: Lateral total stress variation at different stress points

pile-soil interface at $z = 0.25\text{m}$ in the x -direction for all three model cases under the action of the combined monotonic loading. The vertical dashed line represents the transition from the vertical loading phase to the lateral loading phase. There is no significant lateral displacement in the soil for the vertical loading phase. Thus only the ‘lateral loading phase’ pointing towards the right direction of the transition line is presented in Figure 4.5.

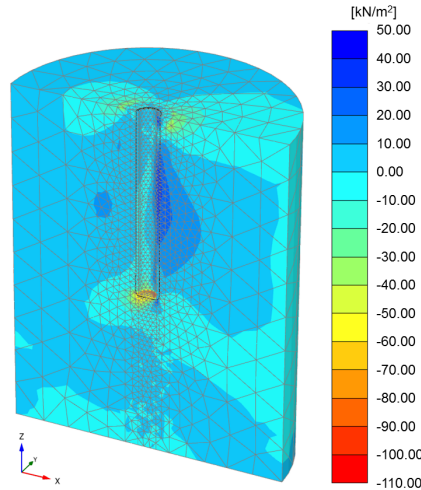


Figure 4.6: Contour plot of shear stress in model soil under combined loading

Notably, the lateral stress at zero lateral displacements is slightly larger than the corresponding lateral membrane stress indicating the influence of vertical load addition on lateral stress distribution, especially close to the pile-soil interface. Before the application of horizontal load, the lateral stress around the model pile is 60 kPa (see Figure 4.5). Notably, the lateral stress at 0.25m depth shall be $\sigma_{xx} + K_o \times \gamma_{soil} \times z \approx 52\text{ kPa}$. The extra 8 kPa appears from the vertical loading phase, where the Poisson’s ratio effect induces lateral stress increase. This is vis-

ible in Figure 4.5 at zero lateral displacements. The ICP method [51] also provides an estimate of the increase in soil radial stress ($\Delta\sigma'_{rd} = 9.1$ kPa) due to vertical load application in the model pile (see Equation 2.9). All three vertical surcharge cases show similar qualitative behaviour. The following analysis, therefore, presents the 100 kPa surcharge case only. Figures 4.7, 4.8 and 4.9, however, also include the different confining stresses.

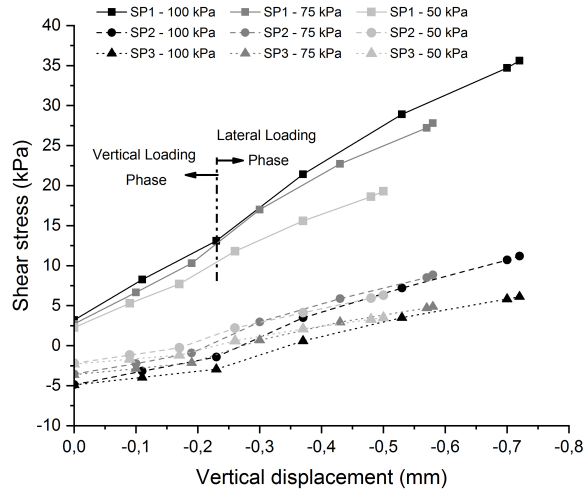


Figure 4.7: Shear stress variation at different stress points

Similarly, Figure 4.6 presents a contour plot of the vertical shear stress for the 100 kPa vertical surcharge case. Figure 4.7 presents the shear stress (σ_{zx}) evolution for the stress points in all three confining stress cases. The shear stress evolution is almost the same for a particular stress point irrespective of the applied vertical surcharge. The shear stress increase for the stress point ‘SP1’ is more significant than the shear stress change in SP2 and SP3.

One objective with the present work is to explore the lateral soil reaction evolution locally at a certain depth to understand the differences from the profiles or equations typically used for the flexible pile cases. Two different approaches are used to obtain the lateral soil reaction profile of the model pile presented hereafter.

4.5.1 Dummy beam approach

The lateral pile-soil interaction is typically defined by soil reaction (p) and lateral displacement (y) curves. In experimental work, the lateral soil reaction profile is estimated from the pile bending moment profile. The Euler-Bernoulli beam theory (see Equation 4.7) is used to evaluate the lateral soil reaction (p) using pile bending moment (M_{pile}) profile. Strain gauges placed along the pile surface at different depths as used to obtain the pile bending moments, for example, as reported by Klinkvort and Hededal [57].

The pile bending moment profile is obtained using a beam element embedded in the axis of the model pile volume. The beam element, named as dummy beam (DB), is assigned a very low flexural rigidity $E_{DB}I_{DB} = 1$ kNm². The low magnitude negligibly affects the overall flexural rigidity of the model pile ($E_p I_p = 115.66$ kNm²).

Figure 4.8a presents the pile bending moment profile and a five-degree polynomial curve fit for all three vertical overburden stress cases. The boundary condition for the bending moment at mudline ($z = 0$) level is also included. The high degree polynomial fit provides a reliable soil reaction profile (Figure 4.8b) as the second derivative of the bending moment profile.

$$M_{pile} = E_p I_p \frac{d^2 y}{dz^2}, \quad (M_{pile})_{z=0} = H \times e \quad (4.7)$$

$$\frac{d^2 M_{pile}}{dz^2} = p, \quad z \in [0, L_e]$$

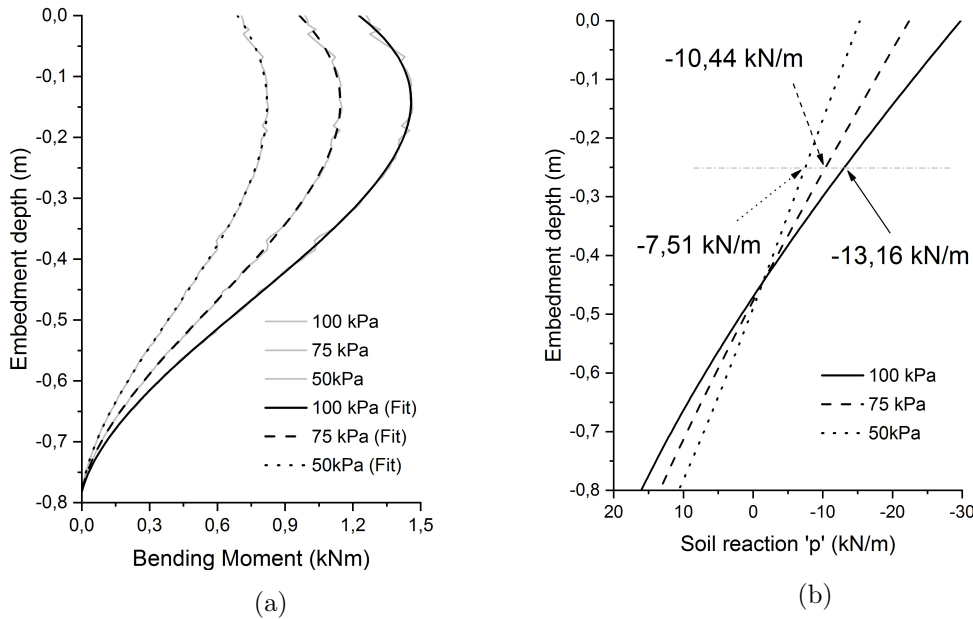


Figure 4.8: Bending moment and lateral soil resistance profiles from dummy beam approach

The soil reaction profile (p), proportional to the pile displacement infers that the different layers of soil have frictionless interaction. The soil layers can be seen as multiple smooth surface plates placed over each other. Upon application of a lateral load, each disk slides freely to a lateral distance inversely proportional the offset from the pivotal point. The frictionless interaction is, however, not a characteristic of the granular material. Therefore, the estimated soil reaction profile especially close to the mudline is arguable. The second derivative of the bending moment profile is seemingly strongly affected by the boundary curvature as per the boundary condition mentioned in Equation 4.7. The estimation close to the boundary up to 150 mm depth is not reliable. A second approach is examined for a more accurate soil reaction estimation.

4.5.2 Structural volume approach

An extension of Equation 4.7 presents a way for extending the soil reaction (p) estimation from shear force (Q_{pile}) profile as first derivative (see Equation 4.8). The single derivation reduces the curvature effects and therefore, shall provide a better estimation.

The 'structural forces in volume' feature of PLAXIS 3D is used to obtain the shear force profile from the 3D volume elements of the model pile. Figure 4.9 presents the shear force in the pile and fifth-degree polynomial smoothed trend lines for derivation accuracy. The shear force at mudline provides the boundary condition for curve fitting. The soil-reaction estimation indicates the frictional interaction between soil layers, as the soil reaction magnitude attains a maximum at non-zero depth. Thus, it provides a better soil reaction estimation, especially for the shallow depths.

$$Q_{pile} = E_p I_p \frac{d^3 y}{dz^3}, \quad (Q_{pile})_{z=0} = H$$

$$\frac{dQ_{pile}}{dz} = p, \quad z \in [0, L_e] \quad (4.8)$$

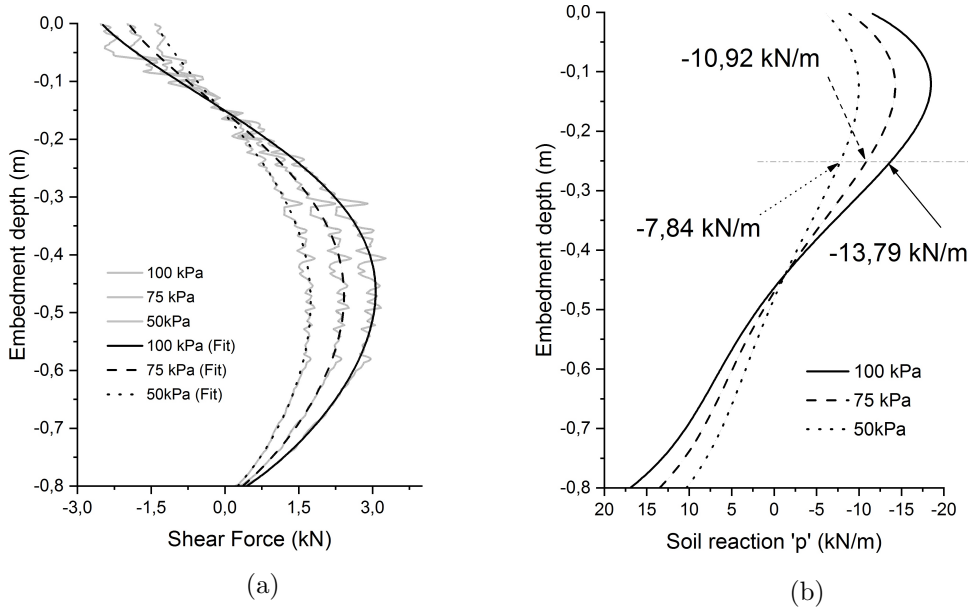


Figure 4.9: Shear force and lateral soil resistance profile pile 3D volume elements

Notably, the estimation of the structural shear forces profile from an experimental pile is not direct. The bending moment profile, however, is extractable using the strain gauges along the pile surface, for example, as reported by Klinkvort and Hededal [57]. The structural volume (STV) approach is, however, useful as a quality check to the soil reaction estimations from bending moments. Figures 4.8 and 4.9 present the marked soil reaction magnitudes for three model confining stress levels at depth 0.25m. The estimations from both approaches are in good agreement with each other.

A hypothesis is presented to estimate the soil reaction from the lateral stress changes in the soil volume. The estimations from dummy beam and structural volume approaches are taken as reference. A qualitative similarity is observed between soil stress evolution for all three vertical overburden stress case. Hence, further analysis is presented for the 100kPa case only.

4.5.3 Lateral stress evolution hypothesis

In experimental conditions, the soil stress transducers (SSTs) will be placed in the soil volume to estimate the stress changes. From Figure 4.3d, we observe that a combined loading alters the lateral stress (σ_{xx}) distribution in the soil volume. The significant changes appear in the close vicinity of the pile-soil interface. Thus, to experimentally study the pile-soil interaction, the SSTs shall be placed very close to the pile-soil interface. A gap between the pile-soil interface and SST position is, however, necessary to prevent damage in experimental conditions.

The lateral soil stress profile (see Figure 4.3d) is examined to decide the optimal SSTs position in the experimental soil volume. The lateral stress at 1.5R is considered representative of the same in the pile-soil interface for practical reasons concerning SSTs utilisation. The stress changes in model soil volume are examined at ‘stress points’ (see Figure 4.10). The stress points located on the plane of model symmetry at different depths are examined. Stress points are analogous to the experimental soil-stress transducers placed in the corresponding locations.

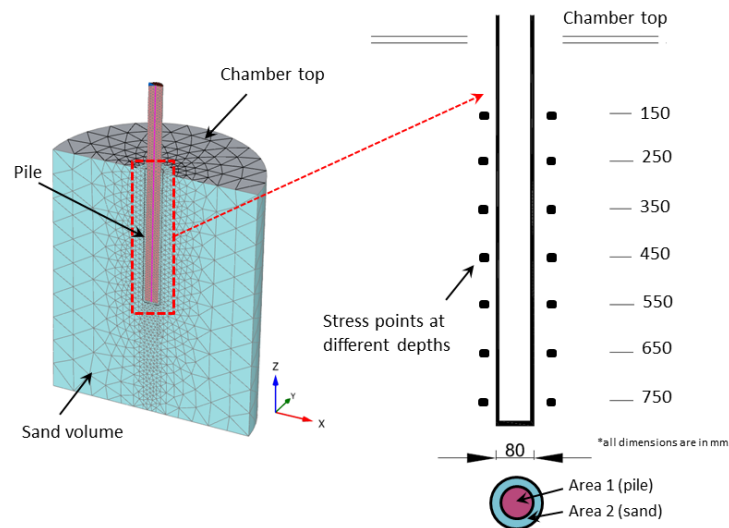


Figure 4.10: The stress points along the pile surface (with 20mm offset) at different depths along pile embedment

The distance between the pile-soil interface and stress transducer position also presents a safe distance concerning the pile installation by jacking in the experimental conditions. During jacking, the 80mm diameter pile can be assumed replacing the existing soil pushing it outwards to occupy a similar cross-sectional area. The estimated radial expansion is 16.56 mm so that the ‘area 1’ equals to the ‘area 2’, as presented in Figure 4.10. Therefore, the 20mm (0.5r) gap is a reasonable choice for experiment stress-transducers placement for both bored and jacked pile cases. In the present work, however, the focus only on the ‘wished in place’ pile case.

A decision was made to ignore pile installation effects on initial ground conditions. Byrne et al. [25] reported that the installation effects are challenging to verify against realistic field conditions and are highly likely to present unknowns which are hard to quantify and to take proper account of in numerical analysis. Consequently, the piles were modelled as ‘wished in place’, in initially undisturbed ground conditions. Nevertheless, an attempt to represent the pile installation effects has been presented in the later sections.

Bhattacharya et al. [18] reported that the pile driving reduces fatigue life. Hence, the wished in place pile model analysis represents a suitable methodology for pile-soil interaction investigations, especially for cyclic long term performance. The static pile capacity is expected to reduce due to cyclic loading application, as experimentally reported in Reese et al. [85] and API [6] by using the reduced (and constant) depth factor for the cyclic loading scenario.

The model stress points allow the analysis of all stress component in 3D space. The soil stress transducers in experiments can capture the stresses only in the direction of its orientation in the soil volume. Thus, the FE model enables for more detailed analysis for soil-pile interaction than similar experimental setup.

The hypothesis for ‘p’ estimation from the lateral stress changes is presented locally at 250mm depth. The hypothesis is further extended to represent other depth levels. At the end of the vertical loading, the soil radial stresses are evenly distributed around the periphery of the pile cross-section, as demonstrated in Figure 4.11a. Lateral stress of 60 kPa is observed from the stress point at 0.25m depth.

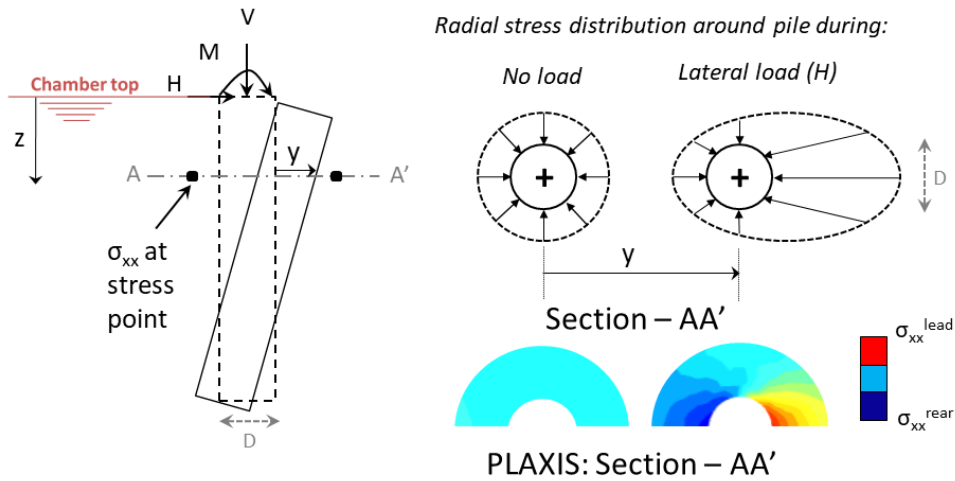


Figure 4.11: Lateral soil resistance evolution around the pile under action of combined loading, modified from Arshad and O’Kelly [11]

The horizontal loading results in the lateral pile displacement (y), altering the radial stress distribution (see Figure 4.11b). The stress magnitudes increase in the ‘lead’ face and decrease on the ‘rear’ face. The lateral stresses of 140 kPa and 30 kPa are observed in the lead and rear faces respectively at 250 mm depth. The passive earth pressure change $\Delta\sigma_{xx1} = 140 - 60 = 80$ kPa and active earth pressure change $\Delta\sigma_{xx2} = 30 - 60 = -30$ kPa results in a total of 110 kPa ($\Delta\sigma_{xx} = \Delta\sigma_{xx1} - \Delta\sigma_{xx2}$) unbalanced earth pressure in the loading direction. The soil reaction (p) is approximated by distributing the unbalanced earth pressure over the pile diameter ‘ D ’. This approximation ($p = \Delta\sigma_{xx} \times D = 110 \times 0.08 = 8.8$ kN/m) presents significantly lower estimation than the dummy beam (13.16 kN/m), or structural volume force (13.79 kN/m) at this depth. Thus, the soil reaction estimation from the earth pressure change only is highly conservative. The pile side frictional drag resistance against the soil volume is included for a more realistic soil reaction estimation. The drag resistance is represented by the second segment of Equation 4.9. It is estimated equal to 5.4 kN/m for 250 mm depth. The total soil reaction approximation ($8.8 + 5.4 = 14.20$ kN/m) from the unbalanced earth pressure and side friction

drag contributions correlates well with the dummy beam and structural volume estimations.

Here, for simplicity, the pile is assumed as a square of side length ‘D’ so that the $\Delta\sigma_{xx1}$ and $\Delta\sigma_{xx2}$ are normal to the front and rear faces of the square pile, presented by the first segment of Equation 4.9. The resulting soil-reaction magnitude from Equation 4.9 are 14.20, 11.10 and 7.72 kN/m respectively for the 100, 75 and 50 kPa model cases. The same side length of an approximated square shape as that of the circular pile diameter is arguable for possible overestimation of soil reaction.

$$p_{approx.} = \Delta\sigma_{xx} \times D + 2(K_o \times \sigma'_v \times \tan \phi' \times D) \quad (4.9)$$

The dummy beam and structural force methods for estimating the soil reaction give 13.16 kN/m (Figure 4.8b) and 13.79 kN/m (Figure 4.9b) respectively for 100 kPa case. A corresponding comparison with the computation from Equation 4.9 using soil stress evolution is 14.20 kN/m. It justifies the relative reliability on the structural force approach in comparison to dummy beam approach.

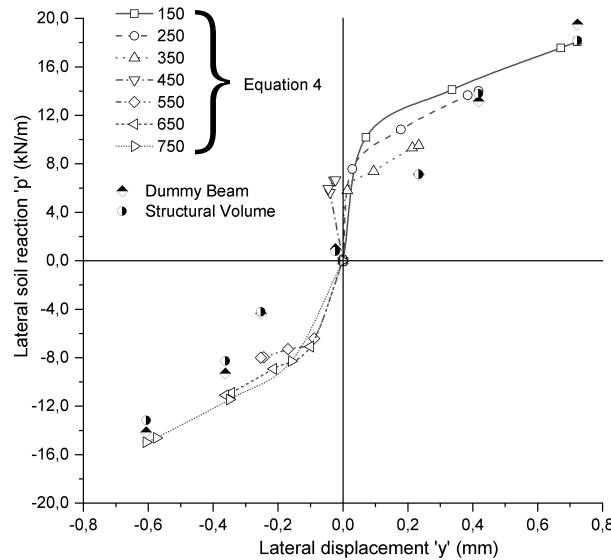


Figure 4.12: Evolution of the lateral soil reaction with lateral displacement at different depths

Figure 4.12 presents the lateral soil reaction evolution extended to all the other depths using Equation 4.9 definition. The initial stiffness presents an expected increasing trend with depth for the soil reaction. The estimations from the dummy beam and structural volume approaches are also included for qualitative comparison. The good agreement with computed soil reaction at the end of the loading at all depths supports the suitability of Equation 4.9. The soil reaction close to zero at 450 mm is estimated from dummy beam, and structural volume approaches. It indirectly presents the pile rotation (pivot point) zone. Equation 4.9 overestimates the soil reaction at 450mm due to the displacement independent side friction component consideration.

In the model analysis, the lateral displacement of the entire soil volume (see Figure 4.13) under combined load input is observed. It is due to the ‘active’ boundary conditions at model chamber periphery. It results in the overestimation of the lateral displacements in the pile-soil interface. Therefore, the relative movements between the periphery and the pile-soil interface

are taken for lateral displacement (y) estimation in model analysis.

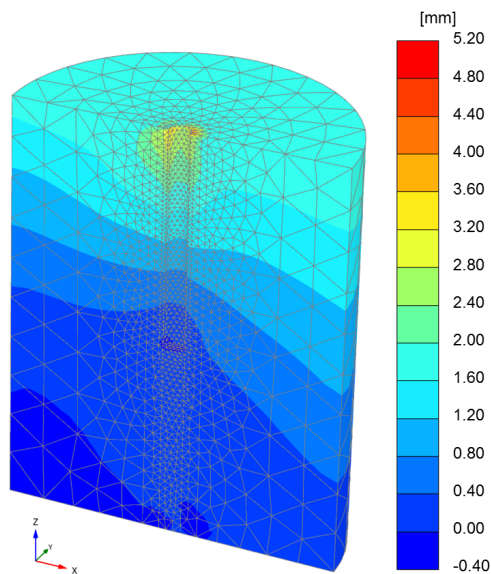


Figure 4.13: Contour plot for the lateral displacement of the model soil under combined loading

The estimation at 450 mm depth is close to zero from two presented approaches, indirectly inferring the zone of pile rotation (pivotal depth). However, equation 4.9 overestimates the soil reaction because of the constant side friction component at this depth.

4.5.4 Distributed moments hypothesis

A rigid pile presents a feature of change in vertical shear stresses at pile-soil interface due to lateral loading. It introduces a distributed moment resistance additional to the p-y resistance. The PISA project [24] reports the significance of this additional contribution for rigid piles. The moment resistance is negligible for a flexible pile analysis. The API based approach has been observed to be conservative by systematically under-predicting foundation stiffness and capacity [97]. The vertical shear stress changes for flexible piles are formulated as a function of vertical load only, for example, T-Z curves reported by API [6].

Figure 4.14 presents the strategy for the distributed moment estimation in a small pile segment inspired by the PISA project guidelines. The vertical shear stresses on the lead, and rear faces of a small pile segment of unit length are the same for vertical load application. The input of lateral load results in the change in the vertical stress distribution around pile as observed PLAXIS model output and presented in PLAXIS: section-AA' sketch. The vertical stress distribution is idealised in terms of the τ_{lead} and τ_{rear} estimated at the stress points for mathematical formulation. This is presented in the section-AA' sketch in Figure 4.14. For demonstration, one segment of the idealised stress distribution is considered such that the shear stress varies from τ_{lead} to zero between estimation at the stress point to the 90 degrees counter-clockwise rotation covering the grey shaded region in the Figure 4.14. The area of this shaded region provides an estimate of the vertical shear stress in one-quarter of the pile segment periphery. The conversion of the estimated shear stress to the distributed moment per unit segment length

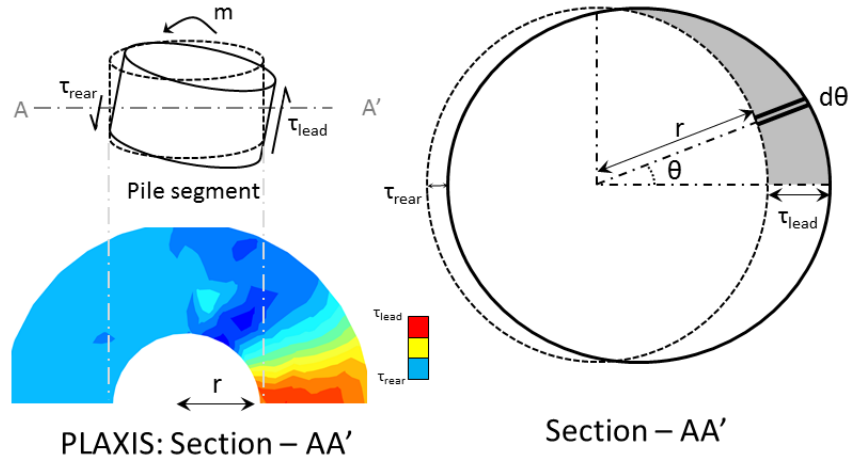


Figure 4.14: Demonstration of the change in vertical shear stresses in the pile segment under combined loading resulting in the distributed moments

for a small infinitesimal part of thickness $d\theta$ of this region is presented in Equation 4.10.

$$m_{segment} = \tau_{segment} r d\theta \times \text{moment arm} = (\tau_{lead} \cos \theta r d\theta) \times (r \cos \theta) \quad (4.10)$$

The resulting Equation 4.11 estimates the distributed moment per unit length of the pile segment by integrating the similar pile segment in the lead face and by extension for two segments in the rear face from vertical shear stress change.

$$m = 2 \int_0^{\frac{\pi}{2}} r^2 \cos^2 \theta \tau_{lead} d\theta - 2 \int_0^{\frac{\pi}{2}} r^2 \cos^2 \theta \tau_{rear} d\theta \quad (4.11)$$

Simplification of Equation 4.11 results in Equation 4.12 estimating the distributed moment in the pile segment from the change in the vertical shear stress estimated at the stress points.

$$m = \frac{\pi}{2} \times \left(\frac{D}{2}\right)^2 \times (\tau_{lead} - \tau_{rear}) \text{ in } Nm/m \quad (4.12)$$

Figure 4.15 presents the distributed moment profile at all pile segment rotation, evaluated from Equation 4.12. The pile segment rotation (θ) is calculated as a ratio of differential lead and rear face pile vertical displacement (Δu_z) and pile diameter (D). The initial rotational stiffness is almost similar at all depths. The 350mm depth presents a different evolution than at remaining depths, possibly due to error in FE stress point estimation. The moment rotation relation at 450 and 550 mm depths (pile rotation zone) is observed linear at remaining depths. The distributed moments increase for depths up to the point of rotation and decreases beyond.

The motivation for the FEM analysis is to support the planning of the calibration chamber experimental setup. A critical question is whether the soil-stress data is representative for the soil reaction and thereby providing sufficient basis for improvement of the conventional p-y method. Therefore, the following section presents an extended analysis of the proposed hypothesis to more combined load cases to generalised load space. It aims to address a robust

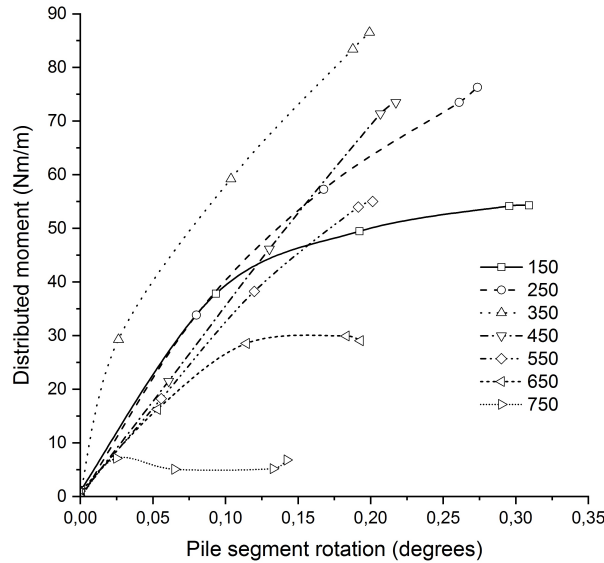


Figure 4.15: Evolution of the vertical shear stress as distributed moment in pile segment under combined loading

pile-soil interaction formulation accounting for the coupled lateral and vertical response and define the local macro-element (LME) model.

4.6 From PLAXIS to LME model definition

This section aims to address a robust pile-soil interaction mathematical formulation accounting for the coupled lateral and vertical response in a rigid pile. The soil reaction ($p - y$) and distributed moments ($m - \theta$) are estimated in a generalised loading space at different pile depths. The vertical (V) and lateral (H) load magnitudes combinations are selected in the limits of their respective capacity. Same lateral load eccentricity is used for all load cases. It results in moment ($M = H \times e$) load function of lateral load only.

The lateral load of 6.5 kN at the eccentricity 0.5 m above mudline is the lateral load capacity (H_f) of model pile-soil system. It represents the load magnitude resulting in ‘0.1D’ lateral displacement at mudline, typically defined as the ultimate limit failure state [102]. The vertical load capacity ($V_f = 15$ kN) is determined by axially loading the pile till the ‘0.1D’ tip displacement, using the Q-Z curve definition from API [6]. The typical bearing capacity formulations estimate the vertical capacity of 14.6 kN with bearing capacity factor (N_q) equal to 20 for the model soil. It supports the displacement dependent vertical capacity estimation.

Figure 4.16 presents the ten different V-H combined load cases numbered 1 to 10 in between the limits of lateral and vertical loading capacities (see Table 4.5). The normalized V-H load combination presumably follows a circular failure surface (see Equation 4.13), as reported by Li et al. [62] and Meyerhof and Ranjan [68] for pile foundations. Notably, for these load cases, the vertical plate load is replaced by the vertical point load and is applied simultaneously with lateral point load. In other words, the two different vertical and lateral loading phases are replaced by a single combined loading phase in PLAXIS simulations. The results from both approaches presented the similar response and hence the simulations are continued with a single

Table 4.5: Normalised load magnitudes collectively composing the circular failure loading surface

Load case	H/H_f	V/V_f
1	1.00	0.00
2	0.98	0.25
3	0.92	0.39
4	0.84	0.54
5	0.76	0.65
6	0.62	0.78
7	0.49	0.87
8	0.34	0.93
9	0.23	0.97
10	0.00	1.00

combined loading phase for the simulation time optimisation.

The evolution of normalised pile head displacement (formulation described in section 4.8.1) is also presented as isolines, in the plot presenting the qualitative characterises of the combined loading input. The contour plots feature inspired by the works reported by Achmus and Thieken [5] and Page et al. [77].

$$\left(\frac{H}{H_f}\right)^2 + \left(\frac{V}{V_f}\right)^2 = 1 \quad (4.13)$$

Figure 4.17 presents the soil reaction profiles from dummy beam, and structural volume approaches. Some particular cases representative of the qualitative trend of all the cases is plotted for the better readability. Two approaches response differ significantly for shallow depths. The observation is in agreement with the results presented in the sections 4.5.1 and 4.5.2. The soil reaction crosses the zero magnitudes between 0.45-0.55 m depth for all load cases.

The local macro-element assembly for the model pile in the calibration chamber is presented in Figure 4.18. The PLAXIS model analysis provides the basis for lab-scale local macro-element model components definition. The lab-scale LME model pile assembly is similar to the simple LME model assembly (see Figure 3.4 in layout. However, the lab-scale LME model pile possesses some addition interaction elements and also presents a new definition of the response of the constituent elements.

4.7 Model components

The model pile in the calibration chamber is defined in the local macro-element definition as an assembly of elastoplastic elements installed at eight levels along with the pile embedment depth ranging from 50 mm depth to 750 mm depth. Notably, in PLAXIS analysis, only seven depth levels were analysed because response at 50 mm depth was affected by the central opening in the calibration chamber setup. However, for the local macro-element model definition, the 50

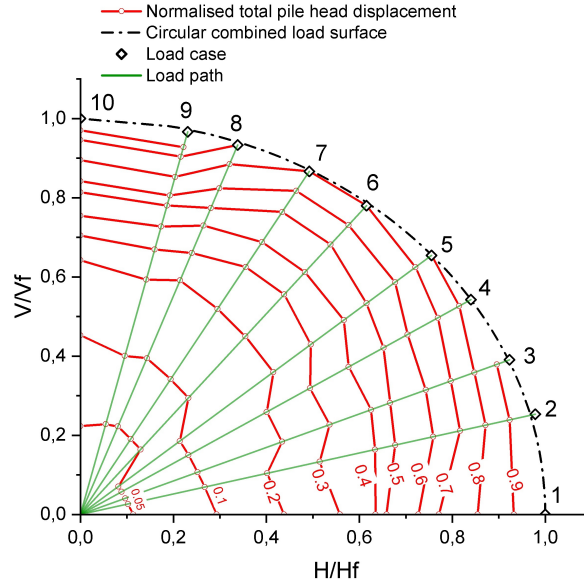


Figure 4.16: Normalised pile head displacement contours evaluated from the 10 combined loading cases on a circular failure surface

mm depth is included for model symmetry and accuracy of estimations. At each local depth level, a combination of elasto-plastic elements is defined representing the pile-soil interaction under combined load application. In practical applications of monopile, the pile is designed to stay within the elastic limit of the constituent material [16]. Therefore, the soil-pile interaction element definition is emphasised over the pile element definition. The pile is modelled as beam element following Timoshenko beam theory to account for the shear deformations in beam element. Byrne et al. [25] reported that for a monopile lateral response, the shear deformations are negligible in comparison to the bending deformations. Nevertheless, use of Timoshenko beam theory in place of typically used Euler-Bernoulli beam theory allow to incorporate the existing shear deformations. The pile-soil interaction elements characteristics and their definition in the model assembly are presented as follows.

4.7.1 Lateral soil-reaction element

The lateral soil reaction is estimated using Equation 4.9. It overestimates the lateral soil reaction in comparison to the dummy beam and structural volume estimations. It is due to a constant side friction segment independent of the applied load and depth level. Equation 4.14 presents the updated soil reaction formulation empirically incorporating the influence of depth and vertical load for side friction estimations.

$$p = (\Delta\sigma_{xx1} - \Delta\sigma_{xx2})D + 2K_o\sigma'_v \tan\phi D \left(1 - \frac{z}{L_e} \frac{V}{V_f}\right) \quad (4.14)$$

Figure 4.19 presents the normalised soil reaction profile estimated using Equation 4.14. All load cases PLAXIS model analysis at 250 mm (a) and 650 mm (b) depths are plotted. The normalisation parameters are explained in the later section of the discussion. The dummy beam and structural volume estimations at the end of each load case are compared for qualitative

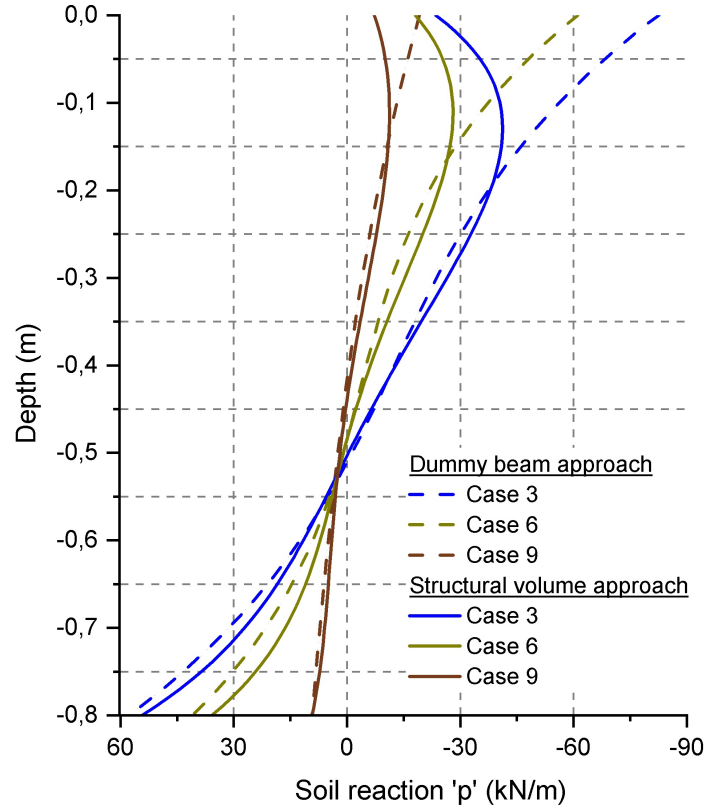


Figure 4.17: Soil reaction profile dummy beam and structural volume approach for the combined loading cases on the failure surface

verification. The soil reaction estimation from Equation 4.14 lies in between the dummy beam and structural volume estimations and thus supporting Equation 4.14 formulation. The soil stress transducers in the soil volume (see Figure 4.10) shall, therefore, provide a reliable estimate of the soil reaction at different depths.

The lateral stresses changes in the pile-soil interface can not be directly estimated in field applications. Hence, a mathematical formulation is introduced using soil properties and geotechnical characteristics for changing earth pressure estimations. Also, the coupled axial and lateral interactions are empirically introduced in the mathematical formulations.

Equation 4.15 presents the standard ultimate lateral soil reaction at a depth 'z' ($\sigma'_v = q + \gamma z$) along the pile embedment. The coefficient of passive earth pressure (K_p) provides an estimate of the lateral earth pressure change representative of the first segment of Equation 4.14. The side friction segment is kept unchanged.

$$p_u^{std.} = K_p \sigma'_v D + 2K_o \sigma'_v \tan(\phi) D \left(1 - \frac{z}{L_e} \frac{V}{V_f} \right) \quad (4.15)$$

The lateral soil reaction (p-y) element is mathematically formulated to follow an elasto-plastic evolution with parabolic hardening. The element definition is presented hereafter. The constitutive parameters are the ultimate lateral soil reaction (p_u), ultimate lateral displacement (y_u) and initial stiffness (K_i).

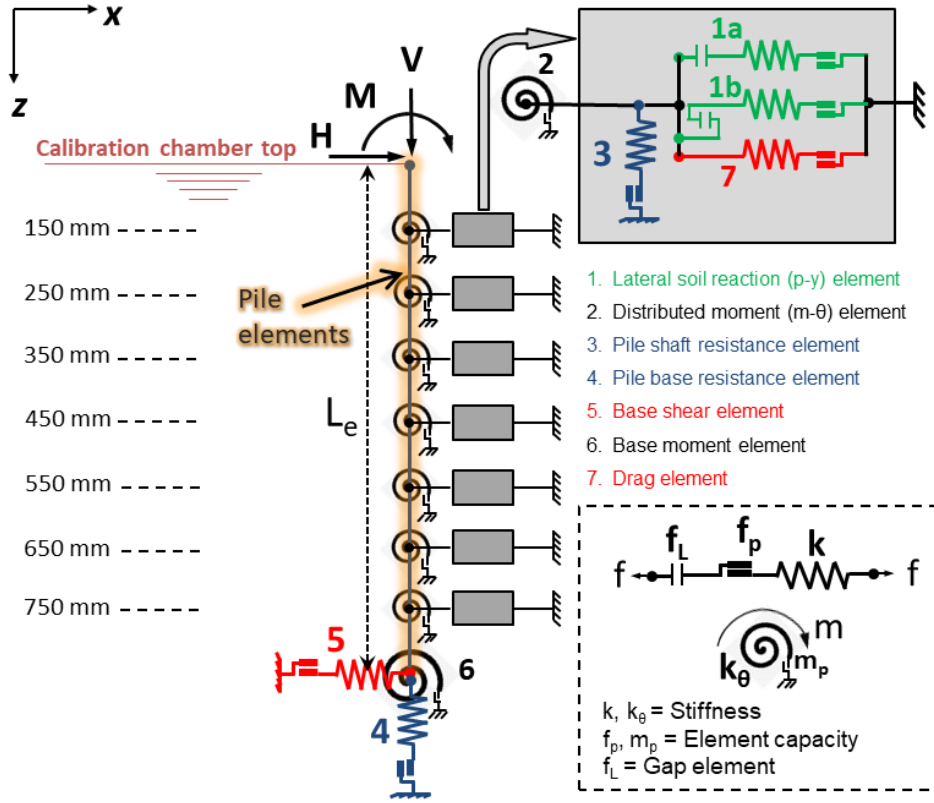


Figure 4.18: The lab scale local macro-element model assembly with new definition of axial and lateral pile-soil interaction elements, distributed moment-rotation elements, pile base shear and moment elements

The ultimate soil reaction estimations from Equation 4.15 for a pure horizontal load case ($H = H_f$) represents the standard soil reaction ($p_u^{std.}$). The increasing vertical load alters the lateral soil-pile interaction due to the coupled interaction. The ten load cases presented in Table 4.5 are simulated in the 3D FE model of the pile in the calibration chamber, and p_u is estimated from the stress points data using Equation 4.9. The increasing vertical load reduces the ultimate soil reaction. Equation 4.16 introduces the empirical coupling parameter for ultimate lateral soil reaction (p_u) estimation from the standard input. Figure (left) presents the development of the empirical relation as a linear trend between the applied vertical load level and estimated ultimate soil reaction.

$$p_u = p_u^{std.} \times \left[1 - 0.75 \left(\frac{V}{V_f} \right)^3 \right] \quad (4.16)$$

The standard ultimate lateral displacement $y_u^{std.}$ is introduced as a function of pile diameter (D). Hong et al. [45] reported that the failure mechanism for semi-rigid pile changes from wedge failure ([44], [15], [50]) at shallow depths to flow around failure at larger depth. Thus, the shallow depths shall reach the ultimate soil reaction p_u at comparably small displacements than the large depths. Based on the model simulation results, $y_u^{std.}$ equal to 3.6 mm is estimated for depth above the pile rotation point. With due consideration to the FE model outcomes, $y_u^{std.}$ for depths below the point of pile rotation is assumed 1.5 times the magnitude for depths

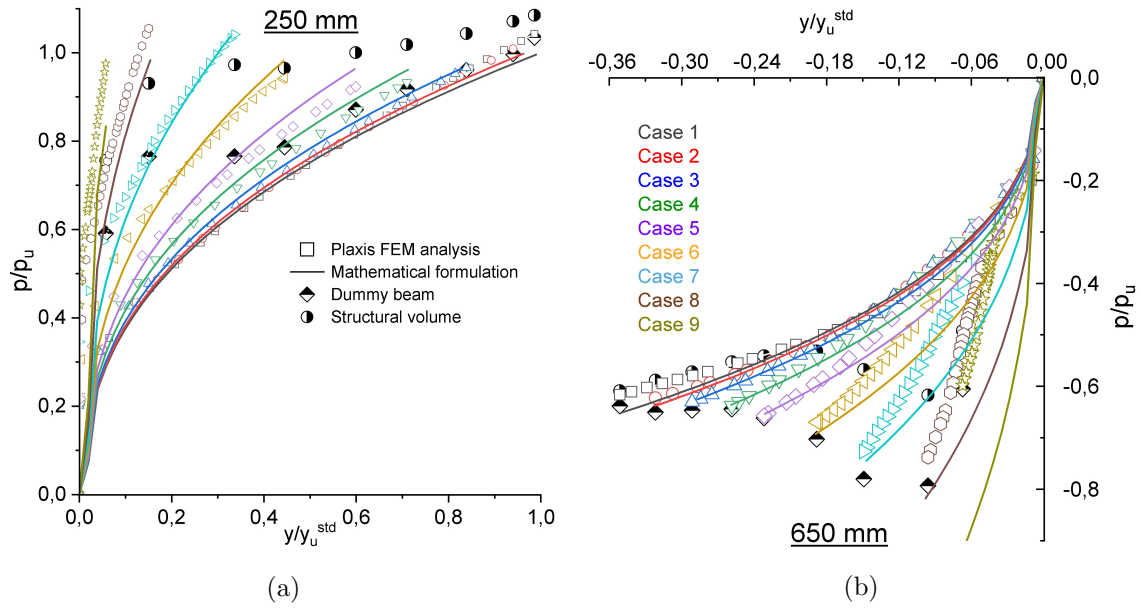


Figure 4.19: FEM analysis and mathematical formulations of the soil reaction evolution at 250 and 650 mm depths for all combined loading cases

above the pivot point. The assumption of taking a constant ultimate displacement magnitude for above (and by extension to below) the rotation point over the entire embedment depth is inspired from work reported by Motta [70] on a theoretical analysis of lateral deflection of laterally loaded piles. The coupled interaction is empirically defined as an increasing vertical load parameter for y_u estimations and presented in Equation 4.17. Figure (right) presents the linear fit between two parameters used for the empirical formulation for all the load cases.

$$y_u = y_u^{std.} \times \left[1 - \left(\frac{V}{V_f} \right)^{2.5} \right] \quad (4.17)$$

The initial stiffness is estimated using the relation presented in the Equation 4.19, as reported by Kodikara et al. [58]. Here, G_o is 48.8 MPa, estimated using the relation presented in Equation 4.18. The reference small strain shear modulus (G_o^{ref}) is estimated from the lab calibration chamber CPT test analysis by the ICP method and reported equal to 65 MPa. Note that, the mean stress level at $z = L_e$ in calibration chamber test is estimated 75 kPa (with 100 kPa vertical stress and 50 kPa lateral stress). The reference modulus shall be estimated at the atmospheric reference stress level. Therefore, the estimated G_o^{ref} is rather chosen conservatively because of the empirical formulation of G_o from the relation reported by Schnaid and Houlsby [90] estimates 39.6 MPa which is in close agreement to the one estimated from FE model. [57] also reported the initial stiffness at very small strain levels approximation to $75 \times Kp$, where Kp is passive earth pressure coefficient. It presents the initial stiffness ≈ 255 MPa for our model soil-pile system and validates the estimation from the relation in Equation 4.19.

$$G_o = G_o^{ref} \left(\frac{\sigma_3}{p_{ref}} \right)^{0.5} \quad (4.18)$$

$$K_i = 4 \times G_o \quad (4.19)$$

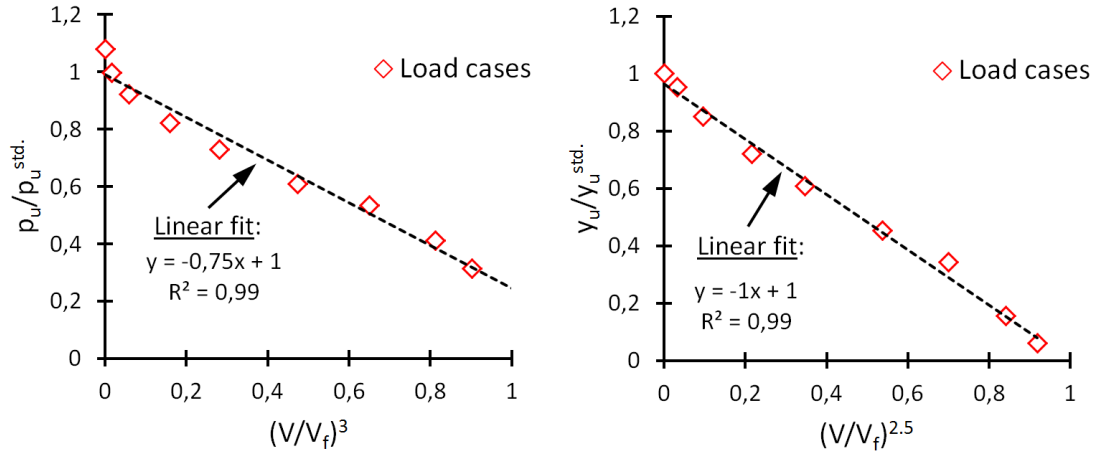


Figure 4.20: The empirical formulation of ultimate soil reaction and lateral displacement for the definition of the lateral soil reaction element

The elastoplastic formulation presents the lateral displacement as a sum of elastic and plastic displacements. Equation 4.20 defines the elastic displacement and Equation 4.21 defines the total displacement following a parabolic hardening formulation.

$$y^{el} = \frac{p}{K_i} \quad (4.20)$$

$$y = y_u \times \left(\frac{p}{p_u} \right)^{2.5} \quad (4.21)$$

Figure 4.19 presents the normalised lateral soil reaction evolution at 250mm and 650 mm depths for all combined load cases. The p_u from Equation 4.16 and $y_u^{std.}$ are used as normalisation parameters. The PLAXIS model analysis and the mathematical formulation are in a good agreement for both above and below pile rotation depths. The parabolic exponent is chosen equal to 2.5 (see Equation 4.21) such that the mathematical lateral soil reaction evolution follows the same path as observed from the FE model analysis. A value between 2 and 4 is usually recommended for the parabolic exponent.

The lateral soil reaction (p-y) element is defined to follow a nonlinear elastoplastic evolution with parabolic hardening. The macro-element definition for the lateral soil-reaction element is presented as follows. The load function is defined as per Equation 4.22.

$$f_{py} = f(p, \alpha) = -sign(p_L) \times p - (p_e + f(\alpha)) = 0 \quad (4.22)$$

Here p_e is the yield limit for the elastic soil reaction. p_L presents the gap element. The gap element is assigned a minimal magnitude (1 N/m), resulting in a negligible effect in the element performance. The lateral load response for a rigid pile is a rotation about a pivot point. Therefore, the lateral soil reaction evolution for depths above and below the point of pile rotation shall be identifiable. The elastic stiffness presented in Equation 4.23 enables the

definition of the leading and rear face elements using the gap element.

$$\begin{aligned}\lim_{p \rightarrow \infty} \frac{K_e}{1 + 2^{p/p_L}} &= K_e \\ \lim_{p \rightarrow \infty} \frac{K_e}{1 + 2^{p/p_L}} &= 0\end{aligned}\quad (4.23)$$

The gap element $p_L = -1$ is used to define the lead face element and $+1$ for rear face element. The function $f(\alpha)$ in Equation 4.22 represents hardening during plastic displacement. The p-y response is formulated as parabolic beginning from the zero displacements. Thus, the elastic soil reaction limit is, therefore, not defined explicitly. The hardening is defined in Equation 4.24.

$$f(\alpha^*) = (p_e + f(\alpha)) = p_u \left(\frac{y}{y_u} \right)^{1/2.5} \quad (4.24)$$

The return mapping algorithm for the p-y element is presented as follows. The soil reaction at n^{th} step for k^{th} iteration is written as p_n^k . Concerning the procedure mentioned in the return mapping algorithm, the plastic multiplier ($\Delta\lambda$) is evaluated.

$$\delta(\Delta\lambda)^k = \frac{f(p_n^k, \alpha_n^{*k})}{K_e \times \left(\frac{\partial f}{\partial p}(p_n^k, \alpha_n^{*k}) \right)^2 - \frac{\partial f}{\partial \alpha^*}(p_n^k, \alpha_n^{*k}) \times \left| \frac{\partial f}{\partial p}(p_n^k, \alpha_n^{*k}) \right|} \quad (4.25)$$

$$f(p_n^k, \alpha_n^{*k}) = -sign(p_L) \times p_n^k - \alpha_n^{*k} \quad (4.26)$$

$$\frac{\partial f}{\partial p}(p_n^k, \alpha_n^{*k}) = -sign(p_L) \quad (4.27)$$

$$\frac{\partial f}{\partial \alpha^*}(p_n^k, \alpha_n^{*k}) = \frac{p_u}{(y_u)^{1/2.5}} \times \frac{1}{2.5} \times \left((y_p)_n^k + \frac{p_n^k}{K_e} \right)^{1.5} \quad (4.28)$$

$$\begin{aligned}p_n^{k+1} &= p_n^k - \delta(\Delta\lambda)^k \times K_e \times \frac{\partial f}{\partial p}(p_n^k, \alpha_n^{*k}) \\ \alpha_n^{*k+1} &= \alpha_n^{*k} + \delta(\Delta\lambda)^k \left| \frac{\partial f}{\partial p}(p_n^k, \alpha_n^{*k}) \right| \\ (y_p)_n^{k+1} &= (y_p)_n^k + \delta(\Delta\lambda)^k \times \frac{\partial f}{\partial p}(p_n^k, \alpha_n^{*k})\end{aligned}\quad (4.29)$$

4.7.2 Pile shaft resistance element

The pile shaft resistance element represents the evolution of the shear force in the pile shaft with the vertical displacement with the basic formulation inspired by the t-z elements [6]. Similar to the soil reaction formulations, the applied vertical load level is empirically incorporated to define the axial and lateral coupled pile-soil interaction. The elastic limit of the vertical displacement (u_e), ultimate vertical displacement (u_{ult}), elastic stiffness (K_u^e) and plastic stiffness (K_u^p) are the constituent parameters for the pile shaft resistance mathematical formulation.

The standard vertical displacement and elastic stiffness parameters are formulated from a pure vertical load case until failure (load case 10). The estimated shear stress (τ_s) at different stress points is converted to the shear force in the pile segment using relation $Q_s = \tau_s \pi D L_r$, where $L_r = 0.1m$ is the pile segment length. Figure 4.21 presents the relation between the pile segment shear force and vertical displacement from the FE model. The standard elastic and ultimate displacements are defined from the observation of the model result. The standard elastic ($u_e^{std.}$) and total ultimate displacements ($u_{ult}^{std.}$) equal to 2 mm and 8 mm (D/10) respectively are observed from FE analysis. The ultimate displacement is observed keeping a constant value over different embedment depths. The standard elastic displacement, however, presents a decreasing trend which is empirically incorporated in Equation 4.30.

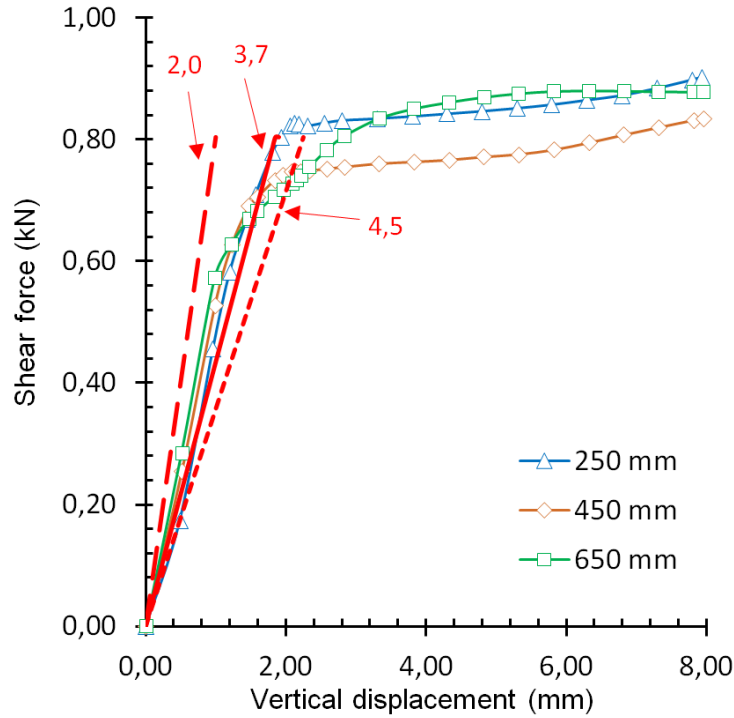


Figure 4.21: Plot for vertical shear force and vertical displacement relation for the determination of standard element parameters

$$u_e^{std.} = 0.25 \times u_{ult}^{std.} \left(1 - 0.35 \frac{z}{L_e} \right) \quad (4.30)$$

With increasing lateral load, both elastic and ultimate displacements reduce from the standard magnitude. Equations 4.31 and 4.32 empirically present the effect of the applied lateral load level, applicable for both elastic (u_e) and ultimate (u_{ult}) displacements. Figure 4.22 presents the basis of the empirical formulation from FE analysis of 10 load cases. The plastic displacement (u_p) is obtained from the difference of ultimate and the elastic displacements.

$$u_e = u_e^{std.} \left[1 - 0.5 \left(\frac{H}{H_f} \right)^{0.75} \right] \quad (4.31)$$

$$u_{ult} = u_{ult}^{std.} \left[1 - 0.8 \left(\frac{H}{H_f} \right)^{1.5} \right] \quad (4.32)$$

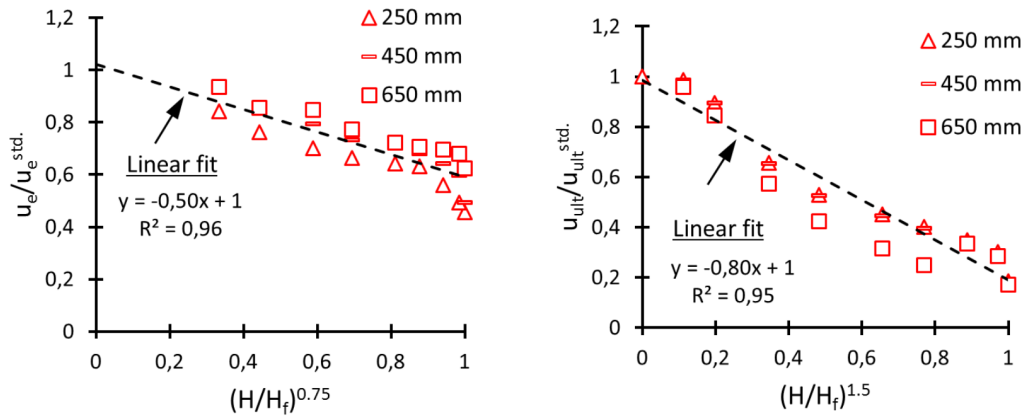


Figure 4.22: The empirical formulation of elastic and ultimate vertical displacement for the definition of the pile shaft resistance element

The formulation of standard elastic stiffness ($K_u^{e(std.)}$) follows the primary shear stress (τ) and shear strain (γ) relation through the use of shear modulus definition. The procedure is presented in Equation set 4.33.

$$\begin{aligned}
 & \text{we know, } G = \frac{\tau}{\gamma}, \quad \text{we want, } K_u^{e(std.)} = \frac{Q_s}{u_e^{std.}} \\
 & \tau = \frac{Q_s}{\pi D L_r}, \quad \implies \frac{Q_s u_e^{std.}}{\pi D L_r u_e^{std.} \gamma} = G \\
 & \text{Rearranging, } \frac{Q_s}{u_e^{std.}} = \frac{G \pi D L_r \gamma}{u_e^{std.}} = K_u^{e(std.)} \quad (4.33) \\
 & \text{Now, } \gamma = \frac{u_e^{std.}}{a D}, \\
 & \text{Therefore, } K_u^{e(std.)} = \frac{G \pi L_r}{a}
 \end{aligned}$$

Here, ‘a’ represents the factor of pile diameter (D) representing the radial distance between pile axis and soil volume where shear displacement is zero; thereby defining the shear strain (γ). In Figure 4.21, the red lines represent the linear elastic zone with different values of ‘a’. Value 3.7 provides the best correlation between FE analysis and mathematical formulation. Consequently, the standard elastic stiffness ($K_u^{e(std.)}$) is formulated as per Equation 4.34. Here, the secant shear modulus (G_{sec}) is considered for element definition and is taken linearly increasing with vertical stress level ($(\sigma_{v(z)} = q + \gamma z)$) at a depth ‘z’.

$$K_u^{e(std.)} = \frac{\pi}{3.7} G_{sec} \frac{\sigma'_{v(z)}}{\sigma'_{v(L_e)}} L_r \quad (4.34)$$

From FE model outcomes, the elastic stiffness is assumed to increase linearly with the horizontal load level, presented in Equation 4.35.

$$K_u^e = K_u^{e(std.)} \left(1 + \frac{H}{H_f} \right) \quad (4.35)$$

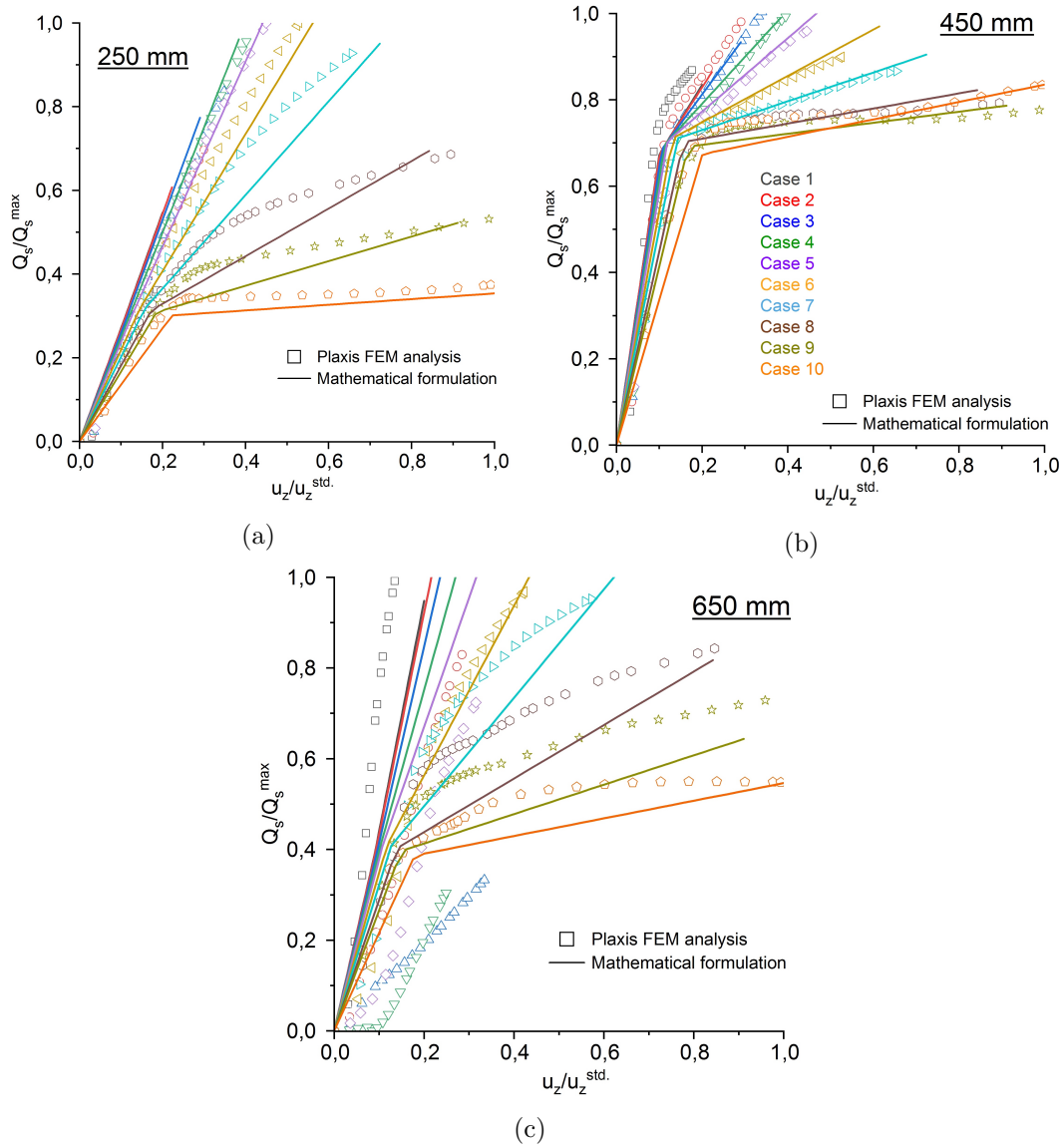


Figure 4.23: FEM analysis and mathematical formulations of the vertical shear force evolution at 250, 450 and 650 mm depths for all combined loading cases

Figure 4.23 presents the FE analysis outcome for all load cases for a relation between pile segment vertical shear force and shear displacement normalised to the respective standard values. The plastic stiffness (K_u^p) is observed to present hardening at all depth levels depth with increasing lateral load level. Hong et al. [45] reported three different soil flow mechanisms, namely cavity, full and rotational flow with increasing pile embedment depths for a semi-rigid pile. Here, the model analysis and observations at 250, 450 and 650 mm depths are taken as representative of three different soil flow mechanisms. The presence of different interaction mechanism indirectly justifies the adequacy of using the coupled macro-elements at several depth levels. Equation 4.36 presents the empirical vertical load level-dependent plastic stiffness formulation for all depth levels. The standard elastic stiffness is taken as a reference for the empirical formulation. The estimation of K_u^p from FE analysis is made by observing the slope of the shear force and vertical displacement plot between elastic limit and the ultimate magnitude for all the load cases. Figure 4.27 presents the observed load cases outputs at three representative

depth levels and linear fit for the empirical definition of the distributed moment element.

$$K_u^p = K_u^{e(std.)} \begin{cases} 0.05 + 4.00\left(\frac{H}{H_f}\right)^{2.15} - 2.00\left(\frac{H}{H_f}\right)^{4.3} & \in \frac{z}{L_e} = [0, 0.5] \\ 0.06 - 0.25\left(\frac{H}{H_f}\right) + 0.67\left(\frac{H}{H_f}\right)^2 & \in \frac{z}{L_e} = (0.5, 0.75) \\ 0.09 - 0.34\left(\frac{H}{H_f}\right) + 2.60\left(\frac{H}{H_f}\right)^2 & \in \frac{z}{L_e} = [0.75, 1] \end{cases} \quad (4.36)$$

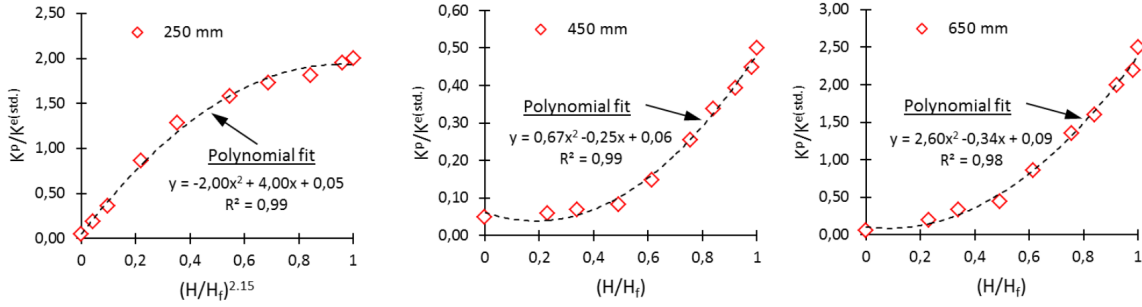


Figure 4.24: The empirical formulation of plastic stiffness for the definition of the pile shaft resistance element

Equation 4.37 presents the estimation of the shaft resistance (Q_s) for all ranges of pile segment vertical displacement.

$$Q_s = \begin{cases} Q_s^e = K_u^e u & \in u = [0, u_e] \\ Q_s^{ep} = K_u^e u_e + K_u^p (u - u_e) & \in u = (u_e, u_{ult}] \end{cases} \quad (4.37)$$

A comparison of the outcomes from simulations and the mathematical formulation is presented in Figure 4.23. The linear formulation results in a simplification of the behaviour. However, there is a quantitative agreement with the simulation results. The vertical displacement (u_z) is normalised to the standard displacement ($u_z^{std.}$). The shaft resistance (Q_s) = $f(H, V, z)$ is normalised to the maximum shaft resistance (Q_s^{max}) estimated from the solution of first derivative of the shaft resistance equation $f'(H, V, z) = 0$.

The macro-element definition for the pile shaft resistance element is presented as follows. The load function is defined as per Equation 4.38.

$$f_{Q_s u_z} = f(Q_s, \alpha) = -sign(Q_L) \times Q_s - (Q_s^e + f(\alpha)) = 0 \quad (4.38)$$

Here Q_s^e is the yield limit for the elastic vertical shear resistance. Q_L presents the gap element. The function of the gap element is the same as presented for the lateral soil reaction element. The gap element $Q_L = -1$ is used to define the lead face element and $+1$ for rear face element. The function $f(\alpha)$ in Equation 4.38 represents hardening during plastic displacement. The hardening function is defined in Equation 4.39.

$$f(\alpha) = K_{u_z}^p (u_z - u_z^e) \quad (4.39)$$

The return mapping algorithm for the pile shaft resistance element is presented as follows. The soil reaction at n^{th} step $(Q_s)_n$. Regarding the procedure mentioned in the return mapping algorithm, the plastic multiplier $(\Delta\lambda)$ is evaluated. Likewise, distributed moment element, the pile shaft resistance element follows the linear hardening; thereby, one iteration is sufficient at each step.

$$\Delta\lambda = \frac{f((Q_s)_n, \alpha_n)}{K_{u_z}^e \times \left(\frac{\partial f}{\partial Q_s}((Q_s)_n, \alpha_n) \right)^2 + \frac{\partial f}{\partial \alpha}((Q_s)_n, \alpha_n) \times \left| \frac{\partial f}{\partial Q_s}((Q_s)_n, \alpha_n) \right|} \quad (4.40)$$

$$f((Q_s)_n, \alpha_n) = -\text{sign}(Q_L) \times (Q_s)_n - (Q_s^e + f(\alpha_n)) \quad (4.41)$$

$$\frac{\partial f}{\partial Q_s}((Q_s)_n, \alpha_n) = -\text{sign}(Q_L) \quad (4.42)$$

$$\frac{\partial f}{\partial \alpha}((Q_s)_n, \alpha_n) = K_{u_z}^p \quad (4.43)$$

$$\begin{aligned} (Q_s)_{n+1} &= (Q_s)_n - \delta(\Delta\lambda) \times K_{u_z}^e \times \frac{\partial f}{\partial Q_s}((Q_s)_n, \alpha_n) \\ \alpha_{n+1} &= \alpha_n + \delta(\Delta\lambda) \left| \frac{\partial f}{\partial Q_s}((Q_s)_n, \alpha_n) \right| \\ (u_z^p)_{n+1} &= (u_z^p)_n + \delta(\Delta\lambda) \times \frac{\partial f}{\partial Q_s}((Q_s)_n, \alpha_n) \end{aligned} \quad (4.44)$$

4.7.3 Distributed moment element

Figure 4.25 presents the distributed moment-rotation ($m-\theta$) relation for all combined load cases at 250mm, 450mm and 650mm depths. The moment is estimated from Equation 4.12 using the PLAXIS model analysis for shear stress ($\Delta\tau$) change. Different depths presents different $m-\theta$ evolution mechanisms. Therefore, a simplified linear elastic with linear hardening/softening behaviour is assumed to define mathematical formulation.

In experimental conditions, the shear stress estimations using soil stress transducers is not possible. The SSTs can only capture the normal stress in the soil volume at the point of interest. Hence, the moment rotation mathematical relations are defined with stiffness and rotation as the independent variables. It enables the indirect estimation of the shear stress level and by extension, the distributed moment.

Similar to the soil reaction formulations, the applied vertical load level is empirically incorporated to define the coupled interaction. The elastic rotation (θ_e), ultimate rotation (θ_u), elastic rotation stiffness (K_θ^e) and plastic rotation stiffness (K_θ^p) are the constituent parameters for the $m-\theta$ mathematical formulation so as to adapt to the responses at all depth levels.

The standard elastic and ultimate rotations are defined from the observation for pure horizontal load case. From model results, the standard ultimate rotation at pile mudline level is observed 1.35° . The standard elastic rotation ($\theta_e^{std.}$) is assumed equal to $1/13.5$ th of $\theta_u^{std.}$ for all depths above and below the pile rotation point and equal to $2/13.5$ th of $\theta_u^{std.}$ for around pile

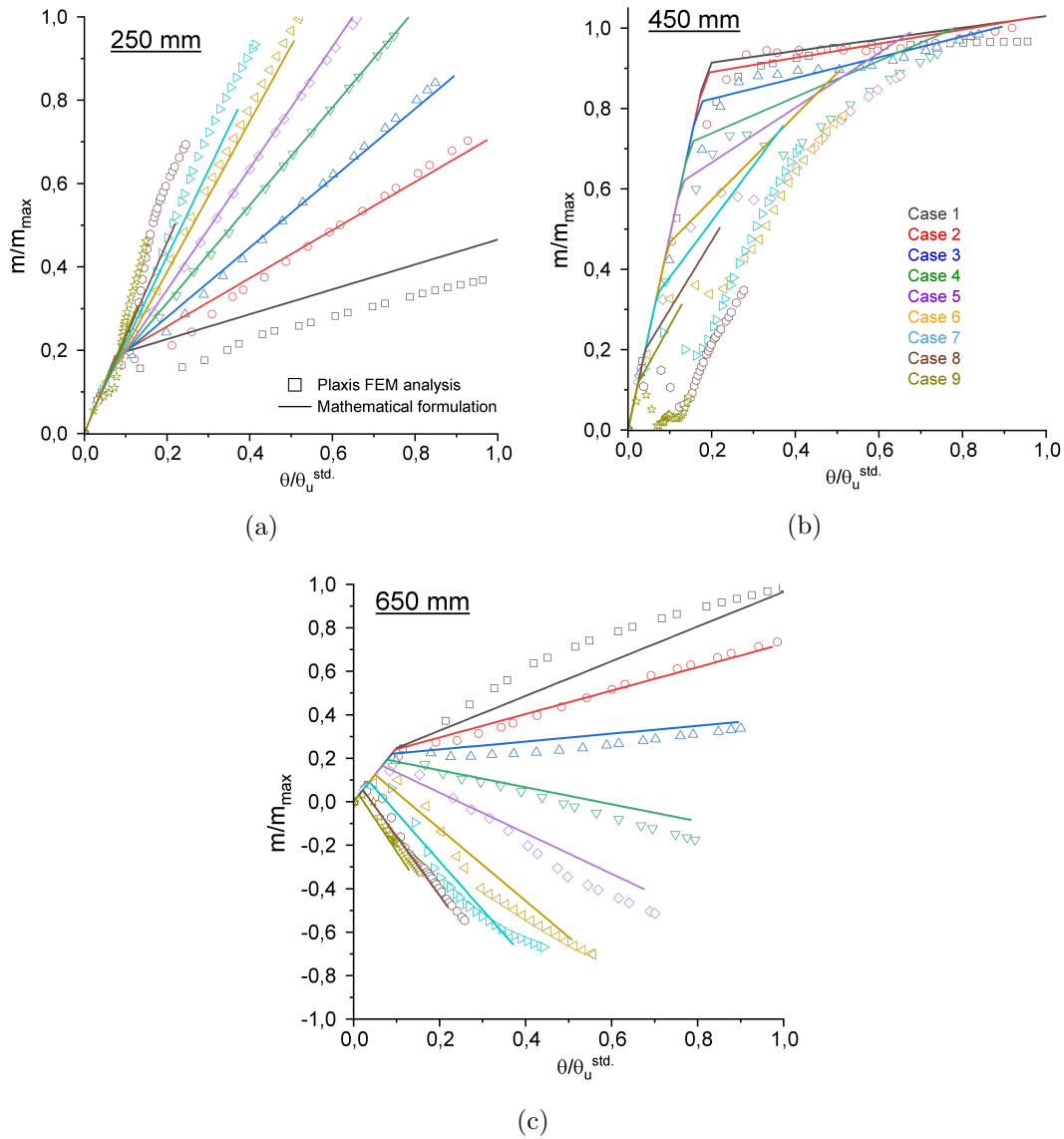


Figure 4.25: FEM analysis and mathematical formulations of the distributed moments evolution at 250, 450 and 650 mm depths for all combined loading cases

rotation point (*i.e.* $z/L_e = 0.5$ to 0.75). For a pure rigid pile, the standard ultimate rotation shall be the same for all pile segments. For the present semi-rigid model pile-soil system, a decreasing trend with embedment depth (z) is observed from the model analysis. Equation 4.45 presents the standard ultimate pile rotation varying from 1.35° at mudline (θ_u^{head}) to 0.9° at pile tip.

$$\theta_u^{std.} = \left(\theta_u^{head} - 0.45 \frac{z}{L_e} \right) \text{ degrees} \quad (4.45)$$

With increasing vertical load, both elastic and ultimate rotations reduce from the standard magnitude. Equation 4.46 empirically presents the effect of the applied lateral load level, applicable for both elastic (θ_e) and ultimate (θ_u) rotations. The equation is formulated by observing the pile segment rotations at three depth levels 250, 450 and 650 mm for all load cases. Figure 4.26 presents the correlation of normalised pile segment rotation to the normalised

horizontal load with a linear fit on the average of three trends. Notably, there is consistency in the pile segment rotation over different pile segments. It indirectly represents the rigid pile rotation and thus supports the model analysis. The standard elastic ultimate rotation is assumed 1/13.5th The plastic rotation (θ_p) is obtained from the difference of ultimate and the elastic rotations.

$$\theta_u = \theta_u^{std.} \left(\frac{H}{H_f} \right)^{1.4} \quad (4.46)$$

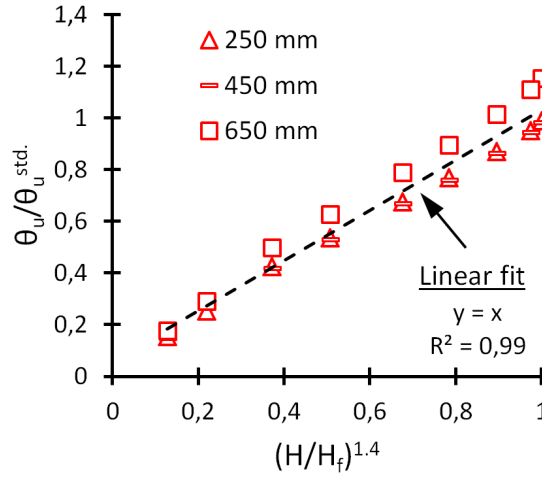


Figure 4.26: The empirical formulation of ultimate pile segment rotation for the definition of the distributed moment-rotation element

The elastic stiffness is calculated as a function of secant shear modulus. Equation 4.47. Here, the secant shear modulus (G_{sec}) is taken linearly increasing with vertical stress level ($\sigma_{v(z)} = q + \gamma z$) at a depth 'z'. The secant modulus is introduced (instead of small strain shear modulus), because, the element response is formulated linear elastic. Thereby, the secant modulus (G_{sec}) provides a good estimate of the element behaviour for the deformation range considered. The small strain shear modulus (G_o) will provide a higher estimation of the initial stiffness in this range. The G_{sec} is estimated at the pile tip embedment depth ($z = L_e$) using the relation $G_{sec} = E_{sec}/(2(1 + \nu))$. The E_{sec} is estimated from the Equation 4.5. The elastic rotation stiffness remains unchanged with the applied vertical or horizontal load. The elastic stiffness is calculated as per Equation 4.47 following the similar guidelines as presented for shaft resistance element (see Equation 4.33). The ratio of shear force and vertical displacement is converted to the ratio of distributing moment and rotation for the K_θ^e formulation.

$$K_\theta^e = \frac{\pi}{3.7} D^2 L_r G_{sec} \frac{\sigma'_{v(z)}}{\sigma'_{v(L_e)}} \quad (4.47)$$

From Figure 4.25 observation, the plastic rotation stiffness (K_θ^p) presents hardening for 250 and 450 mm depths and softening behaviour for the 650mm depth with increasing vertical load level. Here, the model analysis and observations at 250, 450 and 650 mm depths are taken as representative of three different soil flow mechanisms similar to the one presented for pile shaft resistance element. Equation 4.48 presents the empirical vertical load level-dependent plastic

stiffness formulation for all depth levels. The elastic stiffness is taken as a reference for the empirical formulation. The estimation of K_θ^p from FE analysis is made by observing the slope of the moment rotation plot between elastic limit and the ultimate moment-rotation magnitude for all the load cases. Figure 4.27 presents the observed load cases outputs at three representative depth levels and linear fit for the empirical definition of the distributed moment element.

$$K_\theta^p = K_\theta^e \begin{cases} 0.12 + 0.88 \left(\frac{V}{V_f}\right)^{1.5} & \in \frac{z}{L_e} = [0, 0.5] \\ 0.03 + 0.40 \left(\frac{V}{V_f}\right)^3 & \in \frac{z}{L_e} = (0.5, 0.75) \\ 0.32 - 1.62 \left(\frac{V}{V_f}\right)^2 & \in \frac{z}{L_e} = [0.75, 1] \end{cases} \quad (4.48)$$

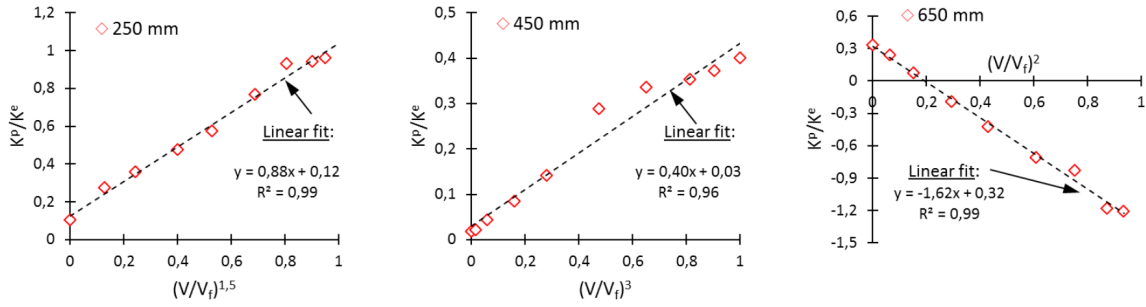


Figure 4.27: The empirical formulation of plastic rotational stiffness for the definition of the distributed moment-rotation element

Equation 4.49 presents the estimation of the distributed moment (m) for all ranges of pile segment rotation θ .

$$m = \begin{cases} m_e = K_\theta^e \theta & \in \theta = [0, \theta_e] \\ m_{ep} = K_\theta^e \theta_e + K_\theta^p (\theta - \theta_e) & \in \theta = (\theta_e, \theta_u] \end{cases} \quad (4.49)$$

A comparison of the outcomes from simulations and the mathematical formulation is presented in Figure 4.25. The linear formulation results in a simplification of the behaviour. However, there is a quantitative agreement with the simulation results. The rotation (θ) is normalised to the standard ultimate rotation (θ_u^{std}). The moment (m) = $f(H, V, z)$ is normalised to the maximum moment (m_{max}) estimated from the solution of first derivative of the moment function *i.e.* $f'(H, V, z) = 0$.

The macro-element definition for the distributed moment-rotation element is presented as follows. The load function is defined as per Equation 4.50.

$$f_{m\theta} = f(m, \alpha) = -sign(m_L) \times m - (m_e + f(\alpha)) = 0 \quad (4.50)$$

Here m_e is the yield limit for the elastic soil reaction. m_L presents the gap element. The gap element is assigned a minimal magnitude (0.01 Nm/m), resulting in a negligible effect in the element performance. The function of the gap element is the same as presented for the lateral soil reaction element.

The function $f(\alpha)$ in Equation 4.50 represents hardening during plastic displacement. The distributed moment element is defined following a linear hardening behaviour. The hardening function is defined in Equation 4.51.

$$f(\alpha) = K_{\theta}^p(\theta - \theta_e) \quad (4.51)$$

The return mapping algorithm for the $m - \theta$ element is presented as follows. The soil reaction at n^{th} step is written as m_n . Concerning the procedure mentioned in the return mapping algorithm, the plastic multiplier ($\Delta\lambda$) is evaluated. Only a single iteration is sufficient for linear hardening variable.

$$\Delta\lambda = \frac{f(m_n, \alpha_n)}{K_{\theta}^e \times \left(\frac{\partial f}{\partial m}(m_n, \alpha_n)\right)^2 + \frac{\partial f}{\partial \alpha}(m_n, \alpha_n) \times \left|\frac{\partial f}{\partial m}(m_n, \alpha_n)\right|} \quad (4.52)$$

$$f(p_n^k, \alpha_n^k) = -\text{sign}(p_L) \times p_n^k - \alpha_n^k \quad (4.53)$$

$$\frac{\partial f}{\partial m}(m_n, \alpha_n) = -\text{sign}(m_L) \quad (4.54)$$

$$\frac{\partial f}{\partial \alpha}(m_n, \alpha_n) = K_{\theta}^p \quad (4.55)$$

$$\begin{aligned} m_{n+1} &= m_n - \delta(\Delta\lambda) \times K_{\theta}^e \times \frac{\partial f}{\partial m}(m_n, \alpha_n) \\ \alpha_{n+1} &= \alpha_n + \delta(\Delta\lambda) \left|\frac{\partial f}{\partial m}(m_n, \alpha_n)\right| \\ (\theta_p)_{n+1} &= (\theta_p)_n + \delta(\Delta\lambda) \times \frac{\partial f}{\partial m}(m_n, \alpha_n) \end{aligned} \quad (4.56)$$

4.7.4 Pile base resistance element

The base resistance element is mathematically formulated based on the simulation results. The control variables for the element definition are the vertical displacement limit and the base capacity. For simplicity and coherence for all the load cases, the vertical displacement (u_z) limit is taken as 10% of the pile diameter. The tip resistance for pure vertical load case is evaluated using a typical pile capacity (V_f) relationship presented in Equation 4.57, and presented in Figure 4.28.

$$\begin{aligned} V_f &= Q_b^{std} + Q_s^{std} \\ Q_b^{std} &= V_f - K_o \times \tan(\delta') \times \pi D_p \left(qL_e + \frac{1}{2} \gamma' L_e^2 \right) \end{aligned} \quad (4.57)$$

where,

Q_b^{std} = Pile base capacity for pure axial load;

Q_s^{std} = Pile shaft capacity for pure axial load;

D_p = Diameter of model pile;

V_f = Vertical load capacity of pile-soil system;

K_o = Earth pressure coefficient at rest = 0.5 for model;

δ' = Pile-soil interface friction angle;

q = Vertical surcharge stress;

L_e = Pile embedment length.

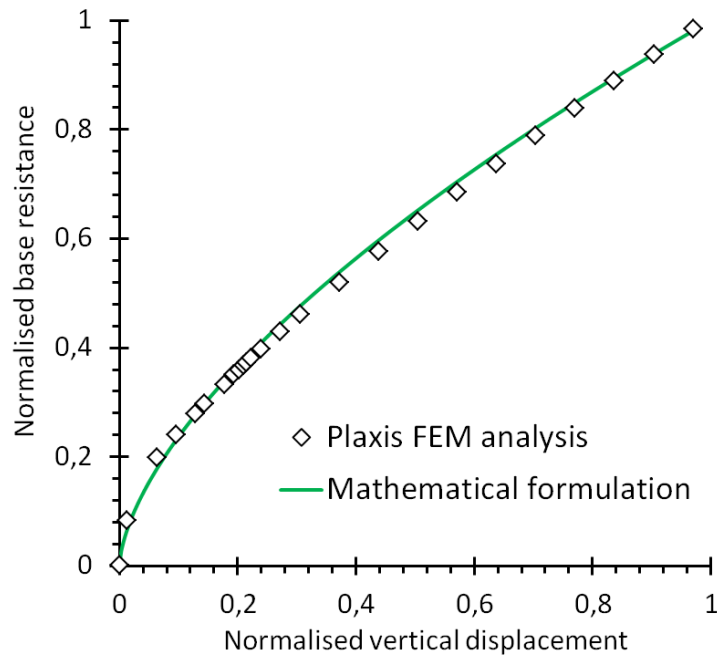


Figure 4.28: FEM analysis and mathematical formulation for the pile base resistance evolution for pure axial loading case

The mathematical formulation of the base resistance element follows a nonlinear elastoplastic evolution with parabolic hardening. The control parameters are tip capacity and the ultimate vertical displacement. The elastic stiffness is defined in Equation 4.58 by the small strain deformation modulus ($E_o = 2G_o (1+\nu) = 127$ MPa). Notably, the empirical relationship for the small strain soil deformation modulus reported by Klinkvort and Hededal [57] estimates 115 MPa for the present model case. A close agreement supports the correctness of the HS soil parameters. The behaviour is described as nonlinear elastoplastic, where the small strain deformation modulus defines the base resistance in the elastic state.

$$K_{u_z}^e = E_o \times \frac{\pi}{3.7} \times D \quad (4.58)$$

From Equation 4.57, we see that the base resistance is dependent on the shaft resistance and applied vertical load level. The application of horizontal load alters the magnitude of

the vertical shear stresses. The circular failure load surface presents the decreasing vertical load levels with increasing lateral load level. Therefore, the effect of the horizontal load application is on both vertical load capacity and shaft resistance. Subsequently, the evolution of the base resistance is empirically formulated from LME calibration such that the vertical tip displacement is equivalent to the pile shaft resistance element for different load cases on failure envelope. Equation 4.59 presents the empirical estimation of change in the baseload by empirically incorporating the applied lateral load level. A decreasing trend of the base resistance is observed with increasing lateral load level up to 80% of the H_f beyond which a constant magnitude is observed. The basis of the empirical formula is presented in Figure 4.29.

$$Q_b^{ult} = Q_b^{std} \times \begin{cases} 1 - 3.5\left(\frac{H}{H_f}\right)^{1.7} + 3.4\left(\frac{H}{H_f}\right)^{3.4} & \in \frac{H}{H_f} < 0.8 \\ 0.5 & \in \frac{H}{H_f} \geq 0.8 \end{cases} \quad (4.59)$$

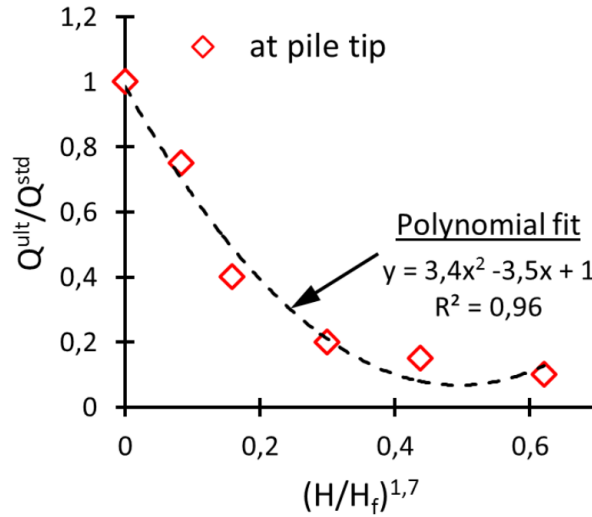


Figure 4.29: Empirical formulation of the changing pile base resistance obtained from the LME model analysis

The elastoplastic formulation presents the lateral displacement as a sum of elastic and plastic displacements. Equation 4.20 defines the elastic displacement and Equation 4.21 defines the total displacement following a parabolic hardening formulation.

$$u_z^e = \frac{Q_b}{K_{u_z}^e} \quad (4.60)$$

$$u_z = u_z^{ult} \times \left(\frac{Q_b}{Q_b^{ult}} \right)^{1.8} \quad (4.61)$$

The macro-element definition for the pile base resistance element is presented as follows. The load function is defined as per Equation 4.62.

$$f_{Q_b u_z} = f(Q_b, \alpha) = -\text{sign}(Q_L) \times Q_b - (Q_b^e + f(\alpha)) = 0 \quad (4.62)$$

Here Q_b^e is the yield limit for the elastic soil reaction. Q_L presents the gap element. The gap element is assigned a minimal magnitude (1 N), resulting in a negligible effect in the element performance. The function of the gap element is the same as presented for the lateral soil reaction element.

The gap element $Q_L = -1$ is used to define the compressive vertical load and $+1$ for tensile load where base resistance will be zero. The function $f(\alpha)$ in Equation 4.22 represents hardening during plastic displacement. The p-y response is formulated as parabolic beginning from the zero displacements. Thus, the elastic soil reaction limit is, therefore, not defined explicitly. The hardening variable is defined in Equation 4.63.

$$f(\alpha^*) = (Q_b^e + f(\alpha)) = u_z^{ult} \times \left(\frac{Q_b}{Q_b^{ult}} \right)^{1.6} \quad (4.63)$$

The return mapping algorithm for the base resistance element is presented as follows. The soil reaction at n^{th} step for k^{th} iteration is p_n^k . Concerning the procedure mentioned in the return mapping algorithm, the plastic multiplier ($\Delta\lambda$) is evaluated.

$$\delta(\Delta\lambda)^k = \frac{f((Q_b)_n^k, \alpha_n^{*k})}{K_e \times \left(\frac{\partial f}{\partial p}((Q_b)_n^k, \alpha_n^{*k}) \right)^2 - \frac{\partial f}{\partial \alpha^*}((Q_b)_n^k, \alpha_n^{*k}) \times \left| \frac{\partial f}{\partial p}((Q_b)_n^k, \alpha_n^{*k}) \right|} \quad (4.64)$$

$$f((Q_b)_n^k, \alpha_n^{*k}) = -sign(p_L) \times (Q_b)_n^k - \alpha_n^{*k} \quad (4.65)$$

$$\frac{\partial f}{\partial Q_b}((Q_b)_n^k, \alpha_n^{*k}) = -sign(p_L) \quad (4.66)$$

$$\frac{\partial f}{\partial \alpha^*}((Q_b)_n^k, \alpha_n^{*k}) = \frac{Q_b^{ult}}{(y_u)^{1/1.6}} \times \frac{1}{1.6} \times \left((y_p)_n^k + \frac{(Q_b)_n^k}{K_e} \right)^{0.6} \quad (4.67)$$

$$\begin{aligned} (Q_b)_n^{k+1} &= (Q_b)_n^k - \delta(\Delta\lambda)^k \times K_e \times \frac{\partial f}{\partial Q_b}((Q_b)_n^k, \alpha_n^{*k}) \\ \alpha_n^{*k+1} &= \alpha_n^{*k} + \delta(\Delta\lambda)^k \left| \frac{\partial f}{\partial Q_b}((Q_b)_n^k, \alpha_n^{*k}) \right| \\ (u_z^p)_n^{k+1} &= (u_z^p)_n^k + \delta(\Delta\lambda)^k \times \frac{\partial f}{\partial Q_b}((Q_b)_n^k, \alpha_n^{*k}) \end{aligned} \quad (4.68)$$

Other than the above presented pile-soil interaction elements, two additional simple linear elastic, perfect plastic elements are defined to account for the shear and moment resistance at pile base. The base shear and base moment elements are just add-ons to more clearly define the rigid pile behaviour [24].

4.7.5 Base shear element

The shear resistance significantly defines the rigid pile behaviour in lateral loading conditions at the base of the pile. Therefore, a base shear element has been introduced to represent this

behaviour following the description given by Leblanc et al. [60]. The pile toe is assumed to shear at the constant volume friction angle ϕ_{cv} . The shear resistance at the bottom of the pile is governed by the effective vertical force arising from the overburden sand. The evolution of this element is assumed to be elastic perfectly plastic.

The linear elastic stiffness of the base shear element is formulated in Equation 4.69 using the secant shear modulus.

$$K_{bs}^e = G_{sec} \times \frac{\pi}{3.7} \times D \quad (4.69)$$

The ultimate base shear resistance is presented in Equation 4.70 using the effective vertical stress at the pile base and $2/3^{rd}$ of the applied vertical load level (V), following the guidelines reported by Leblanc et al. [60].

$$Q_{bs}^{ult} = \left(\frac{2}{3}V + \frac{\pi}{4}D^2(q + \gamma' L_e) \right) \tan \phi_{cv} \quad (4.70)$$

The return mapping formulation of the base shear element as linear elastic, perfect plastic behaviour is presented as follows. The load function is defined in Equation 4.71.

$$f_{Q_{bs}} = |Q_{bs}| - Q_{bs}^{ult} = 0 \quad (4.71)$$

The plastic multiplier is defined as the ratio of the load function and the elastic stiffness.

$$\Delta\lambda = \frac{f_{Q_{bs}}}{K_{bs}^e} \quad (4.72)$$

The base shear element is linearly elastic and therefore, one iteration is sufficient at each time step to evaluate the base shear force and the shear displacement.

$$\begin{aligned} (Q_{bs})_{n+1} &= (Q_{bs})_n - \Delta\lambda \times K_{bs}^e \times \text{sign}(Q_{bs}) \\ (u_z^p)_{n+1} &= (u_z^p)_n + \Delta\lambda \times \text{sign}(Q_{bs}) \end{aligned} \quad (4.73)$$

4.7.6 Base moment element

Similar to the base shear element definition, the base moment element is defined as following a linear elastic, perfect plastic evolution. The stiffness of the base moment element (K_b^e) is taken from the definition presented in DNV, 2017 guidelines.

$$K_b^e = \frac{G_{sec} D^3}{3(1 - \nu)} \quad (4.74)$$

The base moment capacity is presented in Equation 4.75. Notably, it does not account for the effective vertical stress at the pile base. However, the relation is used as such for the element definition.

$$m_b^{ult} = K_{bm}^e \times \theta_{L_e}^{std} \quad (4.75)$$

The return mapping formulation of the base moment element behaviour is presented as follows. The load function is defined in Equation 4.76.

$$f_{m_b} = |m_b| - m_b^{ult} = 0 \quad (4.76)$$

The plastic multiplier is defined as the ratio of the load function and the elastic stiffness.

$$\Delta\lambda = \frac{f_{m_b}}{K_{bm}^e} \quad (4.77)$$

The linear elastic base moment element requires only one iteration at each time step to evaluate the base moment and the base rotation.

$$\begin{aligned} (m_b)_{n+1} &= (m_b)_n - \Delta\lambda \times K_{bm}^e \times \text{sign}(m_b) \\ (\theta^p)_{n+1} &= (\theta^p)_n + \Delta\lambda \times \text{sign}(m_b) \end{aligned} \quad (4.78)$$

4.7.7 Drag element

One more complementary element for lateral soil reaction is defined to account for the side friction as a separate element in cyclic loading conditions. The element definition follows the same guidelines as presented in section 3.6.2 in the previous chapter.

For modelling pile-soil interface friction, the similar drag element, as assumed by Taciroglu et al. [98] is implemented. The drag element models the frictional forces along with the pile-soil interface. It comprises of a parameter, p_d^{ult} (ultimate drag resistance) and the elastic stiffness of the element K_d^e which represents the frictional stiffness determining shear displacements between the pile surface and surrounding soil under the action of lateral loading. The linear elastic, perfect plastic formulation is presented.

The elastic stiffness (K_d^e) is assumed equal to the secant shear modulus considered linearly increasing with depth.

$$K_d^e = G_{sec} \frac{\sigma'_v(z)}{\sigma'_v(L_e)} \quad (4.79)$$

The definition of the lateral soil reaction element is partly used to define the drag capacity. The second component of the Equation 4.15 represents the frictional drag. Consequently, the standard ultimate drag resistance is presented in Equation 4.80.

$$p_d^{ult(std)} = 2K_o\sigma'_v \tan\phi D \left(1 - \frac{z}{L_e} \frac{V}{V_f}\right) \quad (4.80)$$

Similar to the lateral soil reaction element definition, the effect of the increasing vertical load is empirically incorporated to represent the ultimate drag resistance as per Equation 4.81.

$$p_d^{ult} = p_d^{ult(std)} \times \left[1 - 0.75 \left(\frac{V}{V_f}\right)^3\right] \quad (4.81)$$

The return mapping formulation of the drag element behaviour is presented as follows. The load function is defined in Equation 4.82.

$$f_d = |p_d| - p_d^{ult} = 0 \quad (4.82)$$

The plastic multiplier is defined as the ratio of the load function and the elastic stiffness.

$$\Delta\lambda = \frac{f_d}{K_d^e} \quad (4.83)$$

The linear elastic base moment element requires only one iteration at each time step to evaluate the drag resistance and plastic displacement.

$$\begin{aligned} (p_d)_{n+1} &= (p_d)_n - \Delta\lambda \times K_d^e \times \text{sign}(p_d) \\ (y_d^p)_{n+1} &= (y_d^p)_n + \Delta\lambda \times \text{sign}(p_d) \end{aligned} \quad (4.84)$$

All the LME model numerical computations have been performed in the Matlab toolbox ALT4S; a package for nonlinear soil-pile-structure interaction analysis (Grange, 2018).

4.8 Results

The PLAXIS and LME model outcomes are compared for quantitative and qualitative comparison. The results for both monotonic and cyclic loading cases are presented as follows.

4.8.1 Monotonic

Figure 4.30 presents the isolines of normalised pile head displacement, determined as per Equation 4.85 for 10 cases analysed in PLAXIS and evaluated from the LME assembly. A good qualitative agreement is visible for both outcomes. The LME model presents underestimations for lower displacement levels, especially for the high vertical load cases.

$$u_{norm} = \sqrt{\left(\frac{u_x}{u_x^{max}}\right)^2 + \left(\frac{u_z}{u_z^{max}}\right)^2} \quad (4.85)$$

Here, u_x and u_z are the pile head lateral and vertical displacements, respectively. The maximum lateral and vertical displacements are 10% of pile diameter. The deformation contours plot aid to define a failure state in the friction material. Notably, the maximum lateral displacement at the pile head is obtained equal to 9mm (11.3% of pile diameter) for $H = H_f$ load case in the local macro-element model simulation. Thus, the normalised lateral displacement from the LME model is presented concerning the estimated LME model maximum pile head displacement.

4.8.2 Cyclic

The PLAXIS model is examined for one-way cyclic loading^c with a constant vertical load of 3.8 kN. The lateral point load at the eccentricity is applied as a constant amplitude sine wave

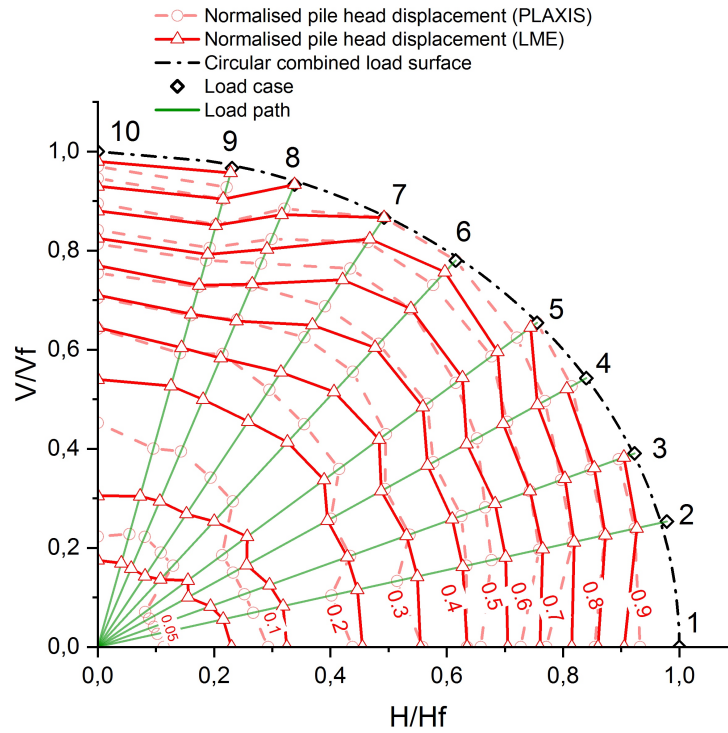


Figure 4.30: Normalised pile head displacement contours evaluated from the 10 combined loading cases on a circular failure surface

of amplitude 2.55 kN. These load magnitudes are representative of the ULS load deduced from the similitude analysis (see Table 4.2). A similar analysis can be performed for the SLS loading case by deducing the relevant similitude relations. However, in the present study, only the ULS load case is analysed for cyclic loading case in PLAXIS model, to make a correlation with the equivalent monotonic load case. Also, the ULS load magnitudes are higher than the SLS load case, resulting in the model response investigation at a larger limit.

All the elements presented in the section 4.7 are formulated with respect to the load magnitudes in the circular failure surface. However, the model response can be estimated for any load combination within the circular load surface. Consider a load case with vertical input load (V') and lateral load (H') inside the circular failure surface, as demonstrated in Figure 4.31. The normalised vertical load (and by extension the lateral load) parameter in the mathematical expressions of the definition of the elements is evaluated using Equation 4.86 for such load cases. The formulation of Equation 4.86 considers the radial load path from origin to the failure surface where the present load combination resides.

$$\left(\frac{V}{V_f}\right) = \sqrt{\frac{(V'/V_f)^2}{(H'/H_f)^2 + (V'/V_f)^2}} \quad (4.86)$$

The conventional hardening soil model is not suitable for cyclic loading cases in FE analysis. The hardening soil model with small-strain stiffness is ideal for such an analysis.

^c Two-way cyclic loading analysis presented a cyclic hardening [15] feature which is a characteristic of a strain-controlled behaviour. Sheil and McCabe [93] pointed out that the hardening soil model leads to the non-conservative predictions for the conditions other than one-way loading and therefore not suitable for the two-way loading conditions. Hence, the two-ways cyclic loading results are not included in the model response investigation.

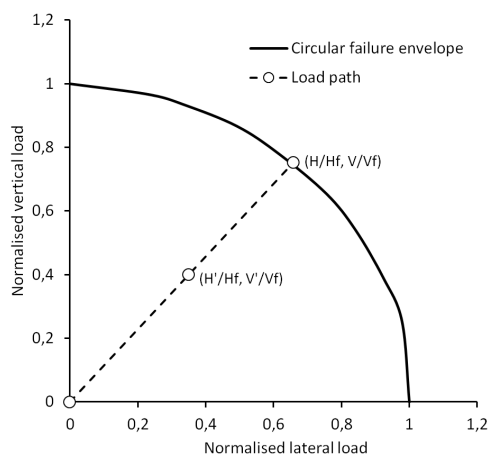


Figure 4.31: Demonstration of the consideration of a load combination within the failure circular load surface for input parameter determination for the element definition

Therefore, the additional parameters, G_o and $\gamma_{0.7}$, characteristics of the HS small model, are added to present the cyclic loading response. In the absence of the requisite database to define $\gamma_{0.7}$, multiple magnitudes are analysed until the response at large strain levels is equivalent to the one presented by the standard hardening soil model. Figure 4.32 presents the PLAXIS model triaxial test outcomes comparing the hardening soil small strain stiffness (HS small) models response with the standard model.

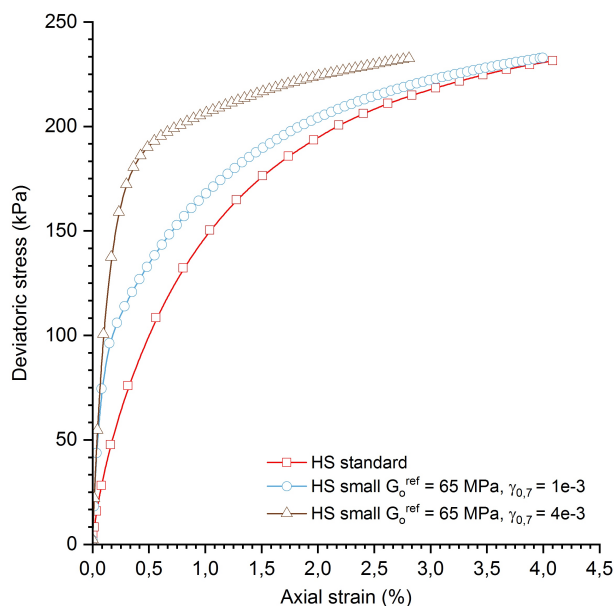


Figure 4.32: Model triaxial test outcomes for Hardening soil model with different small strain stiffness parameters

As a result, the HS Small model with $\gamma_{0.7} = 1e^{-3}$ is selected to represent the cyclic loading response of the model soil. The small strain stiffness feature of HS small model captures the model response with a higher stiffness for very small strain levels. Also, in the cyclic local macro-element model, the lateral soil reaction element is divided to present the earth pressure change and side friction change separately. It is because, upon unloading phase in the cyclic loading application, the passive earth pressure shall reduce to zero, keeping the side friction

resistance intact.

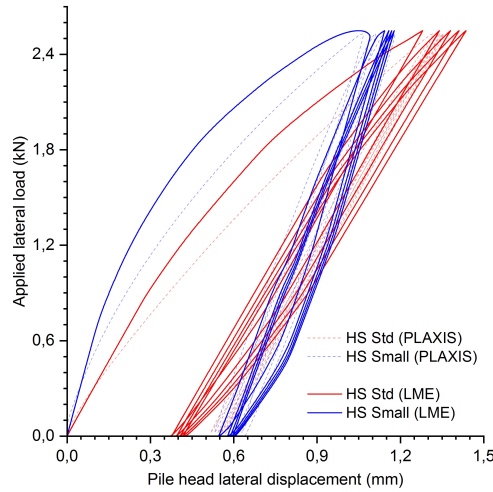


Figure 4.33: Comparative PLAXIS and LME Pile head displacement plot for OW cyclic loading application

Figure 4.33 presents the comparative pile head displacement plot for 5 cycles of the OW loading. The stiffness degradation, as a function of the number of cycles, is presented by the PLAXIS model analysis. This is a characteristic of the long term performance of the offshore wind turbine foundations. The phenomenon is called ratcheting [15]. The local macro-element model also incorporates this behaviour by degrading the initial stiffness of the lateral soil reaction element as a function of the number of cycles, as presented in Equation 4.87. Here, ‘ n_c ’ is the number of cycles, and ‘ a ’ is a dimensionless constant, taken equal to 0.1 in the present study. Leblanc et al. [60] reported that the accumulated rotations at pile head for the increasing number of load cycles present a good fit as a function of $\log_e n_c$ for a small number of cycles ($n_c < 100$). The extrapolation to a greater number of cycles ($n_c > 500$), presents an underestimation of the accumulated rotations. An exponential fit is observed to be more reliable in this large number of cycles range. Nevertheless, in the present study, the local level element behaviour controls the response of the overall assembly. The stiffness degradation with the number of cycles is assumed following a logarithmic evolution as the study is presented for a small number of load cycles.

$$(K_e)_{n_c^{th}} = (K_e)_{(n_c-1)^{th}} - a \times (K_e)_{initial} \times \log_e n_c \quad (4.87)$$

The stiffness change over the number of cycles is taken as independent of the relative density of the soil [60]. Consequently, Equation 4.87 is used to define ratcheting for all the model cases presented from this point onward. Indirectly, the ratcheting phenomenon represents the kinematic hardening feature of the LME model.

The ULS load case is further analysed at all local depth levels to make a comparative analysis of the lateral soil reaction. Figure 4.34 presents the HS standard and HS small soil models outcomes in PLAXIS compared to the LME models. The LME model element initial elastic stiffness is multiplied by a factor 1.5 to account for the stiffer initial response to the counterpart HS small model outcomes. A good quantitative and qualitative agreement is observed between the two model outcomes. The PLAXIS cyclic load case simulation takes around

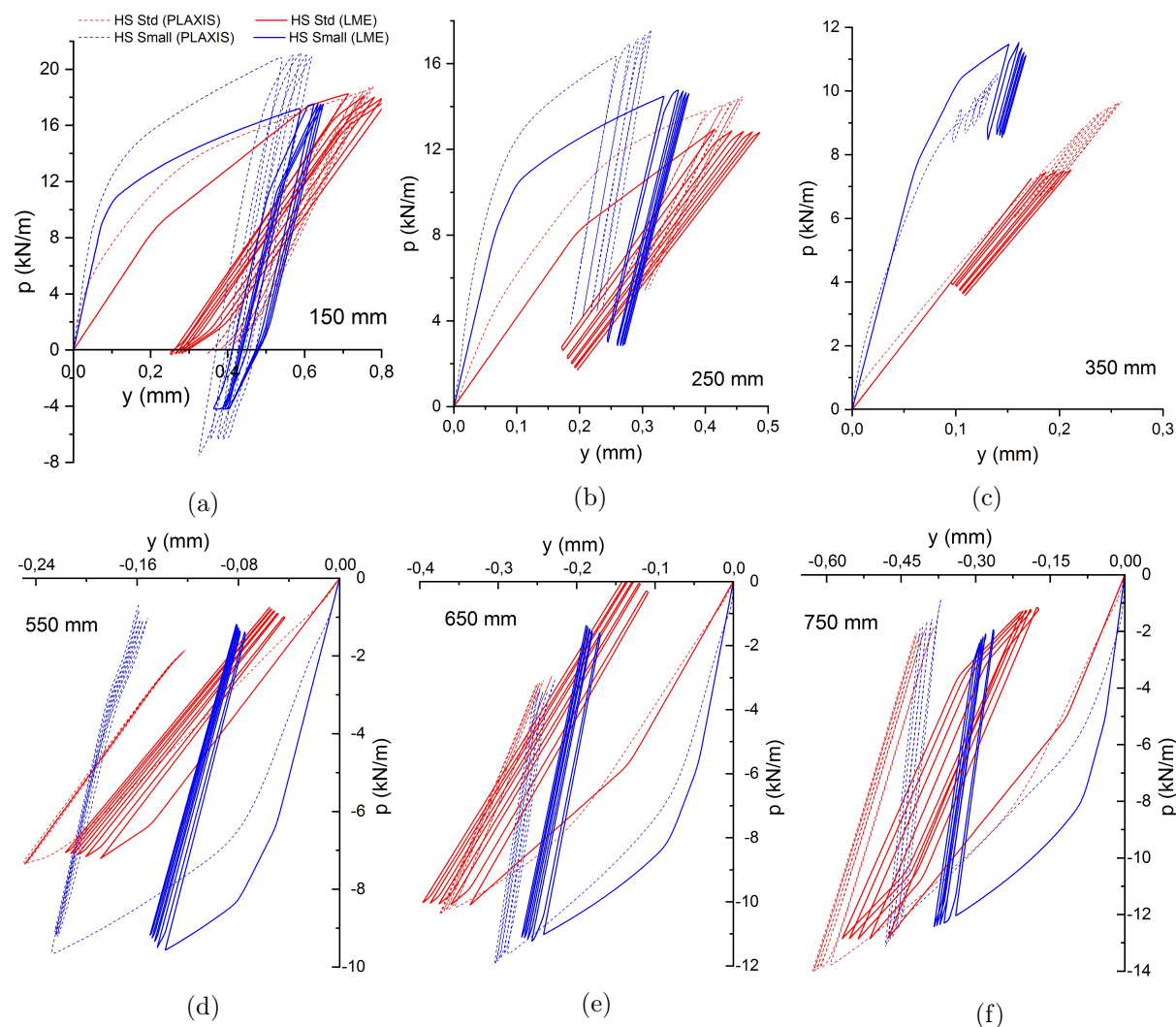


Figure 4.34: FEM analysis and mathematical formulations comparison of lateral soil reaction evolution at all local depth levels for 5 cycles of OW loading

2 hours of computational time. The LME model, on the other hand, presents a similar requisite response in less than 5 minutes.

Similar to the lateral soil reaction element, the distributed moment-rotation response is compared between PLAXIS and LME model results. The LME model presents a very stiff rotational response; however, the order of moment magnitudes is comparable. It is due to the clear moment-rotation response definition for the local macro-element model. Qualitatively, the order of magnitude of pile rotation is similar at all depth ranges, which infers the rigid pile rotation behaviour. The moment rotation response of LME for the higher load magnitudes is expected to be of the same order as the 3D FE model.

The correlation between PLAXIS and LME models for all monotonic loading cases and one cyclic loading case is extended to cyclic loading cases at all loading ranges. As presented in the section 2.4, the backbone curve governs the unloading and reloading behaviour of pile-soil interaction elements and by extension of the model assembly. This feature is demonstrated for the LME model by making multiple load cases computations for different ranges of the cyclic loading. The cyclic profile parameters ζ_b and ζ_c , reported by Leblanc et al. [60] are used to

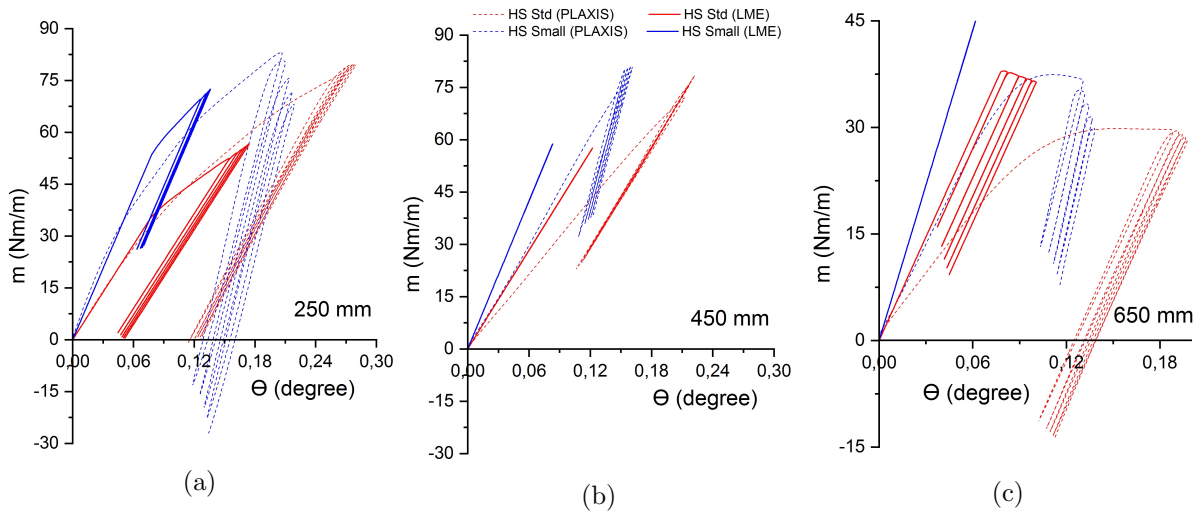


Figure 4.35: FEM analysis and mathematical formulations comparison of distributed moment evolution at some local depth levels for 5 cycles of OW loading

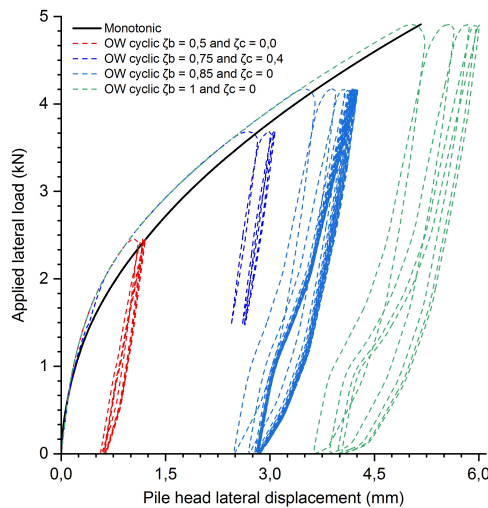


Figure 4.36: Demonstration of the backbone curve feature from the LME model simulations under OW cyclic loading inputs with different amplitudes

define the amplitude of the cyclic loading. Figure 4.36 presents the backbone curve feature of the LME model for the loading magnitudes of case 5 in the failure loading surface. All cyclic load simulations are presented with HS small soil model equivalence. Therefore, a stiffer response is visible for all cyclic load simulations in comparison to the monotonic backbone curve, which is modelled using the stiffness parameters equivalent to the HS standard soil model.

Further, the significance of each model element is presented in Figure 4.37 for rigid pile overall response for one-way cyclic loading using case 4 loading parameters. The typically used lateral soil reaction (p-y) element only provides an overestimation of lateral pile head displacement. The involvement of other components provides a stiffer response. The model pile does not present a significant change in the pile head displacement upon addition of distributed moment and base moment resistance parameters. It is because the model pile diameter is minimal, making a smaller distributed moment estimations (proportional to the second-order of the pile diameter). The feature, however, presents a significantly well contribution for prototype

scale model presented in the next chapter.

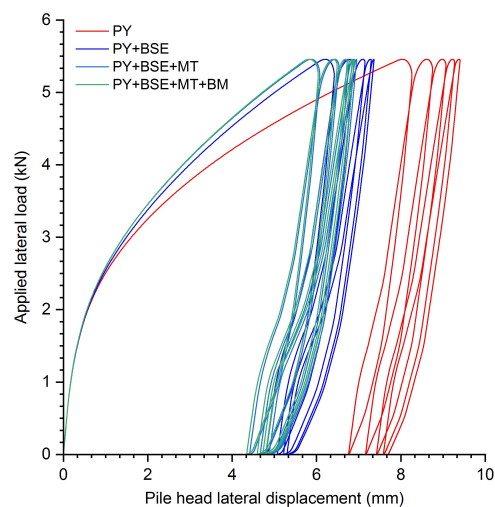


Figure 4.37: Demonstration of each element contribution for the rigid pile behavior case 4 pile head displacements

The characteristics of the hardening soil model for the OW cyclic load case is further explored by observing the stress path evolution at stress points located at 250, 450 and 650 mm depths. Figure 4.38 presents the stress paths along with the normal consolidation (NC), critical state and Mohr-Coulomb (MC) failure paths. The cyclic response resides within the contracting domain under the application of the presented cyclic load magnitudes.

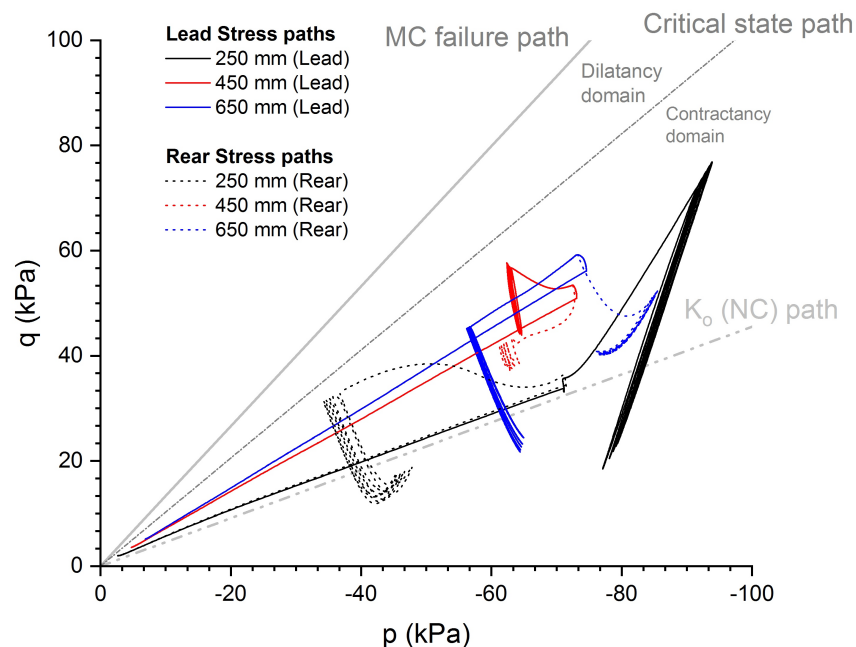
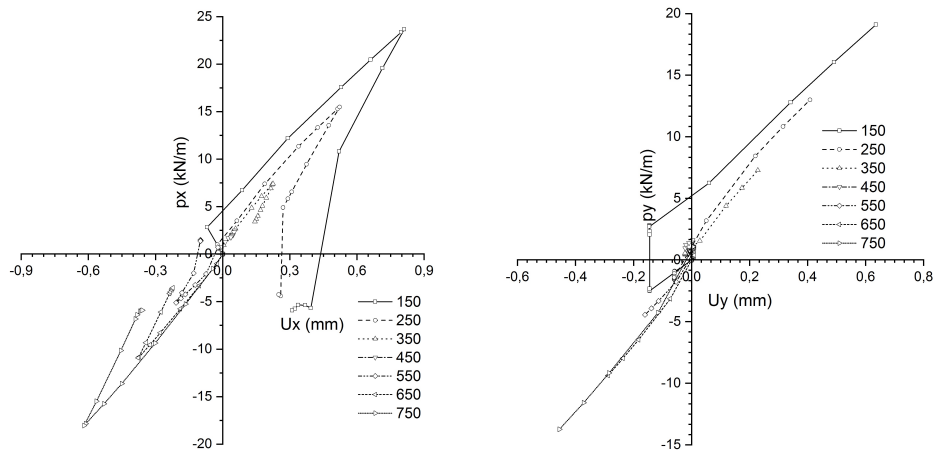


Figure 4.38: Stress path evolution under the application of OW cyclic loading

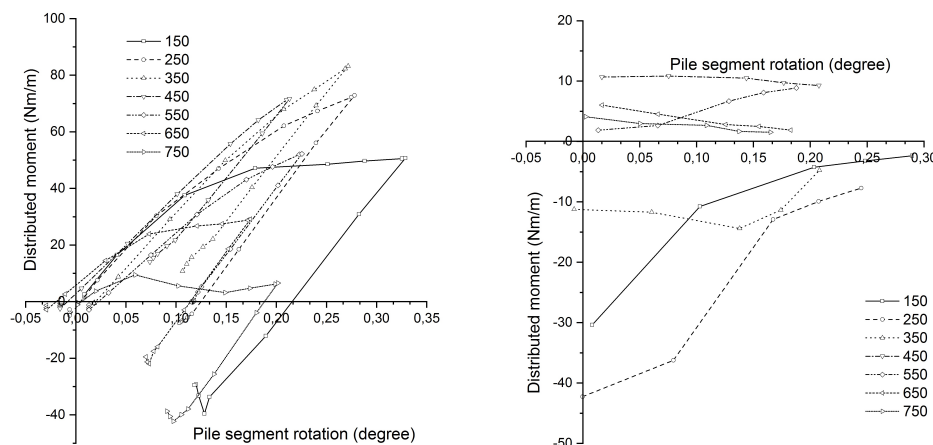
4.8.3 Multi-directional loading

The OWT structure experiences environmental load in many directions which are mechanically incorporated by changing the orientation of the wind turbine through rotor nacelle connections.

This imposes the lateral load in the supporting foundation in multi-directions. Nanda et al. [71] and Nikitas et al. [73] have highlighted the significance of the multi-directional loading by studying the lab-scale models with new lateral load application devices capable of applying load in multi-directions. Nanda et al. [71] reported that Multi-directional cyclic loading generally results in higher displacements and increased stiffness compared to uni-directional loading. This is due to the shear deformation of a larger volume of soil mass adjacent to the pile.



(a) Soil reaction evolution with loading in first direction (b) Soil reaction evolution with loading in second direction



(c) Soil reaction evolution with loading in first direction (d) Soil reaction evolution with loading in second direction

Figure 4.39: Response analysis of the stress points under multi-directional loading application

The effect of multi-directional lateral loading is examined only for the monotonic loading case. Therefore, the multi-directional simulations represent the qualitative analysis only. It involves the application of lateral point load till 2.55 kN in one direction followed by unloading it back to zero and then application of the same loading magnitude from a direction 90 degrees to the older one but in the same XY plane.

Using the equation defined for the $p-y$ and $m - \theta$ estimation, Figure 4.39 presents the results obtained. The lateral soil reaction for the y -direction shows a similar response as for the x -direction when the pile movement is in the respective directions. The displacement magnitudes and the soil reaction magnitudes, however, are lower than the first loading in the x -direction. This presents evidence of the influence of the loading history on the lateral soil

reaction response.

Figures 4.39a and 4.39b presents a similar qualitative response; the stiffness is however increased. This feature is generalised in the LME model by increasing the initial stiffness of the pile-soil interaction elements in the second direction by 25% of that in the first direction of loading as a simplification.

The $m - \theta$ response in the y-direction, the stress points below the point of rotation show almost no evolution of the distributed moment while the pile is rotating to almost a similar magnitude. Notably, the data points in Figure 4.39d are plotted only for the movement in the y-direction to avoid many data points appearing on the zero rotation point during the movement in the x-direction. Besides, for the depths above the point of rotation, the distributed moments decrease with increasing pile segment rotation, suggesting the effect of changed shear stress distribution profile from the first segment load (x-direction).

4.8.4 Modelling of the pile installation

Besides, an attempt to replicate the scenario of the driven pile in calibration chamber inspired from the work of Dijkstra et al. [34] is presented. After replacing the soil volume elements with the pile elements between membrane loading phase (Figure 4.3b) and vertical loading phase (Figure 4.3c), a volumetric strain (46%) is imposed on the model pile material. The total magnitude of the volumetric strain comprises 0.1 L_e (10%) vertical strain (*i.e.* pile elongation with restricted vertically upward movement) and lateral strain (18%) each for x and y directions, equivalent to the pile wall thickness (t). The deformed mesh, vertical and lateral stress contour plots of the expanded pile are presented in Figure 4.40.

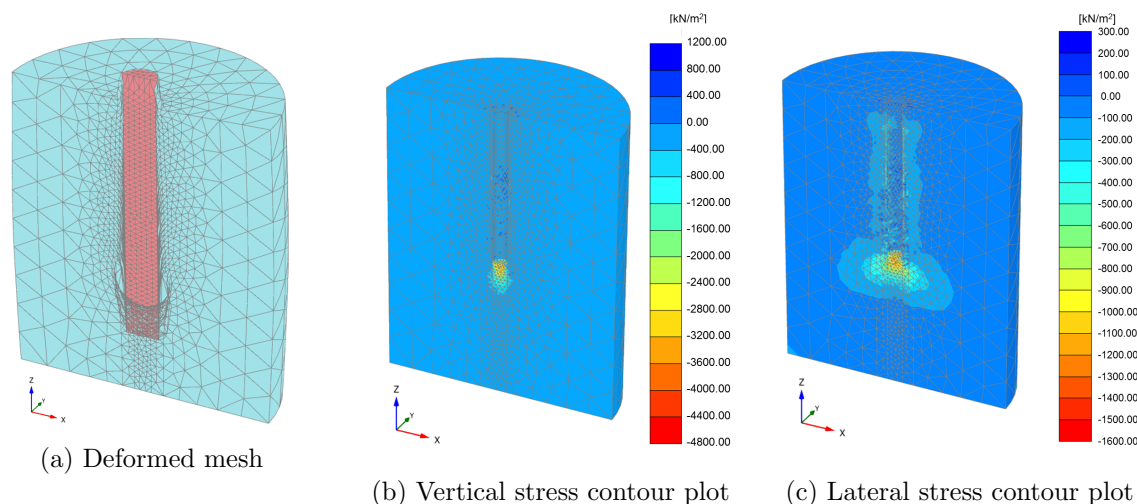


Figure 4.40: Representation of the pile installation effect in jacked pile case

A CPT test is carried out in the laboratory calibration chamber with a similar initial state of stress in the soil volume. ICP method [51] is applied to the CPT test outcomes to obtain a profile of pile base resistance and local radial effective stress. A comparative study between PLAXIS and ICP outcomes (see Figure 4.41) presents the quality and limitations of pile installation modelling in PLAXIS.

A stress point just below the model pile tip (0.82m depth) estimates the pile base

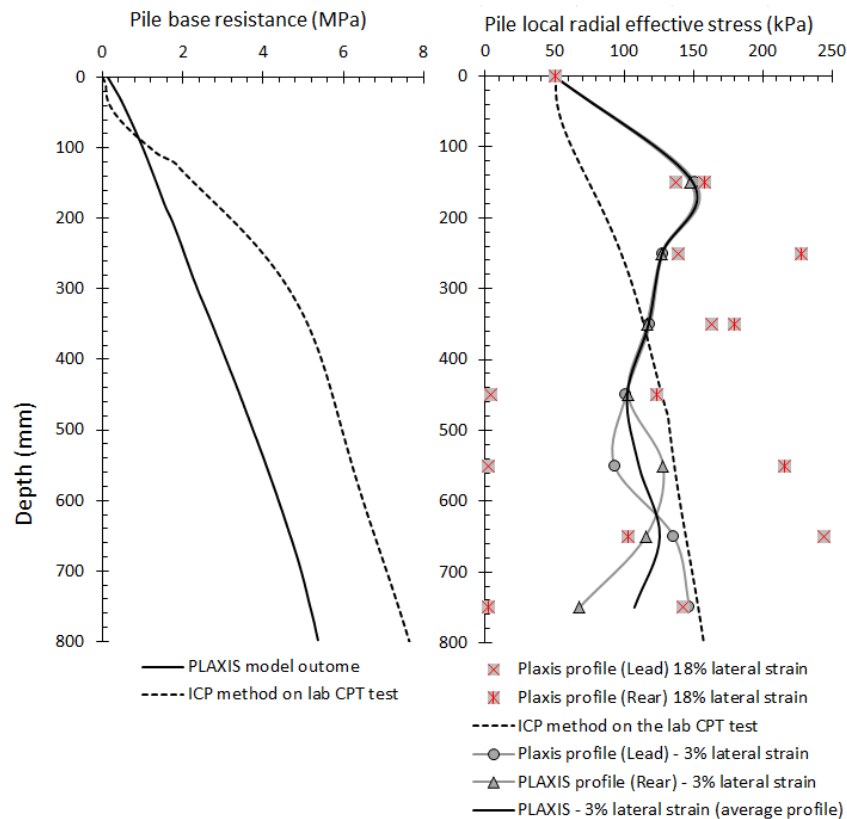


Figure 4.41: Comparison between PLAXIS and ICP method outcomes for pile installation

resistance with the evolution in the vertical expansion (see Figure 4.41, left). Both PLAXIS and ICP method outcomes present an increasing trend with depth with a constant offset between the two profiles. The observed tip resistance is about 5.5 MPa for model pile compared to the ICP method based estimation of 6.9 MPa.

Moreover, the contour plot of the radial stress in the soil (Figure 4.40c) shows an increase of 200-300 kPa along the pile shaft extending up to about one pile diameter from the pile-soil interface with highly uneven stress distribution profile. Similarly, a comparison of the local radial effective stress estimations from ICP and PLAXIS presents the model adequacy. Seven stress points along the pile embedment (at the plane of symmetry) record the evolution of lateral stress in the model pile during imposed expansion. Figure 4.41 (right) shows that the model pile overestimates the magnitude in comparison to the ICP method estimations. Subsequently, following the lateral strain evolution profile, 3% lateral strain agreed well with ICP estimations. Hence, the ICP method estimations aid in decision making of applied lateral strain levels to replicate the pile installation in PLAXIS.

Finally, after the volumetric strain levels application, the mesh deformation is restored to zero while keeping the stresses generated during expansion. Afterwards, the actual pile properties to the pile elements in the 3D FE mesh are assigned. It results in a significant drop in the tip stress to maintain the equilibrium. The vertical and lateral load application is similar to the bored pile situation. Notably, the present work does not include the simulation results for the jacked pile case.

Extendedly, a study with due consideration to the installation effect of a driven pile for

better correlation with field conditions presents the significance and limitations in the present work for installation application.

4.9 Conclusions

A methodology to plan, design and analyse the calibration chamber experimentation on the model monopile is presented. The PLAXIS 3D model of the calibration chamber setup is studied under combined loading conditions. The influence of the vertical load on lateral soil reaction and distributed moments is the basis to represent the coupled interaction. The model soil response is investigated at some stress points, analogues to the experimental soil-stress-transducers.

The model pile presents semi-rigid behaviour as per the stiffness ratio estimation. The consistent pile segment rotation at all depth levels verifies the semi-rigid behaviour. The point of pile rotation is estimated around 2/3rd of pile embedment depth from dummy beam, and structural volume approaches. In experimental conditions, the local lateral displacement at different depths is not direct. The pile rotation magnitude and pivot point information enables an indirect estimation.

The mathematical formulations provide a basis for the local macro element (LME) model definition defined as the coupled interaction elements. Now, reusing similitude relationships to move from the lab-scale failure envelope to prototype scale model shall provide a new prototype macro-element model with coupled interaction capability. It is presented in the next chapter.

The vertical shear stress evolution has one limitation concerning the changes in vertical shear stress capability of the t-z element. Because we have only the constant vertical load and the lateral load application is not considered implicitly. Therefore, even though the cyclic lateral load will change the vertical shear stress, the t-z element will not participate as its stiffness response is exclusive to the applied vertical load level.

The distributed moment and pile shaft resistance elements are developed to follow three different evolution mechanisms over the depth of the pile embedment. Hong et al. [45] reported that the soil flow mechanism shifts from three zones for the semi-rigid pile to two zones for a rigid pile. The LME model component definition enables to implement this transition with ease, if necessary for a particular model case. The transition can be implemented by updating z/L_e ratio range in Equations 4.36 and 4.48.

In the present work, the PLAXIS 3D FE analysis is limited to a few stress points only. A more extensive analysis is likely to provide increased accuracy. However, the objective is to support the planning of the lab-scale experimental campaign in calibration chamber where soil stress transducers shall be installed in the soil volume to capture the pile-soil interaction. The choice of a limited stress points analysis in 3D model thus represents the equivalent lab-scale model analysis.

Chapter 5

Validation

5.1 Objectives

The key objective of the present chapter is to test and emphasise the coupled interaction phenomenon in rigid piles. The similitude framework is presented to extrapolate the lab-scale local macro-element model definition to the field-scale. Consequently, a comparison between the simple and newly developed macro-element models presents the coupled interaction phenomenon.

5.2 General description

In this chapter, the interaction components of the lab-scale local macro-element (LME) model are generalised to present the rigid pile behaviour at prototype scale. A set of similitude relationships is presented to correlate the lab-scale LME model results to the prototype scale. First, the local macro-element model definition is validated against the lab-scale model presented by Leblanc et al. [60]. Afterwards, the local macro-element model is presented at the prototype scale with a pile aspect ratio (L_e/D) of 3. The significance of the coupled interaction is highlighted by making a comparison with the simplified macro-element model presented in chapter 3. The LME model definition is further extended for two more cases with a pile aspect ratio of 4.5 and 6 as a general validation of the local macro-element model. Lastly, the guidelines for the LME model calibration and utilisation are presented.

5.3 Validation 1: LeBlanc [2010] lab-scale model

Leblanc et al. [60] performed a 1g lab-scale model (refer to Figure 2.6 for model setup and pile dimensions information) tests for model monopile in the sand under lateral and moment loading application with a zero vertical load. The geometrical parameters and the soil and pile properties are presented in the Table 5.1 below. The lab-scale model, with 38% of relative density, is selected for the validation. Notably, the dilation angle ($\psi = \phi' - \phi'_{cr}$) is higher for the lab-scale model than in the field scale models described in the following sections. It is because the mean stress level in the model pile is lower than in the field scale pile resulting in higher volumetric deformations.

Table 5.1: Pile and soil parameters for the LME model definition with Leblanc et al. [60] lab scale model features

Copper pile parameters	Value	Leighton Buzzard sand parameters	Value
Outer diameter, D_o (mm)	80	Minimum unit weight, γ'_{min} (kN/m^3)	14.65
Wall thickness, t (mm)	2	Maximum unit weight, γ'_{max} (kN/m^3)	17.58
Embedment length, L_e (mm)	360	Relative density, I_D (%)	38
L_e/D	4.5	Unit weight, γ' (kN/m^3)	15.64
Load eccentricity, e (mm)	430	Internal friction angle, ϕ' (degree)	43
Young's modulus, E_{pile} (GPa)	120	Critical friction angle, ϕ'_{cr} (degree)	34.3

5.3.1 Similitude relations

The similitude relations are presented comparing the static lateral moment load limit (M_R) with the maximum lateral load limit estimated from the PLAXIS model of the pile in the calibration chamber setup. Equation 4.1 presented in the last chapter defines the non-dimensional groups (NDGs) reported by Leblanc et al. [60] for load magnitudes. Table 5.2 presents the similitude relations comparison between the LeBlanc lab-scale model and PLAXIS lab-scale model. A good agreement between the NDGs infers the applicability of the LME model definition on LeBlanc lab-scale model setup.

Table 5.2: Similitude relations for load and displacements between PLAXIS model and LeBlanc lab scale model

NDG	3D FEM model	LeBlanc model
	Leblanc et al. [60]	
\tilde{H}	0.901	1.036
\tilde{V}	2.080	2.158
\tilde{M}	5.634	5.569
	Byrne et al. [25]	
$\tilde{\theta}$	584.579	555.172
	Broms [20]	
\tilde{H}^*	0.432	0.430

The similitude relation for rotation presented by Leblanc et al. [60] does not account for the soil stiffness, and the NDG is overestimated by a factor of three. Consequently, a similar similitude relation is estimated following the NDG presented by Byrne et al. [25] defined in Equation 5.1.

$$\tilde{\theta} = \theta \frac{G_o}{\sigma'_{v(L_e)}} \quad (5.1)$$

Table 5.2 presents one additional similitude relation defined as per Equation 5.2 mod-

ified following the relationship reported in Broms [20] studies.

$$\tilde{H}^* = \frac{H(e + L_e)}{K_p D (q + \gamma L_e) L_e^2} \quad (5.2)$$

5.3.2 LME model parameters calibration

The local macro-element stiffness parameters related to the LeBlanc lab-scale model are calculated such that the static moment rotation evolution agrees with the corresponding relation reported by Leblanc et al. [60], presented in Figure 5.1. The additional parameters for LeBlanc's lab-scale model definition is presented in the Table 5.3.

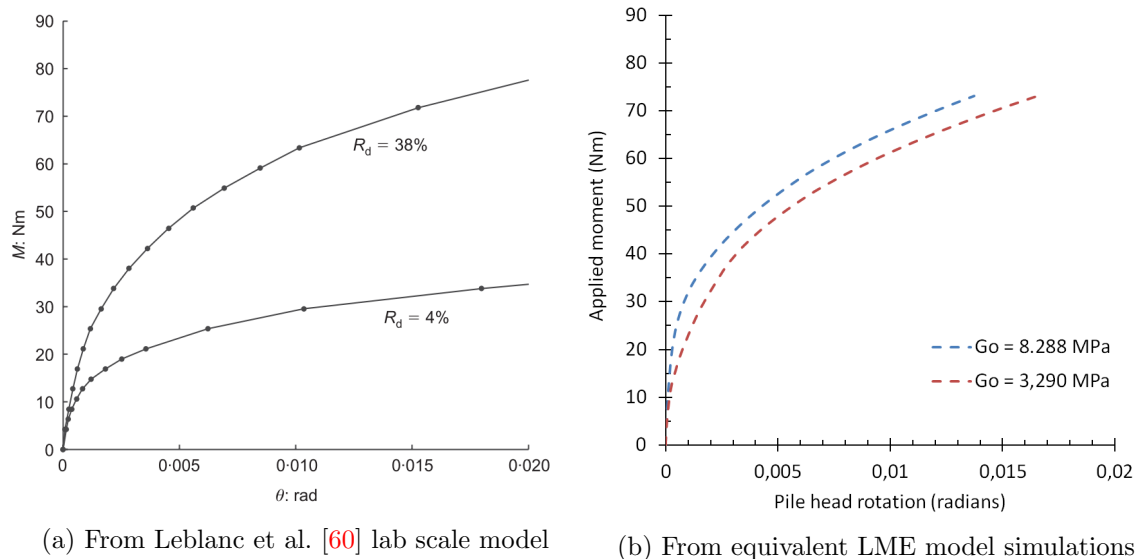


Figure 5.1: The pile head moment-rotation evolution plots

The small strain shear modulus obtained from model calibration ($G_o = 3.290 MPa$) is compared for accuracy using the empirical relationships presented by the previous researchers. The formulation presented by Schnaid and Houlsby [90] estimates $G_o = 8.288 MPa$ empirically with mean stress (p') and relative density (R_d) as input parameters. Figure 5.1b presents the moment rotation relationship obtained from the LME model simulation. The LME calibrated stiffness modulus is 2.5 times lower than the estimation by empirical formulations. The conservative stiffness modulus is, however, assigned for the LME model definition to felicitate the direct comparison and validation.

The maximum pile head rotation is in correlation with LeBlanc's lab-scale model. The lateral pile head deflection is subsequently determined from the rotation assuming the rigid pile rotation about a pivot point. The maximum vertical head displacement is calibrated by application of vertical load to its capacity at pile head and subsequently estimating the settlement from the LME model results. The layer thickness is chosen to have a sufficient number of macro-elements along the pile length to represent the pile-soil interaction response.

Table 5.3: LME model parameters estimated for equivalent LeBlanc lab scale model

Parameter	Value
Small strain shear modulus, G_o (MPa)	3.290
Secent shear modulus, G_{sec} (MPa)	0.453
Lateral load capacity, H_f (N)	168
Vertical load capacity, V_f (N)	350
Moment load capacity, M_f (Nm)	72.24
Layer thickness for LME, L_r (m)	0.045
Maximum head rotation, θ_{head}^{max} (degree)	0.95
Maximum lateral head deflection, $u_{x(head)}^{max}$ (mm)	4
Maximum vertical head deflection, $u_{z(head)}^{max}$ (mm)	4

5.3.3 Results

The local macro-element model assembly with the element definition presented in the last chapter (see section 4.7) is tested for both monotonic and cyclic loading conditions. Different load combinations (within the limits of the circular failure load surface) are simulated to present model features and evidence of coupled interaction. Notably, the results reported by Leblanc et al. [60] characterise the pile-soil system response for a very large number of cycles at the pile head only. Therefore, a direct comparison of model results with the LME model is not presented. The quantitative and qualitative similarity between LeBlanc model and LME model presented via static moment-rotation relation at the pile head (see Figure 5.1) is considered as a reference for the confidence in the LME model results.

Figure 5.2 presents contour (isolines) plot for the normalised pile head displacement assuming the circular failure loading envelop. The plot is developed using ten combined load cases on the failure envelope using similar guidelines as presented in the section 4.8.1. The contour plot infers the significance of the coupled axial and lateral pile-soil interaction. The response pattern also concludes that the application of a vertical load reduces the lateral capacity and vice versa.

The LME model response for one-way (OW) cyclic loading is presented to highlight the ratcheting phenomenon and coupled interaction. Four load cases with same lateral load input ($H = 100$ N) and different vertical load ($V = 0, 87.5, 175$ and 262.5 N) inputs are simulated in LME model assembly to demonstrate these features. Figure 5.3 presents the OW cyclic load response for all load cases after five cyclic of combined loading. All load cases are selected to reside within the failure load envelope (see Figure 5.3 left). The pile head displacement increases with increasing vertical load level while the lateral load level remains unchanged. The cyclic stiffness also reduces with increasing vertical load level as observed from the decreasing slope of the unloading/reloading loop.

Figure 5.4 presents the demonstration of the monotonic backbone envelop feature (see section 2.4) from the LME model simulations with different amplitude cyclic loading. The LME model is simulated for load case with $H = 128$ N and $V = 229$ N. The cyclic load levels are applied

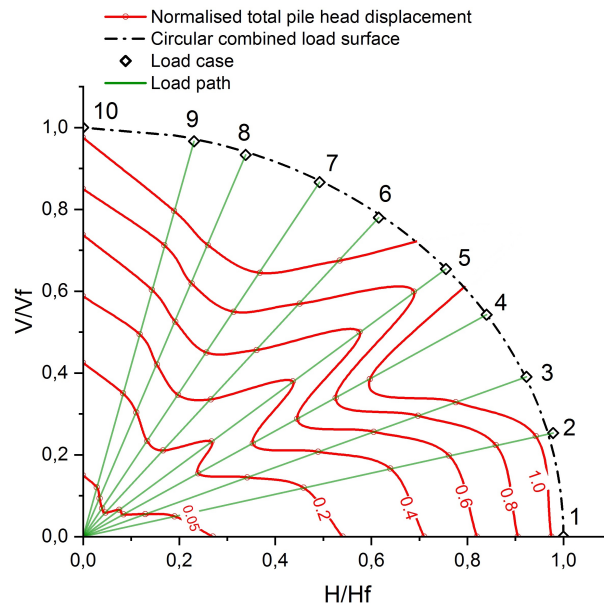


Figure 5.2: The contour plot for the normalised pile head displacement for LME model of LeBlanc lab scale model equivalent

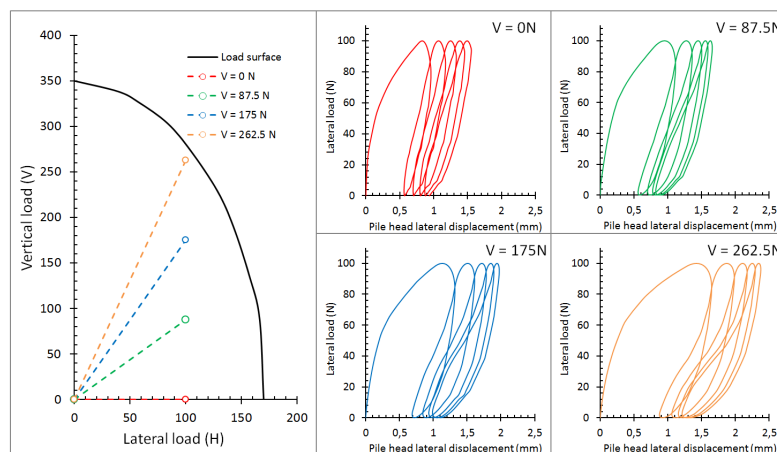


Figure 5.3: Pile head lateral displacement evolution for 5 cycles of one-way cyclic loading

using the cyclic characteristics parameters defined in Equation 2.1, described in section 2.1.2 in chapter 2. The magnitude of stiffness degradation with successive cycles increases with increasing lateral load level.

Next, the local level pile-soil interaction elements response is presented in Figure 5.5. A load case with $V = 190\text{N}$ and $H = 143\text{N}$ is simulated for OW cyclic loading condition with five cycles to demonstrate the local level evolution. Figure 5.5a presents the pile deformation profile as an outcome of the collective response of the macro-elements located at a different depth to define the local interaction behaviour. The lateral soil reaction element evolution is presented in Figure 5.5b only for the elements above the pivot point for better readability. The stiffness of the p-y element increases with depth, and the magnitude of stiffness degradation reduces with increasing depth level. The distributed moment-rotation plot presented in Figure 5.5c demonstrates the different mechanism for the element evolution at different depths. It represents the three zones of lateral pile-soil interaction for changing vertical shear stresses; a core feature

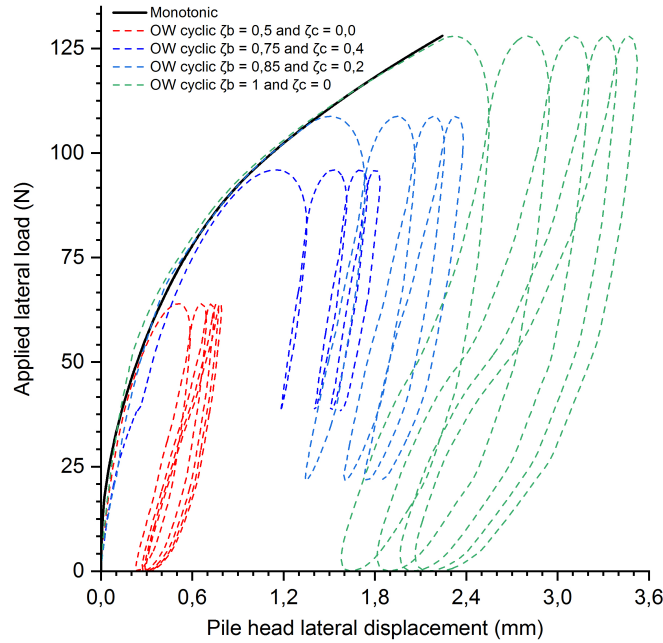


Figure 5.4: The demonstration of the backbone curve feature for different cyclic loading cases simulated using LME model

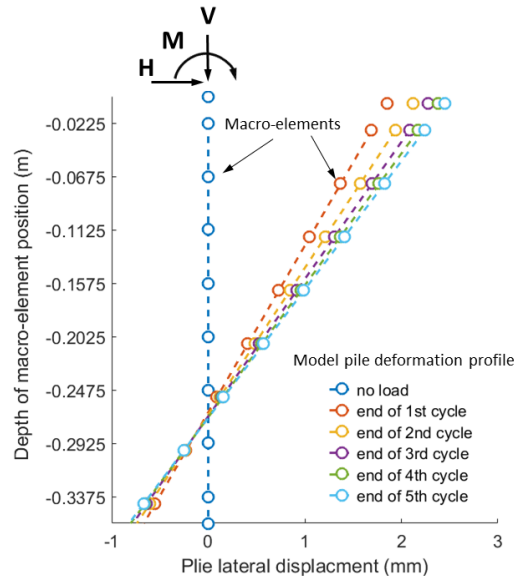
used in the element constitutive behaviour formulation.

The presented results feature the reliability of the new pile-soil interaction elements. The coupled interaction phenomenon is a necessity for rigid pile-soil interaction studies. The validation with an existing lab-scale experimental database provides the right amount of confidence in the LME model definition. It thus is viable to proceed to the model cases representing the prototype scale pile-soil system.

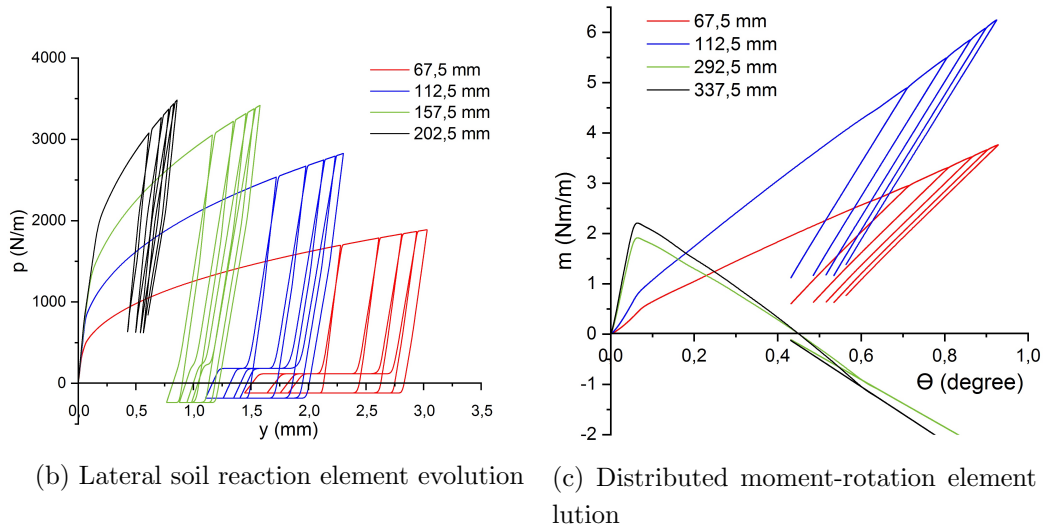
5.4 Validation 2: Prototype scale LME model with $L_e/D = 3$

The second validation is presented for the prototype scale pile-soil system with geometrical parameters and soil properties similar to the one presented for the simplified lab-scale model in chapter 3. The LME model is defined with the new definition of the interaction elements. A comparison with the established p-y methods is presented to highlight the significance of coupled interaction for the rigid monopile. The additional LME model parameters are calibrated respecting the similitude relationships between lab-scale LME model and new prototype scale LME model with $L_e/D = 3$. The additional parameters are presented in Table 5.4.

Notably, two types of numerical correlations are presented. Due to the difference in the aspect ratio of the calibration chamber (CC) model pile and new prototype pile, is it not possible to satisfy the similitude for pile head displacement and rotation at the same time. Therefore, two sets of numerical studies are presented, namely respecting rotation (RR) and respecting displacement (RD) similitude. The maximum displacement and rotation parameters are calibrated from the numerical results such that the normalised displacement or rotation is one at maximum lateral load application at the pile head.



(a) The deformation profile at the end of each cycle under OW combined load application



(b) Lateral soil reaction element evolution (c) Distributed moment-rotation element evolution

Figure 5.5: The local level element evolution for LeBlanc lab scale LME equivalent model

There is a general rule applied concerning similitude most crucial check. All similitude parameters shall entertain length, diameter and surcharge influences. All the relations which are in disagreement not having these parameters shall be discarded. The similitude NDG within 20% of error is accepted.

The G_o parameter presents the shear modulus at small strain stiffness. The measurement is based on the estimation given for Hardening soil small strain stiffness model (see Equation 4.18) where the reference shear modulus is 90MPa selected as an outcome of the NDG for soil stiffness calibration. The secant shear modulus is estimated from the reference stiffness modulus $E_{50}^{ref} = 45$ MPa selected assuming hardening soil model behaviour and such that the E_{soil} is 40 MPa equivalent to the consideration for the simplified prototype scale model (see Table 3.1). In the laboratory, the isotropic stress levels are low, resulting in higher friction angle but lower shear stiffness, in comparison to the full-scale tests. Hence, a smaller reference modulus is assigned for the LME model parameter calibration for the lab-scale Leblanc et al.

Table 5.4: LME model parameters estimated for new prototype model with $L_e/D = 3$

Parameter	Value
Small strain shear modulus, G_o (MPa)	79.986
Secent shear modulus, G_{sec} (MPa)	15.409
Lateral load capacity, H_f (kN)	8000
Vertical load capacity, V_f (kN)	20000
Moment load capacity, M_f (kNm)	200000
Layer thickness for LME, L_r (m)	1
Critical state friction angle, ϕ_{cr} (degree)	31
Maximum head rotation, θ_{head}^{max} (degree)	1.8 (RR), 3.6 (RD)
Maximum lateral head deflection, $u_{x(head)}^{max}$ (m)	0.25 (RR), 0.5 (RD)
Maximum vertical head deflection, $u_{z(head)}^{max}$ (m)	0.2

[60] model in contrast to the prototype scale models.

5.4.1 Similitude relations

Table 5.5 presents the similitude relationship between lab scale calibration chamber model pile and new prototype with $L_e/D = 3$. The similitude relations for load magnitudes reported by Leblanc et al. [60] are as per Equation 4.1. The additional similitude NDGs as reported by Byrne et al. [25], presented in Table 2.6 are also estimated.

Table 5.5: Similitude relations for load and displacements between PLAXIS model and new prototype model with $L_e/D = 3$

NDG	3D FEM model	Prototype $L_e/D = 3$
Leblanc et al. [60]		
\tilde{H}	0.901	0.840
\tilde{V}	2.080	2.101
\tilde{M}	5.634	5.251
$\tilde{\theta}$	1.272	1.278 (RR)
Byrne et al. [25]		
Soil stiffness (I_s)	459.619	567.917
$\tilde{\theta}^*$	584.579	725.822 (RR)
\tilde{u}_x^{head}	49.041	50.404 (RD)

Moreover, it is observed that the pile rotation NDG given by Leblanc et al. [60] agrees for respecting rotation (RR) similitude analysis (see Equation 5.3).

$$\tilde{\theta} = \theta \sqrt{\frac{p_a}{L\gamma'}} \quad (5.3)$$

5.4.2 Results

The new prototype LME model definition presents the significance of the coupled interaction. It is shown by making a comparison with the established p-y methods. Figure 5.6 presents the comparative plot of the lateral soil reaction element response. The evolution for soil reaction element as per the new definition is in agreement with the p-y response reported by Byrne et al. [24] for short piles in sand.

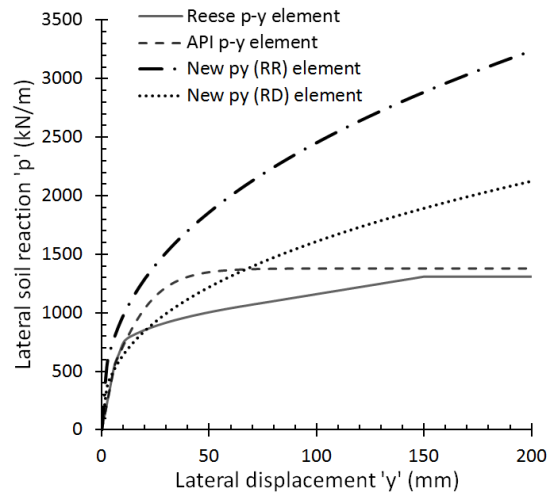


Figure 5.6: The comparative plot for soil reaction evolution

The general contour plot for total displacement at pile head is presented in Figure 5.7. The deformed shape of isolines presents the evidence of coupled interaction in the model pile shared the qualitative features are presented in the Figure 5.2 in the last section.

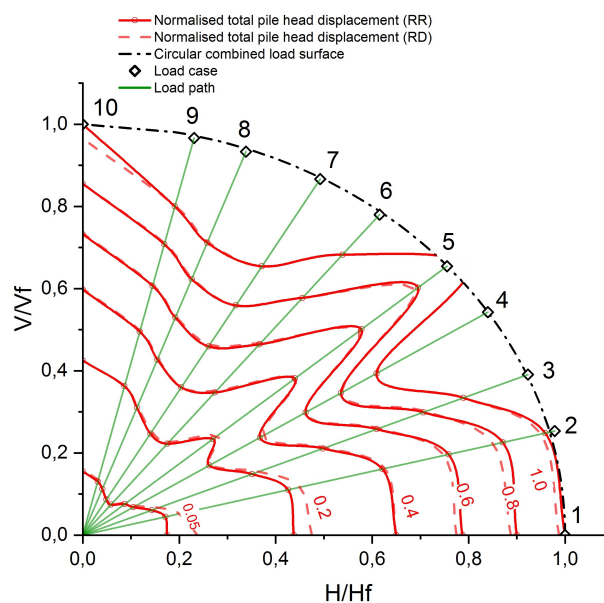


Figure 5.7: Contour plot for combined pile head total displacement with $L_e/D = 3$

The pile head displacement plot for ULS load case ($H = 3400$ kN and $V = 5000$ kN) and SLS load case ($H = 2000$ kN and $V = 5000$ kN) is presented in Figure 5.8. The comparative

responses with simple LME model presents the characteristic features of the new LME model definition, especially for the unloading response in cyclic loading cases.

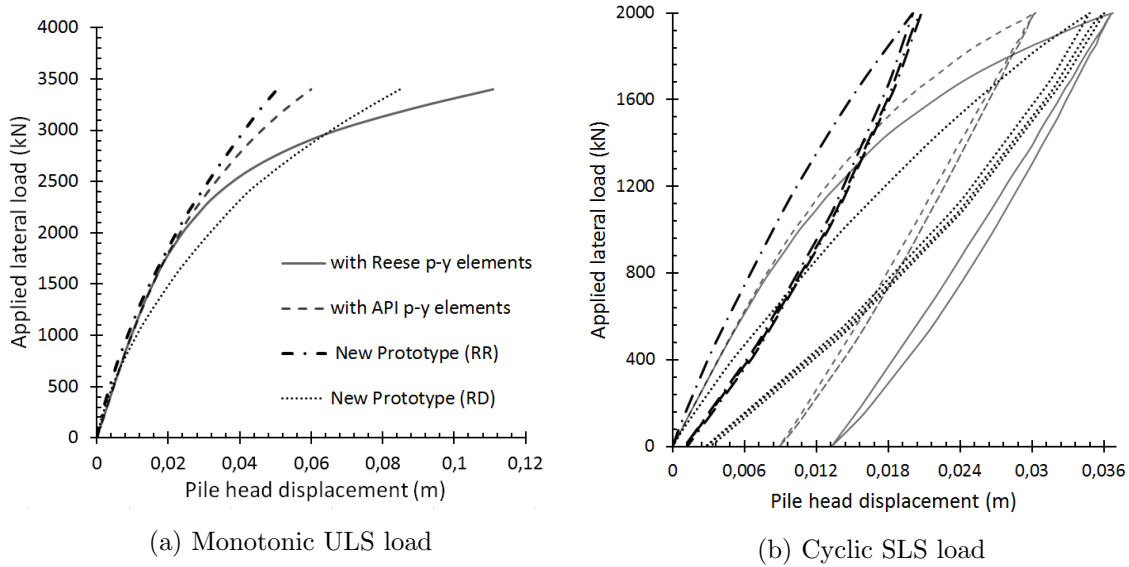


Figure 5.8: The pile head moment rotation plots

The rigid pile-soil interaction incorporates additional reaction components than the simple p-y curve. It is presented for a monotonic combined load case ($H = 6000$ kN, $V = 13000$ kN) implemented in the LME model. The model parameters are calibrated with respecting displacement similitude relationship. Figure 5.9 presents the pile head displacement with an applied lateral load for four types of elements assembly. The first assembly comprises only lateral soil reaction (PY) element. The successive addition of the reaction components, namely base shear element (+BSE), then moment rotation element (+MT) and lastly, base moment element(+BM) presents the other three assemblies. Each component addition increases the model stiffness and therefore the pile head displacement presents a decreasing trend with increasing components.

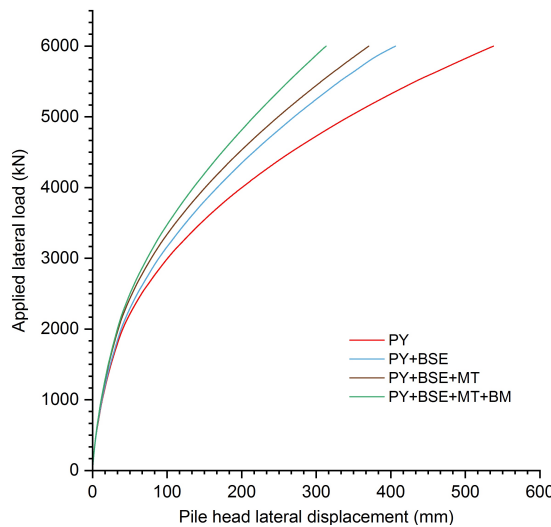


Figure 5.9: Demonstration for the element contribution for new prototype scale model definition with coupled interaction

5.5 Validation 3: New prototype model with L_e/D 4.5 and 6

A similar extension to prototype scale is simulated for LME models with model pile aspect ratios 4.5 and 6. The LME model is defined with the new definition of the interaction elements. The additional LME model parameters are calibrated as per similitude NDGs between lab-scale LME model and new prototype scale models with L_e/D equal to 4.5 and 6. The additional parameters are presented in Table 5.6. Notably, the pile wall thickness is increased two and four times from the [6] minimum thickness estimations for L_e/D equal to 4.5 and 6 prototype cases respectively to ensure the rigid pile behaviour in LME model.

Table 5.6: LME model parameters estimated for new prototype model with $L_e/D = 4.5$ and 6

Parameter	Value	
	$L_e/D = 4.5$	$L_e/D = 6$
Pile outer diameter D_o (m)	4	4
Pile wall thickness t (m)	0.0927	0.1854
Pile embedment length L_e (m)	18	24
Small strain shear modulus, G_o (MPa)	97.962	113.117
Secent shear modulus, G_{sec} (MPa)	18.820	21.701
Lateral load capacity, H_f (kN)	18000	34000
Vertical load capacity, V_f (kN)	42000	78000
Moment load capacity, M_f (kNm)	450000	850000
Layer thickness for LME, L_r (m)	1.5	1.0
Maximum head rotation, θ_{head}^{max} (degree)	2.2 (RR), 2.6 (RD)	2.55
Maximum lateral head deflection, $u_{x(head)}^{max}$ (m)	0.41 (RR), 0.5 (RD)	0.6
Maximum vertical head deflection, $u_{z(head)}^{max}$ (m)	0.26	0.30

The model parameters are determined using the same strategy for similitude, estimation of the shear modulus, lateral and axial deformations as used in the second validation presented in the previous section.

5.5.1 Similitude relations

Table 5.7 presents the similitude relationship between lab scale calibration chamber model pile and new prototype with $L_e/D = 4.5$ and 6. The similitude relations for load magnitudes reported by Leblanc et al. [60] are as per Equation 4.1. The additional similitude relations from Broms [20] and Byrne et al. [25], as formulated in the previous validations are also presented.

5.5.2 Results

The LME model performance is presented for different load combinations of monotonic and cyclic characteristics. The circular failure load surface is assumed for both pile geometries with L_e/D 4.5 and 6. Figure 5.10 presents the contour plot for L_e/D 4.5 and 6 model layout under

Table 5.7: Similitude relations for load and displacements between PLAXIS model and new prototype model with $L_e/D = 4.5$ and 6

NDG	3D FEM model	Prototype	
		$L_e/d = 4.5$	$L_e/d = 6$
	Leblanc et al. [60]		
\tilde{H}	0.901	0.840	0.893
\tilde{V}	2.080	1.961	2.048
\tilde{M}	5.634	5.251	5.580
$\tilde{\theta}$	1.272	1.275 (RR)	1.280
	Broms [20]		
\tilde{H}^*	0.432	0.499	0.453
	Byrne et al. [25]		
Soil stiffness (I_s)	459.619	567.917	567.917
$\tilde{\theta}^*$	584.579	724.327 (RR)	727.081
\tilde{u}_x^{head}	49.041	41.155 (RD)	42.769

combined loading application. Both configurations present a similar qualitative and quantitative profile. It infers the correctness of the similitude relations and the load levels estimates.

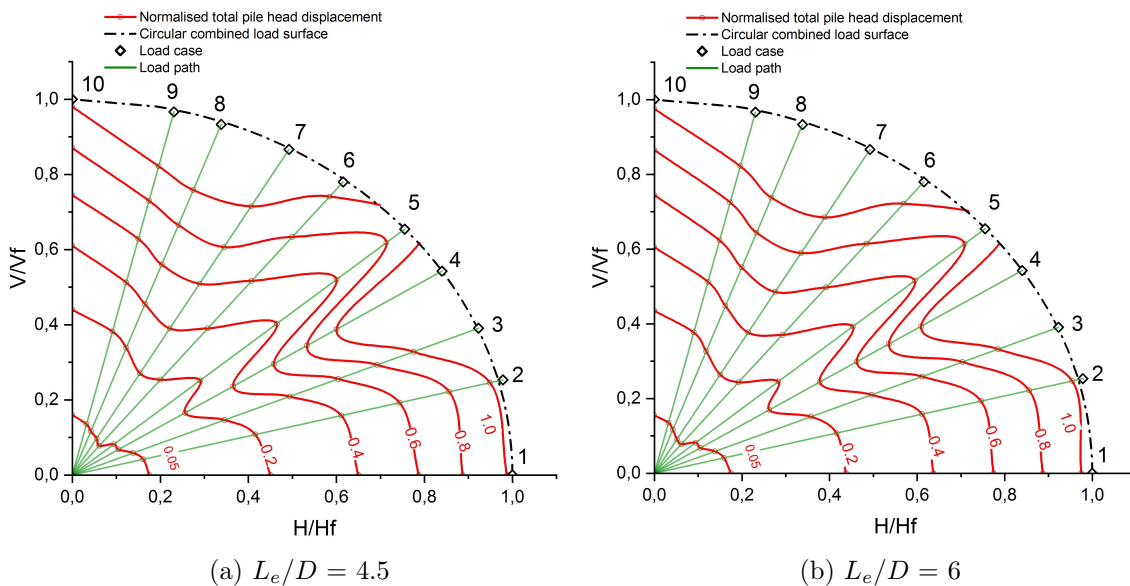


Figure 5.10: The contour plots for the different combined load cases present on the failure surface for two different prototype scale pile geometries

Figure 5.11 presents the response of the two geometries ($L_e/D = 4.5$ and 6) under the application of the same loading combination ($H = 13.5$ MN and $V = 27$ MN). The different response highlights the significance of the failure load surface. The lateral and vertical capacities of the two configurations are different. Thus, the selected load magnitude level resides at different points within the failure load surface. This intern results in the different parent load path defining different element behaviour for the coupled interaction (see Figure 4.31 for reference). Therefore,

the present LME model enables the decision making of the pile geometrical features for the practically estimated on-field load levels resulting in the desired level of pile head displacement and rotation.

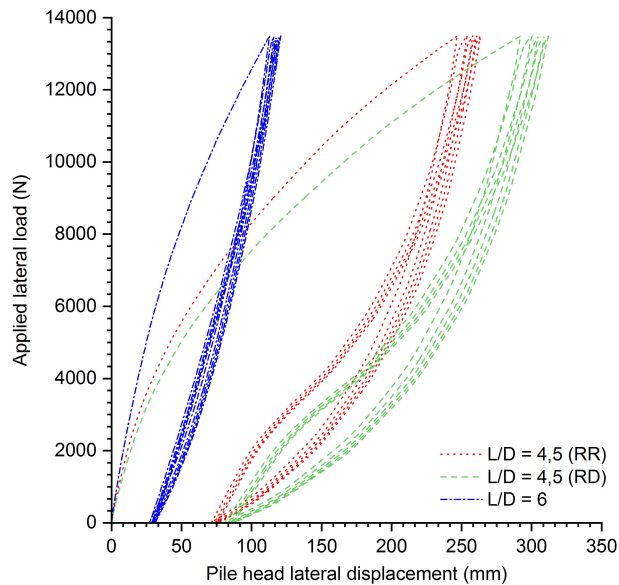


Figure 5.11: Plot for pile head displacement under one-way combined loading ($H = 13.5$ MN and $V = 27$ MN) for L_e/D 4.5 and 6 pile geometry

Figure 5.12 demonstrates the coupled interaction with different pile geometries. A combined monotonic load with $H_{norm} = 0.75$ and $V_{norm} = 0.65$ for respective circular failure surfaces is randomly chosen for this purpose. The model assembly response with successive addition of the contribution from each element of a different type is presented. Notably, the LME model input parameters determined using the RD similitude relations are used for L_e/D 3 and 4.5 pile configurations. The chronological order choice is inspired from work reported by Byrne et al. [24].

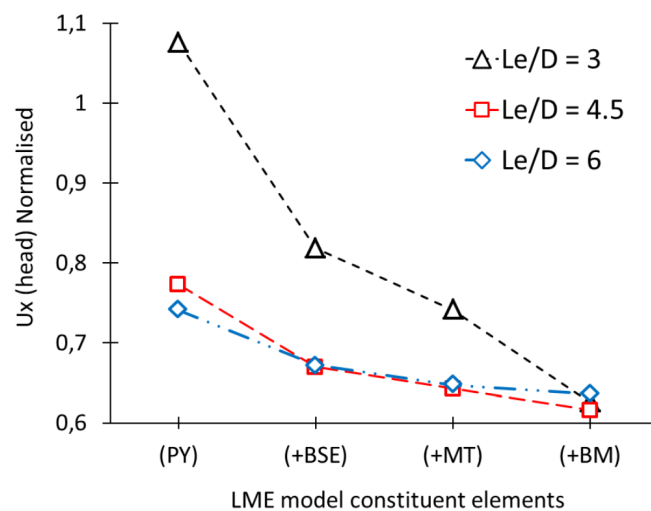


Figure 5.12: Coupled interaction effect demonstration with increasing pile aspect ratio

The plot presents two features: (1) The successive addition of an element in LME model assembly results in the reduced deformation. It signifies that the pile head deformations

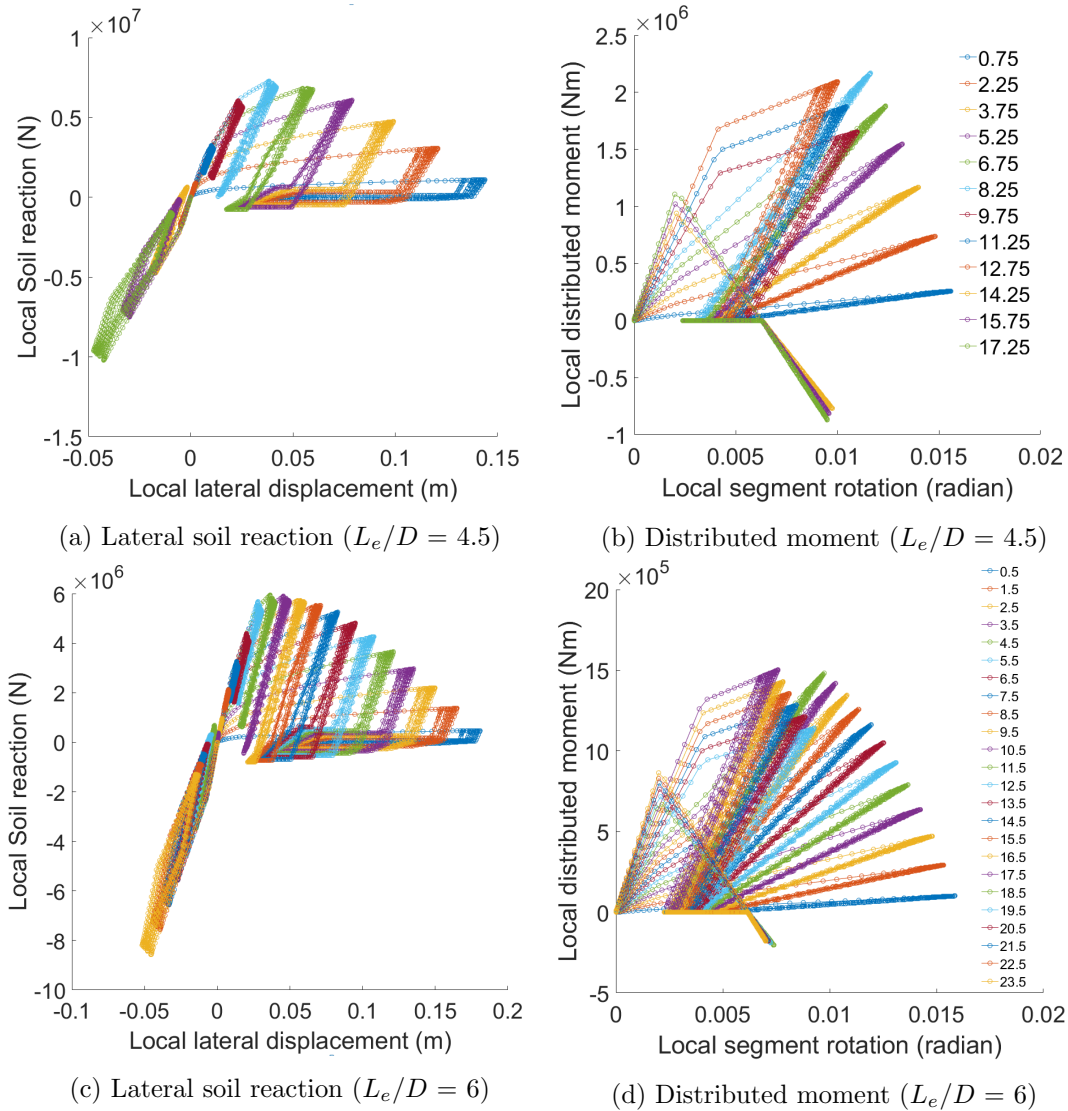


Figure 5.13: Element level evolution demonstrating the lateral soil reaction element response above and below the pile rotation point and three pile-soil interaction zones for the distributed moment element

determinations using the conventional p-y methods overestimates the magnitudes. The shorter is the aspect ratio; higher will be the overestimation. Therefore, the analysis of pile-soil interaction for monopile design necessarily demands to consider the additional interaction components. The results agree with the ones reported by Byrne et al. [24] about the involvement of all reaction components for shorter piles ($L_e/D = 2-3$) and only the p-y reaction component for $L_e/D = 10+$ piles. (2) The coupled interaction is more significant for shorter piles. This feature is demonstrated by the rate of decrease of pile head displacement with successive interaction element addition. Notably, the normalised pile head displacement is greater than 1 for the $L_e/D = 3$ cases with p-y elements only. It infers that the similitude relations for maximum pile head displacement estimation well consider (indirectly) the addition reaction components features for short piles.

Figure 5.13 presented the lateral soil reaction and distributed moment elements behaviour at different depths for both $L_e/D = 4.5$ and 6 pile geometry. A OW cyclic load case

with $H_{norm} = 0.5$ and $V_{norm} = 0.5$ is used for LME models simulation. It demonstrates the equivalent three interaction zones, as reported by Hong et al. [45]. The evolution of lateral soil reaction element for one-way cyclic loading at different depths present the qualitative similarities as reported by Puech and Garnier [83] for one-way lateral loading response for experimental pile in sand.

5.6 Cyclic response for a large number of load cycles

All the model cases are simulated with 100 cycles of combined load application for $H_{norm} = 0.5$ and $V_{norm} = 0.5$ load case evaluated from their respective lateral and vertical load capacities. The load case considered resides within the presumed circular load envelop inferring a plausible, practical load case scenario. Leblanc et al. [60] reported that the accumulated rotation at the pile head upon many load cycles follows a logarithmic evolution for a small number of cycles ($n < 100$) and exponential for a large number of cycles ($n > 500$). In the present work, the local macro elements are formulated to represent the ratcheting phenomenon as a logarithmic decay function of the initial stiffness. Therefore, a small number of load cycles are simulated for qualitative comparison.

Figure 5.14 presents the LME model outcome of normalised pile head rotation (θ/θ_s) with number of load cycle for all five model cases. Here, θ_s is estimated from a monotonic load case under same load magnitudes as for the corresponding cyclic loading case.

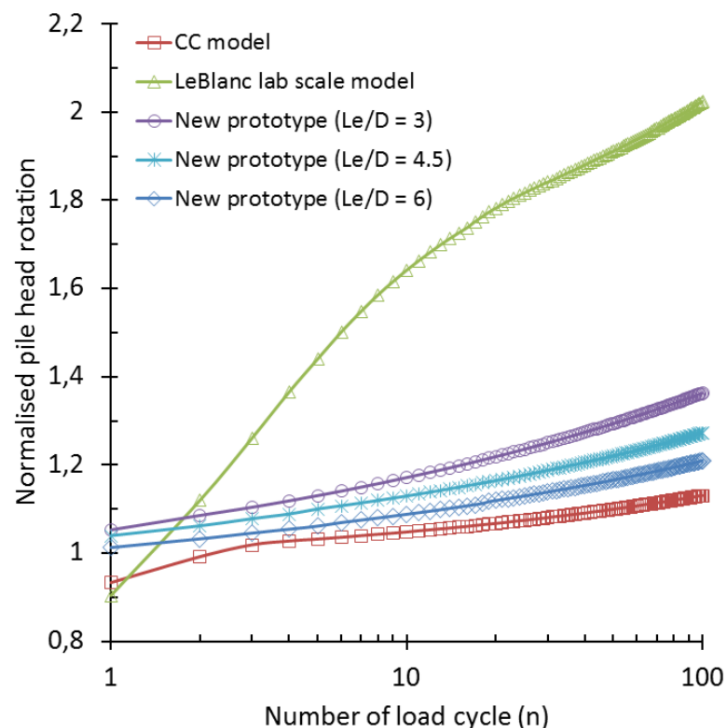


Figure 5.14: The evolution of the normalised pile head rotation with increasing number of lateral load cycles applied at the model pile head

The LeBlanc lab-scale model presents a different qualitative evolution than all the other load cases. It is because the initial stiffness of the LeBlanc lab-scale model is very low due

to a very low effective vertical stress. Therefore, the movement in the surrounding soil upon cyclic lateral load application is comparatively higher than in other cases. The increasing trend is linear in semi-log scale; supporting the observations reported by Leblanc et al. [60]. The plot indirectly highlights the potential significance of the lab-scale model in calibration chamber where an initial state of stress corresponding to the field scale is attainable. The lab-scale model with 1g conditions results in higher strain levels which are susceptible to fall out of the practical strain level requirements, resulting in limited confidence on the lab-scale model outcomes. All simulations are performed with the same LME model components, subsequently supporting the correctness of the similitude relations and model performance for a range of model cases.

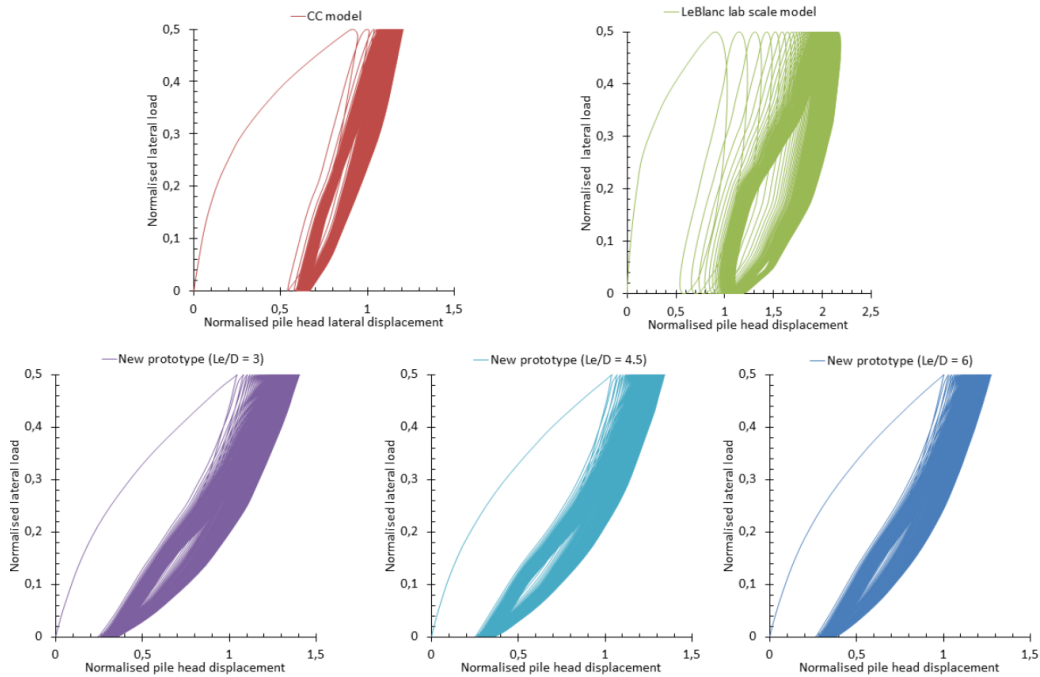


Figure 5.15: The evolution of the normalised pile head displacement with normalised lateral load applied at the model pile head

Similarly, the pile head lateral displacement with an applied lateral load plot is presented in Figure 5.15 to highlight the ratcheting phenomenon in all model cases. The normalised lateral applied load is plotted against the normalised pile head lateral displacement. Similar to the normalised rotation, the normalised lateral displacement is evaluated from the corresponding monotonic load response. The LeBlanc lab-scale model presents a higher rate of stiffness degradation with the increasing number of load cycles in comparison to all the other model cases. The observations from the Figures 5.14 and 5.15 are qualitatively similar while presenting the ratcheting phenomenon in two different ways.

Therefore, use of the LME model for a large number of cycles is essential to understand the domain of the accumulated strains due to cyclic loading and subsequently decide the allowable deformation limits. The computational time of the LME model varies between 30 mins to one hour for 100 cycles. It makes the simulation with a large number of cycles very time consuming while the vital information is the ratcheting deformation. To save the computational time, Abadie et al. [4] introduced a calibration method (see section 2.4 for more information) allowing for the estimation of the ratcheting deformation directly at n^{th} cycle. The model de-

velopment is in the framework of hyper-plasticity [46] and is beyond the scope of the present work.

5.7 Local element level similitude validation

The element level similitude relationships are examined between lab-scale LeBlanc model and three presented prototype models with L_e/D 3, 4.5 and 6. Table 5.8 presents the similitude NDGs reported by Klinkvort and Hededal [57] and Burd et al. [22] describing the prototype and model scale relations at a depth ‘z’ within pile embedment length. These relations are used to validate the local element level behaviour of the LME model. The loading case with pure horizontal load till failure (H_f) is used to estimate the magnitude of NDGs to keep the consistent loading between LME model and as per the Klinkvort and Hededal [57], and Burd et al. [22] studies.

Table 5.8: Similitude parameters estimation for the local level element behaviour definition

Non-Dimensional Group (NDG)	LeBlanc lab- scale model	New prototype with L_e/D		
		3	4.5	6
Modified after Klinkvort and Hededal [57]				
Lateral load, $\tilde{H}^* = H/(K_p\sigma'_{vz}D^2)$	2.821	2.148	2.506	2.905
Lateral soil reaction, $\tilde{p} = p/(K_p\sigma'_{vz}D)$	4.015	6.896	4.889	3.901
As per Burd et al. [22]				
Lateral soil reaction, $\tilde{p}^* = p^*/(\sigma'_{vz}D)$	21.234	27.742	19.669	15.692
Lateral displacement, $\tilde{u}_x^* = u_x^*G_o/(\sigma'_{vz}D)$	51.426	45.727	36.875	27.404
Distributed moment, $\tilde{m} = m/(pD)$	0.010	0.013	0.017	0.013
Pile rotation, $\tilde{\theta} = \theta G_o/\sigma'_{vz}$	7826.165	7092.322	7230.105	7091.960
Base shear load ($\times 10^{-4}$), $\tilde{H}_B = H_B/(\sigma'_{vz}D^2)$	5.4	4.7	4.7	4.7
Base moment, $\tilde{M}_B = M_B/(\sigma'_{vz}D^3)$	0.334	0.872	0.778	0.692

The local level similitude for the lateral soil reaction presents a significant difference for a comparison between the lab-scale CC model and Leblanc et al. [60] lab-scale model. The presence of the surcharge pressure in the CC model results in the higher estimations of the lateral soil reaction, using the similitude relations reported by Burd et al. [22] for local level behaviour comparison. Therefore, a comparison of the local level element behaviour is presented only for all the model cases having no surcharge pressure. It enables a more suitable comparison of different model response using the previously reported local level similitude relationships.

A good agreement between the local level interaction similitude relations presents the quality check of the local macro-element model assembly. The representative depth (z) for each model configuration is selected to satisfy the Lateral load (\tilde{H}^*) NDG using the vertical stress level at that depth. The LME model assembly is simulated, and the relevant interaction response data at the representative depth is extracted from the model output. Notably, the RR similitude relations for L_e/D 3 and 4.5 for the LME model simulations are used. It is because the rigid pile rotation is expected to be similar at all depth levels. Therefore, the agreement of

the similitude at the representative depth can be extrapolated to the other local depth levels. The lateral displacement similitude relation, thus, presents a deviating trend with increasing pile aspect ratio. The base moment similitude is in good agreement between three prototype scale configurations but differs by a factor of 2,5 with the lab-scale model. It is because the similitude relation proposed by Burd et al. [22] for the base moment account for the pile base effective vertical stress. However, the base moment element definition used in the present work is as per DNV, 2017 guidelines where the base moment is defined as a function of stiffness modulus and pile diameter only (see Equation 4.75 for reference).

5.8 Global stiffness check

The global stiffness definition for pile-soil interaction presents the response under vertical, lateral and moment load application by stiffness in the respective direction. The global pile-soil interaction definition reported by Bhattacharya et al. [19] presents an empirical mathematical relationship for the lateral (K_L), rotational (K_R) and cross-coupled stiffness (K_{LR}) relating moment and lateral load interaction towards conservative foundation stiffness. The description of the stiffness parameters is presented in section 2.4. Table 5.9 presents the global stiffness check for all the prototype scale local macro-element profiles, the CC model and LeBlanc lab-scale model.

Table 5.9: Global stiffness response check for all LME model cases simulations

Parameter/model	CC	LeBlanc	$L_e/D = 3$	$L_e/D = 4.5$	$L_e/D = 6$
H (kN)	0.065	0.0017	60	180	340
y_1 (mm)	0.0044	0.0021	0.0672	0.1263	0.1958
θ_1 ($\times 10^{-5}$ rad)	1.56	0.90	0.95	1.46	2.00
M (kNm)	0.0325	0.000731	150	450	850
y_2 (mm)	0.0078	0.0039	0.0237	0.0368	0.0440
θ_2 ($\times 10^{-5}$ rad)	5.17	2.32	0.62	0.88	0.97
D (m)	0.08	0.08	4	4	4
L_e (m)	0.8	0.36	12	18	24
E_{pile} (GPa)	115	120	210	210	210
E_{soil} (MPa)	13.59	8.56	60.03	60.03	60.03
Local macro element model response					
	$\times 10^7$	$\times 10^6$	$\times 10^{10}$	$\times 10^{11}$	$\times 10^{11}$
K_L (N/m^2)	3.1764	2.9036	0.1921	0.0274	0.0324
K_R (N/m^2)	0.1353	0.1131	5.1718	0.9714	1.6397
K_{LR} (N/m^2)	-0.4796	-0.4885	-0.7296	-0.1132	-0.1474
Bhattacharya et al. [19] mathematical relations					
	$\times 10^7$	$\times 10^6$	$\times 10^{10}$	$\times 10^{11}$	$\times 10^{11}$
K_L (N/m^2)	1.4937	5.7318	0.1560	0.0201	0.0240
K_R (N/m^2)	0.3739	0.3198	10.1790	2.8050	0.2914
K_{LR} (N/m^2)	-0.5854	-1.0605	-0.9880	-0.1861	-5.7581

The global stiffness parameters are estimated using the procedure presented in Bhattacharya [15] and summarised in section 2.4. All the load magnitudes shall be selected such that the pile-soil interaction resides in the elastic zone. It is ensured in the LME models simulation by a single iteration (maximum three for the large element assemblies) at each time step as an overall response of the complete element assembly. A comparison with the empirical mathematical formulation reported by Bhattacharya et al. [19] presents a good agreement concerning the order of magnitude. Thus, the existing global macro-element definition established only for the lateral and moment load components (with zero vertical loads) can be potentially updated incorporating the vertical load level definition for a combined VHM global response. Arany et al. [9] presented a method to define the natural frequency of the wind turbine and foundation system by using the global stiffness parameters summarised in the section 2.4. Therefore, with additional information of the mass of the tower and wind turbine rotor-nacelle assembly; the presented LME model can be utilised to estimate the natural frequency in the early concept design stages of an OWT construction project.

5.9 How to use LME model for field-scale structures?

The LME model definition is validated for an assembly of the pile-soil coupled interaction elements. By extensions, the model can be used in the ‘concept design’ stage for a field-scale structure. A flowchart of step-wise guidelines on how to use the LME model is presented in Figure 5.16.

There is an additional calibration required for the cyclic loading case. It is to incorporate the cyclic lateral soil reaction element stiffness and drag element capacity in the model definition. The cyclic (p-y + drag) element is calibrated to presents the same qualitative and quantitative response as for a monotonic p-y element under similar loading conditions. Notably, for cyclic LME model, the stiffness of the drag element is taken equal to the cyclic lateral soil reaction element stiffness.

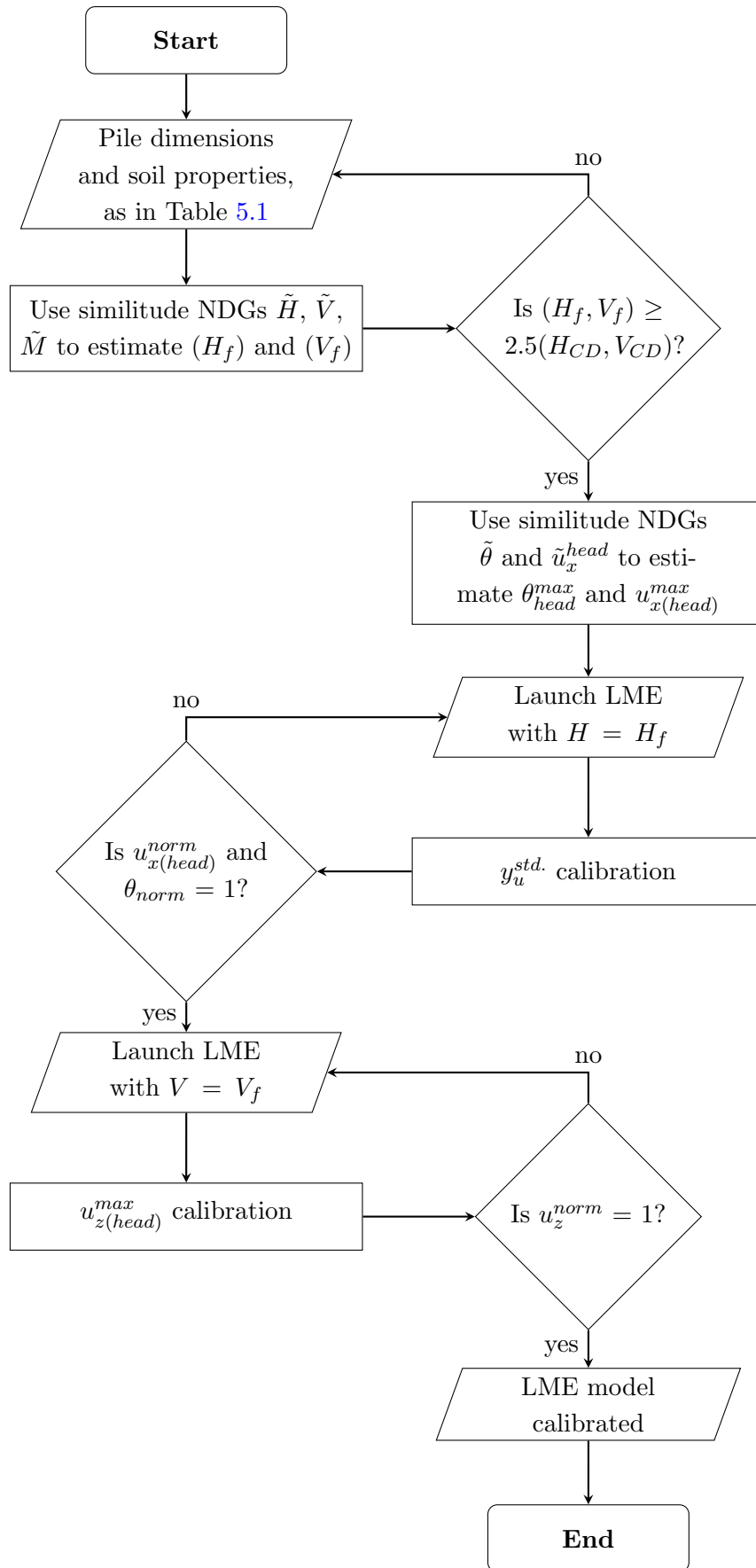


Figure 5.16: Flowchart of the guidelines for LME model calibration and utilisation

5.10 Conclusions

The local macro-element definition incorporating the coupled interaction is validated with an existing database of lab-scale model tests reported in Leblanc et al. [60]. The model element definition is extended to the prototype scale as per the similitude relationships. The comparison of new pile-soil interaction definition with the existing methods highlighted the qualitative and quantitative significance of the coupled interaction, especially for the short piles. The overall response of the local elements assembly is validated against the global stiffness parameters empirically reported by Bhattacharya et al. [19]. The global stiffness check bridges the gap between the presented local macro-element study and the global pile-soil interaction response.

The prototype model with $L_e/D = 10$ is observed to be presenting a flexible pile behaviour from LME model analysis and hence not included in the present chapter. The standard ultimate local lateral displacement ($y_u^{std.}$) is assigned as the input parameter for all model cases. Its magnitude is calibrated for $H = H_f$ load case to meet the similitude requirements of ultimate pile head lateral displacement and rotation. The calibration of the $y_u^{std.}$ parameter indirectly leads to the alteration in the evolution path till $p_u^{std.}$. Therefore, the evolution plot for lateral soil reaction element is extrapolated beyond the estimated $p_u - y_u$ to generalise the element definition for all the model cases. The hypothesis is in line with the observation of Fleming [37], which states that the p_u is higher than the passive earth pressure, due to the three-dimensional characteristics of the lateral pile-soil interaction. The accuracy of this calibration strategy is presented by a good correlation between all model cases for similitude relation for the local level lateral soil reaction (see Table 5.8).

Chapter 6

Conclusions and perspectives

The thesis work presented a numerical study to understand the pile-soil interaction behaviour of rigid monopile under combined load application. Two different numerical studies, namely 3D finite element (FE) analysis in PLAXIS and local macro-element (LME) model development and analysis, are presented to understand and represent the coupled pile-soil interaction. The LME model features and usage is intended for implementation in the concept design stage for a monopile foundation supporting an offshore wind turbine. The general conclusions from the thesis work are discussed hereafter.

A general understanding of the offshore wind turbine environment, foundation and pile-soil interaction is established through a review of the previous studies. The understanding of pile-soil interaction mechanisms and its representation as a macro-element model is established. The ingredients representing the interaction behaviour are investigated to produce a simple macro-element model, which presents the local pile-soil interaction under combined loading scenario.

The significance and limitation of the established methods and techniques are explored for flexible and rigid pile-soil interactions. A similitude study is carried out to establish a representative lab-scale model in calibration chamber setup of field-scale monopile supporting an OWT structure. A 3D FE model representative of the lab-scale experimental setup is analysed with combined monotonic and cyclic load application. A strategy to extract the model response data to define the pile-soil interaction at different local embedment depths is presented. The data extraction and analysis methods are planned to be in correspondence with the equivalent lab-scale experiments. A mathematical formulation of the different components of the pile-soil interaction is developed to define the coupled interaction empirically.

The mathematical developments served as a basis for the definition of a new LME model of lab-scale model pile configuration. The LME interaction elements are formulated with an elastoplastic constitutive law. A comparison between both lab-scale numerical models is presented for quantitative and qualitative features representation and LME model calibration for monotonic and cyclic loading cases.

A second similitude analysis is presented to establish a relation between the new LME model components definition and the corresponding components in the prototype scale pile-soil system. A priori, the new LME definition is validated against an experimental study on a lab-

scale model to present the correctness of the similitude relations and to demonstrate different features of the new LME model. Subsequently, a set of input parameters is established to define the LME model configuration and its calibration respecting the similitude relationships.

A comparison between the simple and new definition of LME models for the same pile-soil system is presented to highlight the significance of coupled interaction for rigid pile behaviour representation by making a comparison with established axial and lateral pile-soil interaction methods. The new definition of the LME model is tested for another two prototype scale pile-soil system highlighting the similitude features, the significance of the coupled pile-soil interaction and cyclic interaction feature called ratcheting.

The new LME model outputs are compared against previous studies on the global monopile-soil interaction behaviour to highlight the model characteristics. Subsequently, the general guidelines for the model usage and calibration are presented for the concept design of the real foundation structure for OWT applications.

Perspectives

The thesis work involves only numerical studies to present a planning strategy for the experimental campaign of model monopile in the calibration chamber setup. The accuracy of the presented results and coupled interaction hypothesis is subjected to the experimental outcomes and comparison. Hence, the established knowledge of the coupled pile-soil interaction methodology can be carried forward further to improve the hypothesis via numerical or experimental investigations.

Moreover, a bored (wished in place) pile case is demonstrated in the present studies where the pile installation effects are highly simplified. As future work, the inclusion of these effects for a jacked pile case shall provide a more realistic measure of the coupled pile-soil interaction. The addition of the pile driving effect component in the model definition can be explored in further numerical and experimental studies by exploring the axial, lateral and coupled pile-soil interaction mechanisms summarised in the literature review chapter.

Lastly, the LME model presents a 1D parametric study of the coupled pile-soil interaction. The 1D numerical framework shall be further extended to 3D stress-strain relationship to model the pile-soil interaction for multi-directional loading. Thereby, the LME model will be able to model the non-co-linearity between the force and displacement relationship by improvement in the stiffness matrix. Also, the dynamic soil-pile interaction feature can be incubated in the macro-element definition by the implementation of a rate-dependent constitutive behaviour.

Bibliography

- [1] C. Abadie, I. Richards, B. Byrne, and G. Houlsby. *Cyclic Loading of Monopiles for Offshore Wind Applications*. Poster, 11 2016.
- [2] C. N. Abadie. *Cyclic Lateral Loading of Monopile Foundations in Cohesionless Soils*. PhD thesis, University of Oxford, 2015.
- [3] C. N. Abadie, B. W. Byrne, and S. Levy-Paing. Model pile response to multi-amplitude cyclic lateral loading in cohesionless soils. *Frontiers in Offshore Geotechnics III*, pages 681–686, 2015. doi: 10.1201/b18442-92.
- [4] C. N. Abadie, G. T. Houlsby, and B. W. Byrne. A method for calibration of the Hyperplastic Accelerated Ratcheting Model (HARM). *Computers and Geotechnics*, 112 (March):370–385, 2019. ISSN 18737633. doi: 10.1016/j.compgeo.2019.04.017. URL <https://doi.org/10.1016/j.compgeo.2019.04.017>.
- [5] M. Achmus and K. Thieken. On the behavior of piles in non-cohesive soil under combined horizontal and vertical loading. *Acta Geotechnica*, 5(3):199–210, 2010. ISSN 18611125. doi: 10.1007/s11440-010-0124-1.
- [6] API. *Recommended Practice 2 GEO*. API, 1220 L Street, NW, Washington, DC 20005, Geotechnical and Foundation Design Considerations, 2011.
- [7] L. Arany, S. Bhattacharya, S. Adhikari, S. J. Hogan, and J. H. G. Macdonald. An analytical model to predict the natural frequency of offshore wind turbines on three-spring flexible foundations using two different beam models. *Soil Dynamics and Earthquake Engineering*, 74:40–45, 2015. ISSN 02677261. doi: 10.1016/j.soildyn.2015.03.007. URL <http://dx.doi.org/10.1016/j.soildyn.2015.03.007>.
- [8] L. Arany, S. Bhattacharya, J. Macdonald, and S. J. Hogan. Simplified critical mudline bending moment spectra of offshore wind turbine support structures. *Wind Energy*, 18 (12):2171–2197, 12 2015. ISSN 1099-1824. doi: 10.1002/we.1812. URL <http://dx.doi.org/10.1002/we.1812>.
- [9] L. Arany, S. Bhattacharya, J. H. Macdonald, and S. J. Hogan. Closed form solution of Eigen frequency of monopile supported offshore wind turbines in deeper waters incorporating stiffness of substructure and SSI. *Soil Dynamics and Earthquake Engineering*, 83, 2016. ISSN 02677261. doi: 10.1016/j.soildyn.2015.12.011.
- [10] L. Arany, S. Bhattacharya, J. Macdonald, and S. J. Hogan. Design of monopiles for offshore wind turbines in 10 steps. *Soil Dynamics and Earthquake Engineering*, 92(November

- 2015):126–152, 2017. ISSN 02677261. doi: 10.1016/j.soildyn.2016.09.024. URL <http://dx.doi.org/10.1016/j.soildyn.2016.09.024>.
- [11] M. Arshad and B. C. O’Kelly. Analysis and Design of Monopile Foundations for Offshore Wind-Turbine Structures. *Marine Georesources & Geotechnology*, 34(6):503–525, 2016. ISSN 1064-119X. doi: 10.1080/1064119X.2015.1033070. URL <http://www.tandfonline.com/doi/full/10.1080/1064119X.2015.1033070>.
- [12] M. Arshad and B. C. O’Kelly. Reducing monopile rotation under lateral loading in sandy soils. *Geomechanics and Geoengineering*, 12(1):14–27, 2017. ISSN 17486033. doi: 10.1080/17486025.2016.1153730. URL <http://dx.doi.org/10.1080/17486025.2016.1153730>.
- [13] A. H. Augustesen, K. T. Brødbæk, M. Møller, S. P. H. Sørensen, L. Ibsen, T. S. Pedersen, and L. Andersen. Numerical Modelling of Large-Diameter Steel Piles at Horns Rev. *Proceedings of the 12th International Conference on Civil, Structural and Environmental Engineering Computing*, pages 1–14, 2009.
- [14] S. Bhattacharya. Challenges in Design of Foundations for Offshore Wind Turbines. *Engineering & Technology Reference*, 2014. ISSN 2056-4007. doi: 10.1049/etr.2014.0041. URL <http://digital-library.theiet.org/content/reference/10.1049/etr.2014.0041>.
- [15] S. Bhattacharya. Soil–Structure Interaction (SSI). In *Design of Foundations for Offshore Wind Turbines*, chapter 5, pages 191–271. John Wiley & Sons, Ltd, 2019. ISBN 9781119128137. doi: 10.1002/9781119128137.ch5. URL <https://onlinelibrary.wiley.com/doi/abs/10.1002/9781119128137.ch5>.
- [16] S. Bhattacharya and S. Adhikari. Experimental validation of soil-structure interaction of offshore wind turbines. *Soil Dynamics and Earthquake Engineering*, 31(5-6):805–816, 2011. ISSN 02677261. doi: 10.1016/j.soildyn.2011.01.004. URL <http://dx.doi.org/10.1016/j.soildyn.2011.01.004>.
- [17] S. Bhattacharya, D. Lombardi, and D. Muir Wood. Similitude relationships for physical modelling of monopile-supported offshore wind turbines. *International Journal of Physical Modelling in Geotechnics*, 11(2):58–68, 2011. ISSN 1346-213X. doi: 10.1680/ijpmg.2011.11.2.58. URL <http://www.icevirtuallibrary.com/doi/10.1680/ijpmg.2011.11.2.58>.
- [18] S. Bhattacharya, N. Nikitas, J. Garnsey, N. A. Alexander, J. Cox, D. Lombardi, D. Muir Wood, and D. F. T. Nash. Observed dynamic soil-structure interaction in scale testing of offshore wind turbine foundations. *Soil Dynamics and Earthquake Engineering*, 54:47–60, 2013. ISSN 02677261. doi: 10.1016/j.soildyn.2013.07.012. URL <http://dx.doi.org/10.1016/j.soildyn.2013.07.012>.
- [19] S. Bhattacharya, G. Nikitas, L. Arany, and N. Nikitas. Soil–Structure Interactions for Offshore Wind Turbines. *Engineering & Technology Reference*, 1(1):1–16, 2017. ISSN 2056-4007. doi: 10.1049/etr.2016.0019. URL <http://digital-library.theiet.org/content/reference/10.1049/etr.2016.0019>.
- [20] B. B. Broms. Lateral Resistance of Piles in Cohesionless Soils. *Journal of the Soil Mechanics and Foundations Division*, 90(3):123 – 158, 1964.

- [21] E. Buckingham. On Physically Similar Systems; Illustrations of the Use of Dimensional Equations. *Physical Review*, 4(4):345–376, 10 1914. doi: 10.1103/PhysRev.4.345. URL <https://link.aps.org/doi/10.1103/PhysRev.4.345>.
- [22] H. Burd, B. Byrne, R. A. McAdam, G. Houlsby, C. Martin, W. Beuckelaers, L. Zdravkovic, D. M. G. Taborda, D. Potts, R. Jardine, K. Gavin, P. Doherty, D. Igoe, J. Skov Gretlund, M. Pacheco Andrade, and A. Muir Wood. Design aspects for monopile foundations. In *TC 209 workshop on foundation design for offshore wind structures, 19th ICSMGE*, pages 35–44, Seoul, 9 2017.
- [23] B. Byrne and G. Houlsby. Foundations for offshore wind turbines. *Philosophical Transactions of the Royal Society A: Mathematical, Physical and Engineering Sciences*, 361:2909–2930, 2003. URL <http://rsta.royalsocietypublishing.org/content/361/1813/2909>.
- [24] B. Byrne, R. McAdam, H. Burd, G. Houlsby, C. Martin, L. C, D. Taborda, D. Potts, R. Jardine, M. Sideri, F. Schroeder, K. Gavin, P. Doherty, D. Igoe, A. Wood, D. Kallehave, and J. Gretlund. New design methods for large diameter piles under lateral loading for offshore wind applications. *Frontiers in Offshore Geotechnics III*, 1(June):705–710, 2015. ISSN 16849981. doi: 10.1201/b18442-96.
- [25] B. Byrne, R. McAdam, H. Burd, G. Houlsby, C. M. Martin, W. Beuckelaers, L. Zdravkovic, D. M.G. Taborda, D. M. Potts, R. Jardine, E. Ushev, T. Liu, D. Abadias, K. G. Gavin, D. Igoe, P. Doherty, J. Skov Gretlund, M. Pacheco Andrade, A. Muir Wood, and M. A.L. Plummer. PISA: New Design Methods for Offshore Wind Turbine Monopiles. In *Offshore Site Investigation and Geotechnics*, pages 142–161. Proceedings of the 8th International Conference 12-14 September 2017 Royal Geographical Society, London, UK, 9 2017.
- [26] F. Celeste. Probing liquefiable soils by cyclic cone penetration, Masters thesis report. Technical report, UGA Grenoble, 2018.
- [27] J. A. Cheney and R. J. Frigaszy. The centrifuge as a research tool. *Geotechnical Testing Journal*, 7(4):182–187, 1984. ISSN 0149-6115.
- [28] W. R. Cox, L. C. Reese, and B. R. Grubbs. Field Testing of Laterally Loaded Piles In Sand, 1974.
- [29] H. M. Coyle and L. C. Reese. Load Transfer for Axially Loaded Piles in Clay. *Journal of the Soil Mechanics and Foundations Division*, 92(2):1–26, 1966.
- [30] C. Cremer, A. Pecker, and L. Davenne. Cyclic macro-element for soil-structure interaction: Material and geometrical non-linearities. *International Journal for Numerical and Analytical Methods in Geomechanics*, 25(13):1257–1284, 2001. ISSN 03639061. doi: 10.1002/nag.175.
- [31] L. Cui and S. Bhattacharya. Soil-monopile interactions for offshore wind turbines. *Proceedings of the Institution of Civil Engineers - Engineering and Computational Mechanics*, 169(4):171–182, 2016. ISSN 1755-0777. doi: 10.1680/jencm.16.00006. URL <http://www.icevirtuallibrary.com/doi/10.1680/jencm.16.00006>.

- [32] Y. F. Dafalias and M. T. Manzari. Simple Plasticity Sand Model Accounting for Fabric Change Effects. *Journal of Engineering Mechanics*, 130(6):622–634, 2004. ISSN 0733-9399. doi: 10.1061/(asce)0733-9399(2004)130:6(622).
- [33] J. Delony. Foundation First: Designing Offshore Wind Turbine Substructures for Maximum Cost Reduction, 2016. URL <https://www.renewableenergyworld.com/2016/12/21>.
- [34] J. Dijkstra, W. Broere, and T. A. F. van. Numerical investigation into stress and strain development around a p displacement pile in sand. *Proceedings of the sixth European Conference on Numerical Methods in Geotechnical Engineering*, pages 595–600, 2006.
- [35] DNV. *Design of offshore wind turbine structures*. Offshore Standard DNV-OS-J101, first edition, 2004.
- [36] DNV. *Design of Offshore Wind Turbine Structures*. Offshore Standard DNV-OS-J101, last edition, 2014.
- [37] W. G. K. Fleming. *Piling engineering*. Blackie A & P John Wiley & Sons, London, 1992. ISBN 0751401943 9780751401943 0470218258 9780470218259.
- [38] J. Garnier, C. Gaudin, S. M. Springman, P. J. Culligan, D. Goodings, D. Konig, B. Kutter, R. Phillips, M. F. Randolph, and L. Thorel. Catalogue of scaling laws and similitude questions in geotechnical centrifuge modelling. *International Journal of Physical Modelling in Geotechnics*, 7(3):1–23, 2007. doi: 10.1680/ijpmg.2007.070301. URL <https://doi.org/10.1680/ijpmg.2007.070301>.
- [39] K. Gavin, D. Igoe, and P. Doherty. Piles for offshore wind turbines: a state-of-the-art review. *Proceedings of the Institution of Civil Engineers - Geotechnical Engineering*, 164(4):245–256, 2011. ISSN 1353-2618. doi: 10.1680/geng.2011.164.4.245. URL <http://www.icevirtuallibrary.com/doi/10.1680/geng.2011.164.4.245>.
- [40] S. Grange. ATLAS—A Tool and Language for Simplified Structural Solution Strategy. Technical report, GEOMAS, INSA-Lyon, Internal Report, GEOMAS, INSA-Lyon: Villeurbanne, France., 2018.
- [41] S. Grange, K. P., and J. Mazars. A macro-element for a circular foundation to simulate 3D soil–structure interaction. *International Journal for Numerical and Analytical Methods in Geomechanics*, 32(10):1205–1227, 6 2008. ISSN 0363-9061. doi: 10.1002/nag.664. URL <https://doi.org/10.1002/nag.664>.
- [42] S. Grange, P. Kotronis, and J. Mazars. A macro-element to simulate 3D soil-structure interaction considering plasticity and uplift. *International Journal of Solids and Structures*, 46(20):3651–3663, 2009. ISSN 00207683. doi: 10.1016/j.ijsolstr.2009.06.015. URL <http://dx.doi.org/10.1016/j.ijsolstr.2009.06.015>.
- [43] M. A. Heib, F. Emeriault, M. Caudron, L. Nghiem, and B. Hor. Large-scale soil–structure physical model (1g) – assessment of structure damages. *International Journal of Physical Modelling in Geotechnics*, 13(4):138–152, 12 2013. ISSN 1346-213X. doi: 10.1680/ijpmg.13.00007. URL <https://doi.org/10.1680/ijpmg.13.00007>.

- [44] M. Heidari, H. El Naggar, M. Jahanandish, and A. Ghahramani. Generalized cyclic p-y curve modeling for analysis of laterally loaded piles. *Soil Dynamics and Earthquake Engineering*, 63:138–149, 2014. ISSN 02677261. doi: 10.1016/j.soildyn.2014.04.001. URL <http://dx.doi.org/10.1016/j.soildyn.2014.04.001>.
- [45] Y. Hong, B. He, L. Z. Wang, Z. Wang, C. W. Ng, and D. Mašín. Cyclic lateral response and failure mechanisms of semi-rigid pile in soft clay: Centrifuge tests and numerical modelling. *Canadian Geotechnical Journal*, 54(6):806–824, 2017. ISSN 12086010. doi: 10.1139/cgj-2016-0356.
- [46] G. Houlsby and A. Puzrin. The Hyperplastic Formalism BT - Principles of Hyperplasticity: An Approach to Plasticity Theory Based on Thermodynamic Principles. In G. T. Houlsby and A. M. Puzrin, editors, *Principles of Hyperplasticity*, pages 53–75. Springer London, London, 2007. ISBN 978-1-84628-240-9. doi: 10.1007/978-1-84628-240-9_{_}4. URL https://doi.org/10.1007/978-1-84628-240-9_4.
- [47] G. T. Houlsby and M. J. Cassidy. A plasticity model for the behaviour of footings on sand under combined loading. *Géotechnique*, 52(2):117–129, 2002. ISSN 0016-8505. doi: 10.1680/geot.2002.52.2.117. URL <http://www.icevirtuallibrary.com.libproxy1.nus.edu.sg/content/article/10.1680/geot.2002.52.2.117>.
- [48] G. T. Houlsby, C. N. Abadie, W. J. Beuckelaers, and B. W. Byrne. A model for nonlinear hysteretic and ratcheting behaviour. *International Journal of Solids and Structures*, 120: 67–80, 2017. ISSN 00207683. doi: 10.1016/j.ijsolstr.2017.04.031. URL <http://dx.doi.org/10.1016/j.ijsolstr.2017.04.031>.
- [49] M. Iskander. *Similitude between Model and Full Scale Piles BT - Behavior of Pipe Piles in Sand: Plugging and Pore-Water Pressure Generation During Installation and Loading*. Springer Berlin Heidelberg, Berlin, Heidelberg, 2011. ISBN 978-3-642-13108-0. doi: 10.1007/978-3-642-13108-0_{_}8. URL https://doi.org/10.1007/978-3-642-13108-0_8.
- [50] S. Jalbi, L. Arany, A. R. Salem, L. Cui, and S. Bhattacharya. A method to predict the cyclic loading profiles (one-way or two-way) for monopile supported offshore wind turbines. *Marine Structures*, 63(May 2018):65–83, 2019. ISSN 09518339. doi: 10.1016/j.marstruc.2018.09.002.
- [51] R. Jardine, F. C. Chow, R. F. Overy, and J. R. Standing. *ICP design methods for driven piles in sands and clays*. Thomas Telford Services Ltd, 2005. ISBN 9780727732729.
- [52] R. J. Jardine, B. T. Zhu, P. Foray, and C. P. Dalton. Experimental Arrangements for Investigation of Soil Stresses Developed Around a Displacement Pile. *Soils and Foundations*, 49(5):661–673, 2009. ISSN 0038-0806. doi: 10.3208/sandf.49.661.
- [53] S. Jung, S. R. Kim, A. Patil, and L. C. Hung. Effect of monopile foundation modeling on the structural response of a 5-MW offshore wind turbine tower. *Ocean Engineering*, 109: 479–488, 2015. ISSN 00298018. doi: 10.1016/j.oceaneng.2015.09.033.
- [54] D. Kallehave, C. L. Thilsted, and M. A. Liingaard. Modification of the API P-y Formulation of Initial Stiffness of Sand, 2012. URL <https://doi.org/>.

- [55] D. Kallehave, B. W. Byrne, C. LeBlanc Thilsted, and K. K. Mikkelsen. Optimization of monopiles for offshore wind turbines. *Philosophical Transactions of the Royal Society A: Mathematical, Physical and Engineering Sciences*, 373(2035), 2015. ISSN 1364-503X. doi: 10.1098/rsta.2014.0100.
- [56] L. Kerner, J.-C. Dupla, G. Cumunel, P. Argoul, J. Canou, and J.-M. Pereira. Experimental Study on a Scaled Model of Offshore Wind Turbine on Monopile Foundation BT - Models, Simulation, and Experimental Issues in Structural Mechanics. In M. Frémond, F. Maceri, and G. Vairo, editors, *Models, Simulation, and Experimental Issues in Structural Mechanics*, pages 249–267. Springer International Publishing, Cham, 2017. ISBN 978-3-319-48884-4. doi: 10.1007/978-3-319-48884-4_{_}14. URL https://doi.org/10.1007/978-3-319-48884-4_14.
- [57] R. T. Klinkvort and O. Hededal. Effect of load eccentricity and stress level on monopile support for offshore wind turbines. *Canadian Geotechnical Journal*, 51(9):966–974, 3 2014. ISSN 0008-3674. doi: 10.1139/cgj-2013-0475. URL <https://doi.org/10.1139/cgj-2013-0475>.
- [58] J. Kodikara, A. Haque, and K. Y. Lee. Theoretical p-y curves for laterally loaded single piles in undrained clay using bezier curves. *Journal of Geotechnical and Geoenvironmental Engineering*, 136(1):265–268, 2010. ISSN 10900241. doi: 10.1061/(ASCE)1090-0241(2010)136:1(265).
- [59] H. L. Langhaar. *Dimensional analysis and theory of models*. Krieger, Huntington, N.Y., 1980. ISBN 0882756826 9780882756820.
- [60] C. Leblanc, G. Houlby, and B. Byrne. Response of stiff piles in sand to long-term cyclic lateral loading. *Géotechnique*, 60(2):79–90, 2010. ISSN 0016-8505. doi: 10.1680/geot.7.00196.
- [61] J. Lee, M. Kim, and D. Kyung. Estimation of Lateral Load Capacity of Rigid Short Piles in Sands Using CPT Results. *Journal of Geotechnical and Geoenvironmental Engineering*, 136(1):48–56, 2010. ISSN 1090-0241. doi: 10.1061/(ASCE)GT.1943-5606.0000199. URL [http://ascelibrary.org/doi/pdf/10.1061/\(ASCE\)GT.1943-5606.0000199%0Ahttp://ascelibrary.org/doi/10.1061/%28ASCE%29GT.1943-5606.0000199](http://ascelibrary.org/doi/pdf/10.1061/(ASCE)GT.1943-5606.0000199%0Ahttp://ascelibrary.org/doi/10.1061/%28ASCE%29GT.1943-5606.0000199).
- [62] Z. Li, P. Kotronis, and S. Escoffier. Numerical study of the 3D failure envelope of a single pile in sand. *Computers and Geotechnics*, 62:11–26, 2014. ISSN 0266352X. doi: 10.1016/j.compgeo.2014.06.004. URL <http://dx.doi.org/10.1016/j.compgeo.2014.06.004>.
- [63] Z. Li, P. Kotronis, S. Escoffier, and C. Tamagnini. A hypoplastic macroelement for single vertical piles in sand subject to three-dimensional loading conditions. *Acta Geotechnica*, 11(2):373–390, 2016. ISSN 18611133. doi: 10.1007/s11440-015-0415-7.
- [64] H. Y. Liu, J. A. Abell, A. Diambra, and F. Pisanò. Modelling the cyclic ratcheting of sands through memory-enhanced bounding surface plasticity. *Géotechnique*, 69(9):783–800, 2019. doi: 10.1680/jgeot.17.P.307. URL <https://doi.org/10.1680/jgeot.17.P.307>.

- [65] D. Lombardi, S. Bhattacharya, and D. Muir Wood. Dynamic soil–structure interaction of monopile supported wind turbines in cohesive soil. *Soil Dynamics and Earthquake Engineering*, 49:165–180, 2013. ISSN 0267-7261. doi: <https://doi.org/10.1016/j.soildyn.2013.01.015>. URL <http://www.sciencedirect.com/science/article/pii/S0267726113000171>.
- [66] G. Masing. Eigenspannungen and verfestigung Beim Messing. *Proceedings of Second International Congress of Applied Mechanics, Zurich, 1926*, 332, 1926. URL <https://ci.nii.ac.jp/naid/10027017634/en/>.
- [67] G. G. Meyerhof and D. P. Ghosh. Ultimate capacity of flexible piles under eccentric and inclined loads. *Canadian Geotechnical Journal*, 26(1):34–42, 2 1989. ISSN 0008-3674. doi: 10.1139/t89-004. URL <https://doi.org/10.1139/t89-004>.
- [68] G. G. Meyerhof and G. Ranjan. The Bearing Capacity of Rigid Piles Under Inclined Loads in Sand. I: Vertical Piles. *Canadian Geotechnical Journal*, 9(4):430–446, 11 1972. ISSN 0008-3674. doi: 10.1139/t72-043. URL <https://doi.org/10.1139/t72-043>.
- [69] Z. S. Z. Mosquera, C. d. H. C. Tsuha, J. A. Schiavon, and L. Thorel. Discussion of “Field investigation of the axial resistance of helical piles in dense sand”. *Canadian Geotechnical Journal*, 52(8):1190–1194, 7 2015. ISSN 0008-3674. doi: 10.1139/cgj-2015-0212. URL <https://doi.org/10.1139/cgj-2015-0212>.
- [70] E. Motta. Lateral Deflection of Horizontally Loaded Rigid Piles in Elastoplastic Medium. *Journal of Geotechnical and Geoenvironmental Engineering*, 139(March):501–507, 2013. doi: 10.1061/(ASCE)GT.1943-5606.0000771. URL [http://dx.doi.org/10.1061/\(ASCE\)GT.1943-5606.0000771](http://dx.doi.org/10.1061/(ASCE)GT.1943-5606.0000771).
- [71] S. Nanda, I. Arthur, V. Sivakumar, S. Donohue, A. Bradshaw, R. Keltai, K. Gavin, P. Mackinnon, B. Rankin, and D. Glynn. Monopiles subjected to uni- and multi-lateral cyclic loading. *Proceedings of the Institution of Civil Engineers - Geotechnical Engineering*, 170(3):246–258, 1 2017. ISSN 1353-2618. doi: 10.1680/jgeen.16.00110. URL <https://doi.org/10.1680/jgeen.16.00110>.
- [72] V. Negro, J. S. López-Gutiérrez, M. D. Esteban, P. Alberdi, M. Imaz, and J. M. Serraclara. Monopiles in offshore wind: Preliminary estimate of main dimensions. *Ocean Engineering*, 133(December 2016):253–261, 2017. ISSN 00298018. doi: 10.1016/j.oceaneng.2017.02.011.
- [73] G. Nikitas, N. J. Vimalan, and S. Bhattacharya. An innovative cyclic loading device to study long term performance of offshore wind turbines. *Soil Dynamics and Earthquake Engineering*, 82:154–160, 2016. ISSN 02677261. doi: 10.1016/j.soildyn.2015.12.008. URL <http://dx.doi.org/10.1016/j.soildyn.2015.12.008>.
- [74] G. Nikitas, L. Arany, S. Aingaran, J. Vimalan, and S. Bhattacharya. Predicting long term performance of offshore wind turbines using cyclic simple shear apparatus. *Soil Dynamics and Earthquake Engineering*, 92(September 2016):678–683, 2017. ISSN 02677261. doi: 10.1016/j.soildyn.2016.09.010. URL <http://linkinghub.elsevier.com/retrieve/pii/S0267726116302184>.

- [75] R. Nova and L. Montrasio. Settlements of shallow foundations on sand. *Géotechnique*, 41(2):243–256, 1991. ISSN 0016-8505. doi: 10.1680/geot.1991.41.2.243. URL <http://www.icevirtuallibrary.com/doi/10.1680/geot.1991.41.2.243>.
- [76] K. Y. Oh, W. Nam, M. S. Ryu, J. Y. Kim, and B. I. Epureanu. A review of foundations of offshore wind energy convertors: Current status and future perspectives. *Renewable and Sustainable Energy Reviews*, 88(February 2017):16–36, 2018. ISSN 18790690. doi: 10.1016/j.rser.2018.02.005.
- [77] A. M. Page, K. S. Skau, H. P. Jostad, and G. R. Eiksund. A New Foundation Model for Integrated Analyses of Monopile-based Offshore Wind Turbines. *Energy Procedia*, 137:100–107, 2017. ISSN 18766102. doi: 10.1016/j.egypro.2017.10.337. URL <https://doi.org/10.1016/j.egypro.2017.10.337>.
- [78] A. M. Page, G. Grimstad, G. R. Eiksund, and H. P. Jostad. A macro-element pile foundation model for integrated analyses of monopile-based offshore wind turbines. *Ocean Engineering*, 167(January):23–35, 2018. ISSN 00298018. doi: 10.1016/j.oceaneng.2018.08.019. URL <https://linkinghub.elsevier.com/retrieve/pii/S0029801818315142>.
- [79] K. Paik and R. Salgado. Determination of Bearing Capacity of Open-Ended Piles in Sand. *Journal of Geotechnical and Geoenvironmental Engineering*, 129(1):46–57, 1 2003. doi: 10.1061/(ASCE)1090-0241(2003)129:1(46). URL [https://doi.org/10.1061/\(ASCE\)1090-0241\(2003\)129:1\(46\)](https://doi.org/10.1061/(ASCE)1090-0241(2003)129:1(46)).
- [80] G. Petrasovits and A. Award. No Title Ultimate lateral resistance of a rigid pile in cohesionless soil. In *5th European Conference on SMFE 3, The Spanish Society for Soil Mechanics and Foundation*, pages 407–412. The Spanish Society for Soil Mechanics and Foundation, 1972.
- [81] H. Poulos and T. Hull. *Role of Analytical Geomechanics in Foundation Engineering*. American Society of Civil Engineers, New York, NY, 1989. ISBN 0872627047.
- [82] Y. V. S. N. Prasad and T. R. Chari. LATERAL CAPACITY OF MODEL RIGID PILES IN COHESIONLESS SOILS. *SOILS AND FOUNDATIONS*, 39(2):21–29, 1999. doi: 10.3208/sandf.39.2{_}21.
- [83] A. Puech and J. Garnier. Design of piles under cyclic loading : SOLCYP recommendations, 2017. URL <https://search.ebscohost.com/login.aspx?direct=true&scope=site&db=nlebk&db=nlabk&AN=1642569>.
- [84] M. F. Randolph and C. P. Wroth. Analysis of deformation of vertically loaded piles. *Journal of Geotechnical and Geoenvironmental Engineering*, 104(ASCE 14262), 1978. ISSN 1090-0241.
- [85] L. C. Reese, W. R. Cox, and F. D. Koop. Analysis of Laterally Loaded Piles in Sand. In *Offshore Technology Conference*, pages 473–485, Houston, Texas, 1974. Offshore Technology Conference. ISBN 978-1-55563-634-0. doi: 10.4043/2080-MS.
- [86] D. Salciarini and C. Tamagnini. A hypoplastic macroelement model for shallow foundations under monotonic and cyclic loads. *Acta Geotechnica*, 4(3):163–176, 2009. ISSN 18611125. doi: 10.1007/s11440-009-0087-2.

- [87] R. Salgado and M. Randolph. Analysis of Cavity Expansion in Sand. *International Journal of Geomechanics*, 1(2):175–192, 4 2001. doi: 10.1061/(ASCE)1532-3641(2001)1:2(175). URL [https://doi.org/10.1061/\(ASCE\)1532-3641\(2001\)1:2\(175\)](https://doi.org/10.1061/(ASCE)1532-3641(2001)1:2(175)).
- [88] R. Salgado, M. J. K., and J. M. Calibration Chamber Size Effects on Penetration Resistance in Sand. *Journal of Geotechnical and Geoenvironmental Engineering*, 124(9):878–888, 9 1998. doi: 10.1061/(ASCE)1090-0241(1998)124:9(878). URL [https://doi.org/10.1061/\(ASCE\)1090-0241\(1998\)124:9\(878\)](https://doi.org/10.1061/(ASCE)1090-0241(1998)124:9(878)).
- [89] T. Schanz, P. Varmeer, and P. Bonnier. The hardening soil model: Formulation and verification. *Beyond 2000 Comput. Geotech. 10 years PLAXIS Int. ProcInt. Symp. beyond 2000 Comput. Geotech. Amsterdam Netherlands 1820 March 1999*, pages 104–144, 1999.
- [90] F. Schnaid and G. T. Houlsby. An assessment of chamber size effects in the calibration of in situ tests in sand. *Géotechnique*, 41(3):437–445, 1991. doi: 10.1680/geot.1991.41.3.437. URL <https://doi.org/10.1680/geot.1991.41.3.437>.
- [91] G. Sedran, D. F. E. Stolle, and R. G. Horvath. An investigation of scaling and dimensional analysis of axially loaded piles. *Canadian Geotechnical Journal*, 38(3):530–541, 2001. ISSN 0008-3674. doi: Doi10.1139/Cgj-38-3-530.
- [92] M. Shadlou and S. Bhattacharya. Dynamic stiffness of monopiles supporting offshore wind turbine generators. *Soil Dynamics and Earthquake Engineering*, 88:15–32, 2016. ISSN 02677261. doi: 10.1016/j.soildyn.2016.04.002. URL <http://dx.doi.org/10.1016/j.soildyn.2016.04.002>.
- [93] B. B. Sheil and B. A. McCabe. Biaxial Loading of Offshore Monopiles: Numerical Modeling. *International Journal of Geomechanics*, 17(2):04016050, 2017. ISSN 1532-3641. doi: 10.1061/(ASCE)GM.1943-5622.0000709. URL <http://ascelibrary.org/doi/10.1061/%28ASCE%29GM.1943-5622.0000709>.
- [94] M. F. Silva Illanes. *Experimental study of ageing and axial cyclic loading effect on shaft friction along driven piles in sands*. PhD thesis, UGA Grenoble, 2014.
- [95] J. C. Simo and T. J. R. Hughes. *Computational inelasticity*, volume 7. Springer Science & Business Media, 1998. ISBN 0387227636.
- [96] S. P. H. Sørensen, K. T. Brødbæk, M. Møller, and A. H. Augustesen. *Review of Laterally Loaded Monopiles Employed as the Foundation for Offshore Wind Turbines*. Number 137 in DCE Technical reports. Department of Civil Engineering, Aalborg University, Denmark, 2012.
- [97] H. Sturm and L. Andresen. On the Use of the Finite Element Method for the Design of Offshore Wind Turbine Foundations BT - Desiderata Geotechnica. In W. Wu, editor, *Desiderata Geotechnica*, pages 193–204. Springer International Publishing, Cham, 2019. ISBN 978-3-030-14987-1.
- [98] E. Taciroglu, C. Rha, J. W. Wallace, and M. Asce. A Robust Macroelement Model for Soil – Pile Interaction under Cyclic Loads. *Journal of Geotechnical and Geoenvironmental Engineering*, 132(October):1304–1314, 2006. ISSN 10900241. doi: 10.1061/?ASCE?1090-0241?2006?132:10?1304?

- [99] C. H. C. Tsuha, P. Y. Foray, R. J. Jardine, Z. X. Yang, M. Silva, and S. Rimoy. Behaviour of displacement piles in sand under cyclic axial loading. *Soils and Foundations*, 52(3): 393–410, 2012. ISSN 00380806. doi: 10.1016/j.sandf.2012.05.002. URL <http://dx.doi.org/10.1016/j.sandf.2012.05.002>.
- [100] W. WindEurope. Wind energy in Europe in 2019 Trends and statistics. Technical report, Wind Europe, Brussels, 2020. URL <https://windeurope.org/about-wind/statistics/european/wind-energy-in-europe-in-2019/>.
- [101] M. Yang, B. Ge, W. Li, and B. Zhu. Dimension Effect on P-y Model Used for Design of Laterally Loaded Piles. *Procedia Engineering*, 143(Ictg):598–606, 2016. ISSN 18777058. doi: 10.1016/j.proeng.2016.06.079. URL <http://dx.doi.org/10.1016/j.proeng.2016.06.079>.
- [102] L. Zdravković, D. M. Taborda, D. M. Potts, R. J. Jardine, M. Sideri, F. C. Schroeder, B. W. Byrne, R. McAdam, H. J. Burd, G. T. Houlsby, C. M. Martin, K. Gavin, P. Doherty, D. Igoe, A. Muirwood, D. Kallehave, and J. Skov Gretlund. Numerical modelling of large diameter piles under lateral loading for offshore wind applications. In *Frontiers in Offshore Geotechnics III - Proceedings of the 3rd International Symposium on Frontiers in Offshore Geotechnics, ISFOG 2015*, pages 759–764. CRC Press, 2015. ISBN 9781138028500. doi: 10.1201/b18442-105.
- [103] B. Zhu, B. B. W., and H. G. T. Long-Term Lateral Cyclic Response of Suction Caisson Foundations in Sand. *Journal of Geotechnical and Geoenvironmental Engineering*, 139(1): 73–83, 1 2013. doi: 10.1061/(ASCE)GT.1943-5606.0000738. URL [https://doi.org/10.1061/\(ASCE\)GT.1943-5606.0000738](https://doi.org/10.1061/(ASCE)GT.1943-5606.0000738).